

Experimental and Theoretical Investigations of the Charge and
Spin Densities of Small Molecules

Kirsty Laura McCormack

Thesis submitted for the degree of Doctor of Philosophy

Department of Chemistry

University of Glasgow

July 1997

UNIVERSITY OF GLASGOW
LIBRARY
1997

ProQuest Number: 11007704

All rights reserved

INFORMATION TO ALL USERS

The quality of this reproduction is dependent upon the quality of the copy submitted.

In the unlikely event that the author did not send a complete manuscript and there are missing pages, these will be noted. Also, if material had to be removed, a note will indicate the deletion.



ProQuest 11007704

Published by ProQuest LLC (2018). Copyright of the Dissertation is held by the Author.

All rights reserved.

This work is protected against unauthorized copying under Title 17, United States Code
Microform Edition © ProQuest LLC.

ProQuest LLC.
789 East Eisenhower Parkway
P.O. Box 1346
Ann Arbor, MI 48106 – 1346



Thesis

10922

copy 1

“Natural Science does not simply describe and explain nature; it is part of the interplay between nature and ourselves; it describes nature as exposed to our method of questioning.”

Werner Heisenberg
in *Physics and Philosophy*, 1959

Abstract

The major part of this thesis is concerned with the determination of the charge densities of small organic molecules, using both experimental and theoretical methods. A smaller section details the theoretical determination of the spin densities of some sulfur-containing model systems.

Chapter 1 traces the historical development of the theory of multipole modelling from the development of the first aspherical scattering factors. The practical implementation of the method, the experimental requirements and subsequent treatment of the data are also discussed. Chapter 2 gives a summary of *ab initio* molecular orbital methods. Particular attention is given to the way in which the atomic and molecular properties which are of interest to the chemist are obtained from the calculated wavefunction.

Throughout the relevant results chapters the experimental and theoretical charge densities are analysed using Bader's theory of Atoms in Molecules. Chapter 3 gives an outline of this analytical approach.

Chapter 4 reports the results of experimental and theoretical charge density studies of 3,3,6,6-tetramethyl-s-tetrathiane. Particular attention is given to the strength of the sulfur-sulfur bond. An *ab initio* study is made of the relative stabilities of the three possible conformers of the molecule. An experimental charge density study of hexakis(mercaptomethyl)benzene is reported in Chapter 5; evidence is found for the existence of intermolecular SH...S hydrogen bonding. Chapter 6 contains experimental and theoretical results for the charge density study of a salt of the antifungal compound *E*-tetraethyl-1,4-diammoniumbut-2-ene.

A quite different area of physical chemistry is investigated in Chapter 7. The results of a series of calculations of the hyperfine coupling constants of muonium in sulfur environments are presented. This work was carried out in order to try to identify the muonic radical species which is observed by μ SR when muons are introduced into elemental sulfur.

Acknowledgements

I would like to thank my supervisors Dr Paul Mallinson and Dr Brian Webster for their help and guidance with the academic aspects of the work described in this thesis. Also, for their support and faith over the last three years. The continuing interest and advice of Dr Dmitrii Yufit and Dr Garry Smith have also been invaluable to me.

The experimental aspects of this research would not have been possible without the availability of good-quality samples. I would therefore like to thank Dr David MacNicol, Lindsay Slater and Prof David Robins for providing the compounds. Thanks are also due to Dr Jamie Platts for running calculations with GAUSSIAN 94.

I would also like to thank my friends here in the department for making the time enjoyable, and in particular Geraldine Boyce for being much more interested in electrons than in running columns.

I wish to acknowledge the use of the EPSRC's Chemical Database Service at Daresbury, and thank the EPSRC for my postgraduate studentship.

Contents

1 The Theory and Practice of Multipole Modelling

1.1 Introduction	1
1.1.1 Historical Perspective	1
1.1.2 Why Do the Experiment?	2
1.1.3 Applications	3
1.2 Scattering by Spherical Atoms	4
1.2.1 General Scattering of X-rays	4
1.2.2 Scattering by a Crystal	5
1.2.3 The Spherical Scattering Factor	7
1.2.4 Temperature Effects	9
1.3 Beyond the Spherical Atom Approximation	10
1.3.1 Limitations of the Independent Atom Model	10
1.3.2 The Kappa Formalism	11
1.3.3 The Development of the First Aspherical Scattering Factor	12
1.4 Development of the Generalised Structure Factor	14
1.4.1 Dawson's Cubic Harmonic Approach	14
1.4.2 Stewart's Spherical Harmonic Approach	16
1.5 The Multipole Model	18
1.5.1 Practical Implementation	19
1.6 Experimental Considerations	21
1.6.1 Data Collection	22
1.6.2 Compound and Crystal Choice	23
1.6.3 Low-Temperature Requirement	24
1.7 Data Reduction	25
1.7.1 Obtaining Raw Reflection Intensities	25
1.7.2 Crystal Decay	26
1.7.3 Absorption Corrections	26
1.7.4 Data Merging	28
1.8 Testing the Reliability of the Model	29

2 Quantum Chemical Methods

2.1 Introduction	31
2.2 Theoretical Background	32
2.2.1 The Schrödinger Equation	32
2.2.2 The Born-Oppenheimer Approximation	33
2.3 Molecular Orbital Theory	35
2.3.1 The Slater Determinant	35
2.3.2 Variational Methods	36
2.3.3 The Roothaan-Hall Equations	37
2.3.4 Practical Implementation	39
2.4 Basis Set Expansions	41
2.4.1 The Effect of Basis Set Choice	41
2.4.2 Slater and Gaussian Type Orbitals	41
2.4.3 Types of Basis Set	43
2.5 Open-Shell Systems	46
2.6 Electron Correlation	47
2.6.1 Full Configuration Interaction	47
2.6.2 Limited Configuration Interaction	48
2.6.3 Møller-Plesset Perturbation Theory	49
2.7 Derivation of Properties	51
2.7.1 Electronic Charge Density	51
2.7.2 Mulliken Population Analysis	51
2.7.3 Electrostatic Potential	52
2.7.4 Spin Density	53

3 The Topology of the Charge Density

3.1 Introduction	54
3.2 Critical Points	54
3.3 Properties of Bond Critical Points	58
3.3.1 Bond Path	59
3.3.2 Bond Strength	59
3.3.3 Bond Ellipticity	60

3.4 The Laplacian	60
4 Experimental and Theoretical Studies of the Charge Density Distribution in 3,3,6,6-Tetramethyl-s-tetrathiane	
4.1 Introduction	62
4.2 Experimental	64
4.2.1 Multipole Refinement	64
4.3 Results and Discussion of the Experimental Study	66
4.3.1 Structural Results	66
4.3.2 Comparison of Experimental and Theoretical Charge Density Distributions	69
4.3.3 Determination of S-S Bond Strength	76
4.4 <i>Ab Initio</i> Studies of the Conformers of 3,3,6,6-tetramethyl-s-tetrathiane	77
4.4.1 The Twist-boat Conformer	77
4.4.2 The Chair Conformer	83
4.4.3 The Boat Conformer	84
4.4.4 Comparison of the Conformers	84
4.5 Conclusions	85
5 Experimental Charge Density Study of Hexakis(mercaptomethyl)benzene	
5.1 Introduction	86
5.2 Experimental	89
5.2.1 Treatment of Data	89
5.2.2 Multipole Refinement	90
5.3 Results and Discussion	91
5.3.1 Treatment of Data	91
5.3.2 Experimental Charge Density Analysis and Comparison with Theory	99
5.3.3 Evidence for Intermolecular SH...S Bonding	101
5.4 Conclusion	103

6	Experimental and Theoretical Studies of the Charge Density Distribution in <i>E</i>-Tetraethyl-1,4-diammoniumbut-2-ene.2PF_6	
6.1	Introduction	104
6.2	Experimental	105
6.2.1	Multipole Refinement	106
6.3	Results and Discussion	108
6.3.1	Structural Results	108
6.3.2	Atomic Charges and Electrostatic Potential	111
6.3.3	Topological Analysis of the Charge Density Distribution	116
6.4	Conclusion	118
7	Hyperfine Coupling Constants for Muonium in Elemental Sulfur Environments	
7.1	Introduction	119
7.2	Avoided Level Crossing Muon Spectroscopy	121
7.2.1	Experimental Method	121
7.2.2	Hyperfine Structure	123
7.3	Muon-Electron Hyperfine Coupling Constants for Muonium in Elemental Sulfur	124
7.3.1	Computation	125
7.3.2	The Muonium-Containing Radical	126
7.3.3	The Interstitial Muonium Atom	130
7.4	Conclusions	135
	Note on Units	136
	References	137
Appendix A	Supplementary Data for 3,3,6,6-Tetramethyl-<i>s</i>-tetrathiane	144

Appendix B	Supplementary Data for	
	Hexakis(mercaptomethyl)benzene	147
Appendix C	Supplementary Data for	
	<i>E</i>-Tetraethyl-1,4-diammoniumbut-2-ene.2PF₆	150
Publications		155

List of Tables

4.1 :	Experimental data for 3,3,6,6-tetramethyl-s-tetrathiane.	67
4.2 :	Comparison of selected structural parameters from this work and the earlier crystal structure determination.	68
4.3 :	Critical point analysis for the twist-boat conformer of 1 at the experimental geometry.	72
4.4 :	Critical point data for S-S bonds.	76
4.5 :	Results of geometry optimisations of 1 at successive basis set levels.	77
4.6 :	Effect of <i>d</i> -orbital polarisation functions on bond lengths.	78
4.7 :	<i>d</i> -orbital populations for different basis sets.	79
4.8 :	Critical point data for the geometry-optimised twist-boat form of 1 , RHF/6-311G**.	80
4.9 :	Critical point data for the twist-boat conformation of 1 , MP2/6-311G**//RHF/6-31G**.	82
4.10 :	Critical point data for the chair conformer of 1 , RHF/6-311G**.	83
4.11 :	Components of the molecular energy for the conformers of 1 .	85
5.1 :	Experimental data for hexakis(mercaptomethyl)benzene.	92
5.2 :	Different treatments of the raw diffraction data.	93
5.3 :	Effects of different 2 θ cut-off values.	99
5.4 :	Critical point data for hexakis(mercaptomethyl)benzene.	101
6.1 :	Experimental data for <i>E</i> -tetraethyl-1,4-diammoniumbut-2-ene.2PF ₆ .	109
6.2 :	Mean-square atomic displacements (\AA^2) for the anion.	111
6.3 :	Atomic charges for the atoms in TEDH ₂ ²⁺ .	112
6.4 :	¹ H NMR data for TED and TEDH ₂ ²⁺ .	112

6.5 :	Critical point data for selected bonds in E-tetraethyl-1,4-diammoniumbut-2-ene. $2PF_6$.	117
7.1:	Physical properties for the proton, the positive muon and the electron.	121
7.2 :	Starting geometries and initial energies and hyperfine coupling constants for the model systems <i>A</i> to <i>F</i> .	127
7.3 :	Energies and hyperfine coupling constants for different heights of the atom above the centre of an S_8 ring.	muonium 131
7.4 :	Model systems and associated Mu...S distances and hyperfine coupling constants for the interstitial muonium atom.	132
7.5 :	The calculated energy and hyperfine coupling constant, A_{μ} , for various positions of the interstitial muonium atom.	134
A1 :	Fractional atomic coordinates	144
A2 :	Mean-square atomic displacements	145
A3 :	Multipole population coefficients	145
A4 :	Local coordinate systems	146
B1 :	Fractional atomic coordinates	147
B2 :	Mean-square atomic displacements	148
B3 :	Multipole population coefficients	148
B4 :	Local coordinate systems	149
C1 :	Fractional atomic coordinates	150
C2 :	Mean-square atomic displacements	151
C3 :	Multipole population coefficients	152
C4 :	Local coordinate systems	154

List of Figures

1.1 :	Plot of the atomic scattering factor, f_j , against $\sin\theta/\lambda$ for O, S and Na^+ .	9
1.2 :	Fourier difference maps for the $(1\bar{1}0)$ plane of diamond.	16
2.1 :	Flow chart for the SCF procedure.	40
3.1 :	Relief and contour plots of the electronic charge density in three planes of the ethene molecule.	57
4.1 :	Molecular structure of 1 in the twist-boat conformation found in the crystal.	65
4.2 :	A view along the c axis showing the packing of 1 in the molecular crystal.	65
4.3 :	Scatter plot of the S-S bond length against torsion angle for all occurrences of the C-S-S-C fragment in the CSD.	69
4.4 :	Residual density map in the C1-S1-S1a plane.	70
4.5 :	Static deformation density map in the C1-S1-S1a plane.	71
4.6 :	Experimental Laplacian distribution showing the S...S intermolecular interaction.	73
4.7 :	Laplacian distribution in the C1-S1-S1a plane: (a) experimental; (b) theoretical.	75
4.8 :	Difference density plot in the mean plane through the ring, 6-31G* - 6-31.	78
4.9 :	Plot of the Laplacian of the geometry-optimised twist-boat form of 1 , showing the S1...S1c closed-shell interaction.	81
4.10 :	The optimised chair conformer of 1 .	83
5.1 :	A view normal to the c axis showing how 2 packs in the crystal.	90
5.2 (a)-(d) :	Residual density in the plane S1-C2-C1 for models A to D respectively.	94

5.2 (e)-(h) : Residual density in the plane S1-C2-C1 for models <i>E</i> to <i>H</i> respectively.	95
5.3 (c), (d) : Experimental Laplacian distribution in the plane S1-C2-C1 for models <i>C</i> and <i>D</i> .	96
5.3 (e), (f), (h) : Experimental Laplacian distribution in the plane S1-C2-C1 for models <i>E</i> , <i>F</i> and <i>H</i> .	97
5.4 : Theoretical Laplacian distribution for the plane S1-C2-C1.	98
5.5 : Laplacian distribution in the plane of the aromatic ring: (a) experimental; (b) theoretical.	100
5.6(a) : Static deformation density map showing the SH...S interaction bond path and associated critical point.	102
5.6(b) : Experimental Laplacian distribution for the SH...S interaction bond path and associated critical point.	102
6.1 : Structures of: (a) the cation TEDH_2^{2+} ; (b) the anion $[\text{PF}_6]^-$.	107
6.2 : Residual density for: (a) the cation in the plane C2-C1-C1'-C2'; (b) the anion in the plane F1-P1-F2.	110
6.3 : The theoretical electrostatic potential of the TEDH_2^{2+} ion in the N1-C1-C1' plane.	114
6.4 : The electrostatic potential surface of the model phosphate group, $[\text{PO}_2(\text{OCH}_3)_2]^-$ in the plane O-P-O.	115
6.5 : Laplacian distribution for TEDH_2^{2+} in the C2-C1-C1'-C2' plane: (a) experimental; (b) theoretical.	116
7.1 : Schematic diagram of the experimental apparatus used for ALC spectroscopy.	122
7.2 : Breit-Rabi diagram for the isolated muonium atom.	123
7.3 : An ALC spectrum showing the resonance which corresponds to the muonium-containing radical.	125
7.4 : Geometry of model <i>F</i> , to scale: (a) initial; (b) optimised.	128
7.5 : Unit cell of γ -sulfur showing the position of the S...S internuclear vector for the interstitial muonium atom model.	133

7.6 : Variation of A_{μ} with distance from S1 for the interstitial muonium atom in S_8 .	134
---	-----

Chapter 1

The Theory and Practice of Multipole Modelling

1.1 Introduction

1.1.1 Historical Perspective

Experimental measurement of electron density distributions depends on the ability of crystals to diffract X-rays. This phenomenon was first observed by von Laue in 1912 and was used to provide evidence for two postulates: that X-rays display wave character, and that a crystal is a periodic three-dimensional arrangement of atoms. Debye was convinced that X-ray diffraction could be used to probe the electronic structure of atoms and wrote in 1915:

“It seems to me that experimental study of the scattered radiation, in particular from light atoms, should get more attention, since along this way it should be possible to determine the arrangement of the electrons in the atoms.”¹

This statement, and Debye’s subsequent work, effectively initiated the field of charge density research. Together with Scherrer he began to study a series of ionic crystals and to draw conclusions about the relative charges on the atoms, based on the X-ray diffraction evidence.² Their work was later criticised by Bragg *et al*:

“It is interesting to see whether any evidence can be obtained as to whether a valency electron has been transferred from one atom to the other or not. ... It appears impossible to do this; and, when we come to consider the problem more closely, it seems that crystal analysis must be pushed to a far greater degree of refinement before it can settle the point.”³

This negative view of the possibility of obtaining charge density information from X-ray diffraction data persisted until technological advances made available the “greater degree of refinement” required for such studies. The advent of automated diffractometers and scintillation counters, as opposed to film techniques, meant that much more accurate intensity and profile information could be extracted from experimental measurements. The addition of computing facilities to perform the necessary mathematical operations ensured that experimental charge density research could become a practical possibility. As a result of these technical developments there has been active research in the area since the 1960s.

1.1.2 Why Do the Experiment?

From a chemist’s point of view there is much to be gained from a knowledge of the electron distribution within a molecule. Fundamental questions about the nature of bonding can be answered, and the physical reality of hypothetical concepts such as VSEPR theory can be investigated.⁴ Add to this the more applied concepts such as information about electrophilic/nucleophilic sites, strained bonds and intermolecular interactions, and it would appear that a wealth of new information is available for the chemist.

Much of this information can be gained from theoretical calculations. It has long been established that quantum chemical calculations are able to reproduce accurate wavefunctions for chemically interesting species. The advent of readily available powerful computing resources and flexible program packages, such as GAMESS⁵, mean that high level *ab initio* wavefunctions are relatively easily obtainable. In contrast to this is the collection of a charge density data set which is a time consuming process, requiring experience and specialised equipment. The question must therefore arise as to why the experimental approach should be pursued.

Perhaps the most fundamental reason that experimental charge density research is of value is the fact that quantum mechanics has yet to provide an analytical solution to the many-body problem. The Hartree-Fock level of theory neglects the correlated motion of electrons. Omission of this effect gives a ground-state wavefunction which is above the true energy of the system, and also affects the calculated electron density of the molecule. Møller-Plesset perturbation theory and configuration interaction calculations both serve to include some of the effects of electron correlation, but at the expense of a dramatic increase in computational time. The result is that only the simplest systems can effectively be treated in this way. In direct contrast to this is the electron density obtained from an experimental multipole model. Since the concept of localised orbitals is not invoked in any way the resultant density is, by definition, correlated.

Many of the recent applications of experimental charge density research have focused on weak interactions.^{6,7} Understanding this type of interaction is of fundamental importance not only to chemistry, but to biochemistry and molecular biology. Whilst quantum chemical calculations are generally well suited to the representation of strong bonds they give much less accurate results for weak interactions.⁸ Also, whilst being able to simulate weak intramolecular bonds, the isolated gas-phase approach of *ab initio* studies cannot account for intermolecular interactions. Calculations can be extended to include more molecules but this will always be done at the expense of either time or level of basis, and in the case of large molecules may not be feasible.

In practice experimental and theoretical charge density studies are often carried out in parallel. If the two sets of results are in accord, confidence is increased in the accuracy of the derived properties. Any discrepancies can be used to identify inadequacies in either one or the other of the models.

1.1.3 Applications

There are a number of areas of research where the application of experimental charge density research is of particular value.

- The study of weak interactions is of importance in biological applications. Drug-receptor and enzyme-substrate binding are governed by this type of interaction, and so better understanding of the nature of the binding process could be applied to rational drug design. Detailed electron density information can be obtained for small biologically

active molecules and used in conjunction with the structures of biological receptors which are being made available by protein crystallography methods. At present the size of the receptor molecules and the resolution of the structures precludes the application of charge density theory to this part of the system. However, there has been some work done on the application of experimental multipole parameters, obtained from small molecules, to polypeptide chains.⁹ The intention is to extend the approach to protein molecules once sufficient experimental parameters are available.

- The application of Hartree-Fock theory to transition metal compounds is hampered by the significance of relativistic and correlation effects in molecules of this type. Also, the standard basis sets are not generally available for transition metals and the necessary use of custom basis sets makes calculations far from routine. The large number of basis functions needed to represent an atom of high atomic number may also mean that the level of calculation is limited by the computing resources available. This is in contrast to the experimental treatment of transition metals which is no more complex than that of first and second row atoms.
- The development of new materials which display useful properties in the crystalline state, such as semi-conductors and catalysts, could be advanced by an understanding of the crystalline electronic charge distribution. In particular, the gas-phase isolated molecule approach of Hartree-Fock theory is inappropriate for semi-conductors and superconductors as the electron distribution is not localised on discrete molecules. Also, the area of non-linear optics is currently being studied using experimental charge density techniques to yield information about molecular dipole moments.

1.2 Scattering by Spherical Atoms

1.2.1 General Scattering of X-rays

In order to develop an expression for the scattering of X-rays by non-spherical atoms, it is necessary to first develop an expression for the simpler case of scattering by spherical atoms. Within the first-order Born approximation, which neglects the effect of inelastic scattering, the coherent elastic component of the scattering by a free atom is:¹⁰

$$I_{coherent,elastic}(\mathbf{H}) = \left| \int \psi_n^* \left| \sum_j \exp(2\pi i \mathbf{H} \cdot \mathbf{r}_j) \right| \psi_n d\mathbf{r} \right|^2 \quad 1.1$$

where I is the intensity of the coherent elastic component of the scattering and ψ is the n -electron wavefunction. \mathbf{H} is the reciprocal lattice vector which defines some point in reciprocal space and is given by $\mathbf{H} = h\mathbf{a}^* + k\mathbf{b}^* + l\mathbf{c}^*$, where h , k and l are the Miller indices of the plane of reflection and \mathbf{a}^* , \mathbf{b}^* and \mathbf{c}^* are the reciprocal lattice vectors. \mathbf{r}_j is the position vector of electron j in real space.

If the integration is over all electrons:

$$I_{coherent,elastic}(\mathbf{H}) = \left(\int \rho(\mathbf{r}) \exp(2\pi i \mathbf{H} \cdot \mathbf{r}) d\mathbf{r} \right)^2 \quad 1.2$$

where $\rho(\mathbf{r})$ is the electron density at point \mathbf{r} . The amplitude of the wave that is scattered by the atom is therefore given by:

$$a(\mathbf{H}) = \left| \int \rho(\mathbf{r}) \exp(2\pi i \mathbf{H} \cdot \mathbf{r}) d\mathbf{r} \right| \quad 1.3$$

It can be seen from expression 1.3 that the amplitude of the scattered wave, $a(\mathbf{H})$, is the modulus of the Fourier transform of the atomic electron density distribution:

$$a(\mathbf{H}) = \left| \mathfrak{F}\{\rho(\mathbf{r})\} \right| \quad 1.4$$

where \mathfrak{F} is the Fourier transform operator.

1.2.2 Scattering by a Crystal

The electron density distribution of a crystal is uniquely represented by the electron density distribution of the unit cell. It is therefore a periodic function in three dimensions and can be expressed as a convolution:

$$\rho_{crystal}(\mathbf{r}) = \sum_n \sum_m \sum_p \rho_{unit\ cell}(\mathbf{r}) * \delta(\mathbf{r} - n\mathbf{a} - m\mathbf{b} - p\mathbf{c}) \quad 1.5$$

where n , m and p are integers and \mathbf{a} , \mathbf{b} and \mathbf{c} are the unit cell vectors. δ is the Dirac delta function, a periodic function which takes values of either zero or unity. If the Fourier convolution theorem is applied to equation 1.5 the following expression for the structure amplitude of the wave scattered by the crystal, $|F(\mathbf{H})|$, is obtained:

$$|F(\mathbf{H})| = \mathfrak{F}\{\rho_{crystal}(\mathbf{r})\} = \sum_n \sum_m \sum_p \mathfrak{F}\{\rho_{unit\ cell}(\mathbf{r})\} \mathfrak{F}\{\delta(\mathbf{r} - n\mathbf{a} - m\mathbf{b} - p\mathbf{c})\} \quad 1.6$$

which gives:

$$|F(\mathbf{H})| = \mathfrak{F}\{\rho_{unit\ cell}(\mathbf{r})\} \sum_h \sum_k \sum_l \delta(\mathbf{H} - h\mathbf{a}^* - k\mathbf{b}^* - l\mathbf{c}^*) \quad 1.7$$

The first factor in expression 1.7 is defined as the structure factor $F(\mathbf{H})$:

$$F(\mathbf{H}) = \mathfrak{F}\{\rho_{unit\ cell}(\mathbf{r})\} = \int \rho_{unit\ cell}(\mathbf{r}) \exp(2\pi i\mathbf{H} \cdot \mathbf{r}) d\mathbf{r} \quad 1.8$$

The spherical atom approach assumes that the electron distribution in the unit cell can be represented by a summation, over all atoms, of the electron density resulting from isolated spherical atoms located at positions \mathbf{R}_j :

$$\rho_{unit\ cell}(\mathbf{r}) = \sum_j \rho_{atom,j}(\mathbf{r}) * \delta(\mathbf{r} - \mathbf{R}_j) \quad 1.9$$

If 1.9 is substituted into 1.8, the following expression for the structure factor is obtained:

$$F(\mathbf{H}) = \sum_j \mathfrak{F}\{\rho_{atom,j}\} \mathfrak{F}\{\delta(\mathbf{r} - \mathbf{R}_j)\} = \sum_j f_j \exp(2\pi i\mathbf{H} \cdot \mathbf{R}_j) \quad 1.10$$

or

$$F(h, k, l) = \sum_j f_j \exp 2\pi i (hx_j + ky_j + lz_j) \quad 1.11$$

where x_j , y_j and z_j are the fractional coordinates of atom j . Since this is a complex function it can be expressed as the sum of real and imaginary parts:

$$F(h, k, l) = A + iB \quad 1.12$$

$$A(hkl) = \sum_j f_j \cos 2\pi (hx_j + ky_j + lz_j) \quad 1.12a$$

$$B(hkl) = \sum_j f_j \sin 2\pi (hx_j + ky_j + lz_j) \quad 1.12b$$

where f_j is the atomic scattering factor or form factor. Inverse Fourier transformation of **1.11** gives:

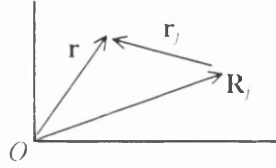
$$\rho(\mathbf{r}) = \frac{1}{V} \sum_{\mathbf{H}} F(\mathbf{H}) \exp(-2\pi i \mathbf{H} \cdot \mathbf{r}) \quad 1.13$$

1.2.3 The Spherical Scattering Factor

The scattering factor f_j is the Fourier transform of the isolated atom density and as such is related to the type of atom scattering the X-ray beam. It can therefore be written as:

$$f_j(H) = \int \rho_j(\mathbf{r}_j) \exp(2\pi i \mathbf{H} \cdot \mathbf{r}_j) d\mathbf{r}_j \quad 1.14$$

where $\mathbf{r}_j = \mathbf{r} - \mathbf{R}_j$, *i.e.* \mathbf{r}_j is the position vector of a point \mathbf{r} , expressed with respect to the nuclear position of atom j , rather than to the position of the unit cell origin, see below.



f_j is expressed as the ratio of the amplitude of the radiation scattered by the atom j , as compared with the amplitude of the wave scattered by a single electron according to classical theory. During the early part of the development of crystallographic theory it was thought that the magnitude of the scattering factor was solely related to the number of electrons present in the scattering atom or ion. In one of their early papers¹¹ the Braggs state that:

“It is reasonable, therefore, to assume provisionally that the weight of the atom in the main defines its effectiveness as a diffracting centre, and that two atoms of equal weight are equally effective.”

For an isolated neutral atom the value of f_j is in fact equal to the atomic number of the atom at the angle $\sin\theta/\lambda=0$. When this condition is fulfilled all of the electrons scatter in phase. However, as the value of $\sin\theta/\lambda$ is increased f_j gradually decreases and approaches zero at large scattering angles. This angular dependency is accounted for in the expression for the scattering factor which is obtained from equation 1.14:

$$f_j(H) = 4\pi \int \rho_j(r) \frac{\sin(2\pi Hr)}{2\pi Hr} r^2 dr \quad 1.15$$

Here we have substituted $r = |r_j|$ and $H = |\mathbf{H}|$ because at this level of theory, the “independent atom model”, the deviation of the electron density from sphericity is neglected and the atom is assumed to be spherically symmetric. However, the graph of f_j versus $\sin\theta/\lambda$ takes a different form for each atom or ion, see Figure 1.1. This is due to differences in the radial charge distribution of each atom and is accounted for in the scattering factor expression by the function $\rho_j(\mathbf{r})$.

In order for 1.15 to be numerically integrated the atomic charge distribution $\rho_j(r)$ must be defined in terms of r . In fact the function $\rho_j(r)$ has been accurately determined for the majority of chemically significant atoms and ions¹². For all of the lighter atoms and ions

($Z \leq 38$) $\rho_j(r)$ has been calculated via the Hartree-Fock method. The scattering factors of many of the heavier atoms and ions have been obtained from Dirac-Slater wavefunctions.

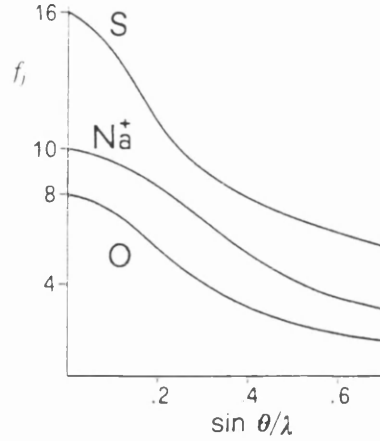


Figure 1.1 : Plot of the atomic scattering factor, f_j , against $\sin\theta/\lambda$ for O, S and Na^+ .¹³

1.2.4 Temperature Effects

Up to this point the atom has been considered to be a static, spherical entity at position \mathbf{R}_j . However, these positions correspond to energy minima and in a real crystal each atom will oscillate about its minimum energy position. At this point the rigid body assumption is made, *i.e.* the electron density is assumed to follow the vibrational motion of the nucleus. The ability of the atom to scatter the incident radiation is affected by the thermal smearing of the electron density. It is therefore necessary to modify the scattering factor to account for thermal motion. In the case of an isotropically vibrating atom the thermally modified atomic scattering factor $f_{j,iso}(H)$ is :

$$f_{j,iso} = f_j(H) \exp \left(\frac{-8\pi^2 U \sin^2 \theta}{\lambda^2} \right) \quad 1.16$$

where U is the mean square displacement of atom j from its equilibrium position, measured in \AA^2 . The factor multiplying $f_j(H)$ is called the temperature factor and given the symbol T_j .

In general, bonding constraints mean that an atom will not be free to vibrate equally in all directions. It is therefore necessary to define a probability ellipsoid for the anisotropic motion of the atom, centred on the atomic position \mathbf{R}_j . In this case the anisotropic scattering factor can be expressed as:

$$f_{j, aniso}(H) = f_j(H) \exp \left[-2\pi^2 \left(U_{11}a^{*2}h^2 + U_{22}b^{*2}k^2 + U_{33}c^{*2}l^2 + 2U_{12}a^*b^*hk \right) \right. \\ \left. + 2U_{13}a^*c^*hl + 2U_{23}b^*c^*kl \right]$$

1.17

where the six parameters U_{ij} define the orientation of the ellipsoid with respect to the unit cell axes, and the lengths of the ellipsoid axes.

1.3 Beyond the Spherical Atom Approximation

1.3.1 Limitations of the Independent Atom Model

It has long been observed that the independent atom model (IAM), which assumes that atoms are both neutral and spherical, is not adequate to describe the scattering from covalently bonded crystals. In particular the experimental observation of the space group-forbidden (222) reflection in diamond has been of historical importance in precipitating the development of an aspherical scattering factor. The observation of this reflection led Sir William Bragg to suggest that:

“...the properties of the atom in diamond are based upon a tetrahedral not a spherical form.”¹⁴

Similarly, the anomalously high intensity of the (100) band in the powder diffraction pattern of graphite was accounted for by Franklin as being due to the non-spherical nature of the carbon atoms.¹⁵

In their letter to the Physical Review¹⁶, on the subject of the electron diffraction pattern of ZnO, James and Johnson point out that the introduction to the model of a concentration of valence charge density in the interatomic Zn O region successfully accounts for the experimentally observed intensities. They also note that the majority of charge must

be placed in the region closer to the zinc atom, and thus introduce the concept of a bonding density which is not equally shared by the bonded atoms.

1.3.2 The Kappa Formalism

The assumption of atomic neutrality inherent in the IAM contradicts a large body of theoretical and experimental evidence which shows that atoms in molecules very often carry whole or partial charges. It might be expected therefore that a model in which the atomic charge is allowed to vary would show some improvement over the IAM. However, it is also necessary to consider the radial dependence of the atomic electron distribution. Any change in the occupation of the electronic valence shell affects the degree to which the nuclear charge is shielded by the electrons, and hence the size of the atom is affected.

Coppens developed a simple extension of the IAM which allowed for both valence charge transfer and expansion/contraction of the valence shell.¹⁷ He termed it the Kappa formalism, as the parameter κ allows for the radial dependence of the valence shell. The structure factor is given by:

$$F(\mathbf{H}) = \sum_j \left[P_{j,core} f_{j,core}(\mathbf{H}) + P_{j,val} f_{j,val}(\kappa_j \mathbf{H}) \right] \exp(2\pi i \mathbf{H} \cdot \mathbf{r}_j) T_j \quad 1.18$$

where $P_{j,core}$ and $P_{j,val}$ are the populations of the core and valence shells of atom j respectively. $f_{j,core}$ is the scattering factor for the core shell in the free atom. The scattering factor for the valence shell is defined as $f_{j,val} = f_{j,val}(free\ atom) \sin\theta/\lambda\kappa_j$. There are only two extra refinable parameters per atom, as compared with the IAM, κ and $P_{j,val}$. The method is therefore not significantly more computationally expensive than the IAM, although Coppens does warn that a higher quality of data is required.

The atomic charges, and magnitudes and directions of molecular dipole moments obtained using the kappa formalism agree well with theoretical results.¹⁷ However, the flexibility of the model is limited and it is incapable of describing non-spherical charge distributions. As Coppens himself says:

“The two parameter monopole model is very computer-time efficient and therefore has been dubbed the *‘poor man’s charge density*

refinement'. But with the present abundant, and still increasing, availability of computer power *poor men* have become increasingly rare and multipole models relatively more popular."¹⁸

1.3.3 The Development of the First Aspherical Scattering Factor

The first non-spherical scattering factors were developed by McWeeney for the isolated atoms hydrogen to neon, and the hybridised valence states of carbon.¹⁹ As a first step, the contributions to the scattering from each atomic orbital are calculated by applying the expression for the scattering factor, **1.14**, to each function in the basis set of atomic orbitals in turn. The atomic scattering factor for any ground-state atom, for which the orbital contributions are known, may now be determined by a summation over the scattering from each basis orbital. Since any non-s function is not spherically symmetric the atomic scattering factor is now, in general, aspherical. However, in an atom where each of the valence orbitals is equally occupied, regardless of the symmetry of those orbitals, the effective scattering factor for the atom is spherical. This is true for valence states involving hybrid orbitals, as well as basic atomic orbitals.

The scattering factors for the hybrid valence states sp , sp^2 and sp^3 are obtained by taking linear combinations of the atomic basis functions. This operation is valid because the n -electron wavefunction of an atom can be represented as an $n \times n$ determinant of one-electron orbitals. The addition of corresponding elements in any two columns of the determinant leaves the value of the determinant unchanged. Thus, linear combinations of any of the basis functions may be substituted into the determinant whilst leaving its wavefunction, and the resultant atomic density, unaltered.

The major disadvantages of this approach are that:

- i*) the many-electron wavefunction is represented by only one determinant and hence the effects of electron correlation are ignored;
- ii*) the effects of bonding are neglected;
- iii*) the hybridisation state of the atom must be specified.

Information about the ground state of the atom must therefore be supplied by the experimentalist and so some assumptions about the nature of the charge distribution are necessarily introduced.

McWeeney extends his development of the aspherical scattering factor to include bonding effects.²⁰ He achieves this by adding a correction factor to the atomic scattering factor to give the 'effective scattering factor f_j^e :

$$f_j^e = f_j + \Delta f_j \quad 1.19$$

where f_j is the valence-state aspherical scattering factor for atom j , as derived in reference 19, and Δf_j is the bonding correction to the atomic scattering factor. The bonding correction is dependent on the distribution of the atomic electrons between core, valence and bonding orbitals. In order to obtain Δf_j the electrons are partitioned into these categories. Any valence electron density associated with a bond is split equally between the two atoms joined by the bond.

The correction term Δf_j is complex and therefore introduces a phase-shift into the diffracted beam. The magnitude and phase difference of Δf_j depends on the scattering angle θ . The correction term and effective scattering factors for the H_2 molecule are plotted against $\sin\theta/\lambda$. In general the effective scattering factor is smaller than the aspherical scattering factor f_j ; this corresponds to the real-space migration of charge away from the atom into the bond.

The major difficulty in the calculation of the effective scattering factor outlined above is the need to integrate Slater functions. McWeeney overcomes this problem by replacing the Slater functions by linear combinations of Gaussian functions, which are much easier to integrate.²¹ The effective scattering factors are evaluated in this way for the H_2 molecule and, in a later paper²², for the carbon atoms in graphite and diamond. McWeeney notes that the effective scattering factor differs from the aspherical scattering factor only at low scattering angles. He concludes from this that bonding electron distributions affect the scattering only at low angles. He also points out that it is the core electrons which tend to follow the vibrational motion of the atomic nuclei and therefore temperature effects are most noticeable in the high angle region. The effects of bonding and vibration on the scattered radiation can therefore be separated out. This is an assumption which has remained central to the development of the theory of multipole modelling.

1.4 Development of the Generalised Structure Factor

1.4.1 Dawson's Cubic Harmonic Approach

Dawson built on McWeeney's work to develop a general expression for aspherical scattering factors.²³ The most important idea that he introduces is the need to consider the character of the atomic density with respect to its reference origin, that is, the time averaged nuclear position. He states that if the distribution is non-centrosymmetric with respect to the origin, then it can be expressed as a sum of centric and acentric parts. The expression for the atomic scattering factor can also be written as:

$$f_j(\mathbf{H}) = f_{c,j}(\mathbf{H}) + if_{a,j}(\mathbf{H}) \quad 1.20$$

where the subscripts *c* and *a* refer to the centric and acentric components of the scattering respectively. The acentric scattering is out of phase with the centric part and so the expression is complex.

The form of the atomic charge density is affected by the vibrational motion and so an analogous treatment of the temperature factor is introduced:

$$T_j(\mathbf{H}) = T_{c,j}(\mathbf{H}) + iT_{a,j}(\mathbf{H}) \quad 1.21$$

Substitution of the expressions for $f_j(\mathbf{H})$ and $T_j(\mathbf{H})$ into the structure factor equation gives a new expression for the structure factor in terms of centric and acentric scattering components:

$$F(\mathbf{H}) = A(\mathbf{H}) + iB(\mathbf{H}) \quad 1.22$$

where:

$$A(\mathbf{H}) = \sum_j \left[(f_c T_c - f_a T_a)_j \cos 2\pi \mathbf{H} \cdot \mathbf{R}_j - (f_c T_a + f_a T_c)_j \sin 2\pi \mathbf{H} \cdot \mathbf{R}_j \right] \quad 1.22a$$

$$B(\mathbf{H}) = \sum_j \left[(f_c T_c - f_a T_a)_j \sin 2\pi \mathbf{H} \cdot \mathbf{R}_j + (f_c T_a + f_a T_c)_j \cos 2\pi \mathbf{H} \cdot \mathbf{R}_j \right] \quad 1.22b$$

The elements of **1.22** necessary for the calculation of the structure factor will depend on the nature of the structure itself. Local symmetry considerations may restrict the nature of the vibrational motion or atomic charge density; *e.g.* an atom at a special position of octahedral site symmetry cannot have asymmetric components of either $f_j(\mathbf{H})$ or $T_j(\mathbf{H})$.

At this stage Dawson recognises that there is no facility for calculating the secondary structure factor elements $f_{a,j}(\mathbf{H})$, which account for the acentric scattering. In a subsequent paper this problem is overcome by expanding the non-spherical components of the atomic charge densities in terms of combinations of Cubic Harmonic functions with radial Gaussian functions.²⁴ The charge density is here decomposed into three components:

$$\rho(\mathbf{r}) = \rho_c(r) + \delta\rho_c(\mathbf{r}) + \rho_a(\mathbf{r}) \quad \mathbf{1.23}$$

where $\rho_c(r)$ is the spherical component, $\delta\rho_c(\mathbf{r})$ is the non-spherical centric part, and $\rho_a(\mathbf{r})$ is the acentric part. Both $\delta\rho_c(\mathbf{r})$ and $\rho_a(\mathbf{r})$ are expanded in terms of Cubic Harmonics which are Fourier transformed to give the aspherical scattering factors $\delta f_c(\mathbf{H})$ and $f_a(\mathbf{H})$.

The scattering factors and associated structure factors for the carbon atoms in diamond are calculated and found to agree well with the experimentally observed values of $F(\mathbf{H})$ for all reflections. This is a great improvement over the results obtained with the IAM where only the calculated structure factors for the $h+k+l=4n$ reflections agree with the experimental values. This is because the $4n$ reflections originate from the centric part of the scattering and are therefore fully accounted for by a spherical atom model with harmonic temperature factors. However, the set of observed odd-order reflections $h+k+l=(4n+1)$ have both centric and acentric scattering components, the latter are discounted in the IAM and this leads to a discrepancy between the calculated and observed structure factors.

The observation of the space-group forbidden (222) reflection can now be explained. The set of reflections where $h+k+l = 4n+2$, which includes the (222) reflection, arise only from the cross-products of centric scattering and acentric vibration terms and vice versa. The $4n+2$ reflections are therefore observed but weak reflections. However, the IAM completely neglects the acentric scattering and vibration terms and so calculates $F(222)$ to be equal to zero, *i.e.* forbidden.

The addition of acentric scattering terms to the structure factor formalism should mean that better descriptions of bonding effects should now be obtainable as these tend, in general, to result in acentric charge distributions. Such a result is achieved by Dawson for the

diamond structure. The results are shown in Figure 1.2 below. 1.2(a) is the conventional difference map for the IAM with coefficients $F_{obs} - F_{calc, spherical}$ in equation 1.13. It is apparent that the spherical scattering factor formalism fails to account for the bonding density. 1.2(b) shows the differences between the densities obtained by the new aspherical scattering formalism and the spherical scattering factor. Again, it is clear that the main difference density is concentrated in the bond regions and this shows the improved description of bonding density which is achieved with Dawson's formalism as compared to the IAM. 1.2(c) is the difference between (a) and (b) and the coefficients are therefore $F_{obs} - F_{calc, aspherical}$. Clearly there is little residual density in this plane and it can be concluded that Dawson's aspherical structure factor formalism accounts well for the observed diffraction intensities.

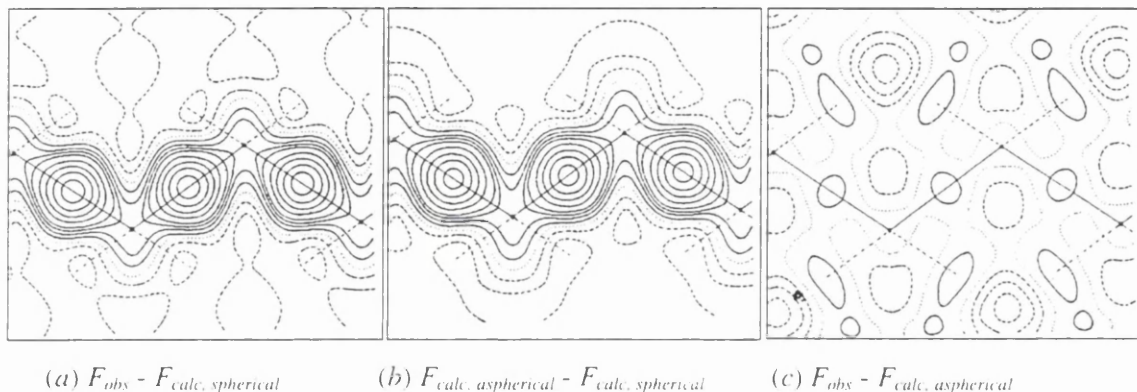


Figure 1.2 : Fourier difference maps for the $(1\bar{1}0)$ plane of diamond.

1.4.2 Stewart's Spherical Harmonic Approach

Stewart built upon the work of McWeeney and Dawson to develop an analytical expression for general scattering factors. As a starting point Stewart takes a minimal basis set representation of the atom; *i.e.* for a first row atom this consists of the $1s$, $2s$ and $2p_{xyz}$ orbitals.²⁵ The components of the generalised scattering factor, f_{uv} , are the Fourier transforms of orbital products. In Stewart's notation this is given by:

$$f_{uv}(\mathbf{S}) = \int \chi_u^* \chi_v \exp(i\mathbf{S} \cdot \mathbf{r}) d\mathbf{r} \quad 1.24$$

where \mathbf{S} is the Bragg vector which is perpendicular to the plane of reflection and χ_{μ} and χ_{ν} are basis functions.

In order to obtain the scattering factor the basis functions must be analytically defined:

$$\chi_{\mu} = Y_{lm}(\theta, \phi) R_{nl}(r) \quad 1.25$$

where $Y_{lm}(\theta, \phi)$ is a spherical harmonic function whose shape is defined by l and orientation by m . $R_{nl}(r)$ is a radial function which can be either an expansion of Slater or Gaussian type orbitals.

The orbital products of the basis functions give a new set of functions which can be considered as a basis set of density functions. For a minimal basis set representation of a first row atom the core density is given by the orbital product of the Hartree-Fock $1s$ atomic ground state orbital. The core contribution to the scattering is assumed to be independent of the bonding environment of the atom. Although this is not necessarily true it is a reasonable approximation as any deviations from spherical symmetry are likely to be very small and therefore difficult to observe. Within the same basis set the following valence orbital products are obtained:

$2s2s$	monopole
$2s2p_x ; 2s2p_y ; 2s2p_z$	dipoles
$2p_x2p_x ; 2p_x2p_y ; 2p_x2p_z$	quadrupoles
$2p_y2p_y ; 2p_y2p_z$	quadrupoles
$2p_z2p_z$	monopole

The scattering characters of the two monopoles are found to be very similar and they are therefore replaced by the spherically averaged Hartree-Fock valence charge density of the ground state atom.

In a subsequent paper²⁶ Stewart includes the sets of $2p3d$ and $3d3d$ orbital products which generate seven octopoles and nine hexadecapoles respectively. He concludes this work by pointing the way forward in the development of the generalised scattering factor:

“The use of atomic orbital products in the generation of generalised X-ray scattering factors is somewhat artificial. We invoke them in this work and earlier studies to provide a quantum chemical basis for a suitable choice of the radial scattering functions. One need not be this restrictive. The atomic densities can be represented with a multipole expansion in spherical harmonics.”

1.5 The Multipole Model

Hansen and Coppens incorporated Stewart’s idea of the multipole expansion into the program MOLLY²⁷ which is capable of the refinement of all structural and charge density parameters. The atomic charge density is expressed as a series expansion of density normalised spherical harmonic functions:

$$\rho_{atom}(\mathbf{r}_j) = P_c \rho_{core} + P_v \kappa'^3 \rho_{val}(\kappa' r) + \sum_{l=0}^{l_{max}} \kappa'^3 R_l(\kappa' r) \sum_{m=-l}^l P_{lm} d_{lm}(\mathbf{r}_j / r) \quad 1.26$$

where $\mathbf{r}_j = \mathbf{r} - \mathbf{R}_j$ and ρ_{core} and ρ_{val} are the core and spherical valence components of the charge density which are chosen as the Hartree-Fock densities of the free atom. The valence density is allowed to expand and contract by means of the refinable parameter κ' . P_c , P_v and P_{lm} are the population coefficients of the core, spherical valence and spherical harmonic functions respectively. The radial functions have the form:

$$R_l(r) = \frac{\xi^{n_l+3}}{(n_l+2)!} r^{n_l} \exp(-\xi_l r) \quad 1.27$$

where n_l can take any positive integer value, and the orbital exponent ξ is scaled by the refinable parameter κ so that $\xi' = \kappa \xi$. The multipoles with $l_{max} > 1$ represent the deviation of the atomic charge density from sphericity and are collectively termed the deformation functions. An expression for the structure factor can be derived from 1.26 and 1.27:

$$F(\mathbf{H}) = \sum_j^{\text{atoms}} \sum_p^{\text{symmetry}} \left[P_c f_{core}(H) + P_v f_{val}(H / \kappa') + \sum_{l=0}^{l_{\max}} \Phi_{jl}(H / \kappa'') \sum_{m=-l}^l P_{jlm} d_{lm}^j(\mathbf{H}_p / H) \right] \exp 2\pi i \mathbf{H} \cdot \mathbf{R}_{jp} T_j(\mathbf{H})$$

1.28

where f_{core} and f_{val} are the Fourier transforms of ρ_{core} and ρ_{val} respectively. Φ_{jl} is the Fourier-Bessel transform of the radial function and \mathbf{H}_p and \mathbf{R}_{jp} are the symmetry-transformed scattering and position vectors.

A fully flexible description of the electronic charge density has now been achieved in terms of an expansion of spherical harmonic functions which are dependent on a set of refinable parameters. In this approach the limitations of McWeeney's model have been overcome *i.e.*;

- i) the effects of electron correlation are fully accounted for as the model provides a direct representation of the electron density in the crystal;
- ii) the effects of bonding are accounted for both in terms of charge transfer and the deformation of the atomic density from sphericity;
- iii) no assumptions need to be introduced about the hybridisation state of the atom.

1.5.1 Practical Implementation

The program MOLLY²⁷ has been further developed and now forms a large component (XDLSM) of the XD program package.²⁸ The details of refinement discussed here will refer to XD as it was used to obtain the experimental results presented later in this thesis.

One of the most fundamental ways to improve the IAM is to allow charge transfer between atoms. Atoms in molecules tend to carry partial charges due to their differing electronegativities; these charges affect the size of the atom through differing amounts of nuclear shielding. The size dependency is accounted for by the inclusion of the κ' and κ'' parameters which allow for the expansion/contraction of the spherical valence densities and deformation functions respectively. The electron population of the atom is given by the sum of the population parameters $P_c + P_v + P_{00}$. In practice²⁷ it has been found that the spherical valence shell, ρ_{val} , is sufficiently flexible to describe the spherical component of the valence density. The Slater-type monopole is therefore usually omitted, *i.e.* $P_{00} = 0$. The higher order multipoles integrate to zero over all space and so the population parameters P_{lm} $l \neq 0$

represent a shift of the electronic charge within the multipole. The normalisation is such that a value of $P_{lm} = 1$ implies a shift of one electron from the positive to the negative lobes of the multipole. Since the core population is fixed, the atomic charge is therefore solely dependent on the valence monopole population.

Although the atomic populations may vary, the total number of electrons in the system will generally balance with the number of protons. XDLSM incorporates an optional electroneutrality constraint to ensure that the charge balance is maintained throughout the refinement. It is also possible to apply additional constraints to smaller sub-sets of atoms to maintain for example the charge on a complex ion, *e.g.* $[\text{PF}_6]$.

The higher multipoles are defined with respect to the local axis system of each atom. In the general case the choice of these axes is arbitrary and is usually specified by the user with respect to bonded or neighbouring atoms. However, for an atom at a special position the charge density must retain the crystallographic point symmetry. There are therefore restrictions on the deformation functions which can be occupied, and this affects the axis choice. Consider, for example, an atom which lies on a two-fold rotation axis. Only the dipole which is oriented along the rotation axis may be occupied. Any other orientation of occupied dipole will break the local symmetry requirements. It is therefore necessary to define the local axis system with regard to any crystallographic symmetry elements. In the above case, if the local z axis is oriented along the rotation axis the z dipole can be occupied, but the population parameters of the x and y dipoles are constrained to zero. The same considerations apply to the higher poles. The rules for axis choice and allowed multipoles have been tabulated²⁹ for all symmetry elements and must be referred to in the case of atoms at special positions.

XDLSM allows for a multipole expansion up to the hexadecapole ($l_{max}=4$) level, which is usually appropriate for second row atoms. However, in the case of first row atoms it is not always necessary to extend the expansion to this level. An octopole expansion is generally sufficient to account for the bonding deformations of the density. The addition of hexadecapole terms may improve the agreement factors, but this is often only an artefact of the inclusion of more parameters. Inspection of the hexadecapole population parameters and associated errors will often show no significant occupation of these functions. Hydrogen atoms are generally modelled either as an expansion of three dipole terms, or as a single bond-directed dipole.

The radial expansion of the monopole and deformation functions are controlled by the refinable parameters κ' and κ'' respectively. For hydrogen atoms both κ' and κ'' are fixed at 1.2, an average value obtained from theoretical models.³⁰ In general, the set of deformation functions are constrained to share a common κ'' value. However, in the case of sulfur the refinement of separate κ'' values for each level of multipole has been shown to result in a significant improvement of the model.³¹ It is observed that κ'' is a very sensitive parameter and that care must be taken to achieve full and stable convergence of the refinement.

The initial positional parameters and temperature factors of all non-hydrogen atoms are taken from a conventional spherical atom approach and then refined along with the other parameters during the least-squares refinement. Since the hydrogen atom formally contains only a single electron little reliable positional information can practically be obtained for H atoms. One approach to this problem is to obtain atomic positions from experimental neutron diffraction data which can then be used in subsequent X-ray diffraction charge density studies.³²⁻³³ The large crystal size required for neutron diffraction and the limited availability of neutron sources means that this is not always a practical proposition. The more usual way to treat the hydrogen atoms is to assume that the bond directions and isotropic temperature factors, obtained from a spherical atom refinement of the data, are correct. The hydrogen atom is then constrained to lie somewhere on the bond vector, and the bond length is taken as the same as that for a similar bond obtained by neutron diffraction. Such neutron bond lengths have been tabulated.³⁴

1.6 Experimental Considerations

The formulation of an expression for the structure factor in terms of a refinable set of parameters, **1.28**, means that the determination of experimental charge densities from single crystal X-ray diffraction data is viable. However, there are certain experimental limitations and pre-requisites for such a study. This section will outline the most important of these, and will focus in particular on those practical considerations which differ from a conventional spherical atom experiment.

1.6.1 Data Collection

The majority of charge density data sets are collected on automated three or four circle diffractometers, although some work has been done with area detector data, see Chapter 5. The bisecting or ω - 2θ geometry is generally used as this improves the accuracy of the observed intensity. In this type of measurement both the detector and the crystal are rotated and the intensity is measured at 96 steps throughout the scan. This approach has the advantage that information is recorded about both the intensity and shape of the peak. The intensity data for each of the steps is integrated to give a total intensity for the reflection, whilst the step-wise data gives the peak profile.

The orientation of the crystal with respect to the diffractometer axes is obtained by driving the detector through reciprocal space until a point of high X-ray intensity is located. The process is repeated until sufficient points have been accumulated for the standard software routines to determine both the unit cell parameters and the crystal orientation matrix. With this information it is possible to accurately position the detector at any point in reciprocal space which corresponds to a diffraction peak in real space. A small set of reflections is now chosen which give a good spread over both reciprocal space and intensity values. These reflections will be measured repeatedly throughout the experiment and the results used to monitor for decay of the crystal or change in the orientation matrix.

In order to obtain precise values for the structure factors, which are used in least-squares refinement of the multipole parameters, the precise determination of the observed intensities is of prime importance. Averaging over several measurements of the same or equivalent reflections will improve the precision. Merging of multiple slow and careful measurements of unique hkl would therefore represent the ideal situation, but time constraints make this an impractical proposition. A more normal distribution of errors is obtained by the rapid measurement and subsequent merging of n symmetry equivalent reflections than by the n -times slower measurement of a single reflection.³⁵ In practice the aim should be to measure at least three symmetry equivalent reflections for each unique hkl as this will allow outlier reflections to be rejected. The fraction of reciprocal space which contains the unique set of reflections depends on the Laue group of the crystal. In the most general case of a triclinic crystal the unique reflections make up half of the reciprocal lattice. For the monoclinic crystal system the data multiplicity is four-fold and only one quarter of the sphere needs to be measured to obtain the unique set of data.

The collection of a certain number of reflections typically takes twice as long for a charge density data set than for a spherical atom refinement. This is due to the slower scan speeds and the forced final scan for all reflections. This fact, together with the increased resolution and consequently larger size of the data set, means that the experiment can often take many weeks to complete. Care must therefore be taken in determining the most appropriate strategy for the collection of the data. There are two main options. The first is to measure the full sphere in shells of $\sin\theta$ until the maximum value of $\sin\theta/\lambda$ is reached. Alternatively the sets of unique data can be measured separately, each set being measured to θ_{\max} . The second approach has the advantage that if the crystal decays at some point during the experiment there may already be enough complete sets of data, measured to θ_{\max} , for the refinement to proceed.

1.6.2 Compound and Crystal Choice

In order to obtain high quality diffraction data care must be taken in the selection of a suitable crystal. The foremost requirement is for a well-defined single crystal; twinned or fractured crystals are unsuitable for this type of experiment. The size of the crystal is also an important factor: the crystal should be small enough that it can be fully centred in the homogenous part of the X-ray beam, whilst being large enough to maximise the diffracted beam intensities. Cutting larger crystals to size is a viable option but all cuts should be made parallel to existing faces, this will maximise the chance of the crystal being cleaved along a lattice plane. Clearly defined faces are desirable as face index information can be used to apply an analytical absorption correction to the data. A degree of mosaicity is also desirable as this reduces the effect of extinction.

As well as the need for a suitable crystal there are also restrictions on the type of compound which is appropriate for a charge density study. The number of atoms in the asymmetric unit should be as small as possible in order to minimise the number of parameters and hence the size of the data set required. Bulky alkyl side chains should be avoided as far as possible as these are liable to large vibrational motions. It is also desirable to minimise the number of hydrogen atoms as no accurate positional information can be obtained for H atoms unless a parallel neutron diffraction experiment can be undertaken.

In a charge density study the primary interest is in the distribution of the valence electrons. For first and second row atoms the valence electrons form a large proportion of the

total number of electrons and bonding effects are readily observed. However, for heavier atoms the core-to-valence ratio is larger and the bonding effects are consequently obscured by the core scattering. The scattering factors are also not as well defined as for the lighter atoms and the question arises as to which level of the periodic table it is appropriate to extend experimental charge density studies. Compounds containing first and second row atoms have been studied extensively and some work has been done on first row transition metals^{36, 37}. It is questionable whether studies of heavier atoms would yield any meaningful information, usually $Z=35$ (Br) is taken as the upper limit.

1.6.3 Low-Temperature Requirement

A large data set is a necessary pre-requisite for a successful multipole analysis. This is because a multipole refinement may involve as many as three times more parameters than a conventional spherical atom refinement. The data set needs to be extensive enough to include a minimum of five observations per parameter, and for a high quality refinement an observations to parameters ratio of ten is desirable. In the majority of organic molecular crystals a room temperature X-ray diffraction experiment observes few reflections of significant intensity beyond $\sin\theta/\lambda=0.7 \text{ \AA}^{-1}$.³⁸ Hence there are too few observations for a multipole refinement to be possible.

At low temperatures the magnitude of the atomic vibration is reduced and more high angle reflections can be observed. It is then meaningful to extend the search for reflections beyond $\sin\theta/\lambda=0.7 \text{ \AA}^{-1}$; a resolution of $\sin\theta/\lambda=1.1 \text{ \AA}^{-1}$ is typical for this type of experiment. The resultant data set is improved in three ways:

- i)* more reflections can be observed and so the observations to parameters ratio is improved;
- ii)* the high-angle scattering is dominated by the core electrons so more accurate positional information is obtained;
- iii)* the reduced atomic vibration means that it is easier to deconvolute vibrational and bonding effects.

In practice there are two methods of performing a low-temperature diffraction experiment. The first uses a stream of cold nitrogen gas which is directed at the sample. This type of device can typically reach temperatures of 100K which is sufficiently low for the majority of charge density studies. This type of device is relatively inexpensive and easily obtainable and can be fitted to a pre-existing diffractometer. The second type of cooling

device is the liquid helium cold finger. The crystal is directly attached to a high-conductivity material which is cooled by evaporation of liquid helium. Temperatures as low as 10K are obtainable but the high cost and mechanical instability of this type of device have made them an unpopular alternative to the gas stream cooler.

1.7 Data Reduction

In order to obtain accurate structure factor information from the raw reflection data certain operations need to be performed on the data. Lorentz, polarisation and absorption corrections must be applied and any crystal decay taken into account. Finally the equivalent reflections are merged to give a set of unique hkl intensities.

For the work detailed in this thesis absorption corrections have been performed with ABSORB³⁹ and all other data reduction operations with DREADD.⁴⁰ Details of the procedures will therefore refer to these programs.

1.7.1 Obtaining Raw Reflection Intensities

The first step in the data reduction is to obtain reflection intensities from the raw reflection data. In order to do this, both the peak centroid positions and the peak widths must be accurately determined. The peak centroids give the exact positions of the reciprocal lattice points, and hence accurate unit cell parameters. The determination of the peak width is essential for the integration of the intensity of the reflections. DREADD determines these parameters by identifying a set of reflections which have large signal-to-noise ratios. The centroids of these peaks are used to calculate a new, and more accurate, crystal orientation matrix which is used throughout the data reduction. The same sub-set of well defined peaks is used to calculate peak width parameters. These parameters are then applied to all of the reflections and used to determine the background count rate for each reflection. This is then subtracted from each step in the scan that is regarded as part of the true peak, to give a background-corrected step intensity.

Lorentz and polarisation corrections are now applied. The Lorentz correction scales the measured intensity at each of the 96 scan steps to account for the differing time that each section of the lattice point takes to cross the Ewald sphere. This is a function of 2θ , the exact form depending on the geometry of the diffractometer. The polarisation correction accounts

for the way in which the diffracted beam intensity is affected when a non-polarised beam is diffracted by a crystal. This is also a function of 2θ . In practice the two corrections are generally applied together, the correction factor is given as LP and the corrected beam intensity, I , is given by:

$$I = \frac{I_{\text{measured}}}{LP} \quad 1.29$$

Once the LP correction has been performed the resultant step-wise intensities are summed across each peak to give the integrated intensity for the reflection.

1.7.2 Crystal Decay

Samples which are exposed to intense X-ray beams are often subject to decay. Crystal decay generally results in a roughly linear reduction in diffracted beam intensity with time. In order to account for this in the data reduction process a set of reflections, which correspond to a wide sample of reciprocal space, are measured repeatedly throughout the experiment. On the CAD-4 diffractometer this is generally done every two hours. A graph of intensity *versus* time is plotted for each of the standard reflections and a linear, quadratic or polynomial function is fitted. With functions of this order the long-range decay can be satisfactorily fitted whereas small random fluctuations in intensity will not be fitted by the function. The polynomials are used to scale the intensities of the rest of the data set with time.

1.7.3 Absorption Corrections

The intensity of an X-ray beam passing through a crystal is reduced as a result of absorption. This occurs when the X-ray photons are of the same energy as an electronic transition in an atom which is present in the crystal. Some of the photons are absorbed to provide energy for this transition and the resultant beam is reduced in intensity. The amount of absorption depends on the atoms present in the compound and the path length of the beam within the crystal. The expression for the absorption of an incident beam is:

$$I = I_0 \exp(-\mu t) \quad 1.30$$

where t is the path length of the particular reflection and μ is the linear absorption coefficient. μ depends on the numbers and types of atoms which are present in the unit cell, according to the formula:

$$\mu = \rho \sum_{i=1}^n f_i \left(\frac{\mu}{\rho} \right)_i \quad 1.31$$

where ρ is the density of the crystal and f_i is the mass fraction of the i th element. $(\mu/\rho)_i$ is the mass absorption coefficient of element i , values of which are recorded in the International Tables for each common type of incident radiation.⁴¹ Absorption is increased by heavy atoms and long wavelength incident radiation. Silver or molybdenum radiation and light atoms result in low absorption and hence represent the ideal situation for a charge density study.

The program ABSORB is used to perform an analytical absorption correction on the data by calculating the transmission factor $T=I/I_0$ for each reflection. Both incident and diffracted beam intensities are attenuated by absorption effects over the path lengths t_0 and t respectively. The transmission factor for the crystal is given by:

$$T = \frac{1}{V} \int \exp - \mu (t_0 + t) dV \quad 1.32$$

where V is the volume of the crystal. This integral is difficult to evaluate as it requires knowledge of t_0 and t for every point in the crystal.

The intensity of a diffracted beam can be considered as the sum of the diffraction effects arising from small volume elements. This fact is used to simplify the calculation of the above integral. The crystal boundaries are described by the Miller indices of the faces, and their distances from the centre of the crystal. This volume is then overlaid with an imaginary grid, typically of 10x10x10 cells. An approximation is invoked that the centre point of each cell can uniquely represent all of the other points in the cell. t_0 and t need only be evaluated for the central cell points and equation 1.32 can now be expressed as a summation:

$$T = \frac{1}{M} \sum \exp - \mu (t_0 + t) \quad 1.33$$

where M is the number of cells.⁴² A numerical solution for the transmission factor can then be obtained from knowledge of the incident and diffracted beam path for each reflection.

1.7.4 Data Merging

The least-squares refinement of the multipole model requires only the unique hkl data. The last step of data reduction is therefore the merging of equivalent reflections. If the data have been collected in shells there will be some overlap between the data sets. These multiple measurements of unique hkl are used to determine appropriate scale factors for the separate data sets. This is necessary in order to allow geometrically equivalent reflections to be merged on the same scale.

A weighted averaging of equivalent reflections is carried out with DREADD. The smaller the esd of a particular reflection, the greater its weight within the average. An estimate of the error on the merged intensity is also obtained, the better the internal agreement of the equivalents the smaller the esd of the average. However, some truly discordant measurements will have been made due to power fluctuations, sticking beam-shutter *etc.*. These should not be included in the average as they will artificially increase the esd of the merged reflection. Statistical tests are used to identify and either down-weight or reject outlier measurements.

An index of the quality of the merged data set is given by:

$$R_{merge} = \sum \frac{\langle I(\mathbf{H}) \rangle - I(\mathbf{H})}{I(\mathbf{H})} \quad 1.34$$

where $I(\mathbf{H})$ is the intensity of reflection \mathbf{H} and $\langle I(\mathbf{H}) \rangle$ is its mean value. The summation is over all measurements of all reflections. Even with the increased precision of merged reflections the signal-to-noise ratio of a particular reflection may not be large enough to consider it to be properly defined. A cut-off is therefore applied to intensities to determine which reflections will be used in the least-squares refinement. The cut-off is generally taken to be somewhere between $2\sigma/I(\mathbf{H})$ and $3\sigma/I(\mathbf{H})$.

1.8 Testing the Reliability of the Model

After the data reduction and subsequent refinement of the multipole model some assessment of the model's suitability must be made. As with a spherical atom refinement the agreement index, R , and the goodness-of-fit, S , are useful indicators of the quality of the model. However, in a refinement of the typical complexity of a multipole study, it is not the best approach to simply optimise these parameters. Several other factors must be considered concurrently as they all give some indication of the model's suitability.

i) Residual density maps: a Fourier map with coefficients $F_{obs}-F_{multi}$ shows how well the multipole model fits to the observed data. Such maps should be obtained for various planes through the asymmetric unit. For a well fitting model the residual density should be random and have no features greater than $\pm 0.2 \text{ e}\text{\AA}^{-3}$.

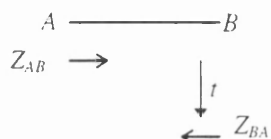
ii) Deformation density maps: these show the difference between the multipole and the spherical atom models and are obtained from the Fourier coefficients $F_{multi}-F_{spherical}$. They can be compared with equivalent results from *ab initio* calculations if such data are available. With experience they can also be used alone as a guide to whether or not the model is sensible by considering such factors as the location or absence of bonding and lone-pair deformation density peaks. However, care must be taken that the preconceptions of the experimenter are not given undue weight.

iii) Errors on parameters: the size of the esds on individual multipole parameters must be carefully examined. For a properly defined parameter, P , $P > 3\sigma(P)$. If this condition is not satisfied then the parameter can not be considered to be meaningfully defined. For higher order multipoles, e.g. hexadecapoles on first row atoms, the failure for this condition to be satisfied probably means that this level of deformation function is not necessary to describe the electron distribution of the atom. However, for lower order functions it may suggest a significant failure of the model.

iv) Correlation coefficients: the extent of correlation between different parameters is a measure of the reliability of the model. The largest correlations are often between temperature and charge density parameters due to the failure to completely deconvolute temperature and bonding effects. The existence of many correlation matrix elements with values greater than 0.7 is a good indication that the model is not reliable.

v) The rigid bond test: the most effective way to assess the physical significance of temperature parameters is to apply Hirshfeld's rigid bond test to these parameters.⁴³ He

assumes that the major component of vibrational motion in a molecular crystal is intermolecular lattice vibration, compared with which bond-stretching amplitudes are negligible. Atoms A and B are therefore assumed to be connected by a rigid bond. The vibration of atom A in the direction of atom B , Z_{AB} , should therefore be equal to the vibration of B in the direction of A at time t later, when the vibrational mode is at its other extreme.



If the bond is rigid we would expect $Z_{AB}^2 = Z_{BA}^2$ *i.e.* the two atoms have equal mean square amplitudes along the bond. In practice Hirshfeld estimated that for a pair of atoms at least as heavy as carbon the difference between Z_{AB} and Z_{BA} , the quantity $\Delta_{A,B}$, should be less than 0.001 \AA^2 . If this is not the case it can be assumed that the structural model is not sufficient to account for the actual behaviour of the system.

If the choice of parameters, level of expansion, $\sigma(I)$ cut-off or any other refinement variable is in doubt, careful consideration of the effect that each option has on the above factors can be used to identify the most suitable model. For a high quality charge density study all of the criteria *i-v* above should be satisfied to a high degree.

Chapter 2

Quantum Chemical Methods

2.1 Introduction

A quantum chemical calculation is one of the most important tools in chemistry. It provides inexpensive and rapid access to a wealth of information at a level of accuracy often comparable with that of experiment. Molecular structure, dipole moments and spin densities are just some of the types of information which are made available by quantum mechanical calculations. Another advantage of the computational approach is that the species under consideration does not actually have to exist. Reaction intermediates or unstable molecules can easily be studied, or the properties of proposed novel molecules be investigated in order to aid the synthetic chemist.

One objection that may be raised to the use of quantum chemical results to replace experimental data is the question of their reliability. It is true that there are certain limitations on the predictive ability of quantum chemical calculations, however the strengths and weaknesses of the majority of techniques are now well understood.⁶ Consideration must be given to both the nature of the molecule in question, and to the type of information required from the calculation. If these two factors are considered when choosing the type of calculation the computational results should be regarded as reliable.

The increasing speed of modern computers means that larger scale calculations are becoming more feasible, and the lowering cost of computational resources is in contrast to the increasing cost of experimental research. These factors should ensure that the computational

approach will play an increasingly significant role in the solution of chemically interesting problems.

2.2 Theoretical Background

2.2.1 The Schrödinger Equation

The energy, E , and properties of a molecule may be obtained by solution of the non-relativistic time-independent Schrödinger equation⁴⁴:

$$\hat{H}\Psi = E\Psi \quad 2.1$$

where \hat{H} is the Hamiltonian differential operator representing the total energy of the system. The wavefunction, Ψ , is dependent on the positional and spin coordinates of all particles in the system, and the product of the wavefunction and its complex conjugate, $\Psi^*\Psi$, is interpreted as a measure of the probability distribution of the particles in the molecule.

As in classical mechanics the energy of the system is composed of kinetic and potential energy components. The Hamiltonian can therefore be rewritten as the sum of kinetic, \hat{T} , and potential, \hat{V} , energy operators:

$$\hat{H} = \hat{T} + \hat{V} \quad 2.2$$

where:

$$\hat{T} = -\frac{h^2}{8\pi^2} \sum_i \frac{1}{m_i} \left(\frac{\partial^2}{\partial x_i^2} + \frac{\partial^2}{\partial y_i^2} + \frac{\partial^2}{\partial z_i^2} \right) \quad 2.3$$

and

$$\hat{V} = \sum_i \sum_j \left(\frac{e_i e_j}{4\pi\epsilon_0 r_{ij}} \right) \quad 2.4$$

In the kinetic energy operator the sum is over all particles i , electrons and nuclei, and m_i is the mass of particle i . h is Planck's constant. In the potential energy operator the sum is over all pairs of particles (i, j) with charges e_i, e_j at a separation of r_{ij} . ϵ_0 is the permittivity of a vacuum.

2.2.2 The Born-Oppenheimer Approximation

It is not possible to solve equation 2.1 for a many-electron system. As it is this type of system which is the primary interest of chemists some approximations need to be introduced to yield a useful level of theory.

The first of these is the Born-Oppenheimer approximation.⁴⁵ The standard interpretation of the BO approximation is based on the fact that nuclear masses, irrespective of atomic species, are much greater than the mass of an electron. The electrons in a molecule therefore move much faster than the atomic nuclei. In the light of this it is a reasonable approximation to regard the electronic distribution in a molecule as depending solely on the instantaneous positions of the nuclei, and not on their velocities. The electronic and nuclear motions have thus effectively been separated and this greatly simplifies the solution of equation 2.1.

However, it has since been shown by Essén that the magnitude of the electron-to-nucleus mass ratio is relatively unimportant.⁴⁶ Rather, the separation of nuclear and electronic motions is based on the distinction between the motion within an atomic sub-system and the collective motion of that sub-system. The kinetic energy of the first is dominated by the electronic motion, whereas the kinetic energy of the second is determined almost completely by the motion of the nucleus. It is therefore still possible to separate the motions of electrons and nuclei although the distinction is made on a significantly different conceptual basis.

The system may now be represented by the electronic wavefunction, Ψ^{elec} . The electronic Hamiltonian, \hat{H}^{elec} , corresponds to the motion of electrons in a field of fixed nuclei and is associated with the effective electronic energy, E^{elec} . The electronic Hamiltonian can be expressed as a sum of kinetic and potential parts:

$$\hat{H}^{elec} = -\frac{\hbar^2}{8\pi^2} \sum_i \frac{1}{m_e} \left(\frac{\partial^2}{\partial x_i^2} + \frac{\partial^2}{\partial y_i^2} + \frac{\partial^2}{\partial z_i^2} \right) + \sum_p \sum_q \frac{Z_p Z_q e^2}{4\pi\epsilon_0 R_{pq}} - \sum_p \sum_i \frac{Z_p e^2}{4\pi\epsilon_0 r_{pi}} + \sum_i \sum_j \frac{e^2}{4\pi\epsilon_0 r_{ij}} \quad 2.5$$

where the subscripts (i, j) and (p, q) refer to electrons and nuclei respectively. The first term is the kinetic energy component; this depends solely on the motion of the electrons and the summation is over all electrons, where m_e is the mass of an electron. The second term is the nuclear-nuclear repulsion energy, the summation is over all possible pairs of nuclei. The value of this term depends on the internuclear distances, R_{pq} , and the atomic numbers of the nuclei, (Z_p, Z_q) ; hence it is a fixed contribution to the energy at a particular nuclear configuration. The third term is the nuclear-electron attraction energy and the fourth is the electron-electron repulsion energy. These two terms depend on the nuclear-electron and electron-electron separations, r_{pi} and r_{ij} , respectively.

It is useful to simplify the operator expressions by rewriting them in atomic units. In this system certain constants obtain the value of unity and are therefore effectively removed from the equations:

$$\hbar = \frac{h}{2\pi} = 4\pi\epsilon_0 = m_e = e = 1 \quad 2.6$$

The electronic Hamiltonian can therefore be rewritten as:

$$\hat{H}^{elec} = -\frac{1}{2} \sum_i \left(\frac{\partial^2}{\partial x_i^2} + \frac{\partial^2}{\partial y_i^2} + \frac{\partial^2}{\partial z_i^2} \right) + \sum_p \sum_q \frac{Z_p Z_q}{R_{pq}} - \sum_p \sum_i \frac{Z_p}{r_{pi}} + \sum_i \sum_j \frac{1}{r_{ij}} \quad 2.7$$

The Born-Oppenheimer approximation is a necessary part of any practically useful level of theory, and so from this point onwards the superscripts denoting the electronic Hamiltonian and the corresponding wavefunction and effective energy will be omitted.

2.3 Molecular Orbital Theory

2.3.1 The Slater Determinant

Now that the Hamiltonian operator has been obtained in a computationally useful form it is necessary to find some way to represent the wavefunction in a similarly manageable fashion. One approach to this is to replace the exact electronic wavefunction by a combination of one-electron spin orbitals. A spin orbital is the product of a molecular orbital ψ , which is a function of the cartesian coordinates (x, y, z) , and a spin component α or β .

The simplest way of obtaining a wavefunction for the many-electron system is to form a product of spin orbitals, χ_i , *i.e.* :

$$\Psi = \chi_1(1)\chi_2(2) \dots \chi_n(n) \quad 2.8$$

where the subscript denotes the spin orbital, and the number in the bracket refers to the electron. However, this approximate wavefunction is not antisymmetric, *i.e.* equivalent to multiplication by -1, with regard to electron exchange, and so it fails to satisfy one of the criteria for a satisfactory wavefunction.

In order to obtain an antisymmetric wavefunction Ψ is represented by a determinant:

$$\Psi \propto \begin{vmatrix} \chi_1(1) & \chi_2(1) & \dots & \chi_n(1) \\ \chi_1(2) & \chi_2(2) & \dots & \chi_n(2) \\ & & \vdots & \\ \chi_1(n) & \chi_2(n) & \dots & \chi_n(n) \end{vmatrix} \quad 2.9$$

The elements of the first row of the determinant correspond to assignments of electron 1 to all of the possible spin orbitals $\chi_1, \chi_2, \dots, \chi_n$, the second row to assignments of electron 2 *etc.* In a determinantal wavefunction electron exchange corresponds to interchange of two rows in the determinant. It is a property of matrices that this does change the sign of the determinant: the wavefunction is therefore antisymmetric with respect to electron exchange. Expansion of the determinant gives a sum of spin orbital products:

$$\Psi = \sum_P (-1)^P \hat{P}[\chi_1(1)\chi_2(2) \dots \chi_n(n)] \quad 2.10$$

where \hat{P} is the permutation operator which generates all possible permutations of the n electrons and $(-1)^P$ is either 1 or -1 for even and odd permutations respectively.

In practice an electron is usually assigned to a molecular orbital, ψ_i a spatial function, and given a spin α or β . This means that molecular orbitals can be doubly or singly occupied, or empty, and in all cases the many-electron wavefunction Ψ will still satisfy the Pauli exclusion principle.

As mentioned earlier, the product of the wavefunction and its complex conjugate is a probability distribution function of all of the particles in the molecule; within the Born-Oppenheimer approximation it is only the distribution of the electrons which is in question. The probability of finding a particular electron in all space is unity and so the individual molecular orbitals are normalised to ensure that:

$$S_{ii} = \int \psi_i^* \psi_i dx dy dz = 1 \quad 2.11$$

For the determinantal wavefunction to be normalised it must be multiplied by a factor of $(n!)^{-1/2}$, where n is the number of electrons in the molecule and there are $n/2$ doubly occupied molecular orbitals.

It is now possible to write an expression for the normalised closed-shell many-electron molecular orbital wavefunction:

$$\Psi = (n!)^{-1/2} \begin{vmatrix} \psi_1(1)\alpha(1) & \psi_1(1)\beta(1) & \psi_2(1)\alpha(1) & \cdots & \psi_{n/2}(1)\beta(1) \\ \psi_1(2)\alpha(2) & \psi_1(2)\beta(2) & \psi_2(2)\alpha(2) & \cdots & \psi_{n/2}(2)\beta(2) \\ & & & \vdots & \\ \psi_1(n)\alpha(n) & \psi_1(n)\beta(n) & \psi_2(n)\alpha(n) & \cdots & \psi_{n/2}(n)\beta(n) \end{vmatrix} \quad 2.12$$

This type of determinant is known as a Slater determinant.⁴⁷

2.3.2 Variational Methods

The Slater determinantal wavefunction is composed of molecular orbitals. These MOs are in turn constructed of linear combinations of the set of M basis functions, ϕ_{ii} , such that:

$$\Psi_i = \sum_{\mu=1}^M c_{\mu i} \phi_{\mu} \quad 2.13$$

where $c_{\mu i}$ is the molecular orbital expansion coefficient for basis function μ in molecular orbital i . Once the basis functions have been chosen, see Section 2.4, the problem of defining the wavefunction Ψ is therefore reduced to determining the most appropriate values for the coefficients $c_{\mu i}$.

Hartree-Fock, HF, theory tackles this problem by applying the variational method. This states that for any antisymmetric normalised wavefunction Ψ , an expectation value for the energy associated with that function can be obtained:

$$E_{approx} = \int \Psi^* \hat{H} \Psi \, d\tau \quad 2.14$$

Integration is over the spatial and spin coordinates of all electrons. If Ψ is an exact solution of the Schrödinger equation then $E_{approx} = E_{exact}$. If Ψ is any other approximate wavefunction then $E_{approx} > E_{exact}$. The best approximate wavefunction is therefore achieved when E_{approx} is minimised and approaches E_{exact} . This limit is achieved within a particular set of basis functions by minimising E_{approx} with respect to $c_{\mu i}$. The set of variational equations:

$$\frac{\partial E_{approx}}{\partial c_{\mu i}} = 0 \quad 2.15$$

are obtained for all combinations of μ and i .

2.3.3 The Roothaan-Hall Equations

The variational equations 2.15 lead to a set of simultaneous equations which can be solved for $c_{\mu i}$. These were developed simultaneously by Roothaan⁴⁸ and Hall.⁴⁹

$$\sum_{\nu=1}^M (F_{\mu\nu} - \epsilon_i S_{\mu\nu}) c_{\nu i} = 0 \quad 2.16$$

where ϵ_i is the one-electron energy for molecular orbital i and the Greek subscripts μ, ν etc. refer to members of the set of M basis functions. $S_{\mu\nu}$ are elements of an $M \times M$ matrix, the overlap matrix:

$$S_{\mu\nu} = \int \phi_{\mu}^*(1)\phi_{\nu}(1)dx_1dy_1dz_1 \quad 2.17$$

$F_{\mu\nu}$ are the elements of another $M \times M$ matrix, the Fock matrix:

$$F_{\mu\nu} = H_{\mu\nu} + \sum_{\lambda=1}^M \sum_{\sigma=1}^M P_{\lambda\sigma} \left[\langle \mu\nu | \lambda\sigma \rangle - \frac{1}{2} \langle \mu\lambda | \nu\sigma \rangle \right] \quad 2.18$$

$H_{\mu\nu}$ is a matrix representing the energy of a single electron in a field of nuclei, its elements are given by:

$$H_{\mu\nu} = \int \phi_{\mu}^*(1)\hat{h}(1)\phi_{\nu}(1)dx_1dy_1dz_1 \quad 2.19$$

$$\hat{h}(1) = -\frac{1}{2} \left(\frac{\partial^2}{\partial x_1^2} + \frac{\partial^2}{\partial y_1^2} + \frac{\partial^2}{\partial z_1^2} \right) - \sum_{I=1}^N \frac{Z_I}{r_{1I}} \quad 2.20$$

It is clear that \hat{h} is made up of the one-electron terms from the electronic Hamiltonian.

The other terms in the Fock matrix are the result of two-electron interactions. The coulomb integral, $\langle \mu\nu | \lambda\sigma \rangle$, is a two-electron repulsion integral caused by the tendency for electrons in space to repel each other. The exchange integral, $\langle \mu\lambda | \nu\sigma \rangle$, is the result of a quantum effect and is related to the energy difference which occurs when identical electrons are exchanged between basis functions. $P_{\lambda\sigma}$ are the elements of the one-electron density matrix:

$$P_{\lambda\sigma} = 2 \sum_{i=1}^{M/2} c_{\lambda i}^* c_{\sigma i} \quad 2.21$$

The summation is over all occupied molecular orbitals and the factor of two indicates that each MO is occupied by two electrons.

An expression for the energy of the system can then be derived in terms of the density, Fock and overlap matrix elements. The energy can then be minimised with respect to $c_{\mu i}$.

2.3.4 Practical Implementation

It is not possible to directly solve the Roothaan-Hall equations for $c_{\mu i}$ as the Fock matrix depends on the values of $c_{\mu i}$ through the density matrix. The solution must therefore be an iterative one. In practice a basis set is chosen and the one and two-electron integrals are calculated. A guess is made at the appropriate values for the MO expansion coefficients and these are used to construct the one-electron density matrix. The Fock matrix can then also be calculated and the Roothaan-Hall equations solved to yield new values for $c_{\mu i}$. The next step is to calculate a total energy for the system. The new coefficients can then be used to construct an improved density matrix and the process repeated.

The best wavefunction is achieved when E_{approx} is as low as possible within the particular basis set in use. The energy of the system is therefore used as a criterion to determine the most appropriate values of $c_{\mu i}$. The cycle of calculations is repeated until the variation in the value of E_{approx} falls below a certain pre-determined cut-off point. The potential field which defines the molecular orbitals is now considered to be self-consistent; the method is therefore often referred to as self-consistent-field (SCF) theory. The calculation cycle is shown diagrammatically in Figure 2.1.

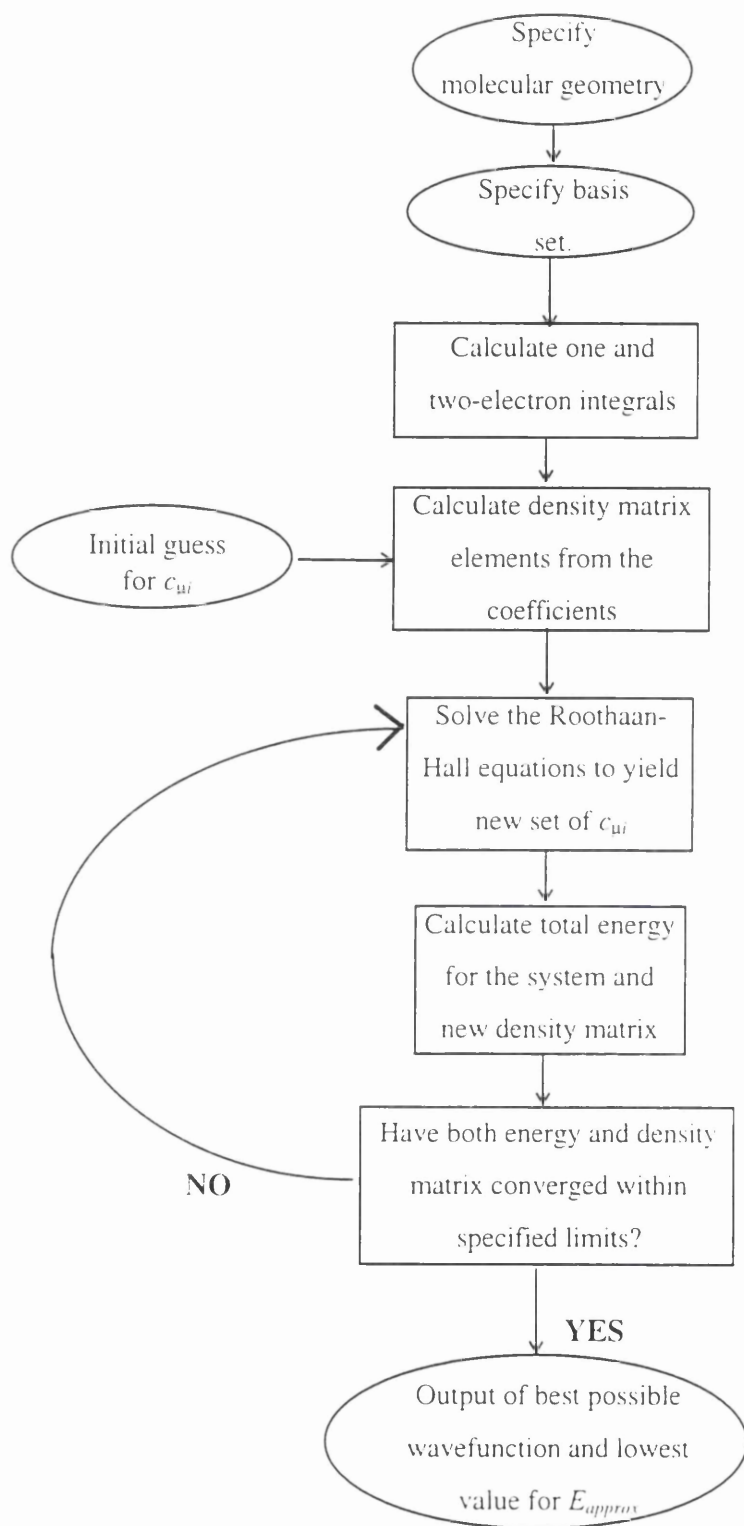


Figure 2.1 : Flow chart for the SCF procedure.

2.4 Basis Set Expansions

2.4.1 The Effect of Basis Set Choice

It is apparent from equations 2.16 - 2.19 that the nature of the basis functions will affect the total energy of the system, and the form of the many-electron wavefunction. The energy is minimised with respect to the molecular orbital expansion coefficients and can therefore only ever reach the best possible energy given the constraints imposed by the limited basis set. If a larger basis set is used the number of variational parameters is increased, and hence the approximate wavefunction obtained will correspond more closely to the actual wavefunction of the system. The accuracy of the derived properties is therefore dependent on the quality of the basis set. The ideal situation, within the limits imposed by the use of a single-configuration wavefunction, is to use a very large basis set which gives complete flexibility. This is termed the Hartree-Fock limit and represents the lowest possible energy obtainable with a single electron configuration.

A well defined basis set should be generally applicable in a variety of chemical situations, this is achieved by defining a sufficiently flexible set of nucleus-centred functions for each element. The same set of basis functions for a particular atom type can then be used regardless of chemical environment. However, there are specific cases where it is appropriate to make alterations to the standard basis, *e.g.* anions typically require extra diffuse functions to be added to the corresponding neutral atom basis to accommodate the increased radial distribution of the electrons.⁵⁰

2.4.2 Slater and Gaussian Type Orbitals

There are two types of atomic basis functions which have been suggested for use in calculations, both are the product of an angular and a radial component. The first type of basis function is the Slater-type orbital,⁵¹ STO, the radial component of which is given by:

$$R_{nl}(r, \zeta) = Nr^{n-1}e^{-\zeta r} \quad 2.22$$

where n is the principal quantum number, ζ is the orbital exponent which determines the radial extent of the function and r is the distance from the nucleus. N is a normalisation factor.

The STO gives a qualitatively correct description of the radial charge distribution. Slater compared values of ionisation potentials, internuclear distances and ionic radii calculated from his atomic basis functions with those observed by experiment and found them to be in reasonably good agreement.⁵¹ However, STOs are not well suited to computational work as they cannot be analytically integrated. This causes problems in the calculation of the one and two-electron integrals in the SCF method.

The second type of commonly used basis function is the Gaussian-type orbital, GTO.⁵² The radial part of the Gaussian function has the form:

$$R_{nl}(r, \alpha) = Nr^{n-1}e^{-\alpha r^2} \quad 2.23$$

where α is the orbital exponent and the other variables are defined as for the STO.

Gaussian-type orbitals do not have a cusp at the nucleus and so give a poor representation of atomic orbitals at small values of r . It is possible to use linear combinations of single or 'primitive' GTOs, g_s , as basis functions; these give much better representations of the atomic orbitals. This type of basis function is referred to as a contracted Gaussian and is formulated in an analogous way to a molecular orbital:

$$\phi_\mu = \sum_s d_{s\mu} g_s \quad 2.24$$

In this case, unlike in a molecular orbital, the coefficients $d_{s\mu}$ are fixed at predetermined values. It is interesting to note that the concept of contracted Gaussian functions was first introduced by McWeeny in his work on aspherical scattering factors, Section 1.3.3.

Huzinaga extensively investigated the accuracy of a variety of contracted GTO functions compared with STOs.⁵³ He concluded that for polyatomic systems within the Hartree-Fock approximation, usefully accurate results can be achieved with a suitable Gaussian contraction that does not involve a prohibitively large number of primitive Gaussian functions. According to Huzinaga the time taken to perform a molecular calculation is proportional to M^4 , where M is the number of basis functions. It might appear then that it is preferable to use STOs rather than contracted GTOs as the former are more accurate and involve less basis functions. However, whereas STOs are difficult to integrate, GTOs can be

analytically integrated and the large number of basis functions required is more than compensated for by the speed at which the integrals can be calculated.

2.4.3 Types of Basis Set

Minimal Basis Sets: the simplest possible basis set. Each atomic orbital, AO, which is occupied in the ground state is represented by one basis function. This basis is extremely inflexible and does not give a satisfactory description of the molecular orbitals. The most common minimal basis is:

- STO-3G: an improved minimal basis.⁵⁴ Each ground state-occupied AO is represented by a set of three Gaussian functions contracted to give the best approximation to an STO. In order to improve efficiency Gaussian functions of the same principal quantum number are given the same exponent α . The exceptions to this are the transition metal atoms, the *d* functions of which are given a different exponent to the *s* and *p* functions of the same shell.

Minimal basis sets have three major problems:

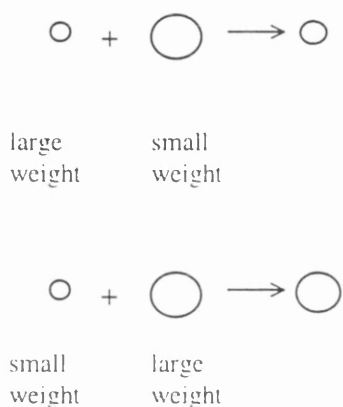
- i*) the number of basis functions is determined by which row of the periodic table the atom is in, rather than by its electron count. Hence atoms on the left of the periodic table have excess basis functions while those on the right do not;
- ii*) the size of the basis functions is fixed by the predetermined exponent. There is therefore no mechanism by which the functions can expand or contract to adjust to differing molecular environments;
- iii*) the use of the same exponent for all functions in the same shell means that the basis set is isotropic and therefore cannot properly describe anisotropic molecular environments. It has been shown that the equilibrium geometries, calculated with minimal basis sets, of highly anisotropic molecules are often significantly in error.

Extended Basis Sets: extra functions are added to the minimal basis set description of the atom. These extra functions may be added for all ground state occupied orbitals, or only the valence shell. Typically the two or more functions of each type are given different exponents so that $\alpha p_x = \alpha p_y = \alpha p_z$ and $\alpha' p_x = \alpha' p_y = \alpha' p_z$ but $\alpha p_x \neq \alpha' p_x$.

This modification allows the three problems outlined above to be overcome:

i) there is now an excess of basis functions for all atoms, not just those to the left of the periodic table;

ii) the different exponents of the two or more radial functions of each symmetry type mean that it is now possible to vary the radial size of the electron distribution by altering the relative weights of the two components in the variational procedure. For example, consider two $1s$ functions, one of which is contracted and the other diffuse. The radial description of the resulting s function can lie anywhere between the two extremes:



iii) the attainment of an anisotropic basis set also depends on the provision of both a contracted and a diffuse set of functions. Consider an atom which is involved in σ -bonding in the x and y directions, and π -bonding in the z direction. The σ -bonding requires contracted p functions which are achieved by giving more weight to the contracted rather than the diffuse p_x and p_y functions. The π -bonding requires a diffuse p_z function. It is apparent that the resulting basis is not isotropic.

There are a large number of ways in which to formulate an extended basis set. Some representative examples of specific basis sets are given below.

- Double-Zeta: the simplest extended basis set. Every function in the minimal basis set is replaced by one diffuse and one contracted function.⁵⁵
- Split -Valence: this type of basis treats the core and valence shells separately. The core AOs remain minimal whilst the valence orbitals are represented by two functions. For example, in the 6-31G basis set⁵⁶ each inner-shell orbital is represented by a single contracted Gaussian composed of 6 primitive Gaussians. The valence AOs are

represented by two GTOs: a contracted Gaussian made up of three primitives, and a single diffuse Gaussian.

- Polarisation: here functions of higher angular quantum number than those that are occupied in the ground state are included in the basis, *i.e.* p -type functions on hydrogen and d -type functions on first and second row atoms. This extension of the basis allows for the displacement of electronic charge away from the nuclei, an effect which is particularly significant in highly polar molecules. For example, mixing of the $1s$ function of hydrogen with a p_x polarisation function has the effect of displacing the centre of the basis function, and hence the charge distribution, along the x axis.

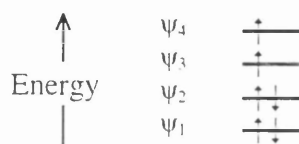


It is possible to add polarisation functions to any basis set, although it is unlikely that their addition to a low level basis set will improve the results enough to make any derived properties comparable with experimental values. 6-31G* and 6-31G** are two of the most frequently used polarisation basis sets.⁵⁷ They are made up of Pople's 6-31G basis with the addition of d functions on first and second row atoms, and this plus p functions on hydrogen, for 6-31G* and 6-31G** respectively.

It has only been practical to outline a small number of the more common basis sets above. A full listing of calculated Gaussian basis sets is available electronically via the World Wide Web.⁵⁸

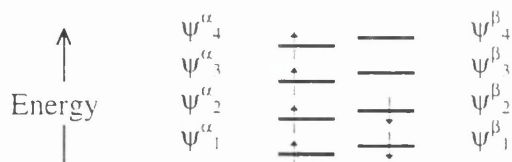
2.5 Open-Shell Systems

The Hartree-Fock method outlined above restricts the paired electrons to occupy the same spatial orbital function. It is therefore referred to as the restricted Hartree-Fock, RHF, method and is valid for closed-shell systems. However, a variant of this method has been developed for open-shell systems, typically doublet radicals or triplet states. The restricted open-shell Hartree-Fock, ROHF, method assigns paired electrons to the same spatial orbital function.⁵⁹ Any unpaired electrons are given spin α and singly occupy progressively higher energy spatial orbitals. For example, a six electron triplet state can be represented by:



The molecular orbital expansion coefficients are determined from the variational conditions **2.15** in the same way as for a closed-shell system.

A second approach to the problem of open-shell systems is the unrestricted Hartree-Fock, UHF, method in which α and β electrons are assigned to different spatial orbital functions.⁶⁰ The six electron triplet is now represented by:



The two sets of orbitals are defined by two sets of coefficients, c_{ui}^{α} and c_{ui}^{β} . They are varied independently and the Roothaan-Hall equations therefore need to be reformulated.

The ROHF function is a specialised case of the UHF function and it follows from the variational theorem that the UHF energy will always be lower than the ROHF energy. This is because a degree of correlation is introduced in the UHF function between electrons which would be paired in the ROHF function. However, this also has the result that the UHF wavefunction is no longer an eigenfunction of the spin operator \hat{S}^2 . Often the expectation value of S^2 does not differ significantly from $S(S+1)$ and the UHF wavefunction can be regarded as representing an almost pure spin state. However, if the deviation of the

expectation value of S^2 from $S(S+1)$ is large, the wavefunction should be regarded with suspicion as it will be contaminated by functions corresponding to states of higher spin multiplicity.

2.6 Electron Correlation

Hartree-Fock theory inadequately treats the correlation between the motions of electrons. The antisymmetrised determinantal form of the wavefunction means that the correlation between electrons of the same spin is partially accounted for. However, there is no allowance for the correlation between electrons of opposite spins. These limitations lead to a value for the Hartree-Fock energy which is above the true energy of the system. At the Hartree-Fock limit the difference between the observed energy after removal of relativistic effects, and the HF energy is the correlation energy. The neglect of electron correlation also leads to qualitative deficiencies in the description of electronic structure, for example the incorrect treatment of dissociation when nuclei move to large separations.

There are two main methods of including electron correlation in quantum chemical calculations; configuration interaction, CI, and Møller-Plesset perturbation theory. Both of these methods replace the single Slater determinant with a linear combination of such determinants and the calculation time is therefore significantly increased.

2.6.1 Full Configuration Interaction

A system with n electrons and M basis functions will have $2M$ spin orbitals, χ_{iM} . Solution of the HF problem results in a wavefunction Ψ_0 where:

$$\Psi_0 = (n!)^{-1/2} \left| \chi_1 \chi_2 \cdots \chi_n \right| \quad 2.25$$

The occupied spin orbitals $\chi_1 \dots \chi_n$ are a sub-set of the total set of spin orbitals, these will be designated χ_i etc.. There are $2M-n$ unoccupied virtual orbitals, these will be designated χ_a ($a=n+1, n+2, \dots, 2M$). It is possible to construct determinants, Ψ_s ($s > 0$), where some of the occupied spin orbitals have been replaced by virtual orbitals, up to a point where all of the orbitals are virtual orbitals. A wavefunction can then be obtained:

$$\Psi = a_0 \Psi_0 + \sum_{s>0} a_s \Psi_s \quad 2.26$$

For full CI the summation is over all possible determinants and the coefficients a_s are determined variationally. This requires the solution of the equation:⁶¹

$$\sum_s (H_{st} - E_i \delta_{st}) a_{st} = 0 \quad t = 0, 1, 2, \dots \quad 2.27$$

where H_{st} is a configurational, or Hamiltonian, matrix element and E_i is an energy. Equation 2.27 is very similar to the Roothaan-Hall equations, 2.16. In this case however, the orthogonality of the determinantal wavefunctions means that the overlap matrix S is replaced by a delta function which takes a value of zero or unity.

As the number of basis functions approaches infinity the resultant wavefunction will approach the exact solution of the non-relativistic Schrödinger equation, within the limits of the Born-Oppenheimer approximation. However, the number of possible substituted determinants is $(2M!)/[n!(2M-n)!]$ and so full CI is only practical for very small systems.

2.6.2 Limited Configuration Interaction

Limited CI is a practical way of introducing electron correlation to a quantum chemical calculation whilst keeping that calculation to a manageable size. This is done by excluding some of the terms from the Hamiltonian matrix, H_{st} . The most usual way to limit the CI expansion is to truncate the series at a certain level of substitution. For example the most commonly used type of configuration interaction calculation, CI singles and doubles, includes only those determinants which result from single or double substitutions. The wavefunction is given by:

$$\Psi_{CISD} = a_0 \Psi_0 + \sum_i \sum_a a_i^a \Psi_i^a + \sum_i \sum_j \sum_a \sum_b a_{ij}^{ab} \Psi_{ij}^{ab} \quad 2.28$$

It is also possible to limit the number of determinants in the expansion by restricting the spin orbitals involved in the substitutions. For example, in the majority of calculations

the chemical interest is in the behaviour of the valence shell electrons. It may therefore be reasonable to exclude from the expansion any determinants which involve excitation of the core electrons. This is known as the frozen-core approximation and is a common way of reducing the size of CI calculations. It is also possible to restrict the number of virtual orbitals which electrons can be excited to: high energy virtual orbitals would not be expected to be significantly occupied.

For any but the smallest systems it is generally necessary to restrict both the allowed level of excitation, and the participating orbitals. Care must be taken to ensure the meaningful selection of occupied and virtual orbitals to include in the excitations.

2.6.3 Møller-Plesset Perturbation Theory

The aim of Møller-Plesset, MP, perturbation theory is to find the lowest energy and corresponding wavefunction for the full Hamiltonian matrix. However, whereas in limited CI the matrix is truncated, MP theory partitions the matrix into two parts. The second part of the matrix (involving the excited states) is taken to be a perturbation on the first part, *i.e.* the Hartree-Fock matrix. The Schrödinger equation is rewritten as:

$$[\hat{H}_0 + \hat{V}]\Psi = E\Psi \quad 2.29$$

where

$$\hat{V} = \hat{H} - \hat{H}_0 \quad 2.30$$

\hat{H}_0 is the zero-order Hamiltonian, the eigenfunction of which is the unperturbed wavefunction, *i.e.* the Hartree-Fock wavefunction. This can be determined using variational theory, as outlined earlier. \hat{H} is the true molecular electronic Hamiltonian operator.

The unperturbed Hamiltonian is taken as the sum of the one-electron Fock operators:⁶²

$$\hat{H}_0 = \sum_{m=1}^n \hat{f}(m) \quad 2.31$$

where

$$\hat{f}(m) = -\frac{1}{2} \nabla_m^2 - \sum_p \frac{Z_p}{r_{mp}} + \sum_{j=1}^n [\hat{j}_j(m) - \hat{k}_j(m)] \quad 2.32$$

and

$$\nabla^2 = \frac{\partial^2}{\partial x^2} + \frac{\partial^2}{\partial y^2} + \frac{\partial^2}{\partial z^2} \quad 2.33$$

\hat{j} is the coulomb operator and \hat{k} is the exchange operator. The electronic Hamiltonian is defined by:

$$\hat{H} = -\frac{1}{2} \sum_i \nabla_i^2 - \sum_i \sum_p \frac{Z_p}{r_{ip}} + \sum_i \sum_{j>i} \frac{1}{r_{ij}} \quad 2.34$$

It is apparent then that the perturbation is given by:

$$\hat{V} = \sum_l \sum_{m>l} \frac{1}{r_{lm}} - \sum_{m=1}^n \sum_{j=1}^n [\hat{j}_j(m) - \hat{k}_j(m)] \quad 2.35$$

This is the difference between the true interelectronic repulsions, and the Hartree-Fock interelectronic potentials. Having determined the form of the perturbation it is now possible to determine the full CI wavefunction and the corresponding energy for a system described by the perturbed Hamiltonian $[\hat{H}_0 + \hat{V}]$. For example, the second-order correction to the Hartree-Fock energy is given by:

$$E^{(2)} = - \sum_s \frac{|\int \Psi_s \hat{V} \Psi_0|^2}{E_0 - E_s} \quad 2.36$$

E_s is the eigenvalue of a particular determinant, Ψ_s , which represents an excited state, and E_0 is the Hartree-Fock energy.

2.7 Derivation of Properties

2.7.1 Electronic Charge Density

The electron density function, $\rho(\mathbf{r})$, is a continuous three dimensional function which is positive at all points in space. It is defined such that $\rho(\mathbf{r}) d\mathbf{r}$ is the probability of finding an electron in the small volume $d\mathbf{r}$ at point \mathbf{r} in space. The function is normalised so that integration of $\rho(\mathbf{r})$ over all space will yield the total number of electrons in the system, n :

$$\int \rho(\mathbf{r})d\mathbf{r} = n \quad 2.37$$

For a single Slater determinantal wavefunction the electron density at point \mathbf{r} is defined by:

$$\rho(\mathbf{r}) = \sum_{\mu}^M \sum_{\nu}^M P_{\mu\nu} \phi_{\mu} \phi_{\nu} \quad 2.38$$

Once the electron density has been determined it is possible to analyse it in some way to obtain further information. The most useful technique is to study the surface features, or topology, of the charge density, see Chapter 3.

2.7.2 Mulliken Population Analysis

Having obtained the charge density distribution for the molecule it is often desirable to partition the electrons to particular parts of the system. For example, it is possible to distribute the charge density between the atoms to obtain an electronic charge for each atom. There are a number of ways in which to partition the charge, the most commonly used method is that developed by Mulliken and is known as Mulliken population analysis.⁶³

Integration of 2.38 gives:

$$\int \rho(\mathbf{r})d\mathbf{r} = \sum_{\mu}^M \sum_{\nu}^M P_{\mu\nu} S_{\mu\nu} = n \quad 2.39$$

where $S_{\mu\nu}$ is the overlap matrix, **2.17**. The basis functions are normalised such that $S_{\mu\mu} = 1$. The diagonal terms in **2.39** are therefore just $P_{\mu\mu}$, the number of electrons associated with a particular basis function ϕ_{μ} . The off-diagonal components occur in pairs of equal magnitude, $P_{\mu\nu}S_{\mu\nu} = P_{\nu\mu}S_{\nu\mu}$, and their sum, $Q_{\mu\nu} = 2P_{\mu\nu}S_{\mu\nu}$, is known as an overlap population.

$Q_{\mu\nu}$ is necessarily associated with pairs of basis functions. However, in order to obtain atomic charges it is desirable to partition the charge only between individual basis functions. Mulliken's method of achieving this is to arbitrarily divide the overlap populations into two equal parts and assign one part to each basis function. The total population of a particular basis function, q_{μ} , is therefore given by:

$$q_{\mu} = P_{\mu\mu} + \sum_{\nu \neq \mu} P_{\mu\nu} S_{\mu\nu} \quad \mathbf{2.40}$$

The total atomic population for a particular atom, q_A , is obtained by summing the populations for those basis functions which are centred on that atom. The atomic charge is then given by $Z_A - q_A$, where Z_A is the atomic number of atom A.

2.7.3 Electrostatic Potential

The electrostatic potential, ESP, at a point is an indication of the electrophilicity of the charge density distribution at that point. Quantitatively, it is the energy change which occurs on bringing a point positive charge from infinity to that point in the charge distribution. A negative electrostatic potential indicates that the system would be of higher energy if the positive charge was at infinity, *i.e.* the point charge is attracted to that region of the charge distribution. A positive ESP indicates that the positive charge is not attracted to the region of charge *i.e.* the system is energetically destabilised over that with the point charge at infinity.

The electrostatic potential at point \mathbf{r} is given by:⁶⁴

$$V(\mathbf{r}) = \int \frac{\gamma(\mathbf{r}_1, \mathbf{R}_A)}{|\mathbf{r} - \mathbf{r}_1|} d\mathbf{r}_1 \quad \mathbf{2.41}$$

where $\gamma(\mathbf{r}_1, \mathbf{R}_A)$ is the total charge distribution of the molecule, and \mathbf{r}_1 and \mathbf{R}_A are the position vectors of electron 1 and nucleus A respectively. $\gamma(\mathbf{r}_1, \mathbf{R}_A)$ is given by:

$$\gamma(\mathbf{r}_1, \mathbf{R}_A) = -\rho(\mathbf{r}_1) + \sum_A Z_A \delta(\mathbf{r}_1 - \mathbf{R}_A) \quad 2.42$$

The first term in 2.42 is the one-electron charge density, and the second term arises from the nuclei of the molecule. If the one-electron density is defined as in 2.38 a substitution can be made to reformulate 2.41 as:

$$V(\mathbf{r}) = -\sum_{\mu} \sum_{\nu} P_{\mu\nu} \int \frac{\phi_{\mu} \phi_{\nu}}{|\mathbf{r} - \mathbf{r}_1|} d\mathbf{r}_1 + \sum_A \frac{Z_A}{|\mathbf{r} - \mathbf{R}_A|} \quad 2.43$$

The problem of calculating the electrostatic potential is therefore reduced to one of evaluating the one-electron integrals over the basis set.

2.7.4 Spin Density

In an open shell system it is possible to obtain two separate charge density distributions, 2.38, for the α and β electrons. The excess of α electrons over β electrons is the spin density function, $\rho^{spin}(\mathbf{r})$.⁶⁵ It is given by:

$$\rho^{spin}(\mathbf{r}) = \rho^{\alpha}(\mathbf{r}) - \rho^{\beta}(\mathbf{r}) = \sum_{\mu} \sum_{\nu} P_{\mu\nu}^{spin} \phi_{\mu} \phi_{\nu} \quad 2.44$$

where $P_{\mu\nu}^{spin}$ are elements of the spin density matrix:

$$P_{\mu\nu}^{spin} = \sum_{i=1}^{\alpha} c_{\mu i}^{\alpha} c_{\nu i}^{\alpha} - \sum_{i=1}^{\beta} c_{\mu i}^{\beta} c_{\nu i}^{\beta} \quad 2.45$$

The resultant spin density data give information about the distribution of the unpaired spins in open-shell systems.

Chapter Three

The Topology of the Charge Density

3.1 Introduction

Having obtained the charge density distribution for a system, whether experimentally or by theoretical methods, it is necessary to analyse it in some way in order to obtain the chemically useful information which it contains. The most flexible form of analysis is due to Bader, and concentrates on the surface features, or topology, of the charge distribution.⁶⁶

3.2 Critical Points

The topology of the charge density distribution at point \mathbf{r} is defined as $\nabla\rho(\mathbf{r})$:

$$\nabla\rho(\mathbf{r}) = \mathbf{i} \frac{\partial\rho}{\partial x} + \mathbf{j} \frac{\partial\rho}{\partial y} + \mathbf{k} \frac{\partial\rho}{\partial z} \quad 3.1$$

where \mathbf{i} , \mathbf{j} , \mathbf{k} are unit vectors. At certain points in the distribution the first derivatives of $\rho(\mathbf{r})$ are zero, hence $\nabla\rho(\mathbf{r})$ also has a value of zero. These positions, \mathbf{r}_i , are either local maxima or minima and are collectively termed "critical points" (CPs). They are one of the most important features of the topology of the charge density distribution.

Whether a critical point is a maximum or a minimum is determined by the sign of the second derivative, or curvature, of $\rho(\mathbf{r})$ at \mathbf{r}_c . Since the charge density distribution is a three-dimensional function it is necessary to consider the sign of the curvature along three orthogonal axes passing through the CP. If the curvature has a positive sign then $\rho(\mathbf{r})$ is a local minimum in that direction; if the curvature is negative $\rho(\mathbf{r})$ is a local maximum. In general, for an arbitrary choice of coordinate axes there are nine second derivatives of the form $\partial^2\rho/\partial x\partial y$ in the determination of the curvatures of ρ at a point in space. Their 3×3 array is called the Hessian matrix of the charge density:

$$\begin{bmatrix} \frac{\partial^2 \rho}{\partial x^2} & \frac{\partial^2 \rho}{\partial x \partial y} & \frac{\partial^2 \rho}{\partial x \partial z} \\ \frac{\partial^2 \rho}{\partial y \partial x} & \frac{\partial^2 \rho}{\partial y^2} & \frac{\partial^2 \rho}{\partial y \partial z} \\ \frac{\partial^2 \rho}{\partial z \partial x} & \frac{\partial^2 \rho}{\partial z \partial y} & \frac{\partial^2 \rho}{\partial z^2} \end{bmatrix} \quad 3.2$$

It is possible to diagonalise this matrix so that the off-diagonal elements vanish. In terms of the coordinate system this is equivalent to rotating the coordinate axes until the three second derivatives, with respect to these axes, obtain their extreme values. The resultant axes are called the principal axes of curvature.

The number of non-zero curvatures of the Hessian matrix is called the rank of the critical point. The signature of a CP is the algebraic sum of the signs of the curvatures and a CP is labelled by giving both its rank and signature. Almost without exception, critical points in stable molecules are of rank three. There are therefore four possible types of critical point:

- (3,-3) all curvatures are negative and ρ is a local maximum at \mathbf{r}_c .
- (3,-1) two negative and one positive curvatures; $\rho(\mathbf{r}_c)$ is a local maximum along two of the axes and a local minimum along the third orthogonal axis. The density represented as a relief map in a section containing the third axis is a saddle.
- (3,+1) two positive and one negative curvatures. The density represented as a relief map appears as a saddle point in any plane containing the axis of negative curvature, and as a local minimum in the plane defined by the two axes of positive curvature.
- (3,+3) all three curvatures are positive and ρ is a local minimum at \mathbf{r}_c .

The significance of these critical point labels with regard to molecular structure is best demonstrated by an example. Figure 3.1 shows $\rho(\mathbf{r})$ for three orthogonal planes through the ethene molecule.

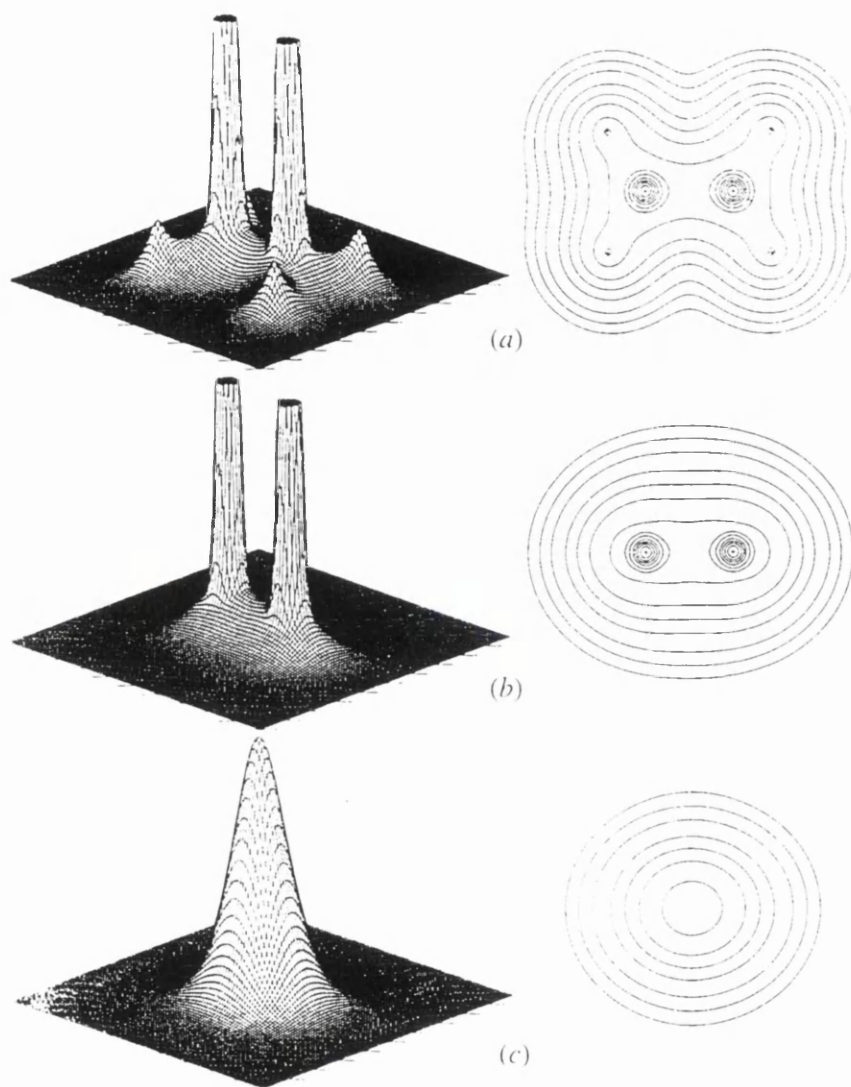


Figure 3.1 : Relief and contour plots of the electronic charge density in three planes of the ethene molecule, C_2H_4 . Reproduced from Ref. 66, Ch. 2, p. 15.

(a) The plane containing all six nuclei.

(b) The plane obtained by a 90° rotation of plane (a) about the C-C axis.

(c) The plane perpendicular to the C-C axis at its midpoint.

Plane (a) shows six local maxima in the charge density distribution corresponding to the six nuclear positions. At these points all three curvatures are negative, they are therefore (3,-3) critical points. This type of CP occurs only at nuclear positions, and is a necessary condition to consider a point to be a nuclear position. A nuclear position will appear as a local maximum regardless of the orientation of the plane through the point. Plane (b) shows a plane at 90° to (a). This plane passes through the carbon nuclear positions and there are therefore two large local maxima. The smaller maxima corresponding to the hydrogen nuclear positions are no longer visible as this plane does not pass through those points.

Plane (c) is orthogonal to the first two, it passes throughout the midpoint of the C-C bond. The central region of the map corresponds to the centre of the C-C bond, it is a local maximum in any two perpendicular directions passing through \mathbf{r}_c in the plane shown. This corresponds to two negative curvatures. The third orthogonal direction is the C-C interatomic vector. Inspection of this region in (b) shows that the bond mid-point is a local minimum, *i.e.* a positive curvature. The mid-point of the C-C bond is therefore a (3,-1), or bond, critical point. This type of CP is found between bonded atoms and is a necessary condition to consider two atoms to be bonded.

A (3,+1) critical point corresponds to a critical point within a ring. There is one negative curvature along the axis passing from below the ring to above it through \mathbf{r}_c ; $\rho(\mathbf{r})$ is a local maximum at \mathbf{r}_c . The other two orthogonal axes are in the plane of the ring; $\rho(\mathbf{r})$ is a local minimum at \mathbf{r}_c in both of these directions, giving two positive curvatures. If the molecule contains a cage structure there will be some point within the cage at which $\rho(\mathbf{r})$ is a local minimum along all three orthogonal axes. This is a (3,+3) critical point.

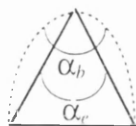
3.3 Properties of Bond Critical Points

Since the chemist is primarily interested in the interaction of atoms it is usually the (3,-1) critical points, and the properties of $\rho(\mathbf{r})$ at these points, which yield the most chemically useful information.

3.3.1 Bond Path

For any pair of bonded nuclei it is possible to plot a path between the two nuclear positions along which $\rho(\mathbf{r})$ is a maximum with respect to any other path between those two nuclei. This line will necessarily pass through the bond critical point, and is termed the bond path. The existence of a (3,-1) critical point and associated bond path is the topological definition of a chemical bond, it is a formalisation of the intuitive notion that a covalent bond is a concentration of electronic charge.

The bond path can also be used to determine whether a ring system is strained or not. Typically in a strained system the bond paths (shown as dotted lines) will bend outwards from the internuclear vectors. A bond path angle, α_b , is defined as shown below:



In an unstrained system in which the bond paths follow the internuclear vectors the geometrical bond angle α_e is equal to α_b . In a strained system $\alpha_e \neq \alpha_b$ and the magnitude of the difference between the two angles gives a measure of how strained the system is.

3.3.2 Bond Strength

ρ_b is defined as the magnitude of the charge density at a bond critical point, and is a measure of how strong the bond is. It is therefore directly related to bond order and it is possible to draw a quantitative relationship between bond order and ρ_b values. However, the values of ρ_b for bonds of a given order will vary considerably for different types of bonded atoms. In any such analysis it is therefore necessary to compare only ρ_b values for bonds between the same atom types.

3.3.3 Bond Ellipticity

The charge density along the bond path attains its minimum value at the bond CP; the associated curvature of ρ , λ_3 , is positive. In the plane that is perpendicular to the bond path ρ is a maximum at \mathbf{r}_i and the two orthogonal curvatures in this plane, λ_1 and λ_2 , are negative. In a bond of cylindrical symmetry, *e.g.* a pure sigma bond, the two negative curvatures of ρ are of equal magnitude. However, if the charge is preferentially accumulated in a particular plane along the bond path the bond will no longer be cylindrical, rather it will have an elliptical cross section and $\lambda_1 \neq \lambda_2$. This is typically the case in a pi bond. Inspection of the contour map in Figure 3.1(c) shows that the C-C bond in ethene has an elliptical cross-section.

A quantitative measure of the deviation of the bond from cylindrical symmetry is given by the bond ellipticity:

$$\varepsilon = \frac{\lambda_1}{\lambda_2} - 1 \quad 3.3$$

where λ_2 is the curvature of smaller magnitude. For example, the bond ellipticity for the C-C bond in ethane is 0.0, whilst in benzene it is 0.23, and in ethene 0.45.

3.4 The Laplacian

The Laplacian of $\rho(\mathbf{r})$ is a scalar quantity; it is defined by:

$$\nabla^2 \rho(\mathbf{r}) = \nabla \cdot \nabla \rho(\mathbf{r}) = \frac{\partial^2 \rho}{\partial x^2} + \frac{\partial^2 \rho}{\partial y^2} + \frac{\partial^2 \rho}{\partial z^2} \quad 3.4$$

It is apparent then that the Laplacian is the trace of the Hessian matrix, and therefore is also the sum of the three curvatures of the charge density at the point \mathbf{r} .

The physical significance of the Laplacian is that it represents areas of local charge concentration and depletion. If $\nabla^2 \rho(\mathbf{r})$ is negative the electronic charge is compressed above its average value in this region. Conversely, in regions where the charge distribution is

expanded relative to its average concentration $\nabla^2\rho(\mathbf{r}) > 0$. The value of the Laplacian is negative at \mathbf{r}_c in a covalent bond as this is a region of charge concentration. In an ionic bond, or a closed-shell interaction such as a hydrogen bond, there is a contraction of the charge density away from the interatomic region and the Laplacian has a positive value at \mathbf{r}_c . It is also possible to observe lone pairs in the Laplacian as these appear as local maxima, *i.e.* (3,-3) critical points in the negative Laplacian.

It should be noted that the Laplacian maps shown throughout this thesis are maps of the negative Laplacian. This widely used convention is applied in order to avoid the counter-intuitive fact that regions of charge concentration correspond to regions of negative Laplacian. In a negative Laplacian map charge concentrations appear as regions of positive contours (solid lines) and charge depleted regions are shown as negative contours (dotted or dashed lines).

Chapter 4

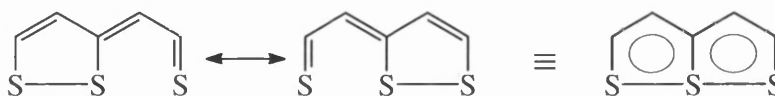
Experimental and Theoretical Studies of the Charge Density Distribution in 3,3,6,6-Tetramethyl-s-tetrathiane

4.1 Introduction

3,3,6,6-tetramethyl-s-tetrathiane, **1**, is a 6-membered ring compound containing C-S and S-S bonds. This molecule is of particular interest as the subject of an experimental multipole refinement as relatively little information has been gained from previous experimental electron density studies of molecules containing S-S bonds. Coppens *et al* carried out X-N and X-X investigations of cyclic octasulfur, S₈, in order to provide a reference point for other studies of more complex molecules containing S-S bonds.⁶⁷ In these types of studies a spherical independent atom model is constructed using the atomic positions determined by either neutron (X-N) or high angle X-ray (X-X) diffraction data. The charge density resulting from the IAM is then subtracted from the observed charge density to give a deformation density map. The sulfur lone pairs show up clearly in the deformation density map as maxima of $0.5 \text{ e}\text{\AA}^{-3}$. Their positioning above and below the S-S-S plane corresponds to *p* atomic orbitals. In contrast there is very little accumulation of deformation density between the sulfur atoms. Wang *et al* conducted X-X and multipole refinement studies of

heptasulfur imide, S_7NH , which is structurally very similar to S_8 . The deformation densities for the S-S bonds are also comparable with those for S_8 .⁶⁸

A series of experimental and theoretical studies have been performed on a number of substituted thiathiophthenes, see Scheme 4.1.^{69, 70, 71, 72}



Scheme 4.1

One of the purposes of this series of studies was to clarify the nature of the bonding in the ring system. X-X, multipole model and *ab initio* molecular orbital results were all interpreted in terms of deformation density analyses. No firm conclusions could be drawn regarding the nature of the ring bonding from the experimental deformation maps; theoretical calculations showed the ring to be a 10 π -electron aromatic system.

Whilst it is apparent that a considerable amount of experimental charge density research has focused on molecules containing S-S bonds it is unfortunate that the interpretation of these results has been in terms of deformation density analyses. Essentially, the conclusions of the experimental studies outlined above are that sulfur bonding and lone pair densities are arranged tetrahedrally around the atoms, and that S-S bonds show little deformation density. In contrast, topological analysis of the charge density provides quantitative information about the one-electron properties of a molecule. While *ab initio* molecular orbital studies have been made of the deformation density and topology of S-S bonds^{73, 74} only one experimental topological treatment can be found.⁷⁵ In that work a multipole model was fitted to data from an earlier deformation density study⁷⁶ of FeS_2 and the resulting charge density analysed topologically. Surprisingly the Laplacian at the critical point in the S-S bond of the disulphide ion is found to be positive. It was suggested in the earlier paper that a degree of covalent Fe-S bonding might be responsible for the destabilisation of the S-S bond and the correspondingly long internuclear distance of 2.16 Å in S_2^{-2} . This may be connected to the positive Laplacian value at the bond critical point.

An experimental study of 3,3,6,6-tetramethyl-s-tetrathiane was undertaken in order to obtain more information about the nature of the S-S bond in terms of its one-electron properties. When the crystal structure was originally determined by Korp and Bernal they

observed that the S-S distance of 2.015(1) Å was short for a single bond, possibly due to a degree of $d\pi-p\pi$ bonding.⁷⁷ This question will be addressed in terms of the results of topological analyses of both experimental and theoretical charge density distributions. A study of the conformational stability of **1** has also been made.

4.2 Experimental

Crystals of $[(\text{CH}_3)_2\text{CS}_2]_2$ are colourless octahedra. The faces of the crystal were indexed and found to correspond to the 011 , $0\bar{1}\bar{1}$, $\bar{1}01$, $10\bar{1}$, 101 , $\bar{1}0\bar{1}$, $0\bar{1}1$ and $01\bar{1}$ planes. This information was used to apply an analytical absorption correction using ABSORB.³⁹ High-resolution low-temperature X-ray diffraction data were collected, using proprietary software,⁷⁸ on an Enraf-Nonius CAD-4 diffractometer equipped with a liquid nitrogen gas-stream cryostat, using graphite-monochromated Mo $K\alpha$ radiation. Data reduction was performed as described in section 1.7 and the least-squares refinement of the multipole model was carried out with XDLSM from the XD package.²⁸

For the molecular geometry found in the crystal *ab initio* MO calculations were performed using the GAMESS program⁵ using the 6-311G** basis set. Details of other calculations are given later in the text. Topological analysis and mapping of the charge density arising from the theoretically determined wavefunctions was carried out using the AIMPAC program package.⁷⁹ The equivalent analysis of the experimental charge density was obtained using the program XDPROP in the XD package.

4.2.1 Multipole Refinement

In the crystal the molecule of **1** has point symmetry D_2 . It lies along the diagonal two-fold axis of the unit cell with C1 in a special position, fractional coordinates $(x, 1/4+x, 1/8)$. The asymmetric unit is composed of the S-C-CH₃ fragment. Figure 4.1 shows the molecular structure of **1**, and the atomic labelling, and Figure 4.2 shows how the molecule packs in the crystal.

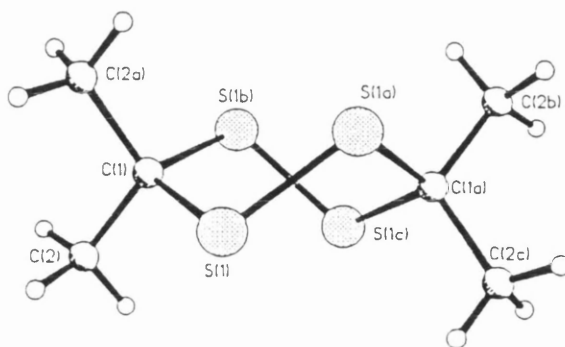


Figure 4.1 : Molecular structure of 1 in the twist-boat conformation found in the crystal.

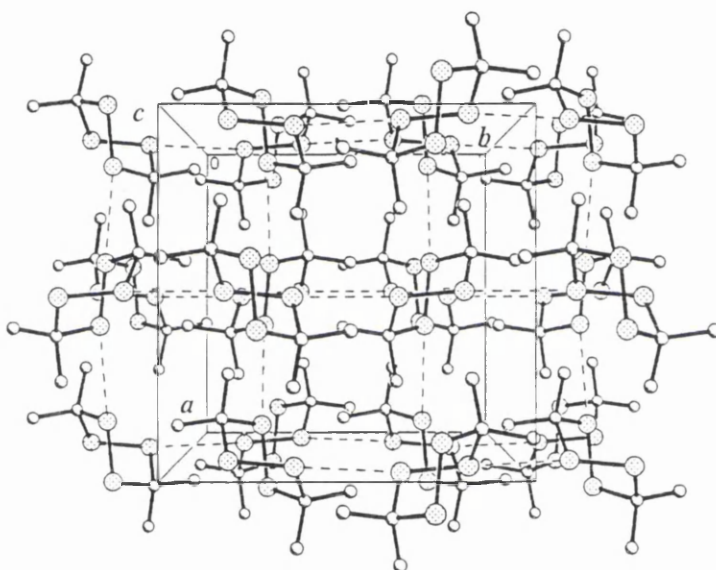


Figure 4.2 : A view along the *c* axis showing the packing of 1 in the molecular crystal.

An overall electroneutrality constraint was applied to the monopole charges. The refinement was truncated at the hexadecapole level for carbon and sulfur, and at the dipole level for the hydrogen atoms. The location of C1 on a two-fold axis restricts the allowed multipoles for this atom to those which have m even. Separate κ' and κ'' were used for the carbon and sulfur atoms. The κ'' parameters for the carbon atom deformation functions ($1 \leq l \leq 4$) were constrained to have the same value. This refined to $\kappa'' = 0.78(1)$ with

$\kappa' = 0.995(6)$. Initially the sulfur κ'' parameters were also constrained to have the same value, but this constraint was lifted in the last stages of the refinement. The refined values for sulfur are $\kappa' = 1.022(5)$, $\kappa''_{l=1} = 1.62(12)$, $\kappa''_{l=2} = 1.12(3)$, $\kappa''_{l=3} = 0.95(3)$ and $\kappa''_{l=4} = 0.94(7)$. The dipole and quadrupole functions are contracted while the octopoles and hexadecapoles are expanded.

Bond directions to hydrogen, and hydrogen atom isotropic temperature factors were fixed at values obtained from a spherical-atom refinement of the data. Bond lengths to hydrogen were fixed at 1.06 Å, the average value obtained from neutron diffraction experiments.³⁴ κ' and κ'' for the hydrogen atoms were fixed at 1.2, an average value obtained from theoretical models.³⁰

The rigid-bond test⁴³ was applied to the thermal parameters obtained from the model described above. The S1-C1 and C1-C2 bonds have $\Delta_{A,B}$ values of 0.0006 and 0.0002 Å respectively. These values are below Hirschfeld's upper limit of 0.001 Å for atoms at least as heavy as carbon, showing that the model satisfies the rigid-bond test.

4.3 Results and Discussion of the Experimental Study

4.3.1 Structural Results

Details of the data collection and refinement are given in Table 4.1. Unit cell parameters, and selected bond lengths and angles from this study are compared with those from the original crystal structure determination in Table 4.2. It is apparent that, of the bond lengths and angles, only the S1-S1a bond and the C1-S1-S1a angle differ significantly between the two structure determinations. The changes in the unit cell parameters can be explained by the temperatures of the X-ray diffraction experiments: this work was carried out at 100(1) K whilst Korp and Bernal⁷⁷ collected data at room temperature.

Formula	$[(\text{CH}_3)_2\text{CS}_2]_2$
Formula weight	212.40
Space group	$I 4_1/acd$
Crystal system	tetragonal
Temperature, K	100(1)
Unit cell dimensions:	
$a / \text{\AA}$	10.452(1)
$c / \text{\AA}$	18.069(2)
$V / \text{\AA}^3$	1973.9(3)
Z	8
$D_c / \text{g cm}^{-3}$	1.43
Crystal dimensions / mm	0.22 x 0.16 x 0.16
Absorption coefficient / mm^{-1}	0.860
Radiation	Mo K_{α} ; $\lambda = 0.71073 \text{\AA}$
Scan type	ω -2 θ
$(\sin\theta/\lambda) \text{ max} / \text{\AA}^{-1}$	1.22
No. of standard reflections	$3(1\ 3\ 2, \bar{3}\ \bar{1}\ \bar{2}, \bar{2}\ 0\ \bar{2})$
No. of reflections measured	11829
No. of symmetry-independent reflections	2759
No. $I > 2\sigma(I)$ reflections	1891
Agreement factor $R = \sum I - \bar{I} / \sum I$	0.020
Range of corrections for absorption	0.896-0.907
Isotropic extinction	no extinction correction
Refined on	F
R	0.0226
R_w	0.0208
S	1.1320
No. of variables	104
Weighting scheme	$w = 1 / \sigma^2(F) = 4F^2 / \sigma^2(F^2)$ $\sigma^2(F^2) = \sigma_{\text{counting}}^2(F^2) + P^2F^4$

Table 4.1 : Experimental data for 3,3,6,6-tetramethyl-s-tetrathiane.

	This work	Ref. 77
Cell parameters / Å		
<i>a</i>	10.452(1)	10.565(2)
<i>c</i>	18.069(2)	18.344(3)
Bond lengths / Å		
S1-C1	1.847(1)	1.843(2)
S1-S1a	2.023(1)	2.015(1)
C1-C2	1.521(1)	1.514(3)
Bond angles / degrees		
C1-S1-S1a	102.4(1)	102.9(1)
S1-C1-S1b	110.3(1)	110.3(1)
S1-C1-C2	105.8(1)	105.4(2)
C2-C1-C2	112.8(1)	113.1(3)

Table 4.2 : Comparison of selected structural parameters from this work and the earlier crystal structure determination.⁷⁷

The S1-S1a bond length is 2.023(1) Å which is significantly longer than the value of 2.015(1) Å reported for the S-S bond in the original crystal structure.⁷⁷ However, this is still shorter than the literature values for the S-S bond in elemental sulfur, which range from 2.035(2) to 2.060(2) Å.⁸⁰ The shortness of the S-S bond in **1** is consistent with the trend, observed by Hordvik, for the length of S-S bonds to decrease with increasing torsion angle, reaching a minimum bond length at a torsion angle of 90°.⁸¹ The C1-S1-S1a-C1a torsion angle measured for **1** is -81.1° and so a short S-S bond would be expected. Hordvik drew his conclusions from a literature survey of only 18 compounds. It was desirable to repeat the survey over a larger range of compounds and a search of the Cambridge Structural Database, CSD, was therefore carried out to locate all occurrences of the C-S-S-C fragment.^{82, 83} The data from such occurrences are shown as a scatter plot with regression line in Figure 4.3. Data points from the original crystal structure determination, from ref. 77, and from this work have been indicated. Points indicating the values obtained from MO geometry optimisation calculations of the twist-boat and chair conformations are also shown. The positions of all of these points fit the distribution established by the other experimentally determined molecular geometries.

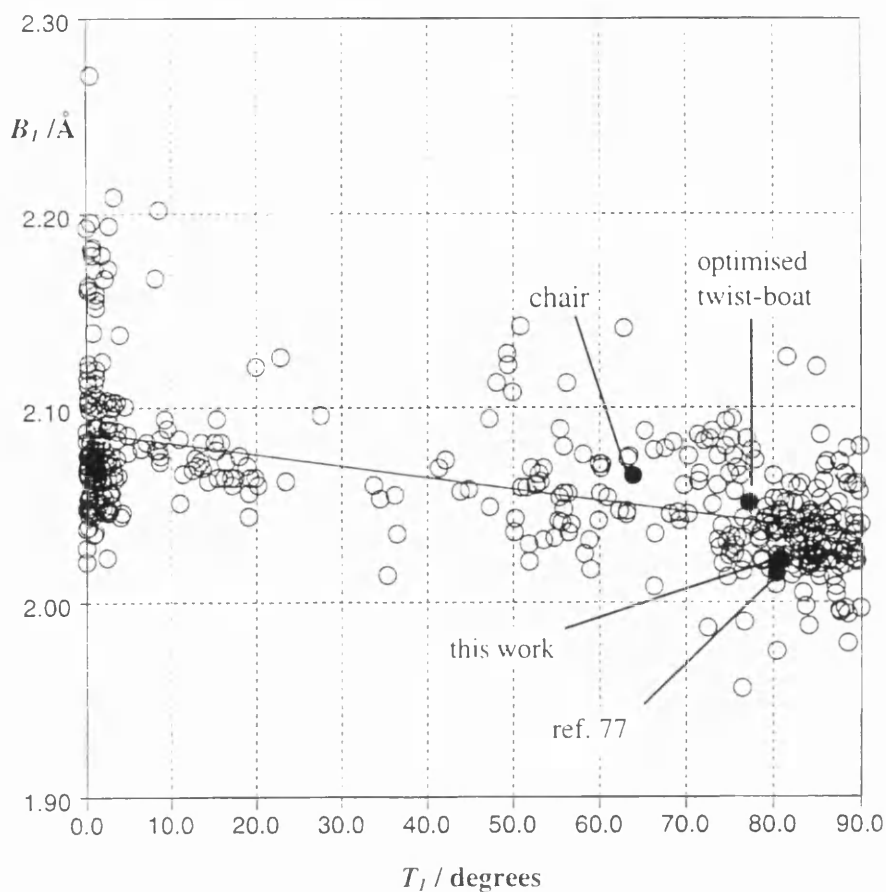


Figure 4.3 : Scatter plot of the S-S bond length against torsion angle for all occurrences of the C-S-S-C fragment in the CSD.

4.3.2 Comparison of Experimental and Theoretical Charge Density Distributions

The residual density map, $F_{obs} - F_{mult}$, for the C1-S1-S1a plane is shown in Figure 4.4. The height of the largest feature is $-0.15 \text{ e}\text{\AA}^{-3}$, while the rest of the map is relatively flat indicating a good fit of the model to the data. Figure 4.5 shows the deformation density map for the same plane. The positioning of the deformation density peaks on the internuclear vectors shows that these bonds are straight and consequently that the ring is not strained. As expected, the deformation density in the S-S bond is relatively low, $0.3 \text{ e}\text{\AA}^{-3}$. The S-S bond also displays a double peak in the deformation density. This effect has been observed before^{67, 68} and appears to be a relatively common feature of S-S bond deformation densities.

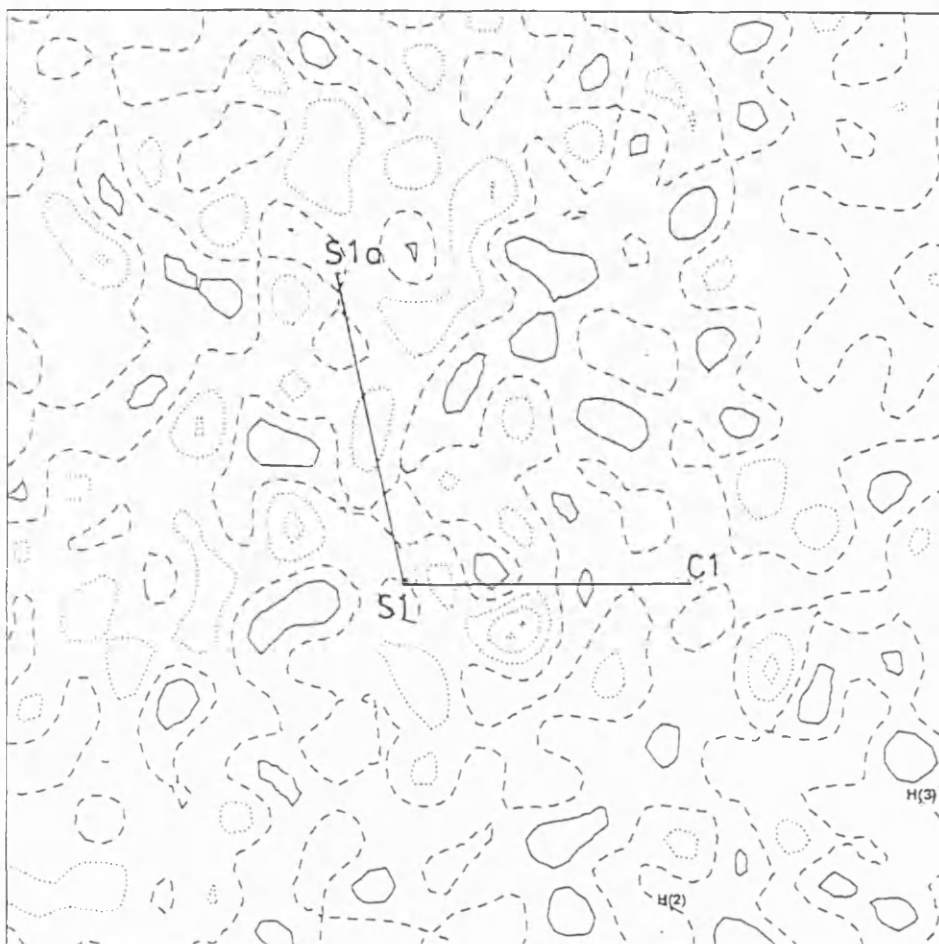


Figure 4.4 : Residual density map in the C1-S1-S1a plane. Contour interval = 0.05 $e\text{\AA}^{-3}$; dashed line is the zero contour and dotted lines are negative contours.

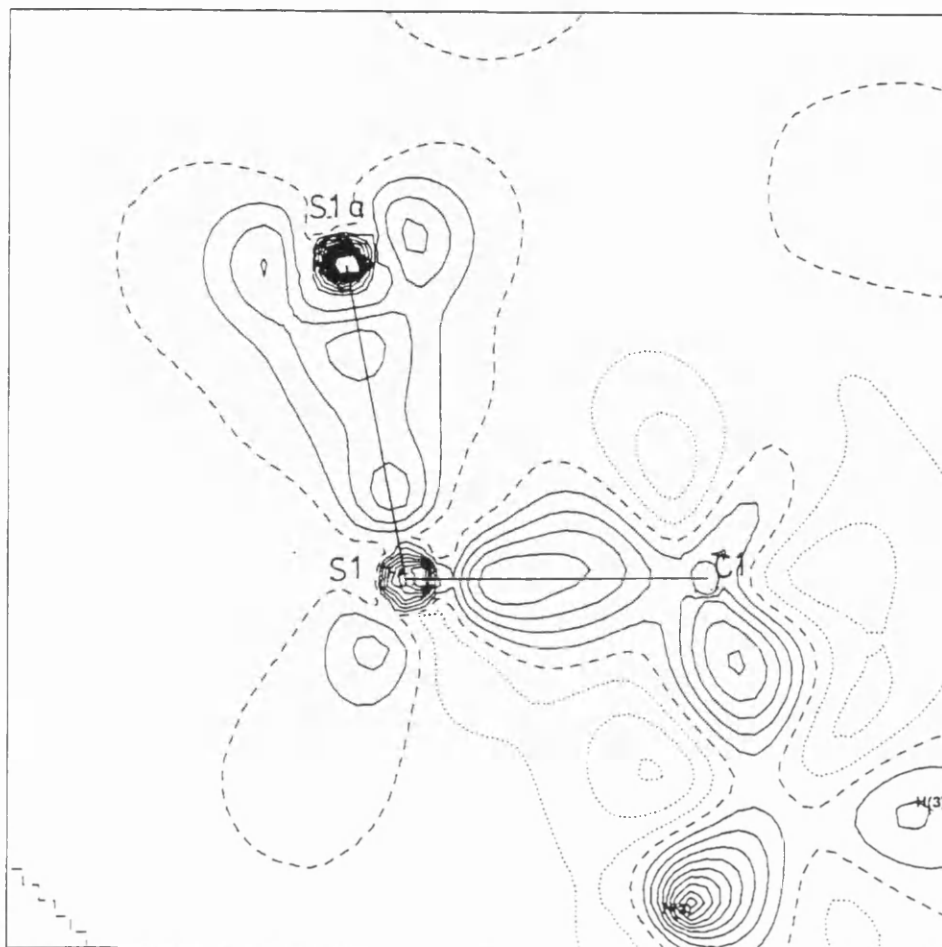


Figure 4.5 : Static deformation density map in the C1-S1-S1a plane. Contour interval = $0.05 \text{ e}\text{\AA}^{-3}$: dashed line is the zero contour and dotted lines are negative contours

The electron density distribution resulting from the multipole model, and that resulting from the MO calculation at the experimental geometry were analysed using Bader's topological treatment.⁶⁶ The results of the critical point analysis are collated in Table 4.3. It is clear that experimentally determined values of ρ_b for the S1-C1 and S1-S1a bonds compare well with the *ab initio* results. There is however a large discrepancy in the values of ρ_b for the C1-C2 bond.

Bond	CP type	Method	Bond length / Å	$\rho_b / \text{e}\text{\AA}^{-3}$	$\nabla^2\rho_b / \text{e}\text{\AA}^{-5}$	ϵ
S1-C1	(3,-1)	experimental	1.847(1)	1.33(3)	-6.82(8)	0.12
		theoretical		1.23	-8.08	0.10
S1-S1a	(3,-1)	experimental	2.023(1)	1.13(3)	-0.59(6)	0.10
		theoretical		1.09	-5.39	0.03
C1-C2	(3,-1)	experimental	1.521(1)	2.07(7)	-24.5(2)	0.09
		theoretical		1.75	-16.8	0.00
Centre of ring	(3,+1)	experimental	na	0.14(1)	1.431(1)	na
	(3,+3)	theoretical		0.100	1.807	na
S...S intermolecular	(3,-1)	experimental	3.669(2)	0.043(1)	0.442(4)	0.12
S1...S1c	(3,-1)	theoretical	3.150(1)	0.119	1.448	0.37
Centroid of 4-membered ring	(3,+1)	theoretical	na	0.116	1.654	na

Table 4.3 : Critical point analysis for the twist-boat conformer of **1** at the experimental geometry.

The major difference between the critical points arising from the theoretical and experimental charge distributions is in their type and number. The experimental results show a (3,+1) critical point, as would be expected at the centroid of a ring system. However, the theoretical results show a (3,+3) CP at the centroid of the ring, indicating the existence of a cage system. The cage is delineated by weak trans-annular interactions between pairs of sulfur atoms S1...S1c and S1a...S1b. These interactions are characterised by the existence of (3,-1) CPs on the internuclear vectors, and low ρ_b values. Associated with these trans-annular interactions are four (3,+1) ring critical points. Although the type and number of the critical points obtained from theory and experiment are quite different, both sets satisfy the Poincaré-Hopf relationship. This defines the number and type of critical points which can coexist in a system. It states that $n-b+r-c=1$ where n is the number of nuclei, and b , r and c are the numbers of bond, ring and cage critical points respectively.

The *ab initio* calculation was performed on an isolated molecule and so no intermolecular interactions could be observed. However, the critical point analysis of **1** in the crystalline environment shows there to be an intermolecular interaction between two sulfur atoms 3.669(2) Å apart. The value of the Laplacian at the intermolecular bond CP is positive and this, together with the low value of ρ_b , indicates that this is a closed-shell interaction. In this type of interaction the atomic charge is not shared between the bonded atoms as in a covalent bond, but rather is contracted away from the interatomic region into the atomic basins. Closed-shell interactions are typical of hydrogen bonded systems and also of hypervalent molecules, as is the case here. Figure 4.6 shows the Laplacian distribution in the region of the S...S interaction. It is clear that the Laplacian distribution in the S...S interatomic region is in direct contrast to the Laplacian distribution in the S1-C1 covalent bond.

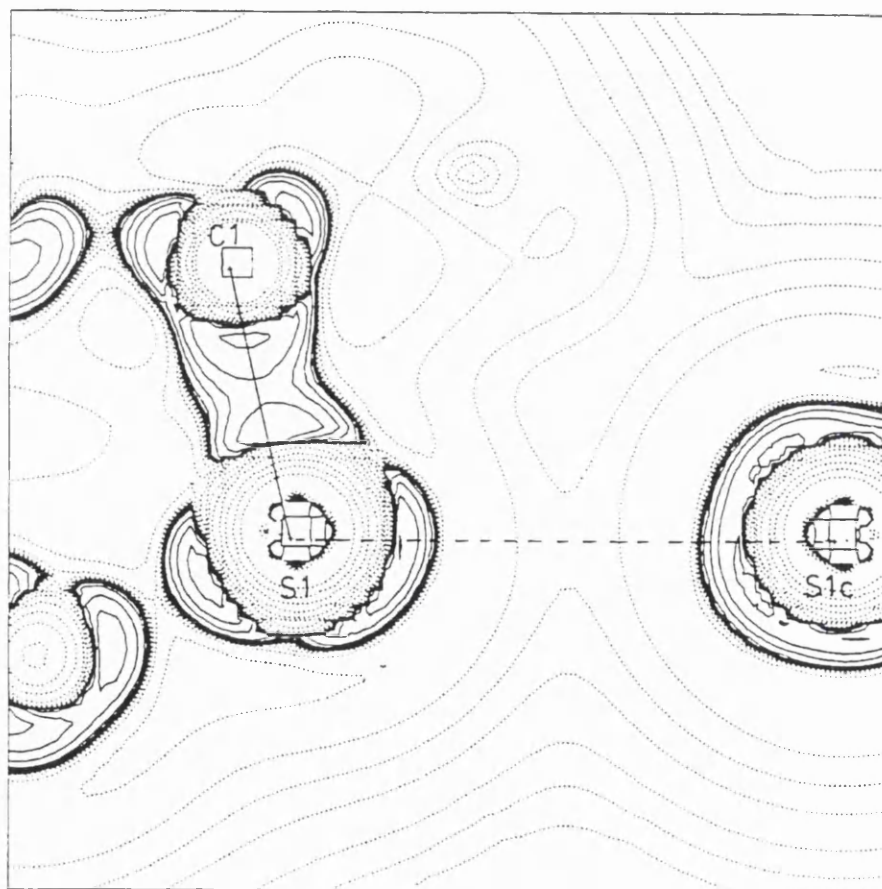
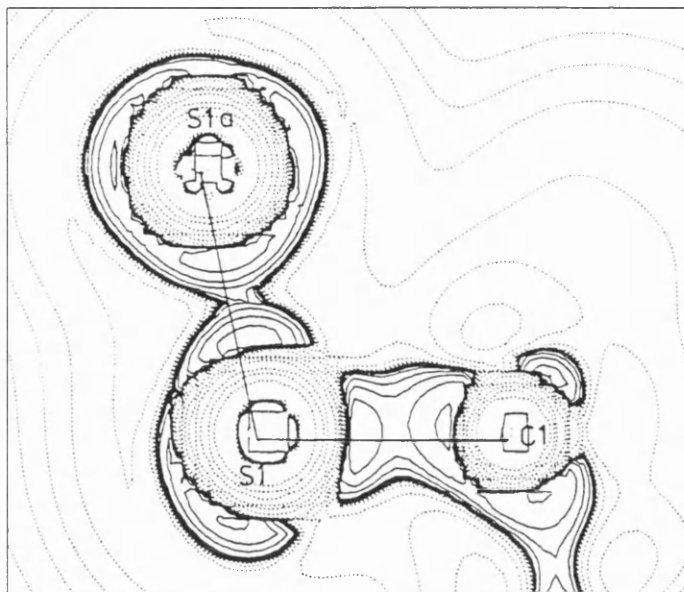
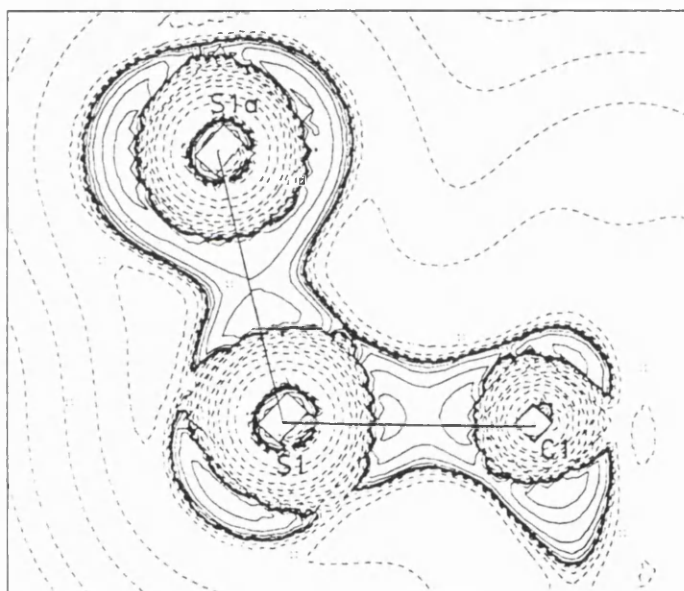


Figure 4.6 : Experimental Laplacian distribution showing the S...S intermolecular interaction.

Although the details of the critical point analyses are quite different, the results of both the experimental and theoretical studies show each of the sulfur atoms to take part in a closed-shell interaction with another sulfur atom. In the crystalline environment it is possible to take account of intermolecular interactions, while in the isolated atom environment of the *ab initio* calculation, no such effects can be observed. It is possible that an *ab initio* calculation which simulated the crystalline environment would show the intramolecular transannular interactions to be replaced by intermolecular interactions, thus removing the apparent differences between the two sets of results. The good agreement between the Laplacian maps of the C-S-S plane, Figure 4.7, and the agreement of certain of the critical point data suggests that the discrepancies between the two sets of results are due to the differences in molecular environment.



(a)



(b)

Figure 4.7 : Laplacian distribution in the C1-S1-S1a plane: (a) experimental; (b) theoretical.

4.3.3 Determination of S-S Bond Strength

In order to address Korp and Bernal's question about the shortness of the S-S bond and the possible existence of $d\pi-p\pi$ double bonding, the critical point data for **1** were compared with *ab initio* results for other molecules. As discussed in Chapter 3 the value of ρ_b for a particular bond is a useful measure of the strength of that bond. However ρ_b values do not lie on an absolute scale and comparisons can only be made between values for bonds involving the same atom types. The critical point data for the S-S bond in **1** were compared with values of ρ_b for S-S single and double bonds. Knop's calculation on H_2S_2 at the 6-31G* basis set level was taken as an example of an S-S single bond.⁸⁴ A geometry optimisation of the S_2 molecule was carried out at the same basis set level to provide data for an S-S double bond. In order for these results to be properly compared with the theoretical results for **1** at the experimental geometry the basis sets should be the same. The calculations on H_2S_2 and S_2 were therefore repeated at the 6-311G** basis set level. The results of all calculations, and the experimental results, are collated in Table 4.4.

S-S bond	Bond length / Å	$\rho_b / e\text{Å}^{-3}$
S_2 (6-31G*)	1.878	1.387
S_2 (6-311G**)	1.879	1.384
H_2S_2 (6-31G*)	2.063	0.999
H_2S_2 (6-311G**)	2.078	0.981
1 (experimental)	2.023(1)	1.13(3)
1 (6-311G**)	2.023	1.093

Table 4.4 : Critical point data for S-S bonds.

Bond length and ρ_b values from experiment and theory are consistent with a slightly strengthened S-S single bond in **1**.

4.4 *Ab Initio* Studies of the Conformers of 3,3,6,6-tetramethyl-s-tetrathiane

The *ab initio* MO calculation for **1** described above was performed at the twist-boat geometry which is found in the crystal. In fact Bushweller has shown that the molecule of **1** can exist as two conformers,⁸⁵ a flexible twist-boat (Figure 4.1) and a rigid chair (Figure 4.10). There is also a hypothetical boat conformation. Geometry optimisations have been performed on all of the conformers using the GAMESS package⁵ and the resulting wavefunctions were analysed using AIMPAC.⁷⁹

4.4.1 The Twist-boat Conformer

The initial geometry for the *ab initio* calculations was that determined experimentally in the original crystal structure study.⁷⁷ The geometry was optimised using a variety of basis sets, the optimised geometry from one calculation being used as the input to the next calculation at a higher basis set level.

The S-S distance is highly dependent on the basis set used, see Table 4.5. In particular, the largest change to the S-S bond length occurs when *d*-orbital functions are added to the basis, *i.e.* on going from 6-31G to 6-31G*. The necessity of including *d*-orbital functions as polarisation functions in calculations involving second row atoms has been widely discussed.^{73, 86, 87} Here, the addition of *d* functions lowers the energy by 0.2359 E_h and shortens the S-S bond by 0.152 Å. Much smaller changes are observed in the S1-C1 and C1-C2 bond lengths, see Table 4.6.

Basis	Energy / E_h	S-S distance / Å
STO-3G	-1804.3103	2.124
STO-6G	-1818.5751	2.120
3-21G	-1815.1515	2.228
6-21G	-1823.8055	2.217
6-31G	-1823.9979	2.195
6-31G*	-1824.2338	2.043
6-31G**	-1824.2526	2.043
6-311G**	-1824.3925	2.051

Table 4.5 : Results of geometry optimisations of **1** at successive basis set levels.

Bond	Basis set	Bond length / Å	Difference / Å
S1-C1	6-31G	1.907	-0.058
	6-31G*	1.849	
S1-S1a	6-31G	2.195	-0.152
	6-31G*	2.043	
C1-C2	6-31G	1.525	0.005
	6-31G*	1.530	

Table 4.6 : Effect of *d*-orbital polarisation functions on bond lengths.

The importance of the inclusion of *d* functions to the correct description of S-S bonding is shown very clearly in Figure 4.8. This shows the difference in the total electron densities derived from the 6-31G* and the 6-31G wavefunctions.

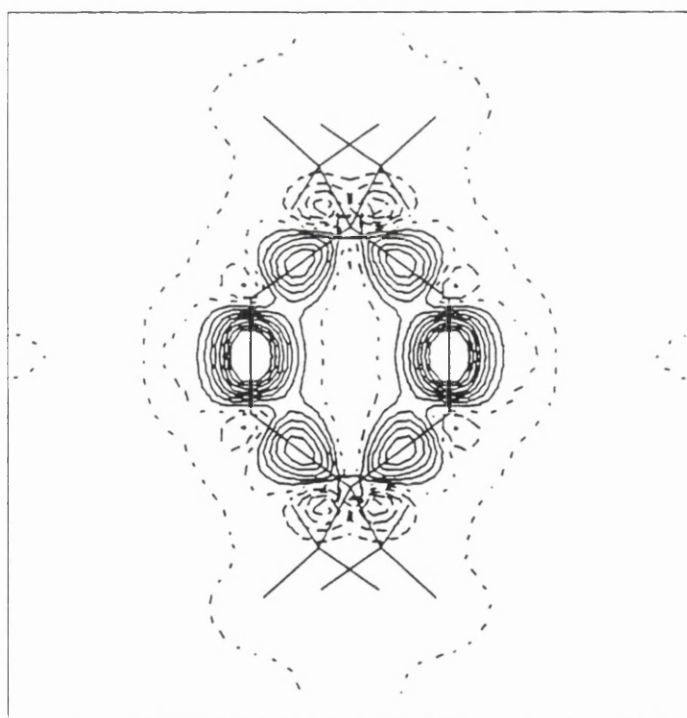


Figure 4.8 : Difference density plot in the mean plane through the ring, 6-31G* - 6-31G.

The high contour levels in the S-S bonds show that the addition of *d* functions is of much greater importance to the description of the sulfur atoms than to either carbon or hydrogen. As expected there is no *d*-orbital participation in the C-H bonds.

In order to further address the question of the existence of $d\pi-p\pi$ bonding in the S-S bond it is necessary to look at the *d*-orbital populations, see Table 4.7. Even at the highest level of population it is clear that the *d*-orbitals are acting as polarisation functions and not as valence orbitals. The population of the *d* functions would have to approach unity before they could be considered to be playing a significant part in the S-S bonding.

Basis set	Atom	<i>d</i> -orbital population
6-31G*	S1	0.111
	C1	0.080
	C2	0.080
6-31G**	S1	0.111
	C1	0.080
	C2	0.040
6-311G**	S1	0.071
	C1	0.139
	C2	0.064

Table 4.7 : *d*-orbital populations for different basis sets.

The changes in S1 and C1 *d*-orbital populations on going from the 6-31G* to the 6-311G** basis set are unexpected. In order to clarify whether or not this is the result of a poor calculation, geometry optimisations were carried out for CS and S₂ using these two basis sets. The differences in *d*-orbital populations between the 6-31G* and the 6-311G** basis sets are as follows: CS, sulfur -0.028, carbon 0.047; for S₂, sulfur -0.026. This shows that the fluctuations in the *d*-orbital populations are caused by basis set dependency effects, rather than being due to inadequate calculations.

A critical point analysis of the charge density arising from the geometry-optimised wavefunction of **1** in the twist-boat conformation was carried out. The results are shown in Table 4.8. The types and numbers of critical points were the same as those found in the critical point analysis of the MO wavefunction of **1** at the molecular crystal geometry, see Table 4.3.

Bond	CP type	Bond length / Å	$\rho_b / e\text{Å}^{-3}$	$\nabla^2\rho_b / e\text{Å}^{-5}$	ϵ
S1-C1	(3,-1)	1.848	1.228	-8.056	0.105
S1-S1a	(3,-1)	2.051	1.034	-4.567	0.039
C1-C2	(3,-1)	1.529	1.724	-16.513	0.002
S1...S1c	(3,-1)	3.240	0.102	1.295	0.848
Centroid of 4-membered ring	(3,+1)	na	0.101	1.404	na
Ring centre	(3,+3)	na	0.090	1.590	na

Table 4.8 : Critical point data for the geometry-optimised twist-boat form of 1, RHF/6-311G.**

Long-range trans-annular interactions, 3.240 Å, exist between pairs of atoms S1...S1c and S1a...S1b. There is structural evidence for the existence of similar long-range cross-ring S...S interactions in the cyclic cation S_8^{2+} .⁸⁸ This is supported by Tang *et al* who observed (3,-1) critical points between sulfur atoms separated by 2.86 Å in an *ab initio* calculation of the same cation.⁷⁴ In **1** the long-range interactions delineate four four-membered rings and hence the critical point at the centroid of the six-membered ring of **1** is a (3,+3) cage CP. Both of the cross-ring sulfur-sulfur distances are considerably shorter than the sum of the van der Waals radii for two sulfur atoms⁸⁹ and so some type of interaction might be expected in both cases. However, there are no trans-annular interactions between the pairs of sulfur atoms, S1-S1b and S1a-S1c, which are 3.072 Å apart. Hence, there is an anomaly in that a critical point is not found between S atoms which are closer together than a pair of sulfur atoms for which one is found. There is no obvious explanation for this.

The Laplacian at the (3,-1) trans-annular CP is positive, indicating a closed-shell interaction in which the electronic charge is contracted away from the interatomic region and into the atomic basins. Figure 4.9 shows the Laplacian in the S1...S1c region. This is similar to the experimental Laplacian for the S...S intermolecular interaction, Figure 4.6. Both maps show closed-shell long-range S...S interactions; their similarity supports the postulation that the differences between the experimental and theoretical results are mainly due to the differences in molecular environment.

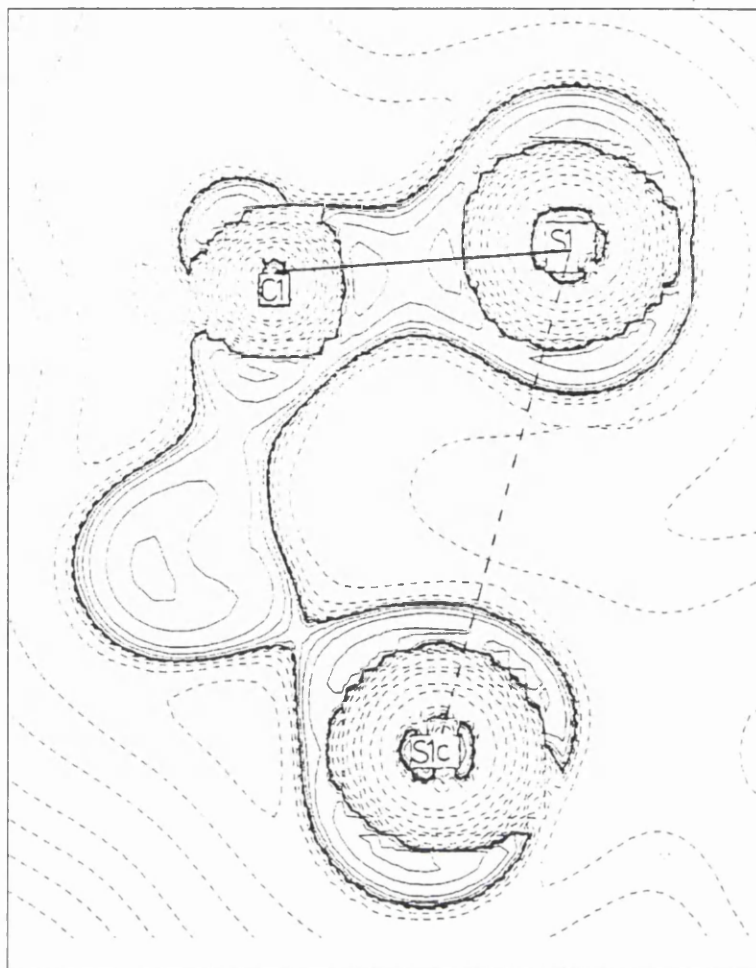


Figure 4.9 : Plot of the Laplacian of the geometry-optimised twist-boat form of **1**, showing the S1...S1c closed-shell interaction.

The value of ρ_b for the S1-S1a bond is $1.034 \text{ e}\text{\AA}^{-3}$, compared with $0.999 \text{ e}\text{\AA}^{-3}$ calculated by Knop *et al* for H_2S_2 . However, these two calculations were performed with different basis sets and so a direct comparison is not advisable. However, the calculation of H_2S_2 at the 6-311G** level, Table 4.4, can be compared with the 6-311G** results given in Table 4.8. The value of ρ_b in H_2S_2 is then $0.981 \text{ e}\text{\AA}^{-3}$ and the S-S bond length is 2.078 \AA compared with $1.034 \text{ e}\text{\AA}^{-3}$ and 2.051 \AA for the geometry-optimised results. This is consistent with the suggestion that the S1-S1a bond in **1** is a slightly strengthened single bond. Beagley and McAloon noted that in compounds of the type X-S-S-X, the higher the electronegativity of X, the shorter the S-S bond.⁹⁰ The electronegativities of C and H are 2.5 and 2.1 respectively,⁹¹ and so the results shown above are in keeping with this trend.

In order to investigate the effect of electron correlation on the electron density distribution, a single point MP2 level calculation was carried out on the twist-boat form of **1**. The calculation was performed using the GAUSSIAN 94⁹² program at the 6-311G** basis set level. The geometry was fixed at the 6-31G** optimised geometry. The energy was -1825.8285 E_h , a reduction of 1.4360 E_h from the RHF/6-311G** energy. A critical point analysis of the resulting wavefunction was carried out, the results of which are collated in Table 4.9.

Bond	CP type	Bond length / Å	$\rho_b / e\text{Å}^{-3}$	$\nabla^2\rho_b / e\text{Å}^{-5}$	ϵ
S1-C1	(3,-1)	1.849	1.144	-5.443	0.107
S1-S1a	(3,-1)	2.043	0.976	-2.480	0.035
C1-C2	(3,-1)	1.530	1.634	-13.270	0.005
S1...S1c	(3,-1)	3.239	0.105	1.323	2.552
Centroid of 4-membered ring	(3,+1)	na	0.104	1.373	na
Ring centre	(3,+3)	na	0.094	1.595	na

Table 4.9 : Critical point data for the twist-boat conformation of **1, MP2/6-311G**//RHF/6-31G**.**

The effect of the inclusion of electron correlation, as in the MP2 calculation, is to lower the value of ρ_b in the covalent bonds compared with the value obtained at the RHF/6-311G** level. The changes to ρ_b are as follows: S1-C1, -0.084; S1-S1a, -0.058; C1-C2, -0.90 $e\text{Å}^{-3}$. This observation is in qualitative agreement with that made by Brown and Smith in their investigations into the effects of electron correlation on small sulfur-containing molecules.⁷³ They compared high-level HF wavefunctions for H₂S₂, S₂ and S₃ with those obtained by configuration interaction singles and doubles. The inclusion of electron correlation resulted in a reduction in the deformation densities at the mid-points of S-S bonds in the range 0.01-0.04 $e\text{Å}^{-3}$. Here the MP2 calculation increases the value of the electron density at all of the other critical points, including the S1...S1c trans-annular interaction, suggesting that electron correlation has the effect of delocalising the electrons in the molecule.

4.4.2 The Chair Conformer

A similar series of geometry optimisation calculations were performed on the chair conformer of **1**. Since this conformation has only been observed in solution there are no structural data available, the starting geometry was therefore taken from standard bond lengths and angles, and suitable torsion angles. The final optimised geometry is shown in Figure 4.10.

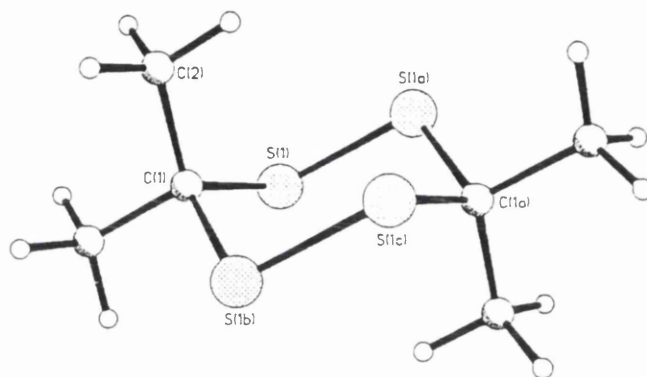


Figure 4.10 : The optimised chair conformer of **1**.

At the highest basis set level used, 6-311G**, the energy is $-1824.3930 E_h$. The sulfur *d*-orbital population is 0.071 and the S-S bond length is 2.065 Å. The results of the critical point analysis are given in Table 4.10.

Bond	CP type	Bond length / Å	$\rho_b / e\text{Å}^{-3}$	$\nabla^2\rho_b / e\text{Å}^{-5}$	ϵ
S1-C1	(3,-1)	1.842	1.245	-8.333	0.085
S1-S1a	(3,-1)	2.065	1.010	-4.266	0.082
C1-C2	(3,-1)	1.526	1.727	-16.648	0.013
Ring centre	(3,+1)	na	0.072	1.161	na

Table 4.10 : Critical point data for the chair conformer of **1**, RHF/6-311G**.

In this conformation the S1...S1c distance is 3.651 Å which is longer than the sum of the van der Waals radii for the two sulfur atoms. Hence, no trans-annular interactions are observed and the critical point at the centre of the 6-membered ring is of (3,+1) type.

4.4.3 The Boat Conformer

There is no evidence for the existence of a boat conformation of **1**, but it is of interest to investigate this hypothetical form in order to compare it to the other conformers of the molecule. The energy of **1** in the boat conformation is $-1824.3204 E_h$. The S-S bond length is 2.13 Å which is very long for this type of bond. The value of ρ_b is correspondingly low, 0.908 eÅ^{-3} . This is possibly due to an extension of the S-S bond to relieve steric crowding of the methyl groups.

4.4.4 Comparison of the Conformers

Since it is the twist-boat conformation which is found to exist in the solid state it might be expected that the isolated molecule would be more stable in the twist-boat than the chair form. This postulation is supported by Bushweller's NMR observations which show the twist-boat to chair ratio to be in the range 2.6 to 3.3, depending on the solvent.⁸⁵ However, the energies from the 6-311G** calculations are -1824.392493 and -1824.393009 for the twist-boat and the chair respectively. The chair is therefore stabilised by $0.000516 E_h$, or 1.355 kJmol^{-1} with respect to the twist-boat. That the calculations showed a different result from that found by experiment is not particularly surprising. The energy difference between the two conformers is very small and crystal packing forces and solvent interactions can alter the relative energies of molecular conformations considerably.

The individual components of the energy are shown in Table 4.11. The nuclear repulsion energy for the chair conformer is $2 E_h$ lower than for the twist-boat. This is unsurprising considering the large number of six-membered ring compounds which exist in the chair form. The boat form has a much lower nuclear repulsion energy than the other conformers, presumably due to the extension of the S-S bond in order to minimise steric crowding of the methyl groups. The associated weakening of this bond could account for the comparatively high value of the electronic energy. The twist-boat is stabilised by $2 E_h$ with respect to the chair, on electronic grounds. This is probably due to the extra stabilisation

afforded by the trans-annular bonds, which arise from the ability of sulfur to form hypervalent species.

Conformer	Molecular energy / E_h	
	Nuclear repulsion	Electronic
Twist-boat	1036.8154	-2861.2079
Chair	1034.9846	-2859.3776
Boat	1018.4430	-2842.7634

Table 4.11 : Components of the molecular energy for the conformers of **1**.

4.5 Conclusions

Topological analysis of the experimental charge density distribution in **1** gives values of ρ_b for the S1-C1 and S1-S1a bonds which agree, within experimental error, with values obtained from *ab initio* calculations for the molecular geometry found in the crystal. There are also (3,-1) critical points between sulfur atoms in adjacent molecules, indicating weak intermolecular closed-shell interactions. The values of ρ_b and the bond lengths for the S1-S1a bond obtained from both experiment and theory indicate that the S-S bond in **1** is a slightly strengthened single covalent bond.

Ab initio MO calculations for optimised geometries of the different conformations of **1** predict a small stabilisation of the chair conformer relative to the twist-boat conformer, in contrast to the situation in the molecular crystal.

Chapter 5

Experimental Charge Density Study of Hexakis(mercaptomethyl)benzene

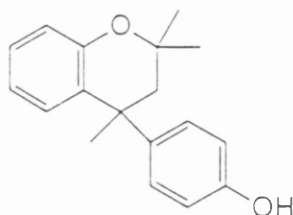
5.1 Introduction

Hexakis(mercaptomethyl)benzene, **2**, belongs to a class of compounds which have the potential to act as inclusion hosts for molecules of other compounds. This can take the form of a single host molecule encapsulating another molecule; good examples of this type of host behaviour are the cyclodextrins which have a hole in their centre capable of housing a smaller guest molecule. This imprisoning action occurs both in the solid phase and in solution.

The other major inclusion compound class is composed of the lattice inclusion hosts. The ability of these molecules to act as hosts depends on the fact that their crystal structures are not close packed. Typically weak intermolecular interactions, such as hydrogen bonding, prevent the host molecules from coming into close contact. The resultant cavities in the lattice can then house guest molecules. The behaviour of these molecules as hosts is therefore generally a property of the solid crystalline phase.

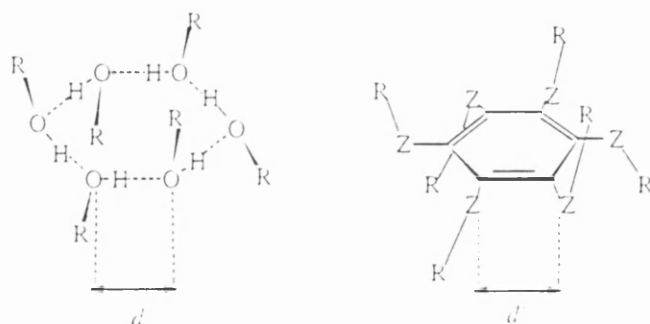
It is the lattice inclusion class of compounds which has attracted the most interest in synthetic chemistry as these offer the greatest opportunity for the rational development of new host molecules. This may take the form of making slight alterations to a known host to yield

new analogues with different inclusion properties to the parent. One such study has investigated the clathration properties of analogues of Dianin's compound which were obtained by replacing the OH group with other functional groups *e.g.* NH₂ and SH. See Scheme 5.1.⁹³



Scheme 5.1

It is also possible to design new hosts which do not have a structural basis in any of the known inclusion compounds. One such set of compounds is the hexa-host class to which **2** belongs. This class is composed of molecules containing one central six-membered aromatic ring, substituted at all positions by the same group. The strategy for the synthesis of this class of compounds is based on the hexa-host analogy⁹⁴ and is particularly interesting as it has resulted in the development of an entirely new class of host molecules which have no direct structural relationship to any previously known host. The analogy originated from the observation that the crystal structures of adducts of some compounds, *e.g.* phenol and hydroquinone, display hexagonal arrangements of molecules linked by OH...O hydrogen bonding. The O...O distance (d) is comparable to the Z...Z distance (d') in a substituted benzene molecule, see Scheme 5.2.

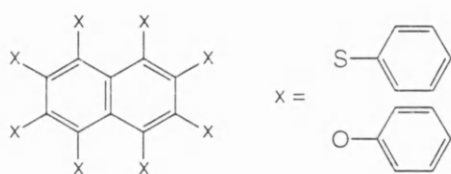


Scheme 5.2

It was thought, therefore, that poly-substituted aromatic rings might show a tendency to crystallise in a similar non-close packed manner. This was indeed found to be the case and a very wide range of such molecules have since been synthesised.⁹⁵

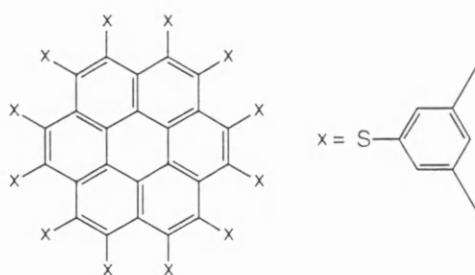
The most common form of crystal packing within this class of compounds is stacking of the molecules in a direction parallel to the $\bar{3}$ axis (the *c*-axis of the trigonal system using hexagonal axes). This, together with the tendency for the side chains to distribute themselves above and below the plane of the aromatic ring, leads to the formation of cavities between adjacent molecules. These cavities may then 'house' a guest molecule, resulting in a clathrate. The size of the cavity can be controlled by the choice of substituent group and can range from the very simple as in **2**, -CH₂SH, to the considerably more complex, *e.g.* -O-Ph-CH₂-Ph.⁹⁶

The development of the hexa-host compounds has since been built upon to yield a new class of octa-substituted naphthalene inclusion compounds. The first of these so-called 'spider' hosts were based on the substituted-benzene analogues which were known to have inclusion properties, see Scheme 5.3.^{97,98}



Scheme 5.3

Further developments on the hexa-host theme have also involved the synthesis of hosts based on substituted coronene. These molecules have six pairs of side-chain units, see Scheme 5.4.⁹⁹



Scheme 5.4

Initially **2** was synthesised as a potential host for hydrogen, but determination of the crystal structure¹⁰⁰ of the molecule showed that the cavity was too small. However, this did not end our interest in the compound as investigation of the molecular packing of **2** indicated that S-H...S intermolecular hydrogen bonding might be present between adjacent molecules in the *c*-direction. Previous postulations of this type of hydrogen bonding, in which the sulfur atom is both a proton acceptor and donor, have been based on the interpretation of molecular packing and spectroscopic data,^{93, 101} and therefore provide indirect evidence. However, the location of a bond critical-point on the internuclear H...S vector in the experimental charge density would provide direct physical support for the existence of S-H...S hydrogen bonding. In the light of recent interest in weak hydrogen bonding^{102, 103} the present study was undertaken in order to determine whether such a critical-point could be observed.

5.2 Experimental

Crystals of C₁₆H₁₈S₆ are colourless, hollow hexagonal tubes. For this experiment a portion of one side of the hexagon was removed. The faces of the resulting cuboidal fragment were indexed, the two largest faces having indices of 110 and $\bar{1}\bar{1}0$; the sides were bounded by the $1\bar{1}0$, $\bar{1}10$, 001 and $00\bar{1}$ faces. Single crystal high-resolution, low-temperature data were collected using a Siemens SMART area detector¹⁰⁴ equipped with a liquid nitrogen cryostat.

For the molecular geometry found in the crystal an *ab initio* molecular orbital (MO) calculation was performed at the 6-311G** basis set level using the GAMESS program.⁵ The critical-point analysis was carried out using the AIMPAC suite of programs.⁷⁹ For the experimental charge distribution, the critical-point information and deformation density and Laplacian maps were obtained using the program XDPROP in the XD package.²⁸

5.2.1 Treatment of Data

The intensity of a reflection is obtained by integrating over the area of the spot recorded by the detector. α_1 / α_2 splitting at high angle may mean that the parameters determined at low angle for the size of spot to integrate over are no longer appropriate at high angle. In this case, either separate integration of high and low angle data, or continued refinement of the spot size parameters may be helpful. In order to obtain the high angle data the position of the

detector had to be changed: it is probably necessary to use different orientation matrices for the high and low angle data. These considerations, together with different absorption correction and data merging options mean that there are many ways to treat the raw data. Several of these possibilities have been investigated here and their efficacies assessed.

5.2.2 Multipole Refinement

The crystal structure was determined previously.¹⁰⁰ The molecule in the crystal has symmetry S_6 , with the six-fold rotation axis passing through the centre of the ring. The asymmetric unit is therefore composed of the C-CH₂-SH fragment, with all of these atoms lying in general positions. Figure 5.1 shows how the molecules pack in the crystal, forming stacks in a direction parallel to the *c*-axis. The atomic labelling for the asymmetric unit is also shown.

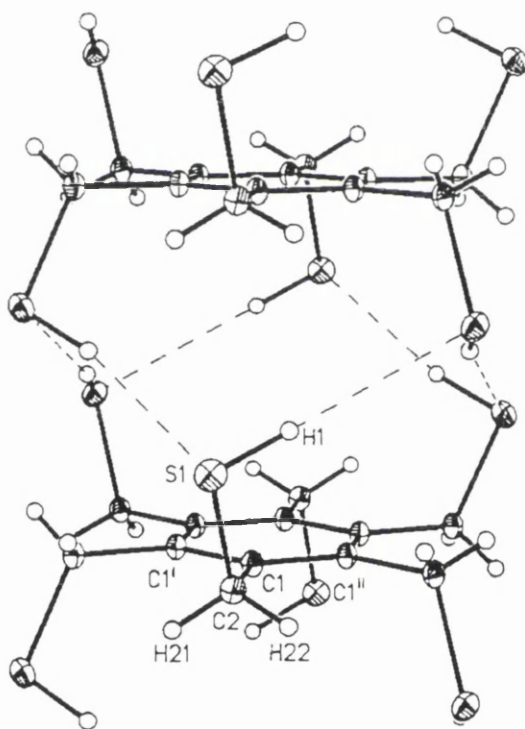


Figure 5.1 : A view normal to the *c* axis showing how 2 packs in the crystal.

The computational details of the multipole refinement are as discussed in Chapter 1. An overall electroneutrality constraint was applied to the monopole charges. The refinement was truncated at the hexadecapole level ($l_{\max}=4$) for sulfur; the octopole level ($l_{\max}=3$) for the carbon atoms, and the dipole level ($l_{\max}=1$) for hydrogen. A model containing hexadecapoles on the carbon atoms was tried but significant occupation of the hexadecapoles was not observed.

Separate κ' and κ'' were employed for each non-hydrogen atom type. It was thought initially that applying separate κ' and κ'' parameters to the two types of carbon atom might be appropriate since they occupy very different chemical environments. However, convergence could not be achieved with this model. For H atoms κ' and κ'' were fixed at 1.2, an average value obtained from theoretical models.³⁰ Values of κ'' were initially fixed at 1.0 for non-H atoms, but were allowed to vary after all other parameters had been refined. The κ'' for the higher multipoles ($l_{\max} \geq 1$) in each κ set were constrained to have the same value. A previous study³¹ showed that significant improvement of the model was achieved if separate κ'' parameters were refined for each of the sulfur multipoles. However, in the present study the κ'' parameters refined to unrealistic values when this was tried. The final κ values are: $\kappa'_c, \kappa''_c = 1.012(6), 0.82(1)$; $\kappa'_s, \kappa''_s = 1.090(8), 1.52(4)$.

The C-H bond length was fixed at 1.06 Å, the average value obtained from neutron diffraction by Allen *et al.*³⁴ Searching of the Cambridge Structural Database provided only one occurrence of an S-H bond determined by neutron diffraction.¹⁰⁵ The S-H bond length was therefore constrained to take this value, 1.338 Å. The bond directions to hydrogen and the H atom isotropic temperature factors were fixed at values obtained from an independent atom model refinement, in which all atoms were treated as spherical.

5.3 Results and Discussion

5.3.1 Treatment of Data

Experimental details of the data collection are given in Table 5.1. Table 5.2 summarises the different ways in which the raw diffraction data were integrated, merged and corrected for absorption to obtain eight different methods of data treatment. The corresponding residual density maps in the S1-C2-C1 plane for these methods are shown in Figures 5.2(a)-(h).

Formula	$C_{12}H_{18}S_6$
Formula weight	354.62
Space group	$R\bar{3}$
Crystal system	trigonal
Temperature, K	120(1)
Unit cell dimensions:	
a / Å	16.108(1)
c / Å	5.211(1)
V / Å ³	1167.3(2)
Z	3
D _c / g cm ⁻³	0.860
Crystal dimensions / mm	0.52 x 0.26 x 0.10
Absorption coefficient / mm ⁻¹	0.860
Radiation	Mo K _α ; λ = 0.71073 Å
No. of reflections measured	11743
No. of symmetry-independent reflections	2858
Range of corrections for absorption	0.659 - 0.863
Isotropic extinction	no extinction correction
Refined on	F
No. of variables	101
Weighting scheme	$w = 1 / \sigma^2(F) = 4F^2 / \sigma^2(F^2)^{\ddagger}$

[‡] The values of $\sigma(F)$ are assigned in the SAINT program and re-scaled in SADABS. We have not been able to determine the exact manner in which this is done.

Table 5.1 : Experimental data for hexakis(mercaptomethyl)benzene.

Data treatment	Intensity integration	Orientation matrices	Spot size refinement	Absorption correction	Data merging
<i>A</i>	high and low angle data together	same for high and low angle data	none	none	using SAINT
<i>B</i>	"	"	"	"	using SORTAV
<i>C</i>	high and low angle data separately	"	"	"	"
<i>D</i>	"	"	"	Face index correction using XPREP	"
<i>E</i>	"	"	"	Empirical correction using XPREP	"
<i>F</i>	"	separate for high and low angle data	"	"	"
<i>G</i>	"	"	Applied	"	"
<i>H</i>	"	"	None	SADABS	"

Table 5.2 : Different treatments of the raw diffraction data.

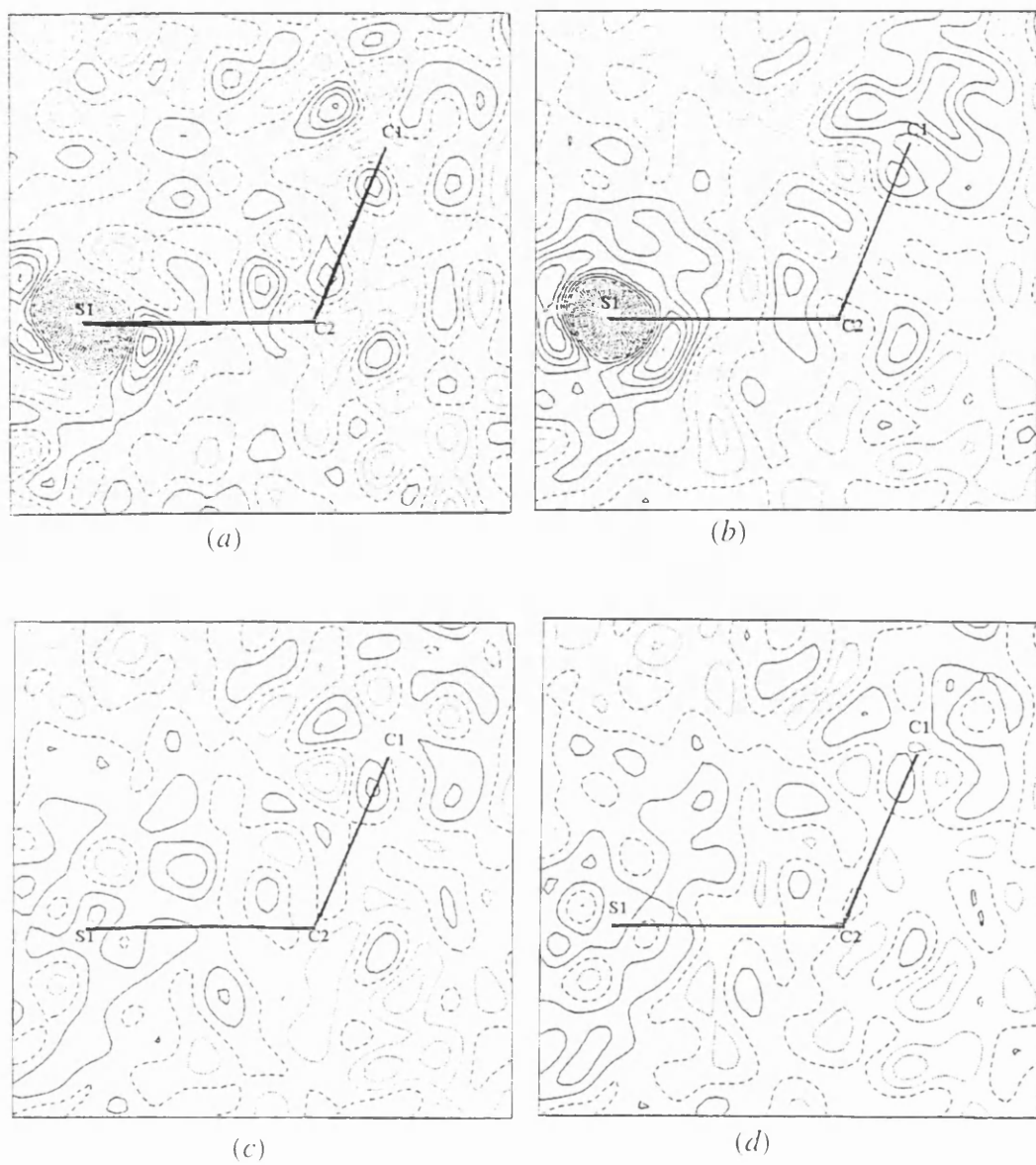


Figure 5.2 (a)-(d) : Residual density in the plane S1-C2-C1 for methods A to D respectively. Contour interval $0.1 \text{ e}\text{\AA}^{-3}$, solid lines are positive contours, dashed line is the zero contour, dotted lines are negative contours.

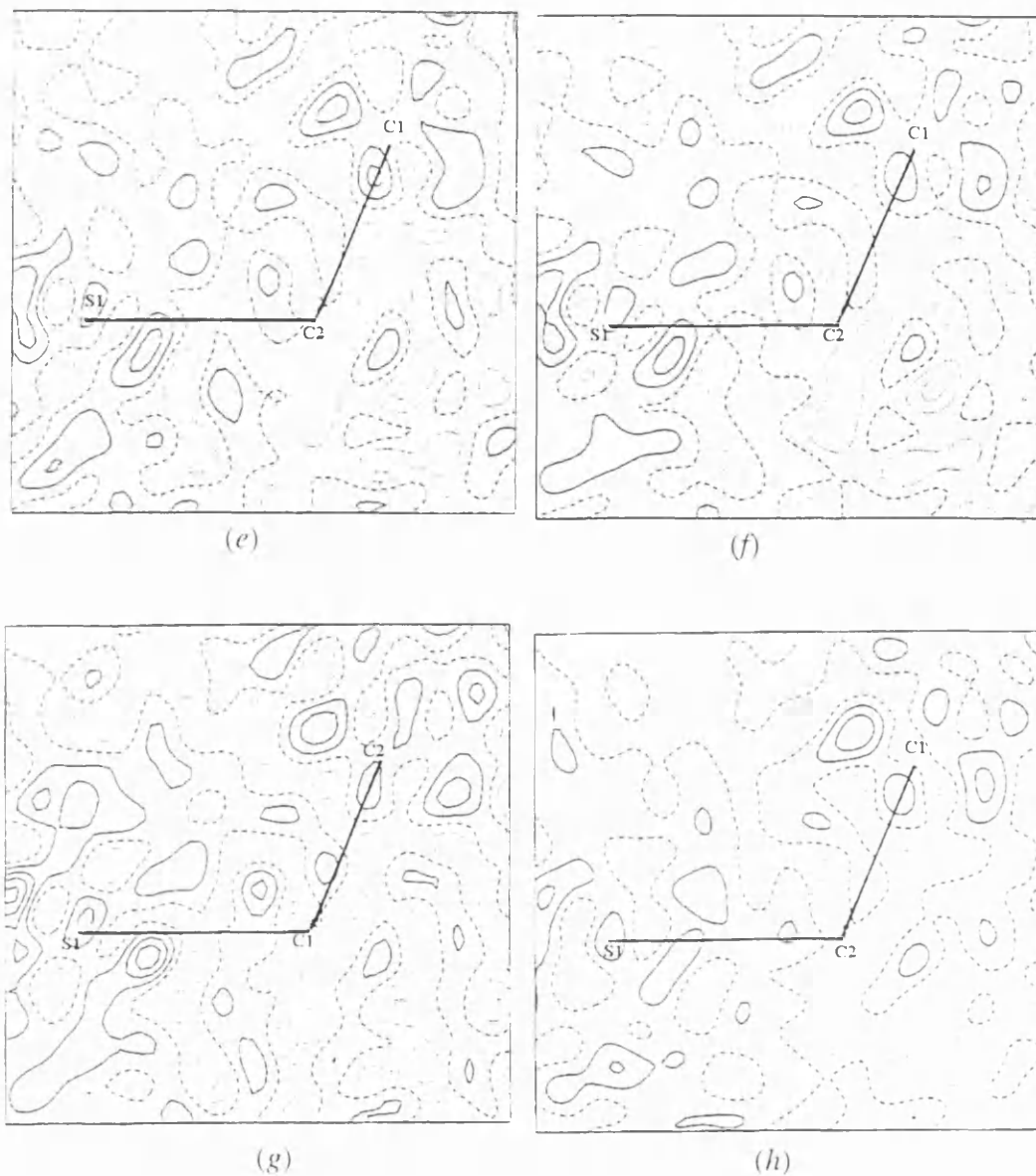


Figure 5.2 (e)-(h) : Residual density in the plane S1-C2-C1 for methods *E* to *H* respectively. Contour interval 0.1 eÅ⁻³, solid lines are positive contours, dashed line is the zero contour, dotted lines are negative contours.

Methods *A* and *B* differ only in the manner in which the data are merged: method *A* uses the SAINT program¹⁰⁶ whilst method *B* utilises SORTAV which is part of the DREADD program package.⁴⁰ Method *B* shows a slightly lower residual density than method *A* and so SORTAV is used to merge the data in all subsequent methods. It is apparent from the residual density maps of the various data treatments (Figures 5.2(a)-(h)), that the biggest improvement is made when the high and low angle data are integrated separately (*C-H*). The region of very high negative residual density centred on the sulfur atom is then no longer present. The spot size refinement (*G*) introduces a region of high positive residual density associated with the sulfur atom. This is not satisfactory and therefore spot size refinement has not been included in any other treatment of the data. In all of the methods *A-H* the residual density in the ring plane is lower and more randomly distributed than in the S1-C2-C1 plane.

There is little to choose between the other methods, on the basis of residual density alone. However, inspection of the Laplacian maps of *C* and *D* (Figures 5.3(c),(d) where the map numbering scheme corresponds to the data treatment) show that these methods are not satisfactory.

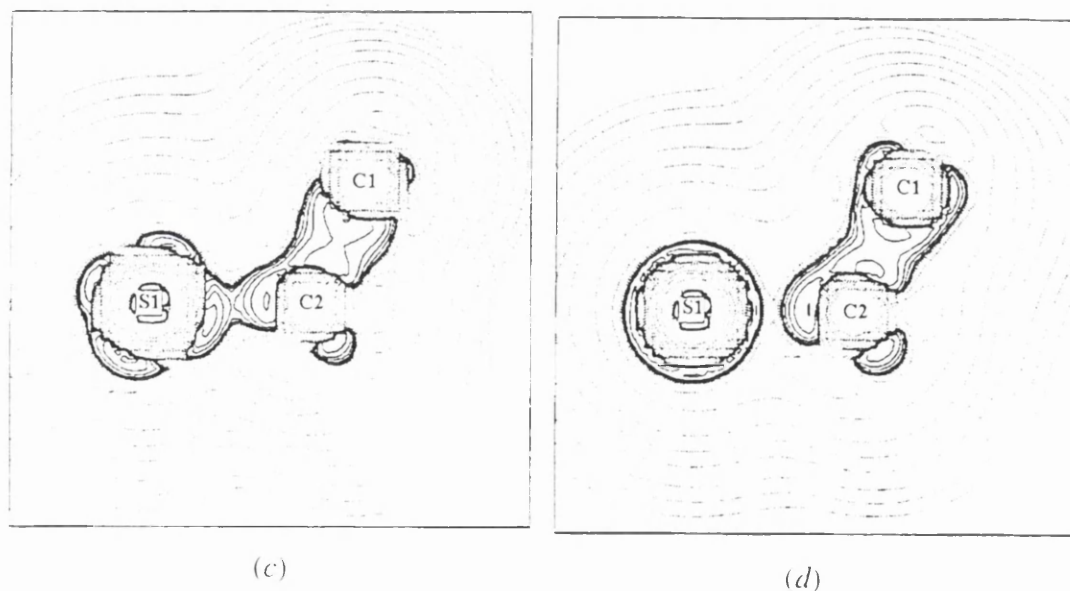


Figure 5.3 (c), (d) : Experimental Laplacian distribution in the plane S1-C2-C1 for methods *C* and *D*. The carbon core density contours have been omitted for clarity.

Method *C* does not have a complete valence shell on the sulfur atom; method *D* shows the S1-C2 bond to be ionic. If a comparison is made between the Laplacian maps of methods *E*, *F* and *H* (Figures 5.3(e), (f) and (h)) and that from the *ab initio* MO calculation (Figure 5.4), method *H* is found to agree best with the theoretical results.

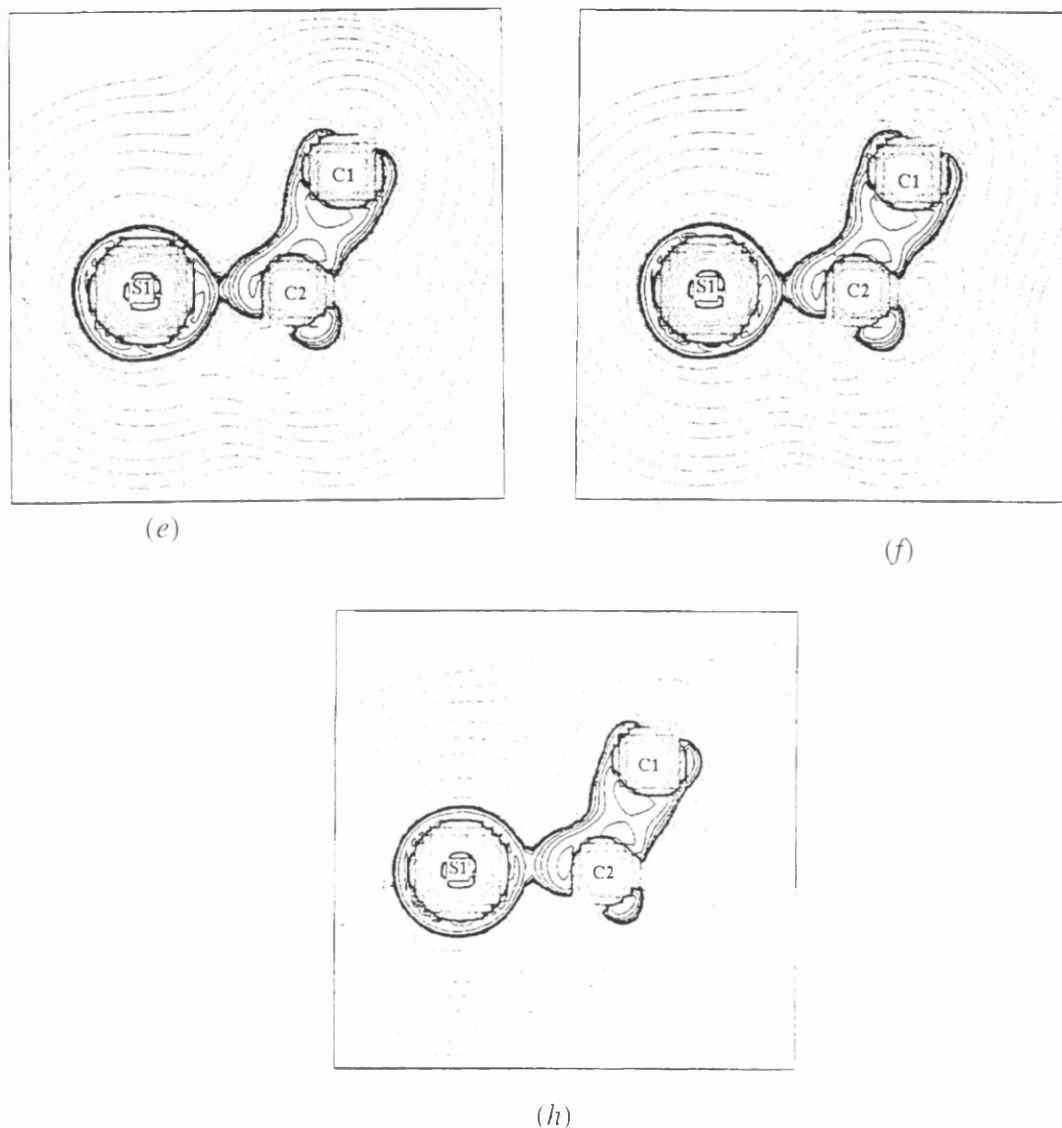


Figure 5.3 (e), (f), (h) : Experimental Laplacian distribution in the plane S1-C2-C1 for methods *E*, *F* and *H*. The carbon core density contours have been omitted for clarity.

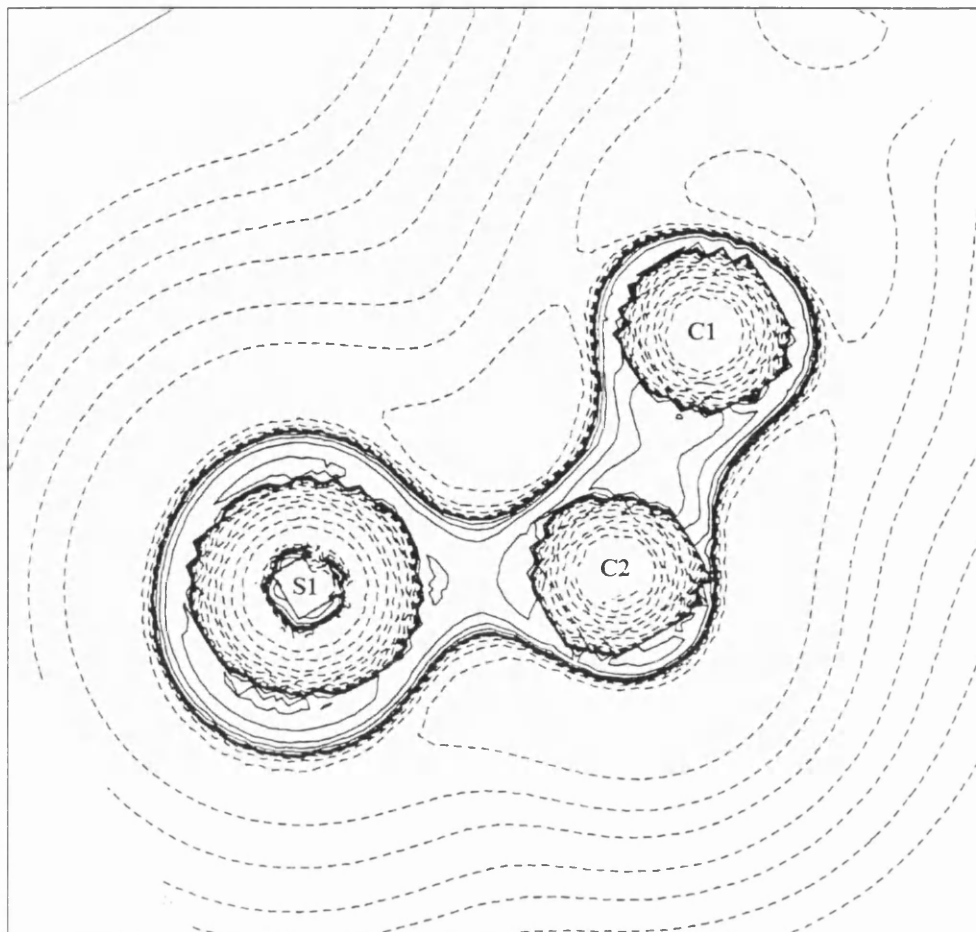


Figure 5.4 : Theoretical Laplacian distribution for the plane S1-C2-C1. The carbon atom core density contours have been omitted for clarity.

In methods *E* and *F* the S1-C2 bond is considerably more pinched and tends towards the ionic. In both of these methods an empirical absorption correction is applied using the XPREP program.¹⁰⁷ This correction uses all of the available data and relies on multiple redundancies. Differences in intensities between equivalent reflections are used to fit an ellipsoid to the crystal. This is then used to correct the data for absorption by the crystal. The improvement in method *H* over methods *E* and *F* appears to be due to the use of the SADABS program¹⁰⁸ to apply a correction to the data. This works in a broadly similar manner to the empirical absorption correction in XPREP but has been written specifically to correct data collected using a Siemens area detector. It is apparent that the way in which the data are integrated, merged and corrected for absorption significantly affects the results of the

multipole refinement. Care must therefore be taken in determining the most effective way to treat the raw data.

Having established the most suitable way in which to treat the data an agreement analysis of observed and calculated structure factors, after multipole refinement of the model, was performed using the program WTANAL.¹⁰⁹ It was found that for the very high angle data the agreement analysis was poor. Successive cut-off values in 2θ were applied in order to determine which would produce the best weighting analysis without introducing significant correlation effects into the model, see Table 5.3. Below $2\theta = 86^\circ$ the rigid bond test is no longer satisfied for bonds between heavy atoms. The results reported correspond to a 2θ cut-off of 86° .

2θ	$\sin \theta_{\max}$	Number of observed reflections ($I > 2\sigma I$)	Goodness of fit, S	R	Observations to variables ratio
102	1.0985	1791	0.7842	0.025	17.7
90	0.9949	1561	0.8448	0.025	15.5
86	0.9596	1449	0.8798	0.025	14.3

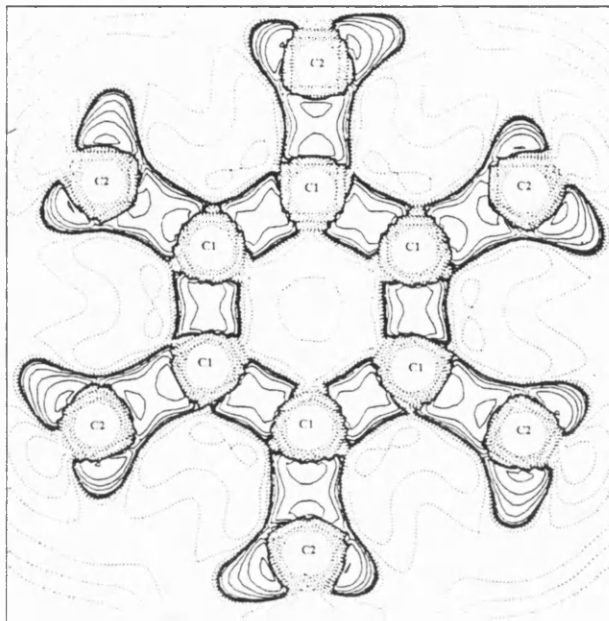
Table 5.3 : Effects of different 2θ cut-off values.

5.3.2 Experimental Charge Density Analysis and Comparison with Theory

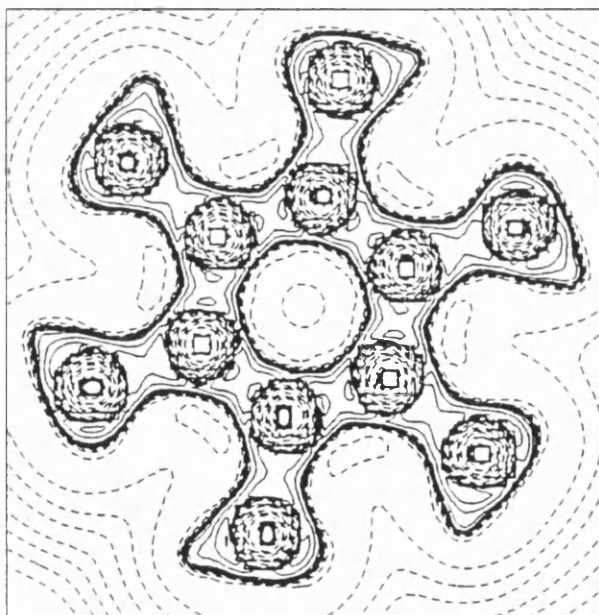
The pinched S1-C2 bond in the experimental Laplacian is an unexpected feature, but compares very well to the theoretical result. A previous experimental charge density study of a sulfur-containing molecule shows no such tendency towards an ionic S-C bond.³¹ The value of the Laplacian at the S-C bond critical-point in this work is $-0.80(6)$ as compared to $-6.82(8) \text{ e}\text{\AA}^{-5}$ in the previous study, indicating a considerably less covalent bond here.

The experimental Laplacian for the ring plane also compares well to that obtained from the MO calculation (Figures 5.5(a),(b)). The bond critical-point of the C-C double bond is located on the interatomic vector showing the bond to be straight and the aromatic ring to be free of strain. The ellipticity of this bond is high, as expected for a double bond.

The critical point data are shown in Table 5.4. In all cases the value of ρ at the bond critical-point is higher in the experimental results than in the corresponding theoretical results, this effect has been observed before, see Chapter 4.



(a)



(b)

Figure 5.5 : Laplacian distribution in the plane of the aromatic ring; (a) experimental (core density contours omitted for clarity); (b) theoretical.

Atoms	Bond length / Å	Experimental			Theoretical		
		$\rho_b / e\text{Å}^{-3}$	Laplacian / $e\text{Å}^{-5}$	Ellipticity	$\rho_b / e\text{Å}^{-3}$	Laplacian / $e\text{Å}^{-5}$	Ellipticity
C1-C2	1.510(1)	1.97(5)	-16.9(1)	0.14	1.61	-11.2	0.01
S1-C2	1.837(1)	1.20(3)	-0.80(6)	0.11	1.01	-3.9	0.11
S1-H1	1.338	1.25(2)	-2.7(5)	0.02	1.20	-7.4	0.18
C2-H21	1.060	1.89(6)	-17.6(1)	0.08	1.89	-21.5	0.02
C2-H22	1.060	1.98(6)	-19.3(1)	0.05	1.91	-22.0	0.03
C1-C1	1.410(1)	2.37(9)	-25.1(2)	0.47	1.94	-15.8	0.16
S1...H1	2.761(2)	0.028(1)	0.644(1)	0.06			

Table 5.4 : Critical point data for hexakis(mercaptomethyl)benzene.

5.3.3 Evidence for Intermolecular SH...S Bonding

It was noted in the earlier report of the crystal structure that geometric considerations suggested the possibility of S-H...S hydrogen bonding. The S...S distance of 4.053(1) Å borders on a van der Waals contact, and the SH...S angle is 165.7(5)°. The proposed intermolecular interaction would exist between adjacent molecules stacked in a direction parallel to the *c*-axis. This region of the experimental charge density was therefore searched for the existence of intermolecular bond paths. Bond critical-points were located between H and S atoms in adjacent molecules. We believe that this is the first experimental observation of S-H...S hydrogen bonding which uses topological charge density information to support geometric and spectroscopic evidence.

The value of ρ_b for the S...H interaction is 0.028(1) $e\text{Å}^{-3}$ and the Laplacian value is 0.644(1) $e\text{Å}^{-5}$. The low value of ρ_b and the positive Laplacian at the (3,-1) critical-point are both characteristic of long-range closed-shell interactions. It is interesting to note that the value of ρ_b obtained here for the S...H interaction is comparable with those values obtained from *ab initio* calculations on the systems H₂S...HF and H₂CS...HF, where $\rho_b=0.020$ and 0.026 $e\text{Å}^{-3}$ respectively.¹¹⁰ However, in this system each sulfur atom acts as both a proton donor, and a proton acceptor; the lone pair electrons can be seen to be directed towards a hydrogen atom in the adjacent molecule (see Figure 5.6a). Unfortunately this effect cannot be observed in the Laplacian map, Figure 5.6b. This may be another artefact of the methods of treatment of the raw area detector data. Other techniques such as the seed-skewness method¹¹¹ may lead to better results. Presently we are constrained by the availability of computer programs tailored to particular instrumentation.

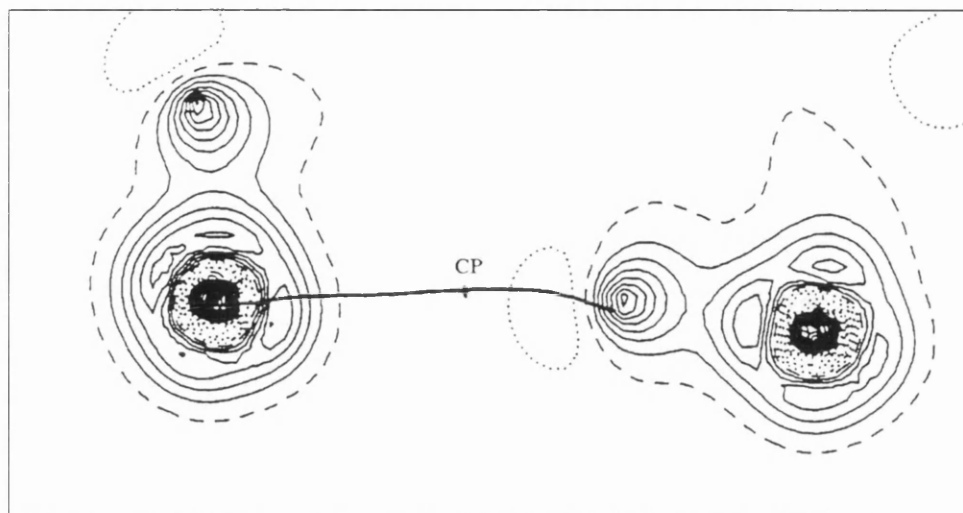


Figure 5.6(a) : Static deformation density map showing the SH...S interaction bond path and associated critical point. Atom labels have been omitted for clarity.

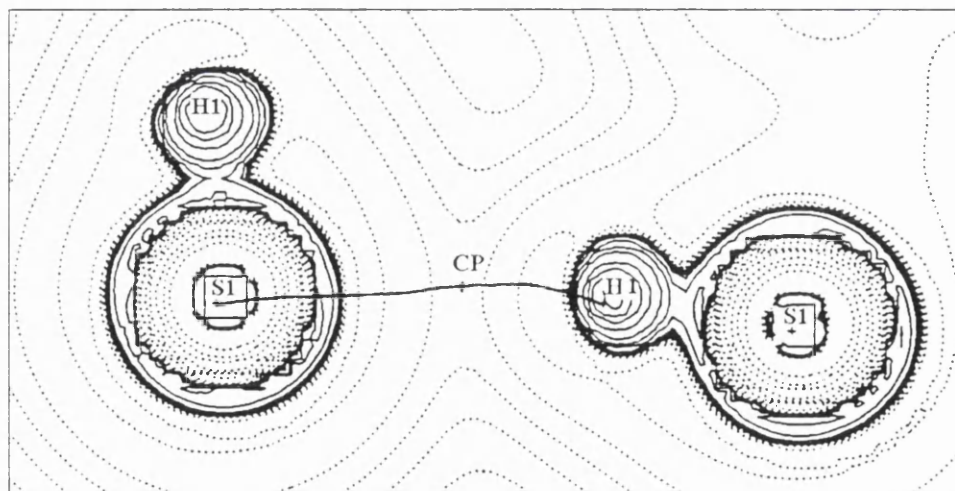


Figure 5.6(b) : Experimental Laplacian distribution for the SH...S interaction bond path and associated critical point.

5.4 Conclusion

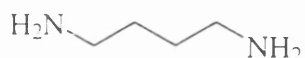
Observation of a bond critical-point on the interatomic vector between H and S atoms of adjacent molecules of **2** provides the first direct experimental evidence of S-H...S hydrogen bonding.

Chapter 6

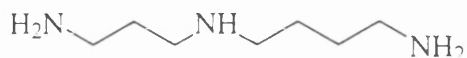
Experimental and Theoretical Studies of the Charge Density Distribution in *E*-Tetraethyl-1,4-diammoniumbut-2-ene. $2PF_6$

6.1 Introduction

The naturally occurring polyamines putrescine and spermidine are ubiquitous in living cells and are essential for normal cell growth and proliferation.¹¹²



Putrescine



Spermidine

Under physiological conditions polyamines are largely protonated; the resultant cations of putrescine and spermidine have positive charges of 2 and 3 respectively.¹¹³ This distributed positive charge allows the polyamine cations to interact with anionic species, such as the phosphate groups of DNA.

Recently it has been shown that some synthetic analogues of the naturally occurring polyamines possess antifungal or anticancer properties.^{114, 115, 116} The exact reason for the activity of these analogues is unclear, although it has been suggested that it could be due to inhibition of polyamine biosynthesis, or to competitive binding to polyamine sites related to

cell proliferation, or to binding at polyamine sites with the resultant disruption of macromolecular structure and function.¹¹⁶ Any of these mechanisms would disrupt the normal action of the naturally occurring polyamines and hence inhibit normal cell growth.

The interaction of the polyamine cations with the negatively charged phosphate groups of DNA is therefore important to the antifungal or anticancer properties of the polyamine cations. The nature of this interaction is dependent upon the electrostatic potential surface of each ion. The characteristics of the potential surface of the polyamine cation, which in turn depend upon the distribution of the +2 charge in the cation, are therefore of interest. It is possible that a series of charge density studies of related polyamines of known antifungal activity would provide information from which structure/property relationships could be drawn. This study has been undertaken as the first of such a series. Its purpose is to determine the charge density distribution of the polyamine cation *E*-tetraethyl-1,4-diammoniumbut-2-ene, TEDH₂²⁺. The cation is an analogue of putrescine and is known to be an effective antifungal agent. Recently, a similar study of spermine phosphate hexahydrate was also reported.¹¹⁷

In order to confirm whether or not an interaction with the DNA phosphate groups is feasible or not, the electrostatic potential surface of the phosphate group must also be determined. Clearly it is not tractable to attempt an experimental charge density study of DNA, and so the charge density distribution of the simplest model group which would approximate to the phosphate groups of the DNA helix, namely [PO₂(OCH₃)₂]⁻, has been calculated by means of *ab initio* molecular orbital methods.

6.2 Experimental

Crystals of C₁₂H₂₈N₂.2PF₆ are colourless plates. The crystal faces were indexed, the two largest faces having indices of 100 and $\bar{1}00$; the sides were bounded by the 011, $0\bar{1}\bar{1}$, $0\bar{1}\bar{1}$ and $0\bar{1}\bar{1}$ faces. This information was used to perform a Gaussian analytical absorption correction for absorption by the crystal using the program ABSORB.³⁹ High-resolution, low-temperature X-ray diffraction data were collected using proprietary software⁷⁸ on a CAD-4 diffractometer equipped with a liquid nitrogen cryostat, using graphite-monochromated Mo K α radiation. The data reduction was performed as described in section 1.7. The least-squares refinement of the multipole model was carried out using XDLSM of the XD

package.²⁸ The topological analysis of the experimental charge density was obtained using the program XDPROP in XD.

Ab initio MO calculations were performed for the cation at the geometry found in the molecular crystal, using the 6-311G** basis set. The initial geometry of the model phosphate group, [PO₂(OCH₃)₂]⁻, was obtained from standard bond lengths and angles, and suitable torsion angles. This was fully optimised at the STO-6G level with no symmetry constraints, and the resulting geometry was used as input for a single-point energy calculation at the 6-311G** basis set level. All calculations were performed using GAMESS.⁵ The critical point information and Laplacian maps of the cation were obtained using the program AIMPAC⁷⁹ and the electrostatic potential map of the phosphate group was plotted using MEPMAP of the GAMESS graphics package.⁵

6.2.1 Multipole Refinement

The crystal structure of C₁₂H₂₈N₂.2PF₆ had not previously been determined. The crystal structure was therefore solved using SHELXS86¹¹⁸ and refined with SHELXL93.¹¹⁹ At room temperature the [PF₆]⁻ group is disordered. Four of the F atoms appear as a spinning wheel around the F2-P1-F4 axis. However, this is clearly a dynamic effect as no significant disorder is observed at low temperature. The space group, *P*2₁/*c*, requires the cation in the crystal to be centrosymmetric, the midpoint of the C1-C1 double bond lying on the centre of inversion. The asymmetric unit is therefore composed of the C₆H₁₄N fragment and one [PF₆]⁻ ion. Figure 6.1 shows the molecular structure of TEDH₂²⁺ and the [PF₆]⁻ counter ion. the atomic labelling is also shown.

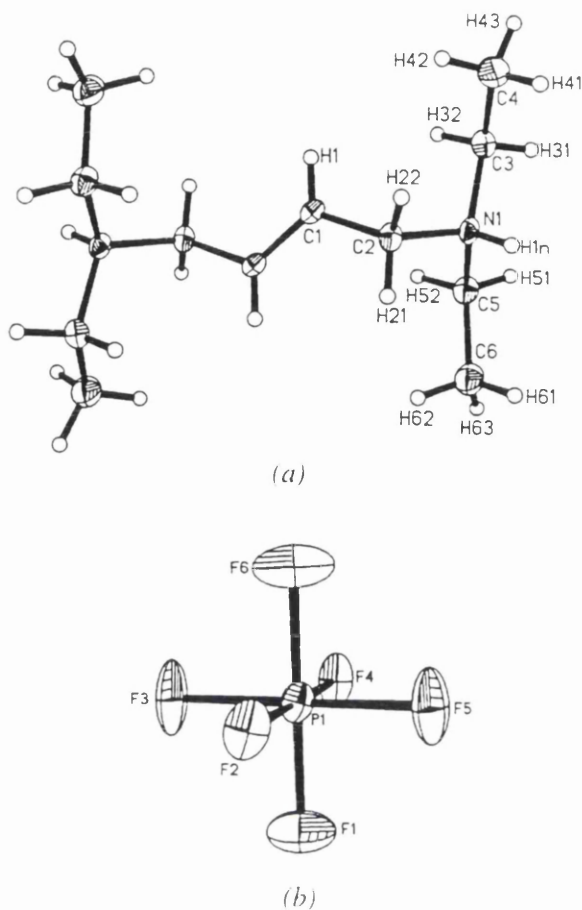


Figure 6.1 : Structures of: (a) the cation $TEDH_2^{2+}$; (b) the anion $[PF_6]^-$. Probability ellipsoids are drawn at 50% probability.

An overall electroneutrality constraint was applied to the monopole charges. In addition the cation and anions were constrained to have charges of +2 and -1 respectively. The refinement was truncated at the hexadecapole level ($l_{max} = 4$) for all non-hydrogen atoms. This level of expansion was considered to be reasonable as there was significant occupation of the hexadecapoles for all non-H atoms. For hydrogen atoms the refinement was truncated at the dipole level ($l_{max} = 1$) with one bond-directed dipole per hydrogen atom. This approach was taken because significant occupation of the other two dipoles was not observed for any of the hydrogen atoms. Removal of the unnecessary dipoles from the model also improved the observations-to-variables ratio.

Separate κ' and κ'' parameters were refined for each of the non-hydrogen atom types. Initially it was thought that employing separate κ' and κ'' parameters for the two sets of

chemically equivalent carbon atoms in the ethyl groups might improve the description of these groups. It was found that the carbon κ sets refined to values which were not significantly different from each other. The carbon atoms were therefore assigned to the same κ set in order to improve the observations-to-variables ratio. For all of the non-hydrogen atoms the κ'' parameters were fixed at 1.00 initially, but were allowed to vary after all of the other parameters had been refined. The final κ values are : $\kappa'_C, \kappa''_C = 0.963(4), 0.835(6)$; $\kappa'_N, \kappa''_N = 0.99(1), 0.84(3)$; $\kappa'_P, \kappa''_P = 1.03(1), 0.71(1)$; $\kappa'_F, \kappa''_F = 0.979(2), 1.03(1)$.

Bond directions to hydrogen, and hydrogen atom isotropic temperature factors were fixed at values obtained from an independent atom model refinement, in which all of the atoms were treated as spherical. Bond lengths to hydrogen were fixed at the average values obtained from neutron diffraction, 1.06 and 1.033 Å for the C-H and N-H bonds respectively.³⁴ κ' and κ'' for the hydrogen atoms were fixed at 1.2, an average value obtained from theoretical models.³⁰

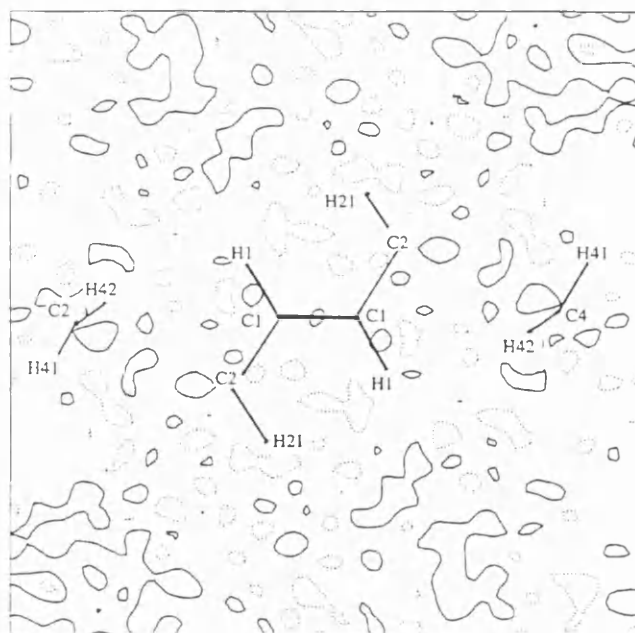
6.3 Results and Discussion

6.3.1 Structural Results

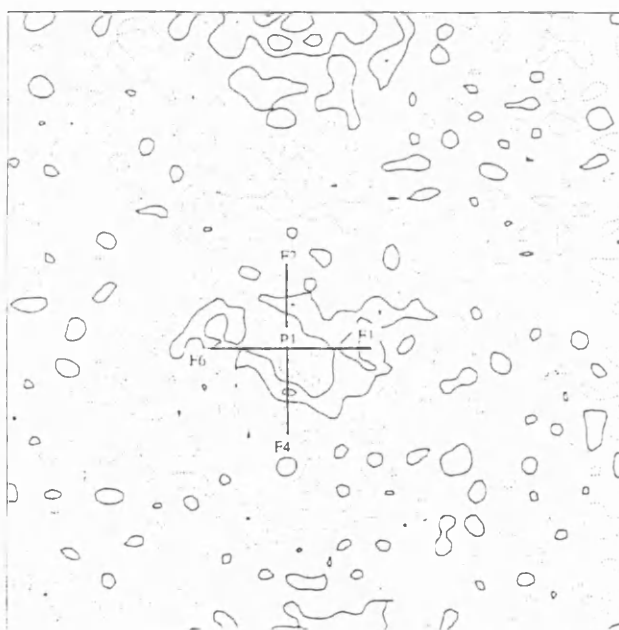
Details of the data collection and refinement are given in Table 6.1. The residual density maps of both the anion and the cation, Figures 6.2(a) and (b), show randomly distributed regions of low residual density, indicating that the multipole model fits well to the data. Application of the rigid bond test⁴³, which is a good indication of the quality of the model, shows that all of the bonds in the cation satisfy the test criteria. However, three of the bonds in the anion, P1-F1, P1-F5 and P1-F6, have $\Delta_{A,B}$ values slightly greater than the limit of 0.001 Å² for bonds involving atoms at least as heavy as carbon. This could be related to a slight degree of residual disorder in the anion which is reflected in the larger than normal displacement amplitudes of these fluorine atoms, see Table 6.2.

Formula	C ₁₂ H ₂₈ N ₂ .2PF ₆
Formula weight	490.3
Space group	<i>P</i> 2 ₁ / <i>c</i>
Crystal system	Monoclinic
Temperature, K	100(1)
Unit cell dimensions:	
<i>a</i> / Å	6.282(1)
<i>b</i> / Å	13.252(1)
<i>c</i> / Å	13.112(1)
β / °	98.08(9)
<i>V</i> / Å ³	1079.5(2)
<i>Z</i>	2
<i>D_c</i> / g cm ⁻³	1.51
Crystal dimensions / mm	0.3 x 0.3 x 0.1
Absorption coefficient / mm ⁻¹	0.300
Radiation	Mo K α ; λ = 0.71073Å
Scan type	ω -2 θ
($\sin\theta/\lambda$) max / Å ⁻¹	1.099
No. of standard reflections	5(2 $\bar{6}$ $\bar{2}$, 3 7 1, 0 $\bar{6}$ 3, $\bar{3}$ 7 $\bar{6}$, $\bar{2}$ 3 11)
No. of reflections measured	19338
No. of symmetry-independent reflections	6884
No. <i>I</i> > 2 σ (<i>I</i>) reflections	3611
Agreement factor $R = \Sigma I - \bar{I} / \Sigma I$	0.034
Range of corrections for absorption	0.931-0.979
Isotropic extinction	no extinction correction
Refined on	<i>F</i>
<i>R</i>	0.021
<i>R_w</i>	0.022
<i>S</i>	1.003
No. of variables	513
Weighting scheme	$w = 1 / \sigma^2(F) = 4F^2 / \sigma^2(F^2)$ $\sigma^2(F^2) = \sigma^2_{\text{counting}}(F^2) + P^2F^4$ $P^2=0.0006$

Table 6.1 : Experimental data for *E*-tetraethyl-1,4-diammoniumbut-2-ene.2PF₆.



(a)



(b)

Figure 6.2 : Residual density for: (a) the cation in the plane C2-C1-C1'-C2'; (b) the anion in the plane F1-P1-F2. Contour interval $0.1 \text{ e}\text{\AA}^{-3}$, solid lines are positive contours, dotted lines are negative.

Atom	U_{11}	U_{22}	U_{33}	U_{12}	U_{13}	U_{23}
P1	0.0106(1)	0.0150(1)	0.0185(1)	-0.0016(1)	0.0024(1)	-0.0044(1)
F1	0.0299(8)	0.0390(10)	0.0404(10)	0.0002(8)	0.0048(8)	0.0155(9)
F2	0.0104(4)	0.0268(6)	0.0341(7)	-0.0034(4)	0.0025(4)	-0.0107(6)
F3	0.0141(5)	0.0388(8)	0.0490(9)	-0.0043(6)	0.0075(6)	-0.0308(8)
F4	0.0107(4)	0.0294(6)	0.0311(6)	-0.0021(4)	0.0051(4)	-0.0134(6)
F5	0.0236(7)	0.0420(9)	0.0405(9)	-0.0098(7)	0.0125(7)	-0.0260(9)
F6	0.032(1)	0.048(1)	0.043(1)	-0.012(1)	-0.004(1)	0.021(1)

Table 6.2 : Mean-square atomic displacements (\AA^2) for the anion. The form of the

anisotropic temperature factor is : $\exp \left[-2\pi^2 \sum_{i=1}^3 \sum_{j=1}^3 U_{ij} h_i h_j a_i^* a_j^* \right]$.

6.3.2 Atomic Charges and Electrostatic Potential

The atomic charges for atoms in the cation are given in Table 6.3. It is clear that there are differences in magnitude between the experimental valence monopole and theoretical Mulliken values. Whilst some differences would be expected, due to the different partitioning of the molecular charges in the two cases, a qualitative comparison would be expected to show the same general trends in the two sets of results. Both experiment and theory show the carbon and nitrogen atoms to carry partial negative charges, whilst all of the hydrogen atoms are positively charged. This is in direct contrast to the formal charges which assign a charge of +1 to each of the nitrogen atoms. Qualitatively similar results have been obtained for a nitrogen ylide compound, the formally positive nitrogen atom carrying a charge of -0.58(6) and the positive charge being distributed over the hydrogen atoms.¹²⁰

Both experiment and theory show the hydrogen with the greatest positive charge to be that bonded to the nitrogen atom. That is with the exception of H51 and H41 in the experiment which have charges not significantly different from that of H1N. It would be expected that the nitrogen atoms would carry a larger negative charge than the carbon atoms, since a formally positive nitrogen is very electronegative. This is shown to be the case in theory, but not from this experiment.

Atom	Atomic charge / electrons	
	Valence monopole	Mulliken
C1	-0.25(7)	-0.067
C2	-0.34(8)	-0.009
N1	-0.04(10)	-0.394
C3	-0.33(9)	-0.068
C4	-0.58(8)	-0.146
C5	-0.44(8)	-0.053
C6	-0.59(8)	-0.145
H1	0.24(4)	0.078
H1N	0.33(5)	0.277
H21	0.22(4)	0.146
H22	0.28(4)	0.174
H31	0.24(4)	0.151
H32	0.29(4)	0.132
H41	0.33(5)	0.110
H42	0.20(5)	0.079
H43	0.24(5)	0.140
H51	0.36(4)	0.144
H52	0.26(4)	0.135
H61	0.19(5)	0.110
H62	0.26(5)	0.076
H63	0.11(5)	0.129

Table 6.3 : Atomic charges for the atoms in $TEDH_2^{2+}$.

The distribution of charge within the cation is confirmed by the 1H NMR data for the non-protonated form of the molecule, TED, and for $TEDH_2^{2+}$, see Table 6.4 below. In $TEDH_2^{2+}$ each of the formally positive nitrogen atoms acts as a powerful electron-withdrawing group. Hence the +2 charge is not located on the nitrogens but is distributed over the hydrogen atoms. The proton environments are therefore deshielded, leading to downfield shifts in δ , *i.e.* higher values of δ , in $TEDH_2^{2+}$ as compared to TED.

Proton environment	TED	$TEDH_2^{2+}$	Δ / ppm
\underline{CH}_3 - \underline{CH}_2	1.04	1.32	+0.28
\underline{CH}_3 - \underline{CH}_2 -N	1.54	2.22	+0.68
N- \underline{CH}_2 -CH	3.12	3.88	+0.76
CH	5.70	6.15	+0.45

Table 6.4 : 1H NMR data for TED and $TEDH_2^{2+}$, δ values in ppm. All spectra were carried out in CD_3OD with TMS as an internal standard.

The downfield shift in δ is greatest for the protons bonded to the carbons which are α to the nitrogen. The shift of the methylene protons next to the nitrogen is of the order of 0.7 ppm. The effect on protons bonded to carbons which are β to the nitrogen is still appreciable. The relative magnitudes of the charge depletion for the hydrogen atoms can be compared with the valence monopole charges. The proton NMR shows the greatest electron depletion to be on the H atoms bonded to C2, followed by those bonded to C3/C5, C1 and C4/C6 in order of decreasing electron depletion. The 1H NMR averages the environments of the chemically equivalent protons. Treating the valence monopole charges in the same way the sequence is: C3/C5, C2, C1 and C4/C6. The H atoms on carbons which are α to nitrogen are thus reordered. The equivalent sequence from the Mulliken charges is C2, C3/C5, C4/C6 and C1.

It is difficult to predict the nature of intermolecular interactions from atomic charges alone, particularly in this case where there is some disagreement between experiment and theory. Rather than discrete atomic charges, it is the cumulative effect of the distribution of charge within the molecule, and the affect that this has on the proposed interacting species, that is of interest. This is best investigated by looking at the electrostatic potential surface of the two interacting species in question. Theoretical electrostatic potential maps were therefore plotted for $TEDH_2^{2+}$ and the model phosphate group. These are shown in Figures 6.3 and 6.4 respectively.

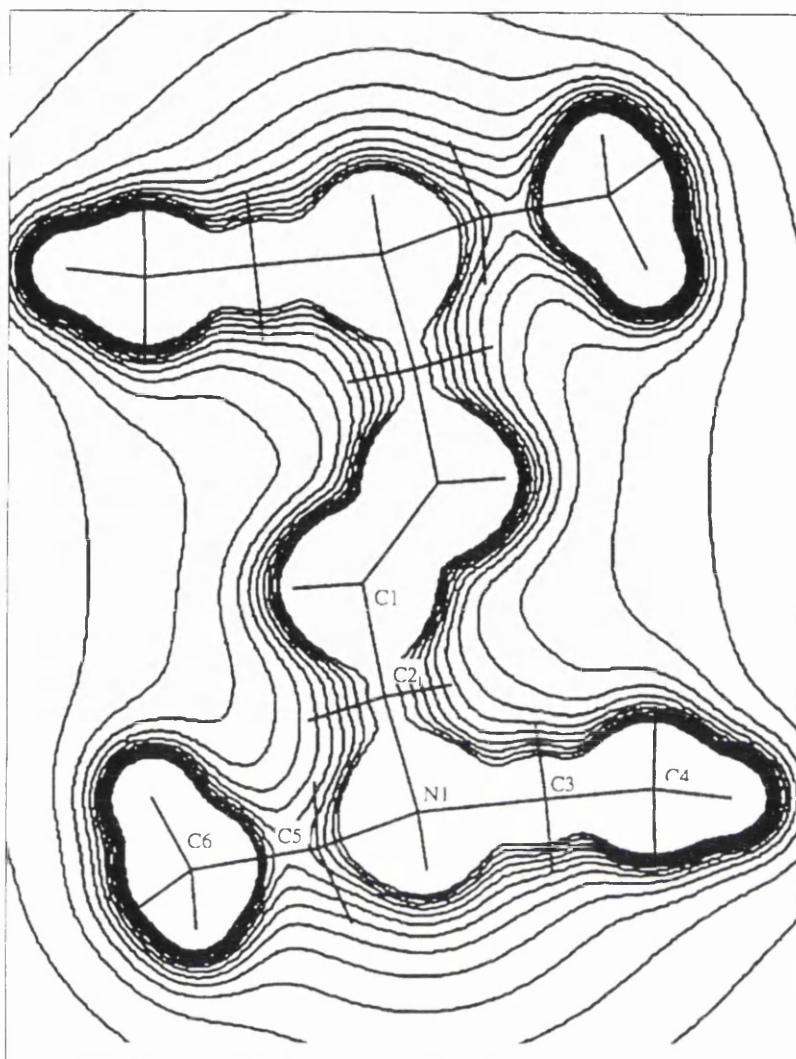


Figure 6.3 : The theoretical electrostatic potential of the TEDH₂²⁺ ion in the N1-C1-C1' plane. Contour interval 100 kJmol⁻¹.

It might be predicted that the negative charges on the carbon and nitrogen atoms would disfavour an interaction with the negatively charged phosphate group. However, these charges are small and diffuse enough not to feature as regions of negative potential. Rather, the surface is dominated by the positive charges on the hydrogen atoms and the whole of the electrostatic potential surface of TEDH₂²⁺ is positive.

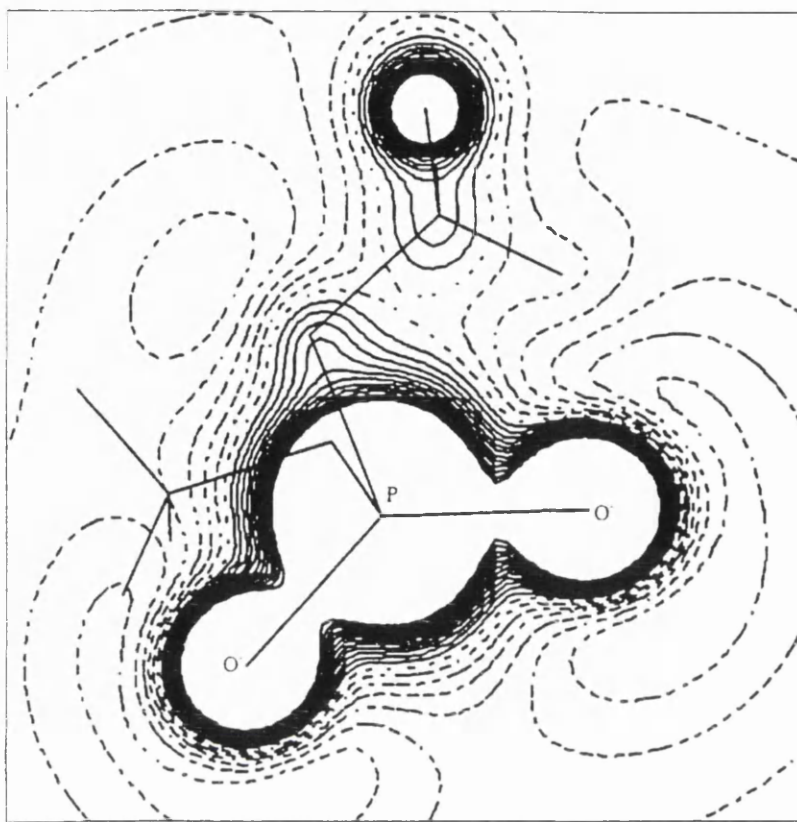
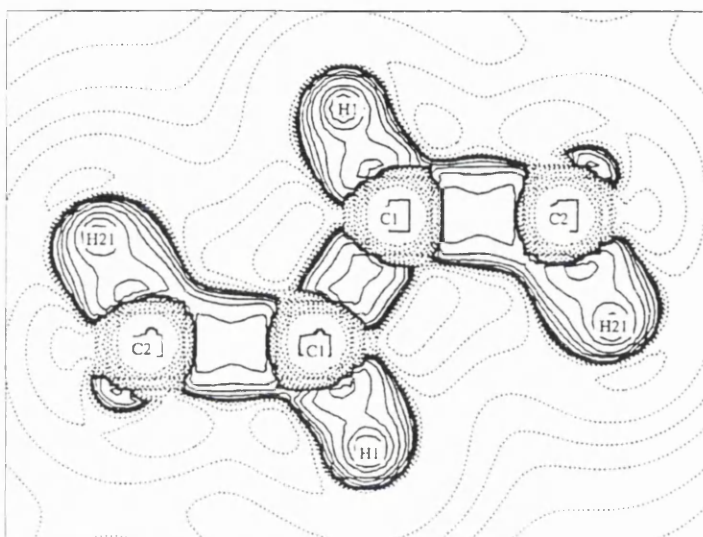


Figure 6.4 : The electrostatic potential surface of the model phosphate group, [PO₂(OCH₃)₂]⁻ in the plane O-P-O. Solid lines are positive contours, dashed lines are negative. Contour interval 100 kJmol⁻¹.

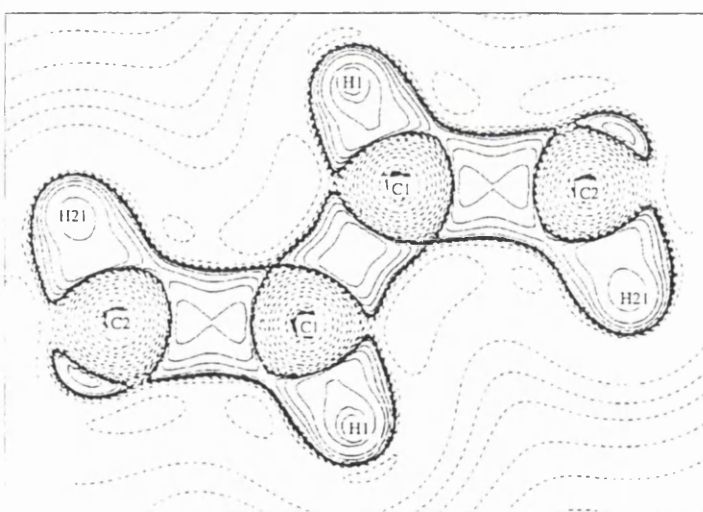
The electrostatic potential map of the model phosphate group shows large regions of negative potential, 700 kJmol⁻¹, associated with the lone-pair electrons of the oxygen atoms. A strong interaction between TEDH₂²⁺ and the DNA phosphate groups is therefore predicted. It is possible that the interaction is not site-specific with respect to the polyamine cation as all points on the surface have large positive potentials. Interestingly a similar conclusion was reached by Cohen *et al* from their charge density study of spermine.¹¹⁷ Independent evidence for this mode of binding of the polyamine cations to the DNA helix is given by a ¹H NMR study of a spermidine derivative which shows the cation to have rotational and translational freedom whilst remaining bound to the DNA helix.¹²¹

6.3.3 Topological Analysis of the Charge Density Distribution

The charge density distributions arising from both the multipole model and the *ab initio* calculation were analysed topologically using Bader's theory of Atoms in Molecules.⁶⁰ Figures 6.5(a) and (b) show experimental and theoretical Laplacian maps for the C1-C1' region. The results of the critical point analysis are collated in Table 6.5.



(a)



(b)

Figure 6.5 : Laplacian distribution for $TEDH_2^{2+}$ in the C2-C1-C1'-C2' plane: (a) experimental; (b) theoretical.

There is very good agreement between the experimental and theoretical Laplacian maps. Both show the Laplacian to be more negative at the C1-C1' bond critical point than in the C1-C2 or the C2-N1 single bonds. The topology of the three-dimensional Laplacian, as distinct from the charge density itself, exhibits no non-bonded local maxima such as those associated with lone pair electrons. The absence of such features would be predicted from the electrostatic potential map of $TEDH_2^{2+}$ which shows the cation to have a continuous positive potential surface.

Atoms	Bond length / Å	Experimental			Theoretical		
		$\rho_b / e\text{Å}^{-3}$	Laplacian / $e\text{Å}^{-5}$	Ellipticity	$\rho_b / e\text{Å}^{-3}$	Laplacian / $e\text{Å}^{-5}$	Ellipticity
C1-C1'	1.334(2)	3.01(9)	-44.3(3)	0.47	2.41	-27.9	0.43
C1-C2	1.493(2)	2.13(6)	-26.9(2)	0.14	1.86	-19.4	0.02
C2-N1	1.511(2)	1.84(7)	-22.3(3)	0.11	1.56	-10.8	0.11
N1-C3	1.507(2)	1.83(9)	-22.6(5)	0.42	1.52	-5.3	0.12
C3-C4	1.512(2)	2.00(6)	-26.4(2)	0.40	1.76	-17.4	0.01
N1-C5	1.506(2)	1.76(9)	-25.4(5)	0.15	1.52	-5.8	0.14
C5-C6	1.512(2)	2.11(6)	-25.0(2)	0.07	1.76	-17.5	0.01
H1N-F3	1.994(2)	0.09(1)	2.1(1)	0.38			
H1N-F4	2.050(2)	0.08(1)	1.7(1)	0.58			

Table 6.5 : Critical point data for selected bonds in *E*-tetraethyl-1,4-diammoniumbut-2-ene. $2PF_6$.

The value of ρ_b for the C1-C1' double bond is high, as expected for a multiple bond. The ellipticity of this bond is close to 0.5, the value expected for a pure carbon-carbon double bond. The experimental values for the ellipticities of the N1-C3 and C3-C4 bonds are anomalous, while the theoretical values for these bonds are in accord with the values expected for single bonds. Both experiment and theory give ellipticity values for the N1-C5 and C5-C6 bonds which are relatively close to zero. Hence the *ab initio* calculation shows the two ethyl groups to be equivalent, whilst the experimental ellipticities show a marked difference between the two groups. However, there is no significant difference between either the total density or the Laplacian at the bond critical points in the two ethyl groups. This, together with the generally good agreement with theory suggests that the multipole model chosen gives a satisfactory description of the charge density distribution. There is no obvious explanation

for the anomalous ellipticity values; they are not due to excessive vibrational motion of the N1-C3-C5 group as the rigid bond test is satisfied. Neither is it likely to be due to the effect of intermolecular interactions as there are no substantial differences between contacts involving the two ethyl groups.

Interionic interactions are observed between H1N of the cation and F3 and F4 of a symmetry-related anion. The internuclear distances are 1.994(2) and 2.050(2) Å respectively, and the N1-H1N-F3/F4 angles are 144.7(1) and 146.9(1)^o. This type of long-range closed-shell interaction is typically characterised by a low ρ_b value and a positive Laplacian, as is found to be the case here.

6.4 Conclusion

Topological analysis of the experimental charge density distribution of TEDH₂²⁺ shows no non-bonded maxima in the Laplacian distribution. This supports the conclusion from the *ab initio* calculation that the cation has a continuous positive electrostatic potential surface. A strong interaction would therefore be predicted between TEDH₂²⁺ and the phosphate groups of DNA.

Chapter Seven

Hyperfine Coupling Constants for Muonium in Elemental Sulfur Environments

7.1 Introduction

Muons are short-lived elementary particles of the lepton family. They occur naturally in cosmic rays, but can also be produced artificially in particle accelerators. A high-energy proton beam (500-800 MeV) is directed onto a production target which is made of a material like carbon or beryllium. This produces a beam of pions which decay with a mean lifetime of 26ns, according to the following reaction:



Decay of a positive pion gives a positive muon and a muon-neutrino. Similarly, if a negative pion decays, a negative muon and a muon-antineutrino are produced. However, the chemical importance of negative muons is very limited and they will not be considered further.

The beam of positive muons which is obtained from the pion decay is spin polarised. The muon spin and momentum vectors are either parallel or antiparallel to each other, depending on the experimental set-up. The muon then decays with a mean lifetime of 2.2 μ s emitting a positron, an electron-neutrino and a muon-antineutrino:



The positron is emitted in a direction that makes an angle of θ to the muon spin direction. The probability, p , of a positron being emitted in a particular direction is given by:

$$p \propto 1 + x \cos \theta \quad 7.3$$

where x is the asymmetry.¹²² This means that the positron is emitted preferentially, but not exclusively, along the direction of the spin vector of the muon at the moment of decay. The techniques of muon spin rotation, resonance and relaxation (collectively known as μ SR) depend upon the measurement of this anisotropic distribution of emitted positrons.

In a μ SR experiment the beam of muons is made to strike the sample under observation, which is located in an applied magnetic field. The muons enter the sample and thermalise within a few centimetres. They may continue to exist as free muons, μ^+ , in the sample in which case the muons will precess at the Larmor frequency, see Table 7.1. It is also possible for a muon to capture an electron from the sample to form a muonium atom, Mu, in which a single orbital electron is associated with a muon nucleus. The newly formed muonium atom can further react with the sample to give diamagnetic muonium species, RMu, or muonium-containing radicals RMu \cdot . The formation of muonium-containing organic radicals is particularly common in samples of unsaturated hydrocarbons.

Muons and protons have the same spin and charge, see Table 7.1, and the muonium atom can be considered as a light isotope of hydrogen. Although the mass of the muon is only one ninth that of the proton, the reduced masses of hydrogen and muonium are virtually identical as both the muon and the proton are much more massive than the electron. Muonium and hydrogen therefore have very similar ionisation energies and Bohr radii.

Quantity	Proton	Positive Muon	Electron
Mass / kg	1.672623×10^{-27}	1.883566×10^{-28}	9.109389×10^{-31}
Mass / m_e	1836.1528	206.7719	1.0
Charge	+1.0	+1.0	-1.0
Spin	1/2	1/2	1/2
Nuclear or Bohr magneton / JT^{-1}	5.050786×10^{-27}	4.485244×10^{-26}	9.274015×10^{-24}
Larmor frequency / $MHzT^{-1}$	42.5771	135.5374	28024.71
g-factor	5.58569	2.002332	2.002319
Gyromagnetic ratio / $MHzT^{-1}$	267.5221	851.6196	1.7609×10^5

Table 7.1: Physical properties for the proton, the positive muon and the electron.¹²³

Data from μ SR experiments can be used in conjunction with results from analogous hydrogen and deuterium experiments to study kinetic isotope effects. Muonium can also be used as a chemical probe in reactions involving hydrogen which cannot be investigated directly. The reaction is performed with muonium taking the place of hydrogen, and μ SR techniques are used to investigate the chemical environment of the muonium atom before decay.

7.2 Avoided Level Crossing Muon Spectroscopy

7.2.1 Experimental Method

In avoided level crossing (ALC) spectroscopy the sample to be studied is placed in a longitudinal magnetic field, B , that is parallel to the direction of the muon beam. The muons interact with the sample and their decay positrons are counted by electronic counters placed in front of and behind the sample. See Figure 7.1 below.

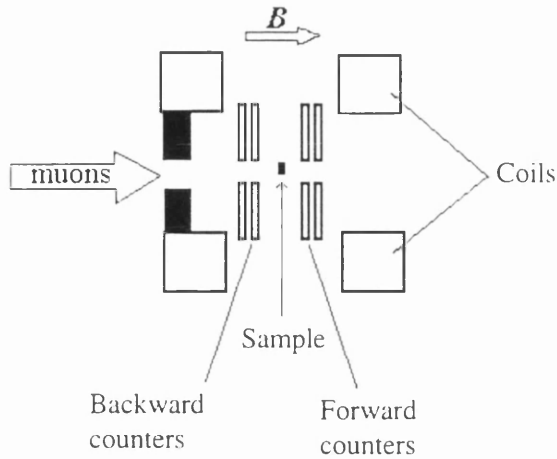


Figure 7.1 : Schematic diagram of the experimental apparatus used for ALC spectroscopy.

Because the muon beam is spin polarised there will be a difference between the amount of positrons registered by the forward and backward counters. The resulting asymmetry, a , is plotted as a function of the field:

$$a = \frac{N_f - N_b}{N_f + N_b} \quad 7.4$$

Where N_f and N_b are the forward and backward counts respectively.¹²⁴

Since the muons are spin polarised parallel to the direction of the field, in general there will be no loss of polarisation with increasing field strength. The asymmetry, a , is therefore constant with regard to the applied magnetic field. However, at certain field strengths there are resonance conditions which result in a loss of the muon spin polarisation, and hence a change in the measured asymmetry. In order to understand the origin of these resonances it is necessary to consider how electron, muon and other nuclear spins interact with each other.

7.2.2 Hyperfine Structure

Muonium is a two spin-1/2 system and can exist as either a singlet state, in which the electron and muon spins are paired, or a triplet in which the spins are unpaired. In the absence of a magnetic field these two states are separated by an energy difference, A_μ , which is called the vacuum muon-electron hyperfine frequency. It has the value 4463 MHz.¹²²

When a magnetic field is applied to the system the energy levels of the states alter with B , and the triplet state is resolved into three levels. It is possible to obtain analytical expressions for the energies of the singlet and the three triplet levels in terms of the applied field strength.¹²⁵ These expressions can then be used to construct a plot, known as a Breit-Rabi diagram, of energy level against applied field strength. Figure 7.2 is a Breit-Rabi diagram for muonium, $x \equiv B / 0.1585$ if the field is measured in Tesla. At low fields, two transitions are possible between triplet levels, these are marked on the diagram as ν_{12} and ν_{23} .

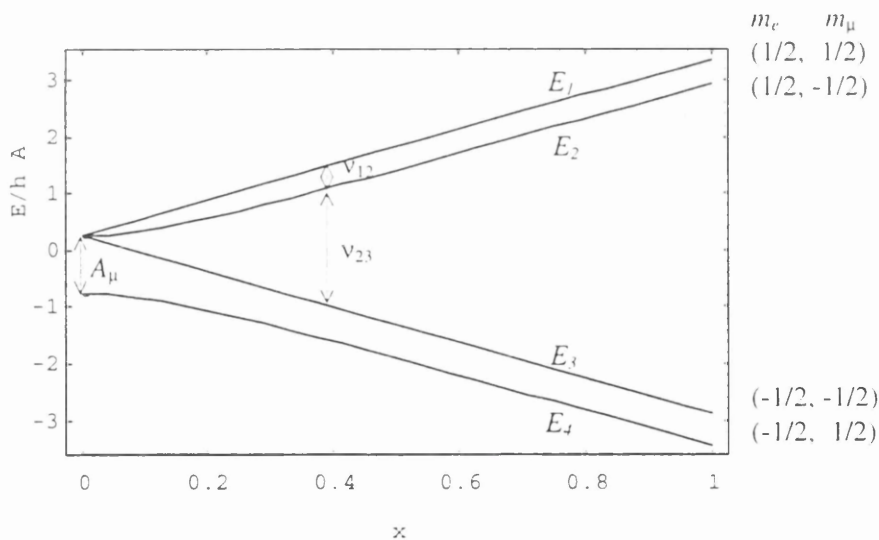


Figure 7.2 : Breit-Rabi diagram for the isolated muonium atom.

At a very high field, $B = 16.38$ T, the two highest lying triplet states are equal in energy and the levels appear to cross over. In fact, at this point the two states mix causing the levels to avoid each other, hence the name of the technique. At this field the muon is

equally free to exist in either the up or down state and can flip between the two, the polarisation of the muon spin is therefore lost.

In a more complicated system in which other atoms are present the frequency of the muon-electron hyperfine coupling will be altered. This is due to the modification of the applied magnetic field by the local fields arising from other electrons and magnetic nuclei. The level-crossing resonance will still exist but at a different value of the applied magnetic field. Experimentally the resonance condition is manifested as a large reduction in the measured asymmetry. The hyperfine coupling constant, A_μ , for the species is obtained from the measured field value using the relationship:¹²⁶

$$B = A_\mu \pi \left(\frac{1}{\gamma_\mu} - \frac{1}{\gamma_e} \right) \quad 7.5$$

where γ_μ and γ_e are the gyromagnetic ratios of the muon and electron respectively. The values of these constants are obtained using the relationship:

$$\gamma = \frac{g \mu}{\hbar} \quad 7.6$$

where g is the g -factor and μ is either the Bohr magneton or the muon magneton for the electron or the muon respectively.¹²⁷ The values of γ_μ and γ_e are given in Table 7.1.

7.3 Muon-Electron Hyperfine Coupling Constants for Muonium in Elemental Sulfur

Recently μ SR experiments have been carried out to determine the behaviour of muons implanted in elemental sulfur. The experiments were intended as a way of predicting the behaviour of hydrogen atoms in the same system. Repolarisation experiments suggest that two paramagnetic muon states coexist in elemental sulfur.¹²⁸ The estimated hyperfine coupling constants of 2000 ± 500 MHz and 220 ± 60 MHz are consistent with an interstitial muonium atom and a muonium-containing radical respectively. ALC experiments were then carried out in order to gain more information about the nature of the radical species. Figure

7.3 shows an ALC spectrum for the muonium-containing radical. The position of the resonance is 8452 G, or 0.845 T in SI units, which corresponds to a hyperfine coupling constant of 233 ± 5 MHz.¹²⁹

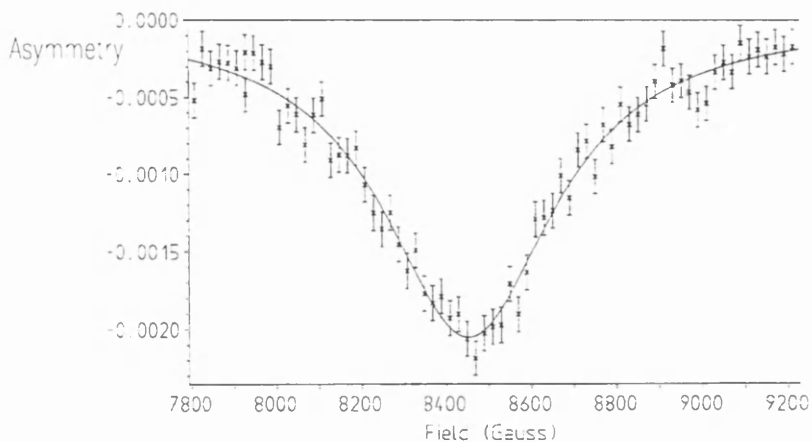


Figure 7.3 : An ALC spectrum showing the resonance which corresponds to the muonium-containing radical.

The principle isotope of sulfur has a nuclear spin, I , of zero and so the only coupling which can be observed is that between the muonium nucleus and the unpaired electron. This does not give enough information for the species to be uniquely identified from the experimental results alone. *Ab initio* molecular orbital studies can help in the assignment of the signals by recreating a variety of possible sulfur environments for the muonium atom, and calculating the associated hyperfine coupling constants.

7.3.1 Computation

The *ab initio* M.O. calculations were performed at the Unrestricted-Hartree-Fock (UHF-SCF) level using the GAMESS program.⁵ The basis set employed was 6-31G**. From the calculated spin density in atomic units, the value of the muon-electron hyperfine coupling constant A_{μ} / MHz is obtained by multiplying by a factor of 14229.0.¹³⁰ In order to compare muon-electron coupling constants with those for proton-electron couplings it is useful to cite A_{μ} in a reduced form, $A_{\mu} = A_{\mu} (\mu_p / \mu_{\mu}) = 0.3141 A_{\mu}$, where μ_p and μ_{μ} are the magnetic moments of the proton and the muon respectively.

7.3.2 The Muonium-Containing Radical

Since no information was available about the likely structure of the radical the problem was approached by constructing several model starting geometries in which a muonium atom was positioned at several points around a puckered S_8 ring. The geometries of the model systems were then optimised under C_1 symmetry. The S_8 ring was taken to be of ideal S_8 symmetry with S-S bond lengths of 2.059 Å, an average value obtained by searching the Cambridge Structural Database for all occurrences of the S-S bond.^{82, 83} In three of the six models the S-Mu bond length was 1.26 Å, also an average value obtained by searching the CSD for occurrences of S-H.^{82, 83} The starting geometries of the models are sketched in Table 7.2. The energies and muon-electron hyperfine coupling constants for the starting geometries are also shown. It is interesting to note that whilst the position of the muonium atom has very little effect on the energy of the system, the value of A_μ is heavily dependent on the position of Mu.





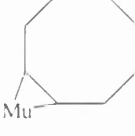
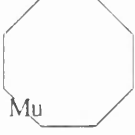

 <p style="text-align: center;">Mu</p>	<p>Isolated S₈ puckered ring and Mu atom fragments</p> <p>Initial energy = -3180.07606+0.49823 = -3180.57429 E_h</p>
 <p style="text-align: center;">Mu</p>	<p style="text-align: center;"><u>Model A</u></p> <p>Mu atom in the plane which bisects an S-S-S angle. Mu directly below the central S atom. S-Mu = 1 Å</p> <p>Initial energy = -3180.36560 E_h A_μ = 908.59 MHz</p>
 <p style="text-align: center;">Mu</p>	<p style="text-align: center;"><u>Model B</u></p> <p>Mu atom in the plane which bisects an S-S-S angle. Mu outside of the ring. S-Mu = 1 Å</p> <p>Initial energy = -3180.41669 E_h A_μ = 9.52 MHz</p>
 <p style="text-align: center;">Mu</p>	<p style="text-align: center;"><u>Model C</u></p> <p>Mu atom bridges an S-S bond. Mu is inside the ring, in the mean plane of the ring. S-Mu = 1.26 Å</p> <p>Initial energy = -3180.36161 E_h A_μ = -509.40 MHz</p>
 <p style="text-align: center;">Mu</p>	<p style="text-align: center;"><u>Model D</u></p> <p>Mu atom bridges an S-S bond. Mu is outside the ring, in the mean plane of the ring. S-Mu = 1.26 Å</p> <p>Initial energy = -3180.38714 E_h A_μ = -163.63 MHz</p>
 <p style="text-align: center;">Mu</p>	<p style="text-align: center;"><u>Model E</u></p> <p>Mu atom bridges an S-S bond. Mu is in the plane above the S-S bond. S-Mu = 1.26 Å</p> <p>Initial energy = -3180.32313 E_h A_μ = 81.10 MHz</p>
 <p style="text-align: center;">Mu</p>	<p style="text-align: center;"><u>Model F</u></p> <p>Mu atom lies on the midpoint of an interatomic vector between S atoms at positions 1 and 7 of the S₈ ring. S-Mu = 1.66 Å.</p> <p>Initial energy = -3180.43221 E_h A_μ = 851.46 MHz</p>

Table 7.2 : Starting geometries and initial energies and hyperfine coupling constants for the model systems A to F.

In systems *A* and *B* one of the S-S bonds to the sulfur which is bonded to the muonium atom is broken during the optimisation. Similarly in systems *C*, *D* and *E* the bond bridged by the muonium atom is broken during the geometry optimisation. The muonium atom remains bonded to one sulfur atom and the ring opens to form a puckered $[S_8\text{Mu}]^{\bullet}$ chain. The optimised systems are energetically stabilised with respect to both the starting geometries and the isolated S_8 and Mu fragments. The optimised systems are pure doublet states with the majority of the unpaired atomic spin density located on the sulfur atom at the opposite end of the chain to the muonium atom. Consequently, the values of the hyperfine coupling constants for these systems are effectively zero. It seems unlikely therefore that the $[S_8\text{Mu}]^{\bullet}$ chain corresponds to the radical species observed by μSR .

When the muonium atom is positioned at the midpoint of the interatomic vector between two sulfur atoms at positions 1 and 7 of the S_8 ring, model *F*, the $S_8+\text{Mu}$ system is found to dissociate to S_7 and the $[\text{SMu}]^{\bullet}$ radical. The initial and optimised geometries for model *F* are shown in Figure 7.4.

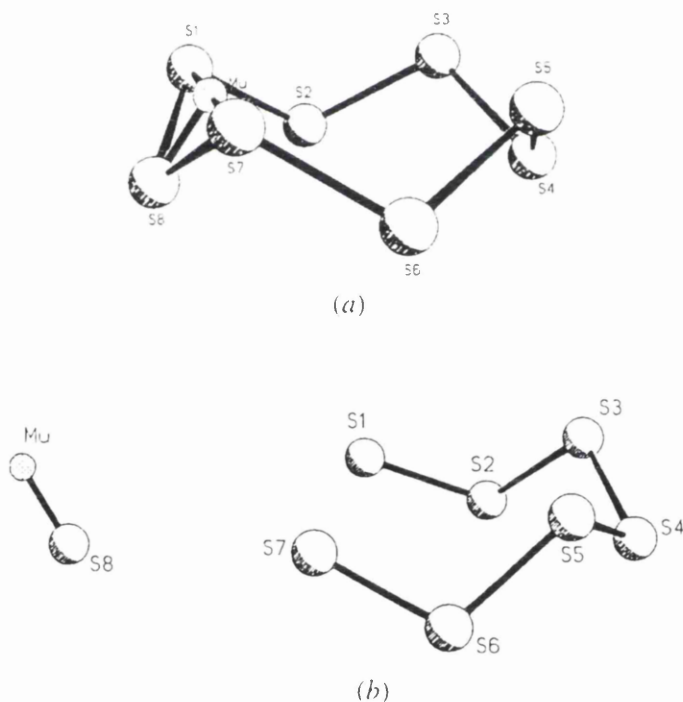


Figure 7.4 : Geometry of model *F*, to scale: (a) initial; (b) optimised.

The hyperfine coupling constant calculated for this system is -208.73 MHz, with an energy of -3180.61170 hartree. However, the expectation value of the spin operator is 1.779, rather than the value of 0.75 which would be obtained for a pure doublet state. Clearly the wavefunction is contaminated by functions of higher spin multiplicity.

The wavefunction at the equilibrium geometry was re-calculated with a spin multiplicity of four. The expectation value of the spin operator is then 3.779, very close to the value of 3.75 which would be obtained for a pure quartet. There is little spin contamination and the system can effectively be considered to be a pure quartet state. The energy of the quartet system is -3180.61172 hartree, stabilised by 0.05 kJmol^{-1} with respect to the doublet system. Inspection of the free valence values shows that two of the three unpaired electrons are located at either end of the S_7 fragment. The third is located on the sulfur atom of the $[SMu]^{\bullet}$ radical which would therefore be predicted to be a doublet state when isolated from the rest of the system.

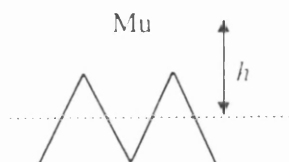
The value of the muon-electron hyperfine coupling constant for the $S_7 + [SMu]^{\bullet}$ quartet system is -208.79 MHz. The value of A_{μ} for an isolated, optimised doublet $[SMu]^{\bullet}$ radical is calculated to be -224.00 MHz using the 6-31G** basis set. It should be noted that whilst the sign of the coupling cannot be determined by an ALC experiment, the *ab initio* results show A_{μ} to be negative. This can be explained qualitatively by assigning the unpaired electron in the $[SMu]^{\bullet}$ radical to a p orbital on the sulfur atom. The unpaired electron will interact unequally with the two paired electrons in the bond. There will be an exchange interaction between the unpaired electron and the paired electron of like spin, these two will therefore be closer together than the unpaired and paired electrons of opposite spins. The muon will therefore 'see' more of the electron which has a spin opposite to that of the electron in the p orbital of sulfur and this gives rise to a negative spin density.¹³¹

Both of the values given above for the muon-electron hyperfine coupling constant for $[SMu]^{\bullet}$ are within the error limits of the observed value for the molecular radical determined by the repolarisation study; the value for the isolated radical is also within the error limits for the value of 233 ± 5 MHz determined by ALC. Ashworth and Brown have determined hyperfine parameters for the $[SH]^{\bullet}$ radical using the technique of laser magnetic resonance.¹³² Taking $b + c/3$ to specify the value of A_p , a value of -52.60 MHz is obtained. This value can be compared directly to the *ab initio* reduced hyperfine coupling constants of -65.58 and -70.36 MHz for the $S_7 + [SMu]^{\bullet}$ and isolated $[SMu]^{\bullet}$ systems respectively, and also to the reduced value determined by ALC, 73.19 ± 1.57 MHz. There is clearly a large difference

between A_p and A_μ . Some difference between the two values would be expected because of isotope effects. For example, Buttar calculates the muon-electron and proton-electron reduced β -hyperfine coupling constants for the substituted ethyl radical to be 144.715 and 166.097 MHz respectively.¹³⁰ This cannot be compared directly to the results for $[\text{SMu}]^\bullet$ and $[\text{SH}]^\bullet$ as the hyperfine values for the ethyl radical are affected by other vibrational modes, in addition to the Mu-X bond stretch. However, Claxton calculates values of 38.55 and 48.11 MHz for A_p and A_μ in the hydroxyl radical.¹³¹ The differences between the measured value of A_p and the measured and calculated values of A_μ for the sulfur system are also of this order. It is suggested therefore that the radical species observed by μSR is $[\text{SMu}]^\bullet$. A prediction of the existence of the $[\text{SMu}]^\bullet$ radical is a particularly significant result as neither this species nor the $[\text{OMu}]^\bullet$ radical have ever been observed and characterised.

7.3.3 The Interstitial Muonium Atom

Cox suggests that the signal at 2000 ± 500 MHz is due to an interstitial muonium atom lodged at the centre of an S_8 ring.¹²⁸ This was taken as the starting point for an investigation of the location of the interstitial muonium atom. The sulfur ring was of the same ideal S_8 geometry as in the calculations on the radical. A series of calculations were performed in which the distance of the muonium atom above the centre of the mean plane through the sulfur ring, h , was varied. The results are shown in Table 7.3.



$h / \text{\AA}$	A_{μ} / MHz	Energy / E_h
0.00	4693.06	-3180.52230
0.25	4665.10	-3180.52390
0.50	4593.09	-3180.52822
0.75	4505.34	-3180.53424
1.00	4430.36	-3180.54088
1.50	4357.59	-3180.55336
2.00	4330.36	-3180.56307
2.50	4296.82	-3180.56931
3.00	4264.79	-3180.57249
3.50	4244.87	-3180.57381
4.00	4237.76	-3180.57425
6.00	4238.82	-3180.57429
10.00	4238.82	-3180.57429

Table 7.3 : Energies and hyperfine coupling constants for different heights of the muonium atom above the centre of an S_8 ring.

At all values of h the hyperfine coupling constant has a much higher value than that measured for the interstitial species. As the height of the muonium atom above the centre of the ring is increased, the hyperfine coupling constant increases. At a height of 6 \AA above the plane the vacuum value for a free muonium atom, calculated at this basis set level, is reached. The energy of the system at $h = 6 \text{\AA}$ corresponds to the energy of the isolated $S_8 + \text{Mu}$ fragments. It is clear that the calculated hyperfine coupling constant for a muonium atom at any height above the centre of an S_8 ring does not correspond with the value of A_{μ} measured for the interstitial muonium atom.

In order to find alternative interstitial sites for Mu it is necessary to examine the structure of solid elemental sulfur. Sulfur exists in a number of crystalline forms, the

majority of which are composed of S_8 rings. γ -sulfur was chosen as a representative S_8 -based form as an accurate crystal structure is available.⁸⁰

Inspection of the unit cell of γ -sulfur shows three plausible symmetry-independent interstitial sites for the Mu atom. In each case the site is located between two adjacent S_8 rings, the muonium is positioned approximately equidistantly from the three or four sulfur atoms surrounding the interstitial site. The systems were modelled by performing *ab initio* calculations at the experimental geometry of the two sulfur rings. The model systems are sketched in Table 7.4. The muon-electron hyperfine coupling constants and Mu...S distances are also shown.


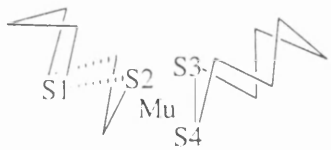
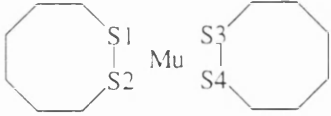
Model system	Muon to sulfur internuclear distances / Å	A_μ / MHz
	Mu...S1 2.02 Mu...S2 1.96 Mu...S3 1.81	3586.98
	Mu...S1 1.98 Mu...S2 2.08 Mu...S3 2.04 Mu...S4 2.02	4082.51
	Mu...S1 2.55 Mu...S2 2.26 Mu...S3 2.45 Mu...S4 2.09	4322.80

Table 7.4 : Model systems and associated Mu...S distances and hyperfine coupling constants for the interstitial muonium atom.

None of the above systems have a value of A_{μ} which is within the error limits of the measured resonance for the interstitial muonium atom. It is apparent however that the value of A_{μ} is dependent on the distance of the muonium atom from the surrounding sulfur atoms. Smaller values for the hyperfine coupling constant are associated with shorter Mu...S distances. A model was therefore investigated where Mu was located at various points along the internuclear vector between two sulfur atoms in adjacent rings. The location of the model system within the unit cell is shown in Figure 7.5, and the results of the calculations are collated in Table 7.5.

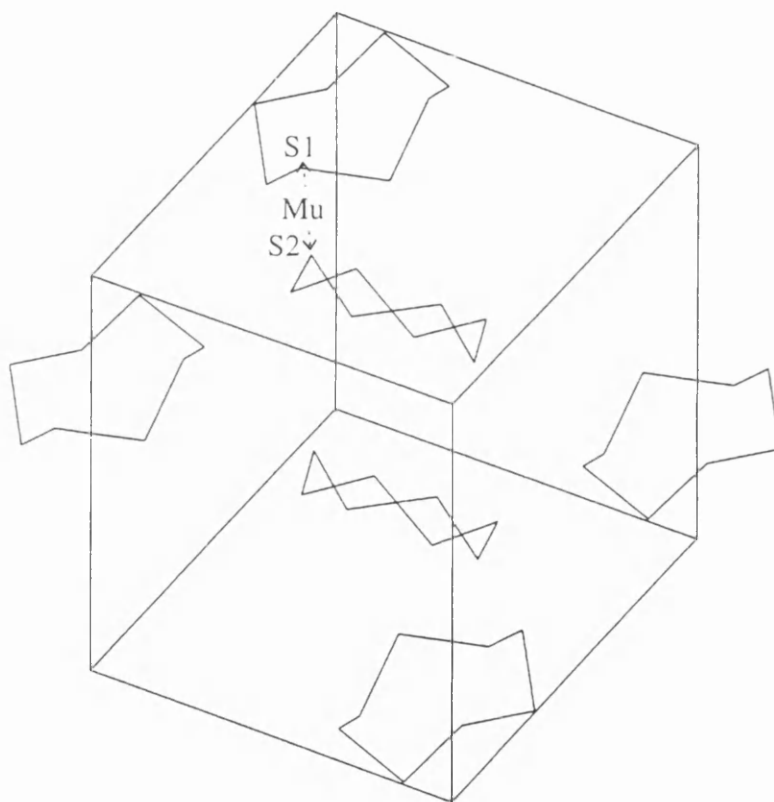


Figure 7.5 : Unit cell of γ -sulfur showing the position of the S...S internuclear vector for the interstitial muonium atom model.

Distance / Å		Energy / E _h	A _μ / MHz
Mu...S1	Mu...S2		
1.99	1.99	-6360.5794	4013.56
1.49	2.49	-6360.5658	2338.68
0.99	2.99	-6360.4470	439.71
0.49	3.49	-6358.1815	1240.21
2.49	1.49	-6360.5693	1653.87

Table 7.5 : The calculated energy and hyperfine coupling constant, A_{μ} , for various positions of the interstitial muonium atom.

When the muonium atom is at a distance of 1.49 Å from S1, A_{μ} has a value of 2339 MHz. It is possible that this is the system having a hyperfine coupling constant of 2000 ± 500 MHz observed in the μ SR experiment. However, the energy of the system lowers when the muonium atom is positioned mid-way between the two sulfur atoms. It is suggested therefore that the signal observed at 2000 ± 500 MHz is a vibrationally averaged value for Mu oscillating about the mid-point of an internuclear vector. Figure 7.6, which is a spline-fit to the calculated points, clearly shows how the value of A_{μ} rapidly decreases with distance from the mid-point of the internuclear vector.

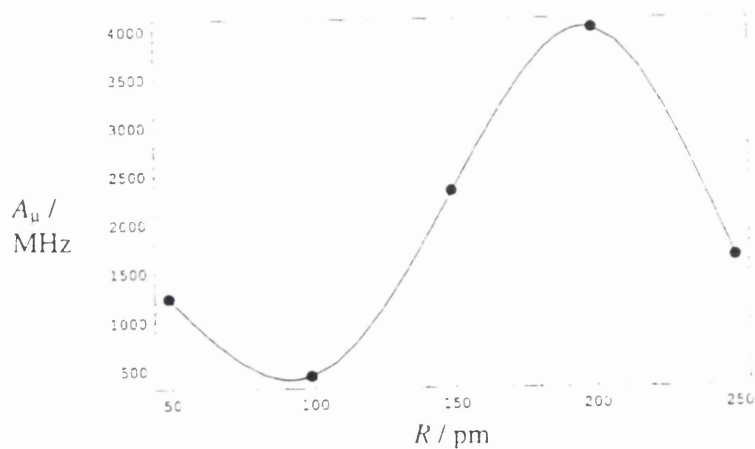


Figure 7.6 : Variation of A_{μ} with distance from S1 for the interstitial muonium atom in S₈.

7.4 Conclusions

The resonances observed by μ SR spectroscopy at 233 ± 5 MHz and 2000 ± 500 MHz are consistent with the hyperfine coupling constants calculated at the 6-31G** level for $[\text{SMu}]^+$, and an interstitial muonium atom vibrating about the midpoint of an S...S internuclear vector of length 4 Å, respectively.

Note on Units

Throughout this thesis the non-SI unit Ångström, Å, has been used instead of the SI unit of length, picometres. This approach was taken because the Ångström is the unit of length which is most widely used by the chemical community, both informally and in the literature. $1 \text{ Å} = 1 \times 10^{-10} \text{ m}$.

IUPAC approved values were used for the fundamental physical constants.¹³³

References

1. P. Debye, *Ann. Phys.*, 1915, **46**, 809.
2. P. Debye and P. Scherrer, *Zeit. Phys.*, 1918, **19**, 474.
3. W.L. Bragg, R.W. James and C.H. Bosanquet, *London, Edinburgh and Dublin Phil. Mag.*, 1922, **44**, 433.
4. R.F.W. Bader, R.J. Gillespie and P.J. MacDougall, *J. Am. Chem. Soc.*, 1988, **110**, 7329.
5. M.W. Schmidt, K.K. Baldrige, J.A. Boatz, S.T. Elbert, M.S. Gorgon, J.J. Jensen, S. Koseki, N. Matsunaga, K.A. Nyugen, S. Su, T.L. Windus, M Dupuis and J.A. Montgomery, *J. Comput. Chem.*, 1993, **14**, 1347.
6. M. Niederhut and B.M. Craven, *Acta Cryst. Section A*, 1996, **52**, C-347.
7. P.R. Mallinson, K. Wozniak and K.L. McCormack, *Acta Cryst. Section A*, 1996, **52**, C-347.
8. W.J. Hehre, L. Radom, P.v.R. Schleyer and J.A. Pople, *Ab Initio Molecular Orbital Theory*, Ch. 6 and references therein, John Wiley and Sons, New York, 1986.
9. V. Pichon-Pesme, C. Lecomte and H. Lachekar, *J. Phys. Chem.*, 1995, **99**, 6242.
10. P. Coppens in *International Tables for Crystallography*, Vol. B, Ch. 1.2, Kluwer Academic Publishers, Dordrecht, 1993.
11. W.L. Bragg and W.H. Bragg, *Proc. Roy. Soc. London (A)*, 1913, **89**, 248.
12. *International Tables for Crystallography*, Vol. IV, Table 2.2A. The Kynoch Press, Birmingham, 1974.
13. C. Giacovazzo in *Fundamentals of Crystallography*, Ch. 3, Ed. C. Giacovazzo, Oxford University Press, Oxford, 1992.

14. W.H. Bragg, *Proc. Phys. Soc.*, 1921, **33**, 304.
15. R.E. Franklin, *Acta Cryst.*, 1950, **3**, 107.
16. H.M. James and V.A. Johnson, *Phys. Rev.*, 1939, **56**, 119.
17. P. Coppens, T.N. Guru-Row, P. Leung, E.D. Stevens, P.J. Becker and Y.W. Yang, *Acta Cryst. Section A*, 1979, **35**, 63.
18. P. Coppens and D. Feil in *The Application of Charge Density Research to Chemistry and Drug Design*, Ch. 2, Eds. G.A. Jeffrey and J.F. Piniella, Plenum Press, New York, 1991.
19. R. McWeeney, *Acta Cryst.*, 1951, **4**, 513.
20. R. McWeeney, *Acta Cryst.*, 1952, **5**, 463.
21. R. McWeeney, *Acta Cryst.*, 1953, **6**, 631.
22. R. McWeeney, *Acta Cryst.*, 1954, **7**, 180.
23. B. Dawson, *Proc. Roy. Soc. London (A)*, 1967, **298**, 255.
24. B. Dawson, *Proc. Roy. Soc. London (A)*, 1967, **298**, 264.
25. R.F. Stewart, *J. Chem. Phys.*, 1969, **51**, 4569.
26. R.F. Stewart, *J. Chem. Phys.*, 1973, **58**, 1668.
27. N.K. Hansen and P. Coppens, *Acta Cryst. Section A*, 1978, **34**, 909.
28. T. Koritsanszky, S.T. Howard, T. Richter, P.R. Mallinson, Z. Su and N.K. Hansen, *XD. A Computer Program Package for Multipole Refinement and Analysis of Charge Densities from Diffraction Data*, 1995.
29. K. Kurki-Suonio, *Isr. J. Chem.*, 1977, **16**, 115.
30. S.T. Howard, personal communication.
31. K.L. McCormack, P.R. Mallinson, B.C. Webster and D.S. Yufit, *J. Chem. Soc. Faraday Trans.*, 1996, **92**, 1709.
32. B. Rees and A. Mitschler, *J. Am. Chem. Soc.*, 1976, **98**, 7918.
33. A. Mitschler, B. Rees and M.S. Lehmann, *J. Am. Chem. Soc.*, 1978, **100**, 3390.
34. F.H. Allen, O. Kennard, D.G. Watson, L. Brammer, A.G. Orpen and R. Taylor, *J. Chem. Soc. Perkin Trans. 2*, 1987, Suppl. 1.
35. R.H. Blessing and C. Lecompte in *The Application of Charge Density Research to Chemistry and Drug Design*, Ch. 7, Eds. G.A. Jeffrey and J.F. Piniella, Plenum Press, New York, 1991.

36. P. Coppens, *J. Phys. Chem.*, 1989, **93**, 7979
37. K. Angermund, K.H. Claus, R. Goddard and C. Krüger, *Angew. Chem.*, 1985, **24**, 237.
38. F.K. Larsen in *The Application of Charge Density Research to Chemistry and Drug Design*, Ch. 8, Eds. G.A. Jeffrey and J.F. Piniella, Plenum Press, New York, 1991.
39. G. DeTitta, *J. Appl. Cryst.*, 1985, **18**, 75.
40. R.H. Blessing, *J. Appl. Cryst.*, 1989, **22**, 396.
41. *International Tables for Crystallography*, Vol. III, Table 3.2.2A, The Kynoch Press, Birmingham, 1962.
42. B.J. Wuensch and C.T. Prewitt, *Z. Kristallogr.*, 1965, **122**, 24.
43. F.L. Hirshfeld, *Acta Cryst. Section A*, 1976, **32**, 239.
44. E. Schrödinger, *Ann. Phys.*, 1926, **79**, 361.
45. M. Born and J.R. Oppenheimer, *Ann. Phys.*, 1927, **84**, 457.
46. H. Essén, *Int. J. Quantum Chem.*, 1977, **12**, 721.
47. J.C. Slater, *Phys. Rev.*, 1929, **34**, 1293.
48. C.C.J. Roothaan, *Rev. Mod. Phys.*, 1951, **23**, 69.
49. G.G. Hall, *Proc. Roy. Soc. London (A)*, 1951, **205**, 541.
50. A.J. Duke, *Chem. Phys. Lett.*, 1973, **21**, 275.
51. J.C. Slater, *Phys. Rev.*, 1930, **36**, 57.
52. S.F. Boys, *Proc. Roy. Soc. London (A)*, 1950, **200**, 542.
53. S. Huzinaga, *J. Chem. Phys.*, 1965, **42**, 1293.
54. First row: W.J. Hehre, R.F. Stewart and J.A. Pople, *J. Chem. Phys.*, 1969, **51**, 2657.
 Second row: W.J. Hehre, R. Ditchfield, R.F. Stewart and J.A. Pople, *J. Chem. Phys.*, 1970, **52**, 2769.
 Third row main group: W.J. Pietro, B.A. Levi, W.J. Hehre and R.F. Stewart, *Inorg. Chem.*, 1980, **19**, 2225.
 Fourth row main group: W.J. Pietro, E.S. Blurock, R.F. Hout, W.J. Hehre, D.J. DeFrees and R.F. Stewart, *Inorg. Chem.*, 1981, **20**, 3650.
 First and second row transition metals: W.J. Pietro and W.J. Hehre, *J. Comput. Chem.*, 1983, **4**, 241.

55. T.H. Dunning, *J. Chem. Phys.*, 1970, **53**, 2823.
56. Carbon to fluorine: W.J. Hehre, R. Ditchfield and J.A. Pople, *J. Chem. Phys.*, 1972, **56**, 2257.
Beryllium: J.S. Binkley and J.A. Pople, *J. Chem. Phys.*, 1977, **66**, 879.
57. Carbon to fluorine: P.C. Hariharan and J.A. Pople, *Theor. Chim. Acta.*, 1973, **28**, 213.
Second row: M.M. Francl, W.J. Pietro, W.J. Hehre, J.S. Binkley, M.S. Gordon, D.J. DeFrees and J.A. Pople, *J. Chem. Phys.*, 1982, **77**, 3654.
58. http://wserv1.dl.ac.uk:800/emsl_pnl/basisform.html.
59. C.C.J. Roothaan, *Rev. Mod. Phys.*, 1960, **32**, 179.
60. J.A. Pople and R.K. Nesbet, *J. Chem. Phys.*, 1954, **22**, 571.
61. W.J. Hehre, L. Radom, P.v.R. Schleyer and J.A. Pople, *Ab Initio Molecular Orbital Theory*, Ch. 2, John Wiley and Sons, New York, 1986.
62. I.N. Levine, *Quantum Chemistry*, Ed. 4, Ch. 15, Prentice-Hall, New Jersey, 1991.
63. R.S. Mulliken, *J. Chem. Phys.*, 1955, **23**, 1833.
64. M.J. Ramos and B. Webster, *J. Chem. Soc. Faraday Trans. II*, 1983, **79**, 1389.
65. M.J. Ramos, *Experimental and Theoretical Studies on Isotopically Substituted Ethyl Radicals*, PhD Thesis, Glasgow, 1983.
66. R.F.W. Bader, *Atoms in Molecules: a Quantum Theory*, Oxford University Press, Oxford, 1990.
67. P. Coppens, Y.W. Yang, R.H. Blessing, W.F. Cooper and F.K. Larsen, *J. Am. Chem. Soc.*, 1977, **99**, 760.
68. C.C. Wang, Y.Y. Hong, C.H. Ueng and Y. Wang, *J. Chem. Soc. Dalton Trans.*, 1992, **23**, 3331.
69. Y. Wang, M.J. Chen and C.H. Wu, *Acta Cryst. Section B*, 1988, **44**, 179.
70. Y. Wang, S.Y. Wu and A.C. Cheng, *Acta Cryst. Section B*, 1990, **46**, 850.
71. Y. Wang, S.K. Yeh, S.Y. Wu, C.T. Pai, C.R. Lee and K.J. Lin, *Acta Cryst. Section B*, 1991, **47**, 298.
72. K.J. Lin and Y. Wang, *J. Phys. Chem.*, 1993, **97**, 3176.
73. A.S. Brown and V.H. Smith, *J. Chem. Phys.*, 1993, **99**, 1837.
74. T.H. Tang, R.F.W. Bader and P.J. MacDougall, *Inorg. Chem.*, 1985, **24**, 2047.

75. Z. Su and P. Coppens, *Acta Cryst. Section A*, 1996, **52**, C-344.
76. E.D. Stevens, M.L. DeLucia and P. Coppens, *Inorg. Chem.*, 1980, **19**, 813.
77. J.D. Korp and I. Bernal, *Tetrahedron Lett.*, 1981, **22**, 4767.
78. Enraf-Nonius, *CAD-4 Express*, Enraf-Nonius, Delft, The Netherlands, 1995.
79. F.W. Biegler-König, R.F.W. Bader and T.H. Tang, *J. Comput. Chem.*, 1982, **3**, 317.
80. A.C. Gallacher and A.A. Pinkerton, *Acta Cryst. Section C*, 1993, **49**, 125.
81. A. Hordvik, *Acta Chem. Scand.*, 1966, **20**, 1885.
82. The United Kingdom Chemical Database Service, D.A. Fletcher, R.F. McMeeking and D.J. Parkin, *Chem. Inf. Comput. Sci.*, 1996, **36**, 746.
83. 3D Search and Research using the Cambridge Structural Database, F.H. Allen and O. Kennard, *Chemical Design Automation News*, 1993, **8**, 1 & 31.
84. O. Knop, R.J. Boyd and S.C. Choi, *J. Am. Chem. Soc.*, 1988, **110**, 7299.
85. C.H. Bushweller, *J. Am. Chem. Soc.*, 1969, **91**, 6019.
86. I. Mayer, *J. Mol. Struct.*, 1987, **149**, 81.
87. D.G. Gilheany, *Chem. Rev.*, 1994, **94**, 1339.
88. C.G. Davies, R.J. Gillespie, J.J. Park and J. Passmore, *Inorg. Chem.*, 1971, **10**, 2781.
89. A. Bondi, *J. Phys. Chem.*, 1964, **68**, 441.
90. B. Beagley and K.T. McAloon, *Trans. Faraday Soc.*, 1971, **67**, 3216.
91. L. Pauling, *The Nature of the Chemical Bond*, Ed. 2, Ch. 2, Oxford University Press, Oxford, 1945.
92. M.J. Frisch, G.W. Trucks, H.B. Schlegel, P.M.W. Gill, B.G. Johnson, M.A. Robb, J.R. Cheesman, T. Keith, G.A. Petersson, J.A. Montgomery, K. Ravhachari, M.A. Al-Laham, V.G. Zakrzewski, J.V. Ortiz, J.B. Foresman, J. Cioslowski, B.B. Stefanov, A. Nanayakkara, M. Challacombe, C.Y. Peng, P.Y. Ayala, W. Chen, M.W. Wong, J.L. Andres, E.S. Replogle, R. Gomperts, R.L. Martin, D.J. Fox, J.S. Binkley, D.J. Defrees, J. Baker, J.P. Stewart, M. Head-Gordon, C. Gonzalez and J.A. Pople, GAUSSIAN 94, Revision C.3, Gaussian Inc., Pittsburgh PA, 1995.
93. A.D.U. Hardy, J.J. McKendrick, D.D. MacNicol and D.R. Wilson, *J. Chem. Soc. Perkin Trans. II*, 1979, 729.
94. D.D. MacNicol in *Inclusion Compounds*, Vol. 2, Ch. 5, p. 124, Eds. J.L. Atwood, J.E.D. Davies and D.D. MacNicol, Academic Press, London, 1984.

95. See for example Ref 94.
96. A.A. Freer, D.D. MacNicol, P.R. Mallinson and I. Vallance, *Tett. Lett.*, 1992, **33**, 261.
97. R.H. Barbour, A.A. Freer and D.D. MacNicol, *J. Chem. Soc. Chem. Commun.*, 1983, 362.
98. A.A. Freer, D.D. MacNicol, P.R. Mallinson and C.D. Robertson, *Tett. Lett.*, 1989, **30**, 5787.
99. G.A. Downing, C.S. Frampton, D.D. MacNicol and P.R. Mallinson, *Agnew. Chem. Int. Ed. Engl.*, 1994, **33**, 1587.
100. P.R. Mallinson, D.D. MacNicol, K.L. McCormack, D.S. Yufit, J.H. Gall and R.K. Henderson, *Acta Cryst. Section C*, 1997, **53**, 90.
101. I.C. Paul in *The Chemistry of the Thiol Group*, Part 1, Ch. 2, Ed. S. Patai, Wiley, London, 1974.
102. J.A. Platts, S.T. Howard and K. Wozniak, *J. Chem. Soc. Chem. Commun.*, 1996, 63.
103. P.G. Sennikov, *J. Phys. Chem.*, 1994, **98**, 4973.
104. *SMART - Siemens Molecular Analysis Research Tool*, V4.050, Copyright 1989 - 95, Siemens Analytical X-ray Instruments.
105. F. Takusagawa, T.F. Koetzle, W.W.H. Kou and R. Parthasarathy, *Acta Cryst. Section B*, 1981, **37**, 1591.
106. *SAINTE - SAXI Area-detector Integration*, V4.050, Copyright 1992 - 95, Siemens Analytical X-ray Instruments.
107. *XPREP- Data Preparation and Reciprocal Space Exploration*, Ver. 5.04, Copyright 1995, Siemens Analytical X-ray Instruments.
108. G.M. Sheldrick, 1996, University of Göttingen, Germany.
109. P.R. Mallinson and K. W. Muir, *J. Appl. Cryst.*, 1985, **18**, 51.
110. J.A. Platts, S.T. Howard and B.R.F. Bracke, *J. Am. Chem. Soc.*, 1996, **118**, 2726.
111. R. Bolotovskiy, M.A. White, A. Darovskiy and P. Coppens, *J. Appl. Cryst.*, 1995, **28**, 86.
112. D.R. Walters, *Mycol. Res.*, 1995, **99**, 129.
113. B. Ganem, *Acc. Chem. Res.*, 1982, **15**, 290.
114. N.D. Havis, D.R. Walters, S.A. Foster, W.P. Martin, F.M. Cook and D.J. Robins, *Pestic. Sci.*, 1994, **41**, 61.

115. N.D. Havis, D.R. Walters, W.P. Martin, F.M. Cook and D.J. Robins, *Pestic. Sci.*, 1994, **41**, 71.
116. C.W. Porter and J.R. Suffrin, *Anticancer. Res.*, 1986, **6**, 525.
117. A.E. Cohen, J.R. Ruble and B.M. Craven, *Acta Cryst. Section A*, 1996, **52**, C-261.
118. G.M. Sheldrick, SHELXS86, *Program for the Solution of Crystal Structures*, University of Göttingen, Germany, 1985
119. G.M. Sheldrick, SHELXL93, *Program for Crystal Structure Refinement*, University of Göttingen, Germany, 1993.
120. G.T. Smith, *The Electron Density: Experimental Determination and Theoretical Analysis*, PhD Thesis, Durham, 1997.
121. S. Besley, P.M. Cullis, R. Partridge, M.C.R. Symons and R.T. Wheelhouse, *Chem. Phys. Lett.*, 1990, **165**, 120.
122. D.C. Walker, *Muon and Muonium Chemistry*, Ch. 3, Cambridge University Press, Cambridge, 1983.
123. B.C. Webster, *Annu. Rep. Prog. Chem. Section C*, 1984, **81**, 3.
124. E. Roduner, *The Positive Muon as a Probe in Free Radical Chemistry*, Springer-Verlag, Berlin, 1988.
125. A. Schenck, *Muon Spin Rotation Spectroscopy: Principles and Applications in Solid State Physics*, Hilger, Bristol, 1985.
126. M. Heming, E. Roduner, B.D. Patterson, W. Odermatt, J. Schneider, H. Baumeler, H. Keller and I.M. Savic, *Chem. Phys. Lett.*, 1986, **128**, 100.
127. P.W. Atkins, *Physical Chemistry*, Ed. 4, Ch. 18, Oxford University Press, Oxford, 1990.
128. S.F.J. Cox, S.P. Cottrell, G.A. Hopkins, M. Kay and F.L. Pratt, *Hyperfine Interact.*, in press.
129. S.F.J. Cox, I.D. Reid, K.L. McCormack and B.C. Webster, *Chem. Phys. Lett.*, to be published.
130. D. Buttar and B.C. Webster, *J. Chem. Soc. Faraday Trans.*, 1991, **87**, 2901.
131. T.A. Claxton, *Chem. Soc. Rev.*, 1995, **24**, 437.
132. S.H. Ashworth and J.M. Brown, *J. Mol. Spectrosc.*, 1992, **153**, 41.
133. I. Mills, T. Cvitas, K. Homann, N. Kallay and K. Kuchitsu, *Quantities, Units and Symbols in Physical Chemistry*, Ed. 2, Blackwell Scientific Publications, Oxford, 1993.

Appendix A

Supplementary Data for 3,3,6,6-Tetramethyl-s-tetrathiane

A1. Fractional atomic coordinates

Atom	x/a	y/b	z/c
S1	0.49128(2)	0.65364(2)	0.20089(1)
C1	0.37618(4)	0.62592(4)	0.12500
C2	0.39892(7)	0.48924(5)	0.09927(4)
H1	0.49064	0.48279	0.07381
H2	0.39531	0.43089	0.14760
H3	0.32217	0.46906	0.06218

A2. Mean-square atomic displacements / Å²

The form of the anisotropic temperature factor is : $\exp \left[-2\pi^2 \sum_{i=1}^3 \sum_{j=1}^3 U_{ij} h_i h_j a_i^* a_j^* \right]$

Atom	U_{11}	U_{22}	U_{33}	U_{12}	U_{13}	U_{23}
S1	0.0172(1)	0.0131(1)	0.0110(1)	-.0012(0)	-.0023(0)	0.0023(0)
C1	0.0142(1)	0.0142(1)	0.0125(2)	-.0022(2)	-.0007(1)	0.0007(1)
C2	0.0332(3)	0.0145(2)	0.0214(2)	-.0029(2)	-.0046(2)	-.0027(2)
H1	0.24					
H2	0.46					
H3	0.39					

A3. Multipole population coefficients

Atom	P_v	P_{00}	P_{11}	P_{1-1}	P_{10}
S1	6.28(5)	0.00(0)	-0.01(1)	0.04(1)	-0.03(1)
C1	1.95(4)	0.00(0)	0.00(0)	0.00(0)	0.02(2)
C2	4.21(7)	0.00(0)	-0.13(3)	0.01(3)	0.14(4)
H1	0.85(4)	0.00(0)	0.04(2)	0.00(0)	0.00(0)
H2	0.98(5)	0.00(0)	0.23(2)	0.00(0)	0.00(0)
H3	0.74(4)	0.00(0)	0.05(2)	0.00(0)	0.00(0)

Atom	P_{20}	P_{21}	P_{2-1}	P_{22}	P_{2-2}
S1	0.09(1)	-0.15(2)	-0.08(1)	0.01(1)	0.03(1)
C1	-0.01(2)	0.00(0)	0.00(0)	-0.05(2)	-0.04(2)
C2	-0.02(3)	-0.05(3)	-0.08(3)	-0.07(3)	-0.09(3)

Atom	P_{30}	P_{31}	P_{3-1}	P_{32}	P_{3-2}	P_{33}	P_{3-3}
S1	0.02(1)	-0.03(1)	0.01(1)	0.05(1)	-0.05(1)	0.15(2)	0.04(1)
C1	-0.03(2)	0.00(0)	0.00(0)	-0.18(2)	-0.03(2)	0.00(0)	0.00(0)
C2	0.04(3)	-0.26(3)	-0.15(3)	0.02(2)	0.05(3)	0.24(3)	-0.01(2)

Atom	P_{40}	P_{41}	P_{4-1}	P_{42}	P_{4-2}	P_{43}	P_{4-3}	P_{44}	P_{4-4}
S1	-0.01(2)	0.00(1)	0.00(1)	0.02(2)	0.02(2)	-0.02(2)	-0.04(2)	0.05(2)	0.02(1)
C1	0.00(2)	0.00(0)	0.00(0)	0.03(2)	0.05(3)	0.00(0)	0.00(0)	0.04(2)	0.01(2)
C2	-0.02(3)	-0.06(3)	-0.11(3)	-0.09(3)	0.13(3)	0.14(3)	0.02(3)	0.06(3)	0.06(3)

A4. Local coordinate systems

ATOM	ATOM0	AX1	ATOM1	ATOM2	AX2	R/L
S1	C1	X	S1	C2	Y	R
C1	DUM0	Z	C1	S1	X	R
C2	C1	X	C2	H1	Y	R
H1	C2	X	H1	H2	Y	R
H2	C2	X	H2	H3	Y	R
H3	C2	X	H3	H1	Y	R

DUM0 0.28000 0.5300 0.125000

Appendix B

Supplementary Data for Hexakis(mercaptomethyl)benzene

B1. Fractional atomic coordinates

Atom	x/a	y/b	z/c
S1	0.12756(2)	0.42627(2)	-0.00861(5)
C1	0.25638(4)	0.57150(4)	-0.33383(13)
C2	0.17435(5)	0.46934(4)	-0.33241(14)
H21	0.11488	0.46340	-0.43776
H22	0.19658	0.42312	-0.41544
H1	0.21137	0.45158	0.10540

B2. Mean-square atomic displacements / Å²

The form of the anisotropic temperature factor is : $\exp \left[-2\pi^2 \sum_{i=1}^3 \sum_{j=1}^3 U_{ij} h_i h_j a_i^* a_j^* \right]$

Atom	U_{11}	U_{22}	U_{33}	U_{12}	U_{13}	U_{23}
S1	0.0187(1)	0.0150(1)	0.0197(1)	0.0066(1)	0.0029(1)	0.0030(1)
C1	0.0100(2)	0.0096(2)	0.0169(2)	0.0046(2)	0.0001(2)	0.0001(2)
C2	0.0119(2)	0.0106(2)	0.0184(3)	0.0044(2)	-0.0001(2)	-0.0008(2)
H21	0.020					
H22	0.021					
H1	0.048					

B3. Multipole population coefficients

Atom	P_s	P_{00}	P_{11}	P_{1-1}	P_{10}
S1	5.63(5)	0.00(0)	0.02(1)	0.00(1)	0.00(1)
C1	4.20(4)	0.00(0)	0.01(4)	0.03(5)	0.05(2)
C2	4.41(7)	0.00(0)	0.03(2)	0.03(3)	0.00(3)
H21	0.89(4)	0.00(0)	0.00(0)	0.00(0)	0.09(2)
H22	0.93(4)	0.00(0)	0.00(0)	0.00(0)	0.13(2)
H1	0.93(2)	0.00(0)	0.00(0)	0.00(0)	0.17(2)

Atom	P_{20}	P_{21}	P_{2-1}	P_{22}	P_{2-2}
S1	-0.05(2)	0.02(2)	-0.11(2)	0.01(2)	0.16(2)
C1	0.03(2)	0.03(3)	-0.03(4)	-0.06(2)	0.14(2)
C2	0.06(3)	-0.01(2)	0.00(2)	-0.04(3)	-0.06(2)

Atom	P_{30}	P_{31}	P_{3-1}	P_{32}	P_{3-2}	P_{33}	P_{3-3}
S1	0.08(2)	0.05(1)	-0.03(1)	0.09(1)	0.00(2)	0.00(1)	-0.02(1)
C1	0.32(3)	0.00(4)	-0.05(5)	0.08(2)	-0.16(2)	-0.01(4)	-0.02(4)
C2	0.26(3)	0.04(3)	0.03(2)	-0.01(3)	-0.01(2)	-0.03(3)	-0.25(3)

Atom	P_{40}	P_{41}	P_{4-1}	P_{42}	P_{4-2}	P_{43}	P_{4-3}	P_{44}	P_{4-4}
S1	0.07(2)	-0.03(2)	0.04(2)	0.05(2)	0.05(2)	0.10(2)	0.08(2)	-0.05(2)	0.01(2)
C1	0.00(0)	0.00(0)	0.00(0)	0.00(0)	0.00(0)	0.00(0)	0.00(0)	0.00(0)	0.00(0)
C2	0.00(0)	0.00(0)	0.00(0)	0.00(0)	0.00(0)	0.00(0)	0.00(0)	0.00(0)	0.00(0)

B4. Local coordinate systems

ATOM	ATOM0	AX1	ATOM1	ATOM2	AX2	R/L
S1	H1	Z	S1	C2	Y	R
C1	C2	Z	C1	H21	Y	R
C2	H22	Z	C2	H21	Y	R
H21	C2	Z	H21	H22	Y	R
H22	C2	Z	H22	H21	Y	R
H1	S1	Z	H1	C2	Y	R

Appendix C

Supplementary Data for

E-Tetraethyl-1,4-diammoniumbut-2-ene. $2PF_6$

C1. Fractional atomic coordinates

Atom	x/a	y/b	z/c
P1	-0.54040(2)	0.32589(1)	0.81703(1)
F1	-0.5598(4)	0.4123(3)	0.7306(2)
F2	-0.28358(19)	0.32999(14)	0.82658(14)
F3	-0.5454(3)	0.2391(2)	0.7293(2)
F4	-0.80117(19)	0.31994(14)	0.80455(13)
F5	-0.5399(3)	0.4124(2)	0.9030(2)
F6	-0.5249(4)	0.2415(2)	0.9055(3)
N1	0.03394(14)	0.15113(7)	0.66671(7)
C1	0.02006(13)	0.00150(7)	0.55129(6)
C2	0.16022(12)	0.08027(6)	0.60768(7)
C3	-0.07967(15)	0.09909(7)	0.74585(8)
C4	0.0703(2)	0.0368(1)	0.8213(1)
C5	-0.12225(14)	0.21602(7)	0.59781(7)
C6	-0.01186(18)	0.28627(8)	0.53094(8)
H1N	0.14435	0.20155	0.70358
H1	-0.05209	-0.05110	0.59754
H21	0.23463	0.12926	0.55878
H22	0.28646	0.04835	0.66073
H31	-0.15134	0.16106	0.78016
H32	-0.20143	0.05363	0.70350
H41	0.20279	0.08011	0.85740
H42	0.13769	-0.02473	0.78432
H43	-0.01908	0.01506	0.88103
H51	-0.20150	0.25920	0.64985
H52	-0.23562	0.16643	0.55539
H61	0.11609	0.32818	0.57311
H62	0.05942	0.24735	0.47317
H63	-0.14250	0.33166	0.49627

C2. Mean-square atomic displacements / Å²

The form of the anisotropic temperature factor is : $\exp \left[-2\pi^2 \sum_{i=1}^3 \sum_{j=1}^3 U_{ij} h_i h_j a_i^* a_j^* \right]$

Atom	U_{11}	U_{22}	U_{33}	U_{12}	U_{13}	U_{23}
P1	0.0106(1)	0.0150(1)	0.0185(1)	-0.0016(1)	0.0024(1)	-0.0044(1)
F1	0.0299(8)	0.0390(10)	0.0404(10)	0.0002(8)	0.0048(8)	0.0155(9)
F2	0.0104(4)	0.0268(6)	0.0341(7)	-0.0034(4)	0.0025(4)	-0.0107(6)
F3	0.0141(5)	0.0388(8)	0.0490(9)	-0.0043(6)	0.0075(6)	-0.0308(8)
F4	0.0107(4)	0.0294(6)	0.0311(6)	-0.0021(4)	0.0051(4)	-0.0134(6)
F5	0.0236(7)	0.0420(9)	0.0405(9)	-0.0098(7)	0.0125(7)	-0.0260(9)
F6	0.032(1)	0.048(1)	0.043(1)	-0.012(1)	-0.004(1)	0.021(1)
N1	0.0137(3)	0.0120(3)	0.0143(4)	-0.0006(2)	0.0022(3)	-0.0030(2)
C1	0.0152(3)	0.0119(3)	0.0138(3)	-0.0015(2)	0.0028(3)	-0.0017(3)
C2	0.0119(3)	0.0145(3)	0.0169(3)	-0.0006(2)	0.0027(2)	-0.0038(3)
C3	0.0207(3)	0.0165(3)	0.0180(4)	-0.0007(3)	0.0071(3)	-0.0011(3)
C4	0.0371(5)	0.0198(4)	0.0208(4)	0.0040(4)	0.0057(4)	.0032(4)
C5	0.0167(3)	0.0165(3)	0.0184(4)	0.0024(3)	0.0031(3)	-0.0008(3)
C6	0.0287(4)	0.0195(4)	0.0195(4)	-0.0006(4)	0.0038(3)	0.0024(3)
H1N	0.022					
H1	0.030					
H21	0.034					
H22	0.021					
H31	0.025					
H32	0.015					
H41	0.031					
H42	0.039					
H43	0.042					
H51	0.021					
H52	0.025					
H61	0.053					
H62	0.034					
H63	0.051					

C3. Multipole population coefficients

Atom	P_{γ}	P_{00}	P_{11}	P_{1-1}	P_{10}
P1	4.41(15)	0.00(0)	0.06(4)	0.07(4)	0.01(4)
F1	7.14(4)	0.00(0)	0.06(4)	-0.48(6)	0.24(4)
F2	7.37(3)	0.00(0)	0.04(3)	-0.05(3)	0.06(2)
F3	7.38(4)	0.00(0)	0.04(3)	0.14(5)	0.20(3)
F4	7.35(3)	0.00(0)	-0.01(3)	0.05(3)	0.04(2)
F5	7.16(4)	0.00(0)	0.01(3)	-0.01(5)	0.19(3)
F6	7.19(5)	0.00(0)	0.08(4)	-0.16(6)	0.23(5)
N1	5.04(10)	0.00(0)	0.01(3)	0.06(3)	0.09(3)
C1	4.25(7)	0.00(0)	0.02(4)	-0.11(4)	0.05(5)
C2	4.34(8)	0.00(0)	-0.06(4)	0.08(4)	0.11(4)
C3	4.33(9)	0.00(0)	-0.10(4)	0.12(4)	0.01(4)
C4	4.58(8)	0.00(0)	0.17(4)	0.08(4)	0.14(4)
C5	4.44(8)	0.00(0)	-0.02(4)	0.15(4)	0.18(4)
C6	4.59(8)	0.00(0)	-0.09(4)	-0.01(4)	0.09(4)
H1N	0.67(5)	0.00(0)	0.00(0)	0.00(0)	0.14(2)
H1	0.76(4)	0.00(0)	0.00(0)	0.00(0)	0.08(2)
H21	0.78(4)	0.00(0)	0.00(0)	0.00(0)	0.13(2)
H22	0.72(4)	0.00(0)	0.00(0)	0.00(0)	0.09(2)
H31	0.76(4)	0.00(0)	0.00(0)	0.00(0)	0.12(2)
H32	0.71(4)	0.00(0)	0.00(0)	0.00(0)	0.04(2)
H41	0.67(5)	0.00(0)	0.00(0)	0.00(0)	0.05(2)
H42	0.80(5)	0.00(0)	0.00(0)	0.00(0)	0.10(3)
H43	0.76(5)	0.00(0)	0.00(0)	0.00(0)	0.07(3)
H51	0.64(4)	0.00(0)	0.00(0)	0.00(0)	0.01(2)
H52	0.74(4)	0.00(0)	0.00(0)	0.00(0)	0.09(2)
H61	0.81(5)	0.00(0)	0.00(0)	0.00(0)	0.10(3)
H62	0.74(5)	0.00(0)	0.00(0)	0.00(0)	0.04(3)
H63	0.89(5)	0.00(0)	0.00(0)	0.00(0)	0.19(3)

Atom	P_{20}	P_{21}	$P_{2,j}$	P_{22}	$P_{2,2}$
P1	0.21(6)	-0.04(3)	0.06(3)	-0.13(4)	0.16(5)
F1	-0.20(5)	-0.04(4)	-0.01(5)	-0.09(5)	-0.26(5)
F2	-0.04(3)	0.01(3)	-0.07(3)	0.07(4)	-0.11(3)
F3	-0.05(4)	0.04(3)	0.00(5)	0.08(4)	0.07(4)
F4	-0.05(3)	-0.04(3)	-0.05(3)	0.01(4)	0.04(3)
F5	-0.18(5)	-0.09(3)	0.05(5)	-0.18(4)	-0.18(5)
F6	-0.23(6)	-0.04(4)	-0.14(6)	0.00(6)	0.10(6)
N1	0.01(3)	-0.01(2)	0.00(2)	0.00(3)	0.01(3)
C1	0.21(4)	0.01(3)	0.07(3)	-0.18(3)	-0.02(4)
C2	0.10(3)	-0.03(3)	-0.03(3)	-0.10(3)	0.06(3)
C3	0.06(4)	-0.03(3)	-0.03(3)	-0.19(4)	0.06(3)
C4	0.02(4)	-0.03(3)	-0.02(3)	-0.02(4)	-0.01(4)
C5	0.20(3)	-0.13(3)	0.00(3)	-0.14(4)	-0.10(3)
C6	0.11(4)	-0.03(3)	0.04(3)	0.08(4)	0.02(3)

Atom	P_{30}	P_{31}	$P_{3,j}$	P_{32}	$P_{3,2}$	P_{33}	$P_{3,3}$
P1	-0.05(5)	-0.06(4)	-0.13(4)	-0.04(3)	-0.01(3)	-0.14(4)	0.00(3)
F1	-0.19(2)	-0.03(2)	0.13(2)	-0.17(2)	-0.15(2)	-0.14(2)	0.07(2)
F2	-0.02(1)	0.00(1)	0.03(2)	-0.03(2)	-0.03(1)	0.04(2)	0.01(2)
F3	-0.13(2)	-0.01(1)	-0.04(2)	-0.11(2)	0.03(2)	-0.05(2)	-0.09(2)
F4	-0.05(1)	0.02(1)	0.01(2)	-0.05(2)	0.03(1)	0.03(2)	-0.03(2)
F5	-0.27(2)	0.01(2)	-0.03(2)	-0.28(2)	0.01(2)	-0.05(2)	-0.04(2)
F6	-0.23(2)	0.01(2)	0.07(2)	-0.19(2)	0.05(2)	-0.07(2)	-0.01(2)
N1	0.29(4)	-0.03(2)	0.03(2)	0.04(2)	0.00(2)	-0.03(3)	-0.15(3)
C1	0.37(3)	0.08(2)	-0.07(4)	0.21(3)	0.02(3)	-0.02(3)	-0.06(3)
C2	0.41(4)	-0.13(3)	0.03(3)	0.05(3)	-0.02(3)	0.04(3)	-0.31(3)
C3	0.37(4)	-0.14(3)	-0.02(3)	0.02(3)	-0.06(3)	0.02(3)	-0.21(4)
C4	0.39(4)	0.01(3)	0.03(3)	0.01(3)	-0.11(3)	0.00(3)	-0.23(3)
C5	0.38(4)	0.10(3)	0.08(3)	0.04(3)	0.01(3)	-0.08(3)	-0.22(4)
C6	0.35(4)	0.04(3)	0.03(2)	-0.13(3)	0.08(3)	0.18(3)	-0.27(3)

Atom	P_{40}	P_{41}	P_{41}	P_{42}	P_{42}	P_{43}	P_{43}	P_{44}	P_{44}
P1	0.43(7)	0.13(4)	0.02(5)	-0.08(4)	0.17(4)	-0.01(4)	0.10(3)	-0.29(4)	-0.27(5)
F1	-0.15(3)	-0.01(2)	0.05(3)	-0.02(3)	0.01(3)	-0.10(3)	0.03(3)	0.01(3)	0.03(3)
F2	-0.08(2)	-0.01(2)	-0.04(2)	-0.01(2)	0.04(2)	0.01(2)	0.04(2)	-0.11(2)	-0.01(2)
F3	-0.17(2)	-0.01(2)	-0.02(3)	-0.04(3)	-0.04(2)	0.04(2)	-0.03(3)	-0.03(3)	0.01(2)
F4	-0.13(2)	0.02(2)	-0.03(2)	-0.02(2)	-0.02(2)	0.00(2)	0.03(2)	-0.16(2)	0.00(2)
F5	-0.15(3)	0.00(2)	-0.06(3)	-0.01(3)	0.10(2)	0.00(3)	-0.07(3)	0.01(3)	0.07(3)
F6	-0.14(3)	-0.01(2)	0.07(3)	-0.03(3)	-0.04(3)	-0.06(3)	0.05(3)	-0.04(3)	0.05(3)
N1	0.09(3)	0.02(2)	0.05(2)	-0.05(3)	-0.08(3)	0.08(3)	0.01(3)	0.07(3)	-0.03(3)
C1	-0.04(4)	0.03(3)	-0.07(4)	0.02(3)	0.04(3)	0.02(4)	0.04(3)	0.09(3)	-0.03(4)
C2	0.12(4)	-0.04(3)	0.08(3)	-0.04(3)	0.08(3)	0.04(3)	0.13(4)	-0.04(3)	-0.04(3)
C3	0.05(4)	0.02(3)	0.07(3)	0.06(3)	-0.02(3)	-0.05(3)	0.07(4)	-0.04(4)	-0.01(4)
C4	-0.04(4)	-0.10(3)	-0.06(3)	0.00(3)	-0.05(3)	0.05(3)	0.13(3)	0.00(3)	-0.10(3)
C5	0.13(4)	-0.06(3)	0.07(3)	-0.04(3)	0.03(3)	0.06(3)	0.09(4)	0.00(4)	0.10(4)
C6	0.03(4)	-0.01(3)	0.02(3)	0.06(3)	0.06(3)	-0.17(3)	0.16(3)	0.02(3)	0.08(3)

C4. Local coordinate systems

ATOM	ATOM0	AX1	ATOM1	ATOM2	AX2	R/L
P1	F6	Z	P1	F1	Y	R
F1	P1	Z	F1	F5	Y	R
F2	P1	Z	F2	F1	Y	R
F3	P1	Z	F3	F6	Y	R
F4	P1	Z	F4	F6	Y	R
F5	P1	Z	F5	F1	Y	R
F6	P1	Z	F6	F5	Y	R
N1	H1N	Z	N1	C3	Y	R
C1	H1	Z	C1	C2	Y	R
C2	H21	Z	C2	H22	Y	R
C3	H31	Z	C3	H32	Y	R
C4	H41	Z	C4	H42	Y	R
C5	H51	Z	C5	H52	Y	R
C6	H62	Z	C6	H63	Y	R
H1N	N1	Z	H1N	C5	Y	R
H22	C2	Z	H22	H21	Y	R
H31	C3	Z	H31	H32	Y	R
H32	C3	Z	H32	H31	Y	R
H41	C4	Z	H41	H42	Y	R
H42	C4	Z	H42	H41	Y	R
H43	C4	Z	H43	H41	Y	R
H51	C5	Z	H51	H52	Y	R
H52	C5	Z	H52	H51	Y	R
H61	C6	Z	H61	H62	Y	R
H62	C6	Z	H62	H61	Y	R
H63	C6	Z	H63	H62	Y	R

Publications

1. Experimental and Theoretical Studies of the Charge Density Distribution in 3,3,6,6-Tetramethyl-s-tetrathiane.

Kirsty L. McCormack, Paul R. Mallinson, Brian C. Webster and Dmitrii S. Yufit, *J. Chem. Soc. Faraday Trans.*, 1996, **92**, 1709.

2. Hexakis(mercaptomethyl)benzene: a Structure Possessing Well Ordered Homodromic [SH...S]₆ Interactions

Paul R. Mallinson, David D. MacNicol, Kirsty L. McCormack, Dmitrii S. Yufit, James H. Gall and R. Keith Henderson, *Acta Cryst. Section C*, 1997, **53**, 90.

3. Experimental and Theoretical Studies of the Charge Density Distribution in *E*-Tetraethyl-1,4-diammoniumbut-2-ene.2PF₆.

Kirsty L. McCormack, Paul R. Mallinson, Brian C. Webster, Dmitrii S. Yufit, Lindsay A. Slater and David J. Robins, *Acta Cryst. Section B*, 1997, **53**, 181.

4. A Charge Density Analysis of Cationic and Anionic Hydrogen Bonds in a "Proton Sponge" Complex.

Paul R. Mallinson, Krzysztof Wozniak, Garry T. Smith and Kirsty L. McCormack, submitted to *J. Am. Chem. Soc.*

5. Muonium Radical Formation in Elemental Sulphur.

Stephen F.J. Cox, Ivan D. Reid, Kirsty L. McCormack and Brian C. Webster, *Chem. Phys. Lett.*, in press.

6. Paramagnetic States in Elemental Sulphur.

Brian C. Webster, Kirsty L. McCormack and Roderick M. Macrae, submitted to *J. Chem. Soc. Faraday Trans.*

Experimental and theoretical studies of the charge-density distribution in 3,3,6,6-tetramethyl-S-tetrathiane

Kirsty L. McCormack, Paul R. Mallinson,* Brian C. Webster and Dmitrii S. Yufit

Chemistry Department, University of Glasgow, Glasgow, UK G12 8QQ

A multipole model of the charge-density distribution in a ring containing C—S and S—S bonds has been obtained using high-resolution X-ray diffraction data from a single crystal of 3,3,6,6-tetramethyl-S-tetrathiane. Analysis of the bond critical points in both experimental and *ab initio* densities suggests a sulfur-sulfur bond order only slightly greater than unity. For isolated molecules, *ab initio* geometry optimisations predict a small energy stabilisation of the chair conformer relative to the twist-boat conformer observed in the crystalline state.

There have been relatively few experimental electron-density studies of molecules containing S—S bonds. Of those that exist, the treatment has been in terms of a deformation density analysis. Coppens *et al.*¹ performed an X-N study of cyclic octasulfur, S₈, for comparison with charge distributions in more complex systems containing S—S bonds. The sulfur lone pairs were shown to be mostly of p character. Wang *et al.*² conducted a multipole refinement study of S₇NH. This is a crown-shaped molecule, similar in many features, including structure, to S₈. A series of experimental and theoretical studies have been performed on thiathiophthene derivatives.^{3–6} These molecules contain a linear S—S—S part which was shown to have an electron-density distribution consistent with a three-centre four-electron bond.

Limited information can be drawn from deformation density analyses. Earlier work³ showed the deformation density between sulfur atoms to be small. However, a topological analysis of the charge density provides direct information about the one-electron properties of a molecule. While *ab initio* molecular orbital studies have been made of the topology of S—S bonds in various environments^{7,8} no experimental treatments of this type appear to have been made.

An experimental study of 3,3,6,6-tetramethyl-S-tetrathiane (**1**) has been undertaken to promote further understanding of the S—S bond in terms of its one-electron properties. Korp and Bernal⁹ noted in a crystal-structure analysis of **1** that the S—S distance of 2.015(1) Å was short for a single bond, possibly due to a degree of dπ–pπ double bonding. We will address this question in terms of the results of topological analyses of both experimental and *ab initio* distributions of the molecular charge density. The experimental results reported here were obtained from a multipole model of the crystalline charge density fitted to high-resolution X-ray diffraction data.

Experimental

Crystals of [(CH₃)₂CS₂]₂ are colourless octahedra. Single-crystal, high-resolution, low-temperature X-ray diffraction data were collected using the same equipment and procedure as described in an earlier paper.¹⁰ Data reduction was performed with the DREAM program package.¹¹ The intensities of standard reflections were fitted to cubic polynomials, which were used for scaling the data. A correction for absorption by the crystal was made using ABSORB,¹² but no correction was made for thermal diffuse scattering. Crystal data and other experimental details are given in Table 1.

For the molecular geometry found in the crystal, *ab initio* molecular orbital (MO) calculations were performed using the GAMESS program.¹³ The calculation of the wavefunction of

1 was carried out using a 6-311G** basis set. The critical-point analysis was carried out using the AIMPAC suite of programs.¹⁴ For the experimental charge distribution, the critical-point information and Laplacian maps were obtained using the program XDPROP in the XD package.¹⁵

Multipole refinement

The crystal structure was determined previously.⁹ The space group requires the molecule in the crystal to have point symmetry *D*₂, lying along the diagonal two-fold axis of the unit cell with C(1) in a special position having fractional coordinates (*x*, 1/4 + *x*, 1/8). The refinement minimised the function $\sum w(|F_0| - K|F_c|)^2$, where $w = 1/\sigma^2(F) = 4F^2/\sigma^2(F^2)$; $\sigma^2(F^2) = \sigma_{\text{counting}}^2(F^2) + P^2F^4$, *F*₀, *F*_{*c*} are the observed and calculated structure factors respectively; *K* is a scale factor, and

Table 1 Experimental data for 3,3,6,6-tetramethyl-S-tetrathiane

formula	[(CH ₃) ₂ CS ₂] ₂
formula weight	212.40
space group (tetragonal)	I4 ₁ /acd
temperature/K	100 (1)
unit-cell dimensions/Å:	
<i>a</i>	10.452 (1)
<i>c</i>	18.069 (2)
<i>V</i> /Å ³	1973.9 (3)
<i>Z</i>	8
<i>D</i> _c /g cm ⁻³	1.43
crystal dimensions/mm	0.22 × 0.16 × 0.16
absorption coefficient/cm ⁻¹	8.60
range of corrections for absorption	0.896–0.907
radiation	Mo-Kα; λ = 0.7107 Å
scan type	θ–2θ
$\left(\frac{\sin \theta}{\lambda}\right)_{\text{max}}/\text{Å}^{-1}$	1.22
(<i>hkl</i>) lower limit–upper limit	–8 22; –8 25; –13 43
no. standard reflections	3 (1 3 2, $\bar{3}$ $\bar{1}$ $\bar{2}$, 0 $\bar{2}$)
no. reflections measured	11829
no. symmetry-independent reflections	2759
no. <i>I</i> > 2σ(<i>I</i>) reflections	1819
agreement factor $R = \sum I - \bar{I} /\sum I$	0.020
refined on	<i>F</i>
<i>R</i>	0.0226
<i>R</i> _w	0.0208
<i>S</i>	1.1320
no. variables	104
weighting scheme	$w = \frac{1}{\sigma^2(F)} = \frac{4F^2}{\sigma^2(F^2)}$ $\sigma^2(F^2) = \sigma_{\text{counting}}^2(F^2) + P^2F^4$

σ^2 denotes a variance. The instrumental instability factor P was estimated from errors in the time-dependent scaling polynomials and the fluctuations of the standards. Anisotropic temperature factors were used to describe the thermal motion of the non-hydrogen atoms. Scattering factors for C, S and H were derived from wavefunctions tabulated in ref. 16. The program XDLSM of XD¹⁵ was used for the multipole refinement. The rigid pseudoatom model¹⁷ has become an established tool in the extraction of the charge density from experimental data; a detailed account of a recent application of the technique is given in ref. 10. The electron density $\rho(\mathbf{r})$ in the crystal is described by a sum of aspherical 'pseudoatoms' with nuclear positions $\{\mathbf{R}_j\}$

$$\rho(\mathbf{r}) = \sum_j \rho_j(\mathbf{r} - \mathbf{R}_j) \quad (1)$$

In XDLSM the pseudoatom density has the form

$$\rho_j(\mathbf{r}_j) = P_c \rho_c(\mathbf{r}_j) + \kappa'^3 P_v \rho_v(\kappa' \mathbf{r}_j) + \sum_{l=0}^{l_{\max}} \sum_{m=-l}^{+l} \kappa''^3 P_{lm} R_l(\kappa'' \mathbf{r}_j) d_{lm}(\theta_j, \phi_j) \quad (2)$$

where $\mathbf{r}_j = \mathbf{r} - \mathbf{R}_j$. Each pseudo-atom is described by three components. The first, $P_c \rho_c$ describes the core density. The core population P_c is fixed (at 2 for first-row atoms) and ρ_c is the spherically averaged Hartree-Fock core density for the atom. The second term describes the spherical part of the valence density. This is usually also obtained from the Hartree-Fock wavefunction; κ' is an expansion-contraction coefficient which modifies the radial density distribution, being varied in the least-squares refinement along with the valence population P_v . The final, double summation term describes the deviation of the pseudo-atom density from sphericity. This is represented by deformation functions taking the shape of density-normalised spherical harmonics d_{lm} of order l oriented with index m and sign p .¹⁸ The radial term for the deformation functions can take the form of a normalised Slater-type function $R_l(r) = N r^{n_l} \exp(-\kappa'' \zeta r)$ with an expansion-contraction parameter κ'' again in place to alter the radial dependence of the functions. The values of n_l and ζ are taken from ref. 18. Alternatively, Hartree-Fock radial functions may be used in the deformation term. The deformation functions with $l \geq 1$ are defined with respect to cartesian axes which are local to each pseudoatom. This enables any chemical or crystallographic symmetry in the molecule to be described.

XDLSM provides an overall neutrality constraint, which may be expressed as a constraint on the monopole charges q_j :

$$\sum_j (Z_j - P_c - P_v) = \sum_j q_j = 0 \quad (3)$$

Further, specified groups of atoms may be constrained so that each has a particular net charge. The population parameters are on an absolute scale, and an overall scale factor is usually

refined to scale the calculated to the observed structure factors.

In this refinement the expansion was truncated at the hexadecapole level ($l_{\max} = 4$) for carbon and sulfur, and at the dipole level ($l_{\max} = 1$) for hydrogen atoms. The location of C(1) on a two-fold axis restricts the allowed multipoles, d_{lm} , on this atom to those which have m even.

Separate κ' and κ'' were employed for C and S, while for H, κ' and κ'' were fixed at 1.2, an average value obtained from theoretical models.¹⁹ The κ'' parameters for the four sets of multipoles ($1 \leq l \leq 4$) on carbon were constrained to have the same value. This refined to $\kappa'' = 0.78(1)$, with $\kappa' = 0.995(6)$. In the final refinement cycles the multipoles on sulfur were allowed to take different κ'' values. The final values are $\kappa' = 1.022(5)$, $\kappa''_{l=1} = 1.62(12)$, $\kappa''_{l=2} = 1.12(3)$, $\kappa''_{l=3} = 0.95(3)$ and $\kappa''_{l=4} = 0.94(7)$. Thus the dipole and quadrupole functions are contracted while the higher level functions are expanded.

Bond lengths to hydrogen atoms were fixed at the average value 1.06 Å obtained from neutron diffraction;²⁰ the bond directions and hydrogen atom isotropic temperature factors were fixed at values obtained from an independent atom model (IAM) refinement, in which all atoms were treated as spherical.

Results

Details of the final R factors and goodness of fit for the 1819 reflections used in the multipole refinement are given in Table 1. The observations: variables ratio is 17.5. Atom labelling is shown in Fig. 1. Atomic coordinates and anisotropic temperature factors are given in Table 2. Bond lengths and angles from this work† are listed in Table 3, together with those from the earlier crystal structure analysis.

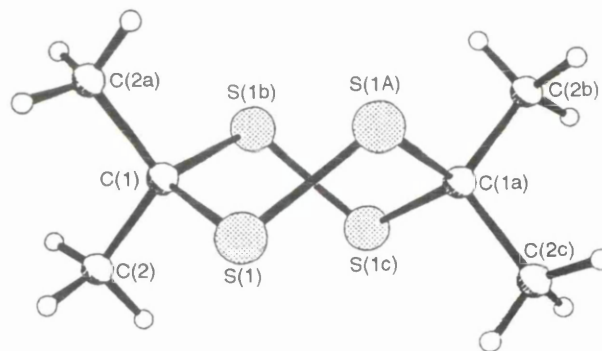


Fig. 1 Molecular structure of 1 in the twist-boat conformation found in the crystal

† Observed and calculated structure factors, multipole population coefficients and local coordinate systems are available as supplementary material (SUP 57138, 10 pp.) deposited with the British Library. Details are available from the Editorial Office.

Table 2 Fractional atomic coordinates and mean-square atomic displacements

atom	fractional atomic coordinates			mean-square atomic displacements ^a /Å ²					
	<i>x/a</i>	<i>y/b</i>	<i>z/c</i>	<i>U</i> ₁₁	<i>U</i> ₂₂	<i>U</i> ₃₃	<i>U</i> ₁₂	<i>U</i> ₁₃	<i>U</i> ₂₃
S(1)	0.49128 (2)	0.65364 (2)	0.20089 (1)	0.0172 (1)	0.0131 (1)	0.0110 (1)	-0.0012 (0)	-0.0023 (0)	0.0023 (0)
C(1)	0.37605 (4)	0.62605	0.12500	0.0142 (1)	0.0142	0.0125 (2)	-0.0022 (2)	-0.0007 (1)	0.0007
C(2)	0.39892 (7)	0.48924 (5)	0.09927 (4)	0.0332 (3)	0.0145 (2)	0.0214 (2)	-0.0029 (2)	-0.0046 (2)	-0.0027 (2)
H(1)	0.49064	0.48279	0.07381	0.024					
H(2)	0.39531	0.43089	0.14760	0.046					
H(3)	0.32217	0.46906	0.06218	0.039					

^a The form of the anisotropic temperature factor is: $\exp\left[-2\pi^2 \sum_{i=1}^3 \sum_{j=1}^3 U_{ij} h_i h_j a_i^* a_j^*\right]$. *a*, *b*, *c* are unit cell constants (see Table 1); *a*^{*}, *a*^{*} are reciprocal cell constants; *h*_{*i*}, *h*_{*j*} are Miller indices; *u*_{*ij*} are elements of the anisotropic thermal vibration tensor.

Table 3 Selected bond lengths and angles

	this work	ref. 9
bond lengths/Å		
S(1)–S(1a) ^a	2.023 (1)	2.015 (1)
S(1)–C(1)	1.847 (1)	1.843 (2)
C(1)–C(2)	1.521 (1)	1.514 (3)
bond angles/degrees		
C(1)–S(1)–S(1a)	102.4 (1)	102.9 (1)
S(1)–C(1)–S(1b) ^b	110.3 (1)	110.3 (1)
S(1)–C(1)–C(2)	105.8 (1)	105.4 (2)
C(2)–C(1)–C(2)	112.8 (1)	113.1 (3)

^a Symmetry code: $1 - x, 3/2 - y, z$. ^b $-1/4 + y, 1/4 + x, 1/4 - z$.

Fig. 2 shows the experimental deformation density, obtained from the multipole model, in a plane defined by C(1), S(1) and S(1a). The residual map after the last stage of the multipole refinement is shown in Fig. 3, for the same plane.

Fig. 4 shows a plot of the Laplacian distribution found experimentally, showing the S–S intermolecular interaction. The experimental and theoretical Laplacian maps for the S–S bond region are shown in Fig. 5. Critical-point data are given in Table 4.

Hirshfeld's rigid-bond test²¹ was applied to the thermal parameters obtained from the refinement. It is assumed that

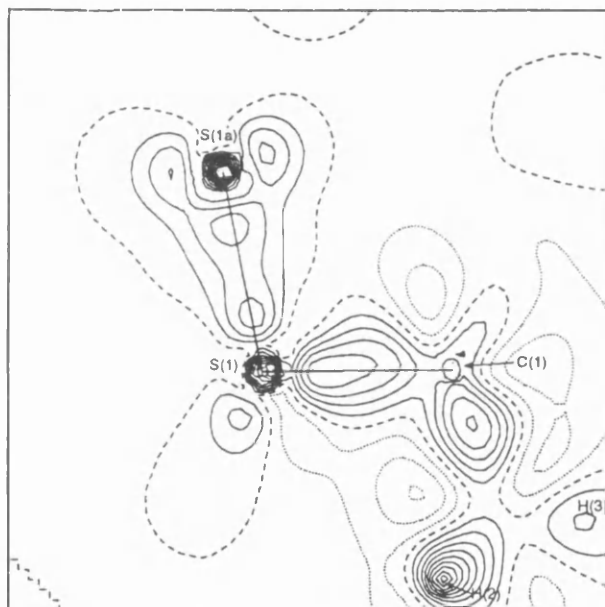


Fig. 2 Static deformation density in the C(1), S(1), S(1a) plane: contour interval = 0.1 eÅ^{-3} ; (---) zero and (· · ·) negative contours

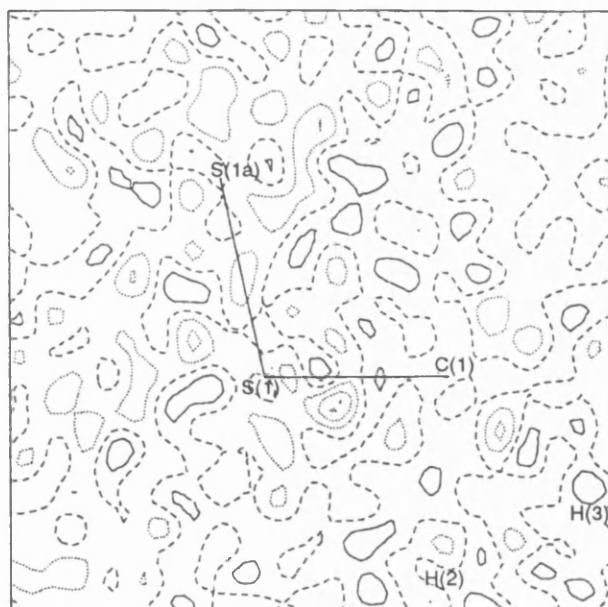


Fig. 3 Residual density in the C(1), S(1), S(1a) plane: contour interval = 0.05 eÅ^{-3} ; (---) zero and (· · ·) negative contours

the relative vibrational motion of a pair of covalently bonded atoms has an effectively vanishing component in the direction of the bond. If $z_{A,B}^2$ denotes the mean square displacement amplitude of atom A in the direction of atom B, then for every

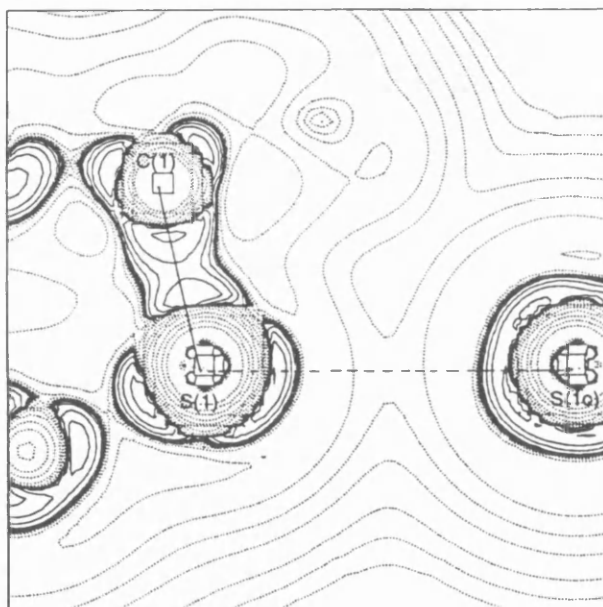


Fig. 4 Experimental Laplacian distribution showing the S···S intermolecular interaction

Table 4 Critical-point analysis for 3,3,6,6-tetramethyl-S-tetrathiane

bond	type	method	bond length/Å	$\rho_b/e \text{ Å}^{-3}$	$\nabla^2 \rho_b/e \text{ Å}^{-5}$	ϵ
S(1)–C(1)	(3, –1)	experimental	1.847 (1)	1.33 (3)	–6.82 (8)	0.12
		theoretical		1.233	–8.076	0.10
S(1)–S(1a)	(3, –1)	experimental	2.023 (1)	1.13 (3)	–0.59 (6)	0.10
		theoretical		1.093	–5.386	0.03
C(1)–C(2)	(3, –1)	experimental	1.521 (1)	2.07 (7)	–24.5 (2)	0.09
		theoretical		1.745	–16.841	0.00
S(1)–S(1c) ^a	(3, –1)	theoretical	3.150	0.119	1.448	0.37
S···S intermolecular	(3, –1)	experimental	3.669 (2)	0.043 (1)	0.442 (4)	0.12
centre of ring centroid of	(3, +1)	experimental	na	0.14 (1)	1.431 (4)	na
four-membered ring	(3, +3)	theoretical	na	0.100	1.807	na
	(3, +1)	theoretical	na	0.116	1.654	na

^a Symmetry code: $5/4 - y, 5/4 - x, 1/4 - z$.

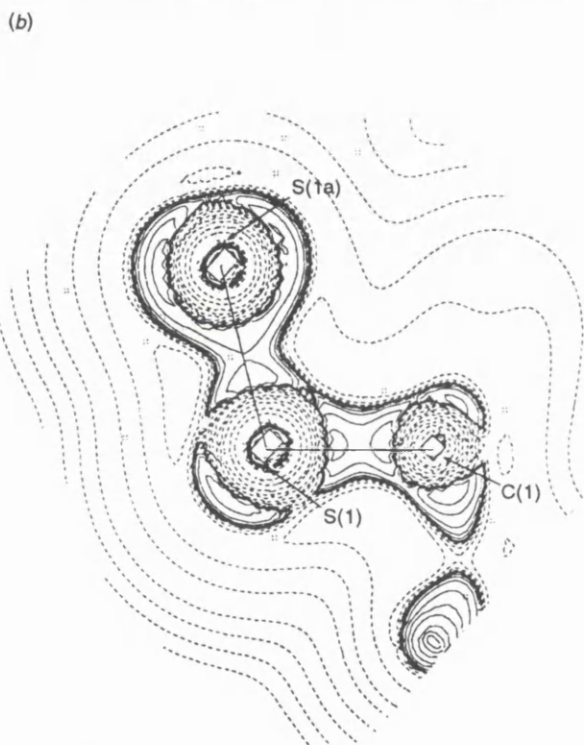
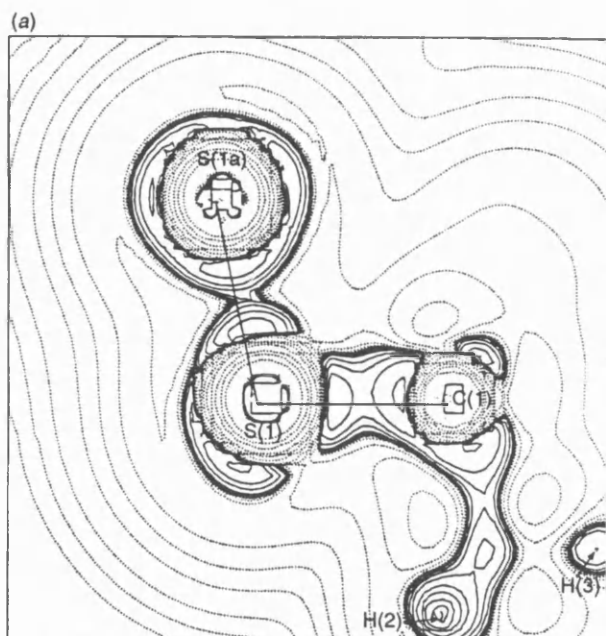


Fig. 5 Laplacian distribution in the C(1), S(1), S(1a) plane: (a) experimental; (b) theoretical

covalently bonded pair of atoms A and B

$$\Delta_{A,B} = z_{A,B}^2 - z_{B,A}^2 = 0$$

The bonds S(1)–C(1) and C(1)–C(2) have $\Delta_{A,B}$ values of 0.0006 and 0.0002 Å², respectively, less than Hirshfeld's upper limit of 0.001 Å² for atoms at least as heavy as carbon. Evidently the model satisfies the rigid-bond hypothesis.

Discussion

Experimental charge-density distribution and comparison with theory

The molecule of [(CH₃)₂CS₂]₂, a methyl-substituted six-membered ring containing four sulfur atoms, adopts a twist-

boat conformation in the solid state having crystallographic D₂ symmetry. The S(1)–S(1a) bond length is 2.023(1) Å, significantly longer than the S–S bond length of 2.015(1) Å reported in the original crystal-structure determination. It is, however, shorter than the literature values for the S–S bond in elemental sulfur which range from 2.035(2) to 2.060(2) Å.²²

The C(1)–S(1)–S(1a)–C(1a) torsion angle of –81.1° is consistent with the trend observed by Hordvik²³ for S–S bonds: the S–S bond length decreases with increasing torsion angle, reaching a minimum bond length at a torsion angle of 90°. Hordvik drew his conclusions from a literature survey which included experimental results for 18 compounds. To examine this relationship for a larger sample we carried out a search of the Cambridge Structural Database (CSD). Fig. 6 shows a scatter plot with a regression line for all occurrences of the C–S–S–C fragment in the CSD. The points for the experimentally determined and *ab initio* MO optimised geometries for the twist-boat and chair forms of **1**, discussed below, are indicated in this figure. Their positions fit the pattern established by the experimentally determined geometries of the other compounds.

The experimental deformation density map (Fig. 2) shows that both the S–S and C–S bonds are straight and consequently that the ring is not strained. The lone pairs on the sulfur atoms are well defined, with a deformation electron density of around 0.3 eÅ⁻³. The S(1)–S(1a) bond has a double peak in the deformation density. This is a common phenomenon, often seen in S–S bonds.^{1,6}

The electron-density distribution resulting from the multipole model was analysed using Bader's treatment of the topology of the charge density.²⁴ The results are compared in Table 4 with those obtained by *ab initio* MO calculation for the molecular geometry in the crystal. The values ρ_b of the electron density at the bond critical points for C–S and S–S bonds are in good agreement with the *ab initio* results, but for the C(1)–C(2) bond there is a large discrepancy.

The major difference between the two sets of critical points is, however, in their type and number. The experimental results show a (3, +1) ring critical point at the centroid of the six-membered ring. The *ab initio* study locates closed-shell trans-annular interactions between pairs of sulfur atoms, S(1)–S(1c) and S(1a)–S(1b). As a result, the critical point at the centre of the six-membered ring is of (3, +3) type, *i.e.* a

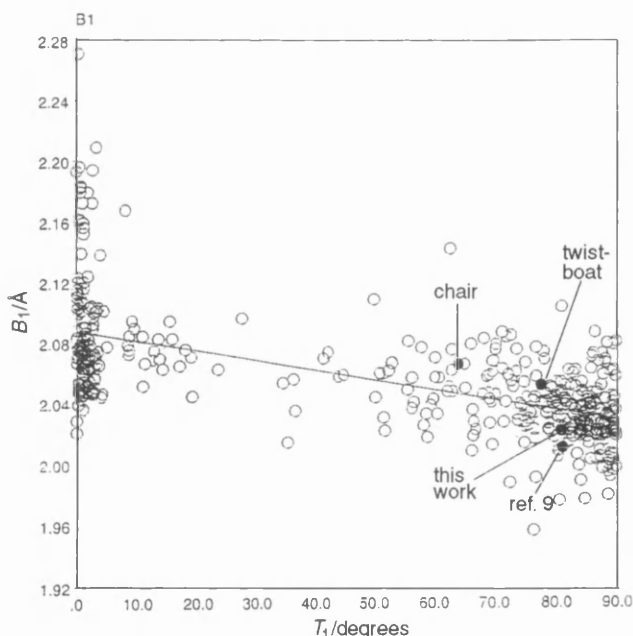


Fig. 6 Scatter plot of S–S bond length against torsion angle for C–S–S–C fragments

cage critical point. There are also four (3, +1) critical points near the centres of the four-membered rings which delineate the cage. It is apparent that both the theoretical and experimental results satisfy the Poincaré–Hopf relationship²⁵ for the number and type of critical points that can coexist in a system. The relationship states that $n - b + r - c = 1$ where n is the number of nuclei, b is the number of bonds, r is the number of rings and c is the number of cages.

The *ab initio* calculation was performed on an isolated molecule and so a study of possible intermolecular interactions was not possible. The experimental results however, show a closed-shell intermolecular interaction between two sulfur atoms 3.669(2) Å apart. The low value of ρ_b and the positive Laplacian value (Table 4) at a (3, -1) critical point located between these atoms are both characteristic of the bonds formed in hypervalent species. A plot of the Laplacian, Fig. 4, for this interaction shows the contraction of charge away from the interatomic region and into the atomic basins. This results in the positive value of the Laplacian at the bond critical point.

Comparison of the experimental and theoretical Laplacian distributions in the S—S bond (Fig. 5) reveals that they have very similar features. This, together with the agreement of certain of the experimental and theoretical critical point data, suggests that the discrepancies between the two sets of results may be due to the differences in molecular environment. In the crystalline environment it is possible to take account of intermolecular interactions, while in the hypothetical isolated molecule environment of the *ab initio* calculation, no such effects can be observed. However, in both cases each sulfur atom is shown to take part in a closed-shell interaction with another sulfur. Possibly, an *ab initio* calculation which simulated the crystalline environment would show intermolecular, rather than intramolecular, closed-shell interactions, thus removing these apparent differences between the experimental and theoretical densities.

To address Korp and Bernal's question concerning the existence of double bonding between the S atoms in **1**, the critical-point data were compared with those expected for S—S single and double bonds. A comparison with *ab initio* densities was made, reproducing Knop's calculation²⁶ on H₂S₂ as an example of an S—S single bond. A new calculation (with a 6-31G* basis set) for an S₂ molecule was carried out to obtain data for a double bond. The comparison is shown in Table 5. The results of the *ab initio* analysis for **1** at the experimental geometry seem to be consistent with a slightly strengthened S—S single bond, and the same is true of the experimental density, which does not differ significantly in the value of ρ_b .

Theory: *ab initio* molecular orbital calculations of the conformation

The critical-point data in Tables 4 and 5 for the theoretical density distribution are based on an *ab initio* calculation performed with the molecular geometrical parameters obtained in the experimental charge-density analysis. In fact compound **1** has been shown to exist in two conformations,²⁷ a flexible twist boat and a rigid chair; shown in Fig. 1 and 7, respectively. There is also a hypothetical boat conformer. We have carried out a theoretical study of all three possible conforma-

Table 5 Electronic properties at (3, -1) critical points in S—S bonds

S—S bond	bond length/Å	$\rho_b/e \text{ \AA}^{-3}$	ϵ
S ₂ (<i>ab initio</i>)	1.878	1.387	0.00
H—S—S—H (<i>ab initio</i>)	2.063	0.999	0.00
1 (experimental)	2.023 (1)	1.13 (3)	0.10
1 (theoretical)	2.023	1.093	0.03

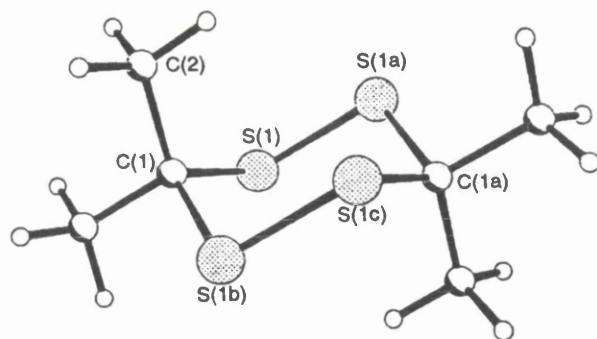


Fig. 7 Calculated structure of **1** in the chair conformation

Table 6 Results of *ab initio* geometry optimisations of the twist-boat form of **1**

basis ^a	energy/ E_h	S—S distance/Å
STO-3G	-1804.3103	2.124
STO-6G	-1818.5751	2.120
3-21G	-1815.1515	2.228
6-21G	-1823.8055	2.217
6-31G	-1823.9979	2.195
6-31G*	-1824.2338	2.043
6-31G**	-1824.2526	2.043
6-311G**	-1824.3925	2.051

^a 6-31G* has one shell of d-functions on non-hydrogen atoms; 6-31G** with an added shell of p-functions on hydrogen atoms; 6-311G** triple zeta basis set with both p and d polarisation functions.

Table 7 Effect of d orbital polarisation functions on bond lengths

bond	length/Å	basis set	difference/Å
S(1)—C(1)	1.849	6-31G*	-0.058
	1.907	6-31G	
C(1)—C(2)	1.530	6-31G*	0.005
	1.525	6-31G	
S(1)—S(1a)	2.043	6-31G*	-0.152
	2.195	6-31G	

tions. All of the calculations, except for the MP2 level calculation, were performed using GAMESS.¹³ Direct self-consistent field (SCF) was used and the full symmetry of the molecule was exploited in each case. The topology of the electron density was analysed using AIMPAC.¹⁴

Twist boat. This is the form which exists in the crystalline state, the molecule having D_2 symmetry. The initial geometry for the *ab initio* calculations was that determined experimentally by Korp and Bernal.⁹ This was optimised at the Hartree–Fock (HF) SCF level using a series of basis sets, the optimised geometry from one basis was used as the input to the next calculation using a higher level basis set (see Table 6). The necessity of including d functions as polarisation functions on second-row atoms has been widely discussed.^{7,28,29} In this case the addition of d functions on non-hydrogen atoms lowers the energy by 0.2359 E_h ,† and considerably changes the S—S bond length. While the introduction of d functions makes a small difference to both the S—C and C—C bond lengths, in neither case does it have such a large influence as on the S—S bond (see Table 7). Fig. 8 shows a

† 1 E_h (hartree) $\approx 4.35975 \times 10^{-18}$ J.

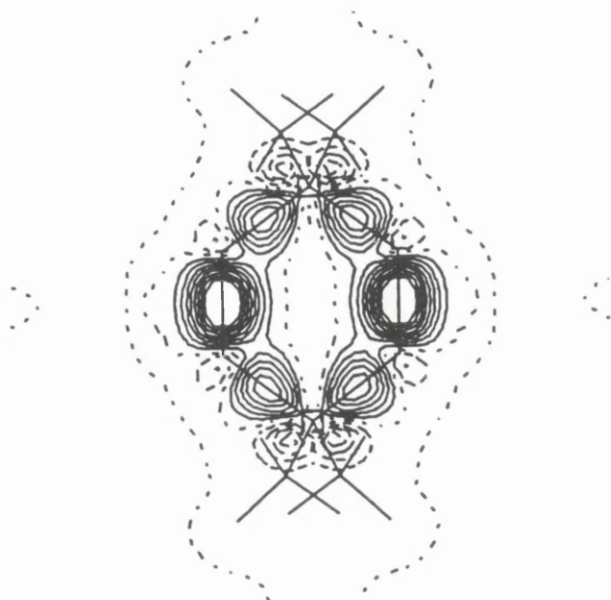


Fig. 8 Difference density plot, 6-31G* - 6-31G

plot of the difference in the electron densities derived from the 6-31G* and 6-31G wavefunctions. It is apparent from the high contour levels in the S—S bond that the addition of d functions has a greater effect on the sulfur atoms than on carbon or hydrogen. There is, as expected, no d orbital participation in the C—H bonds. The total d orbital populations are shown in Table 8. Even at the highest level of population it is apparent that the d orbitals are acting as polarisation functions and not as valence orbitals. The population would have to approach unity before the functions could be considered as true valence orbitals. The change in d orbital populations of C(1) and S(1) from the 6-31G** to the 6-311G** basis set is unexpected. To investigate whether this resulted from an inadequacy in the calculation, geometry optimisations were performed for the molecules CS and S₂ (triplet state). The differences in d orbital populations between the 6-31G* and the 6-311G** basis sets are, for CS, sulfur -0.028, carbon 0.047; for S₂, sulfur -0.026.

These values show that rather than being the result of a poor calculation, the fluctuations in d orbital population

Table 8 d Orbital population

basis set	atom	d orbital population
6-31G*	S(1)	0.111 38
	C(1)	0.080 42
	C(2)	0.080 46
6-31G**	S(1)	0.111 37
	C(1)	0.080 22
	C(2)	0.040 16
6-311G**	S(1)	0.071 09
	C(1)	0.138 80
	C(2)	0.063 59

Table 9 Electronic properties of critical points in the twist-boat conformation of 1, RHF/6-311G**

atoms	type	$\rho/e \text{ \AA}^{-3}$	Laplacian/ $e \text{ \AA}^{-5}$	ellipticity	bond length/ \AA
C(1)—S(1)	(3, -1)	1.228	-8.056	0.105	1.848
S(1)—S(1a)	(3, -1)	1.034	-4.567	0.039	2.051
C(1)—C(2)	(3, -1)	1.724	-16.513	0.002	1.529
S(1)··S(1c)	(3, -1)	0.102	1.295	0.848	3.240
C(1)S(1)S(1a)S(1b)	(3, +1)	0.101	1.404	na	na
ring centre	(3, +3)	0.090	1.590	na	na

result from basis-set dependency. In the CS molecule the increase in d orbital population can be partially explained by a transfer of charge from the sulfur atom. In 1, however, this is not the case as the charge on both the C(1) and sulfur atom becomes more negative. The explanation lies in the reordering of the electronegativities of the orbitals.

The S(1)··S(1c) and S(1)··S(1b) trans-annular distances are 3.240 and 3.072 Å respectively. Both of these distances are considerably shorter than the sum of the van der Waals radii for two sulfur atoms,³⁰ and so some type of interaction may be expected. This type of long-range S··S interaction has been observed in the S₈²⁺ cation³¹ which shows weak cross-ring bonding in the range 2.86 to 3.00 Å. A critical-point analysis of the 6-311G** *ab initio* density locates (3, -1) critical points midway between the pairs of sulfur atoms which are 3.240 Å apart, *i.e.* S(1)··S(1c) and S(1a)··S(1b). No such interactions are observed between the S(1)··S(1b) and S(1a)··S(1c) pairs. The S—C—S angle is 112.4°, a slight deviation from the tetrahedral angle, probably because of the large size of the sulfur atoms. An interaction between S(1) and S(1b) would compress this angle causing steric repulsion and so such an interaction is not favoured.

As a result of the long-range trans-annular interactions, the critical point at the centre of the ring is of (3, +3) type, a cage critical point, rather than the ring critical point which would be observed if there were no such interactions. However, four ring critical points do exist, also due to the long-range interactions, so that the Poincaré–Hopf relationship is satisfied.

The value of ρ_b for the S—S bond is $1.034 e \text{ \AA}^{-3}$ compared with $0.999 e \text{ \AA}^{-3}$ calculated by Knop *et al.*²⁶ for H₂S₂. The S—S distance is slightly shorter for 1 than for H₂S₂: 2.05 and 2.06 Å, respectively. Although both of these factors suggest a slightly stronger bond in 1 than in H₂S₂, it would be unwise to draw a direct comparison as the two calculations were performed with different basis sets. However, if we compare the results for 1 obtained with the same basis set as that of Knop *et al.*, 6-31G*, $\rho_b = 1.044 e \text{ \AA}^{-3}$ and the bond length is 2.04 Å, reinforcing the suggestion that the S—S bond in 1 is stronger than the pure single bond in H₂S₂. Beagley noted that in compounds of type X—S—S—X, the higher the electronegativity of X the shorter the S—S bond.³² The electronegativities of C and H are 2.5 and 2.1, respectively,³³ and so the above observation is in keeping with this trend. The properties of all of the symmetry-unique critical points found in the molecule are given in Table 9.

The Laplacian at the (3, -1) critical points has a negative value, with the exception of the trans-annular interaction. A positive Laplacian value indicates an interaction where the electron density has been contracted towards the nuclei. This is typical of closed-shell interactions which are seen, as here, in hypervalent molecules and also in hydrogen bonds. Fig. 9 shows the Laplacian at the S(1)··S(1c) interaction. Evidently there is no shared concentration of charge, rather the electrons are localised in the separate atomic basins of the interacting atoms. However, the charge in each of the atomic basins is polarised towards the other S atom.

To investigate the effects of electron correlation on the charge density, a single point MP2 level calculation was performed using GAUSSIAN 94.³⁴ This used the 6-311G** basis

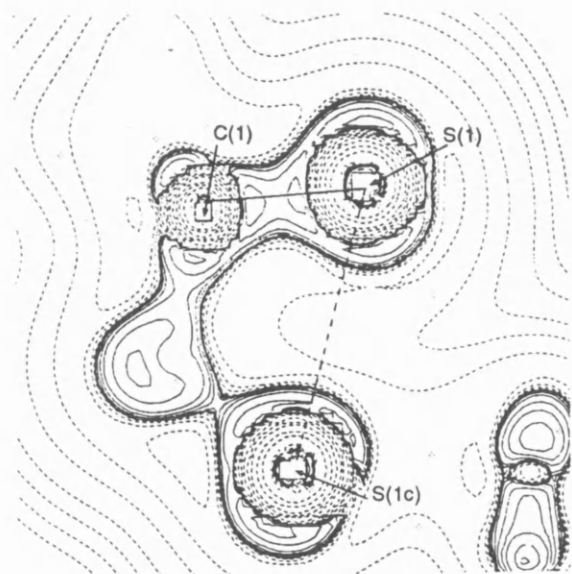
Table 10 Electronic properties of critical points in the twist-boat conformation of **1**, MP2/6-31G**//RHF/6-31G**

atoms	type	$\rho/e \text{ \AA}^{-3}$	Laplacian/ $e \text{ \AA}^{-5}$	ellipticity	bond length/ \AA
C(1)—S(1)	(3, -1)	1.144	-5.443	0.107	1.848
S(1)—S(1a)	(3, -1)	0.976	-2.480	0.035	2.051
C(1)—C(2)	(3, -1)	1.634	-13.270	0.005	1.529
S(1) · S(1c)	(3, -1)	0.105	1.323	2.552	3.240
C(1)S(1)S(1a)S(1b)	(3, +1)	0.104	1.373	na	na
ring centre	(3, +3)	0.094	1.595	na	na

Table 11 Electronic properties of critical points in the chair conformation of **1**, RHF/6-311G**

atoms	type	$\rho/e \text{ \AA}^{-3}$	Laplacian/ $e \text{ \AA}^{-5}$	ellipticity	bond length/ \AA
C(1)—S(1)	(3, -1)	1.245	-8.333	0.085	1.842
S(1)—S(1a)	(3, -1)	1.010	-4.266	0.082	2.065
C(1)—C(2)	(3, -1)	1.727	-16.648	0.013	1.526
ring centre	(3, +1)	0.072	1.161	na	na

set at the optimised RHF/6-31G** geometry. The final energy was found to be $-1825.8285 E_h$, a reduction of $1.4360 E_h$ from the RHF/6-311G** energy. The critical-point properties resulting from the MP2 wavefunction are shown in Table 10. For the three covalent bonds the effect of the MP2 calculation was to lower the electron density at the bond critical point by 0.084, 0.058 and $0.090 e \text{ \AA}^{-3}$ for the C(1)—S(1), S(1)—S(1a) and C(1)—C(2) bonds respectively. This observation is in broad agreement with that made by Brown and Smith⁷ in their investigation into the effects of electron correlation on the wavefunctions of small sulfur-containing molecules. They compared high-level HF wavefunctions with those obtained by configuration interaction singles and doubles (CISD) calculations for H_2S_2 , S_2 and S_3 , showing that the inclusion of electron correlation led to a reduction in the electron density in the range 0.01 – $0.04 e \text{ \AA}^{-3}$ at the midpoint of the S—S bond. Here the MP2 calculation increases the magnitude of the electron density at all other critical points, including the (3, -1) closed shell interaction, suggesting that electron correlation has the effect of delocalising the electrons in the molecule. This is particularly apparent in the increase of the ellipticity of the S(1) · S(1c) bond from 0.848 (RHF/6-311G**) to 2.552 (MP2).

**Fig. 9** Plot of the Laplacian of the *ab initio* geometry-optimised density distribution showing the S—S closed shell interaction

Chair. A similar series of geometry optimisations was performed on **1** in the chair conformation (see Fig. 7). Since the chair exists only in solution there are no structural data available. The highest level basis set used was 6-311G** which resulted in a final energy of $-1824.3930 E_h$. The total d orbital population for sulfur is 0.07086 and the S—S bond length is 2.065 \AA . In this conformation no trans-annular interactions are observed, the cross-ring distance is longer than the sum of the van der Waals radii, and so the critical point at the centre of the ring is of (3, +1) type. The critical-point data are given in Table 11.

Boat. There is no evidence for the existence of a boat form of the molecule, but it is of interest to investigate a hypothetical model of this conformation. The final energy of the isolated molecule, optimised at the 6-311G** level, is $-1824.3204 E_h$. The S—S bond length optimised to 2.13 \AA . This is very long for an S—S bond and has a correspondingly low ρ_b of $0.908 e \text{ \AA}^{-3}$. This is possibly due to an extension of the S—S bond to relieve the steric crowding of the methyl groups.

Comparison of the conformers. Since it is the twist-boat conformation which is found in the solid state, it might be expected that the isolated molecule would have a lower energy in the twist-boat form than in the chair. The final energies from the RHF/6-311G** calculations are, for the isolated twist-boat molecule: $-1824.392493 E_h$; for the isolated chair molecule: $-1824.393009 E_h$; difference: $0.000516 E_h$. This corresponds to an energy stabilisation of $1.355 \text{ kJ mol}^{-1}$ of the chair over the twist boat. That the calculation showed the opposite result to that found by experiment is not particularly surprising since the energy difference is very small and crystal packing forces can alter the relative energies of molecular conformations considerably. The individual components of the molecular energy are shown in Table 12. We note that the chair conformer is stabilised by $2 E_h$ over the twist-boat form on purely steric grounds. This is expected considering the large number of ring compounds which are found to exist in the chair form. The boat has a lower nuclear repulsion energy

Table 12 Components of molecular energy for the conformers of **1**

	molecular energy/ E_h		
	twist-boat	chair	boat
nuclear repulsion	1036.8154	1034.9846	1018.4430
electronic	-2861.2079	-2859.3776	-2842.7634

than either of the other two conformers, owing to the extension of the S—S bond to minimise steric crowding of the methyl groups. The associated weakening of the S—S bond can account for the high value of the electronic energy. The twist boat is stabilised with respect to the chair by $2 E_h$ on electronic grounds. This is presumably due to the transannular bonds arising from the presence of sulfur and its associated capability for forming hypervalent species.

Conclusions

Multipole analysis of the charge-density distribution in **1** identified bond critical points in the C—S and S—S bonds in which the value of ρ_b agrees within experimental error with values obtained from *ab initio* MO calculations for the molecular geometry found in the crystal. The Laplacian values are characteristic of weak covalent bonds between adjacent sulfur atoms, while interaction between sulfur atoms in neighbouring molecules in the crystal is indicated by topological analysis. The experimentally derived S—S bond lengths and values of ρ_b are consistent with a bond order greater than, but close to, unity.

Ab initio MO calculations for optimised geometries of isolated molecules predict a small energy stabilisation of the chair relative to the twist-boat conformer, in contrast to the situation in the crystal.

We thank the UK Engineering and Physical Sciences Research Council for a research fellowship for DSY (GR/J22702) and a postgraduate studentship for KLM (94310222); Dr. D. D. MacNicol for a crystalline sample of the tetrathiane derivative; Dr. S. T. Howard and Mr. J. A. Platts for running the calculations with GAUSSIAN 94 at the University of London Computer Centre. We also acknowledge use of the EPSRC-funded Chemical Database Service at Daresbury.

References

- P. Coppens, Y. W. Yang, R. H. Blessing, W. F. Cooper and F. K. Larsen, *J. Am. Chem. Soc.*, 1977, **99**, 760.
- C. C. Wang, Y. Y. Hong, C. H. Veng and Y. Wang, *J. Chem. Soc., Dalton Trans.*, 1992, **23**, 3331.
- Y. Wang, M. J. Chen and C. H. Wu, *Acta Crystallogr., Sect. B: Struct. Sci.*, 1988, **44**, 179.
- Y. Wang, S. Y. Wu and A. C. Cheng, *Acta Crystallogr., Sect. B: Struct. Sci.*, 1990, **46**, 850.
- Y. Wang, S. K. Yeh, S. Y. Wu, C. T. Pai, C. R. Lee and K. J. Lin, *Acta Crystallogr., Sect. B: Struct. Sci.*, 1991, **47**, 298.
- K. J. Lin and Y. Wang, *J. Phys. Chem.*, 1993, **97**, 3176.
- A. S. Brown and V. H. Smith, *J. Chem. Phys.*, 1993, **99**, 1837.
- T. H. Tang, R. F. W. Bader and P. J. MacDougall, *Inorg. Chem.*, 1985, **24**, 2047.
- J. D. Korp and I. Bernal, *Tetrahedron Lett.*, 1981, **22**, 4767.
- S. T. Howard, M. B. Hursthouse, C. W. Lehmann, P. R. Mallinson and C. S. Frampton, *J. Chem. Phys.*, 1992, **97**, 5616.
- R. H. Blessing, *J. Appl. Crystallogr.*, 1989, **22**, 396; and references therein.
- G. DeTitta, Program ABSORB, Medical Foundation of Buffalo, USA, 1984.
- M. W. Schmidt, K. K. Baldridge, J. A. Boatz, S. T. Elbert, M. S. Gordon, J. J. Jensen, S. Koseki, N. Matsunaga, K. A. Nguyen, S. Su, T. L. Windus, M. Dupuis and J. A. Montgomery, *J. Comput. Chem.*, 1993, **14**, 1347.
- F. W. Biegler-König, R. F. W. Bader and T. H. Tang, *J. Comput. Chem.*, 1982, **3**, 317.
- T. Koritsanszky, S. T. Howard, P. R. Mallinson, Z. Su, T. Richter and N. K. Hansen, XD—a computer program package for multipole refinement and analysis of charge densities from diffraction data, 1995.
- E. Clementi and C. Roetti, *Atomic Data and Nuclear Data Tables*, 1974, **14**, 177.
- R. F. Stewart, *Acta Crystallogr., Sect. A*, 1976, **32**, 565.
- N. K. Hansen and P. Coppens, *Acta Crystallogr., Sect. A*, 1978, **34**, 909.
- S. T. Howard, personal communication.
- F. H. Allen, O. Kennard, D. G. Watson, L. Brammer, A. G. Orpen and R. Taylor, *J. Chem. Soc., Perkin Trans. 2*, 1987, Suppl. 1.
- F. L. Hirshfeld, *Acta Crystallogr., Sect. A*, 1976, **32**, 239.
- A. C. Gallacher and A. A. Pinkerton, *Acta Crystallogr., Sect. C: Cryst.*, 1993, **49**, 125.
- A. Hordvik, *Acta Chem. Scand.*, 1966, **20**, 1885.
- R. F. W. Bader, *Atoms in Molecules: A Quantum Theory*, Oxford University Press, Oxford, 1990.
- K. Collard and G. G. Hall, *Int. J. Quantum Chem.*, 1977, **12**, 623.
- O. Knop, R. J. Boyd and S. C. Choi, *J. Am. Chem. Soc.*, 1988, **110**, 7299.
- C. H. Bushweller, *J. Am. Chem. Soc.*, 1969, **91**, 6019.
- D. G. Gilheany, *Chem. Rev.*, 1994, **94**, 1339.
- I. Mayer, *J. Mol. Struct.*, 1987, **149**, 81.
- A. Bondi, *J. Phys. Chem.*, 1964, **68**, 441.
- C. G. Davies, R. J. Gillespie, J. J. Park and J. Passmore, *Inorg. Chem.*, 1971, **10**, 2781.
- B. Beagley and K. T. McAloon, *Trans. Faraday Soc.*, 1971, **67**, 3216.
- L. Pauling, *The Nature of the Chemical Bond*, Oxford University Press, Oxford 1960.
- M. J. Frisch, G. W. Trucks, H. B. Schlegel, P. M. W. Gill, B. G. Johnson, M. A. Robb, J. R. Cheeseman, T. Keith, G. A. Petersson, J. A. Montgomery, K. Raghavachari, M. A. Al-Laham, V. G. Zakrzewski, J. V. Ortiz, J. B. Foresman, J. Cioslowski, B. B. Stefanov, A. Nanayakkara, M. Challacombe, C. Y. Peng, P. Y. Ayala, W. Chen, M. W. Wong, J. L. Andres, E. S. Replogle, R. Gomperts, R. L. Martin, D. J. Fox, J. S. Binkley, D. J. Defrees, J. Baker, J. P. Stewart, M. Head-Gordon, C. Gonzalez and J. A. Pople, GAUSSIAN 94, Revision C.3, Gaussian, Inc., Pittsburgh PA, 1995.

Paper 5/08368K; Received 28th December, 1995

Frankie & Kresge, 1982); in the title compound, the sum of the angles at the N24 atom is 340.2(4)°.

Both phenyl rings are oriented roughly perpendicular to the guanidine plane [the dihedral angles with the guanidine plane are 78.2(1)° for ring I and 68.9(1)° for ring II]; the dihedral angle between the phenyl rings is 54.4(1)°. The ethyl groups attached to the phenyl rings exhibit very large displacement parameters, indicating strong thermal vibrations or maybe even possible disorder (Fig. 1).

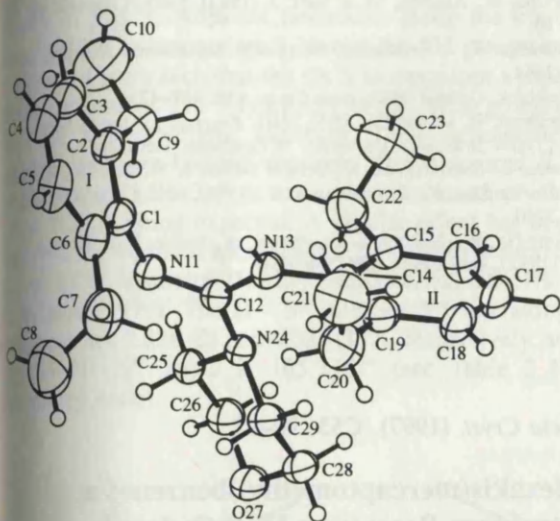


Fig. 1. The molecular structure and atom labelling of the title compound, with displacement ellipsoids drawn at the 30% probability level. The structure cannot be drawn without some overlap.

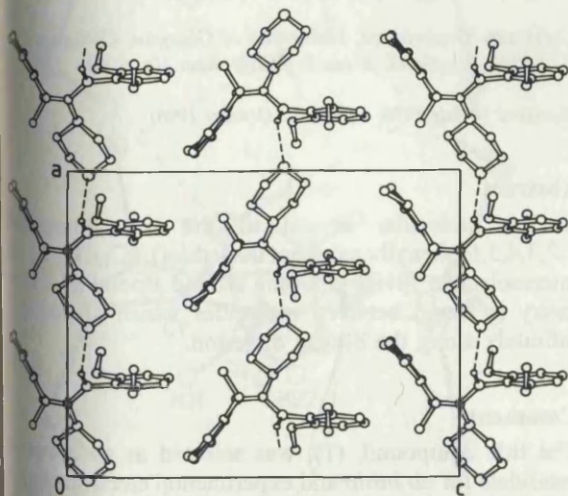


Fig. 2. The crystal-packing arrangement shown in the section $y/b = \frac{1}{2}$. H atoms have been omitted for clarity, except for the H atom of the N—H group, which is involved in hydrogen bonding.

The guanidine N—H group donates a hydrogen bond to the oxydiethyl O atom of a neighbouring molecule [N13...O27($\frac{1}{2} + x, \frac{1}{2} - y, z$) 3.000(4) Å]. The crystal packing is shown in Fig. 2.

Experimental

The title compound, (1), was synthesized at and supplied by the SPIC Science Foundation, Madras, India. The synthesis involves desulfurization of 1,3-diaryl thiourea in the presence of an appropriate amine (Ramadas & Srinivasan, 1995).

Crystal data

$C_{25}H_{35}N_3O$
 $M_r = 393.56$
 Orthorhombic
Aba2
 $a = 14.978(3) \text{ \AA}$
 $b = 16.703(3) \text{ \AA}$
 $c = 18.847(3) \text{ \AA}$
 $V = 4715.1(15) \text{ \AA}^3$
 $Z = 8$
 $D_x = 1.109 \text{ Mg m}^{-3}$
 D_m not measured

Cu $K\alpha$ radiation
 $\lambda = 1.54176 \text{ \AA}$
 Cell parameters from 25 reflections
 $\theta = 10.2\text{--}24.3^\circ$
 $\mu = 0.525 \text{ mm}^{-1}$
 $T = 293(2) \text{ K}$
 Prism
 $0.55 \times 0.15 \times 0.10 \text{ mm}$
 Colourless

Data collection

Enraf-Nonius Turbo-CAD-4 diffractometer
 ω - 2θ scans
 Absorption correction: none
 1808 measured reflections
 1808 independent reflections
 1523 observed reflections
 $[I > 2\sigma(I)]$

$\theta_{\max} = 59.90^\circ$
 $h = 0 \rightarrow 16$
 $k = 0 \rightarrow 18$
 $l = 0 \rightarrow 21$
 3 standard reflections
 frequency: 60 min
 intensity decay: 0.6%

Refinement

Refinement on F^2
 $R(F) = 0.0450$
 $wR(F^2) = 0.1331$
 $S = 1.056$
 1804 reflections
 262 parameters
 $w = 1/[\sigma^2(F_o^2) + (0.0843P)^2 + 0.7239P]$
 where $P = (F_o^2 + 2F_c^2)/3$
 $(\Delta/\sigma)_{\max} < 0.001$

$\Delta\rho_{\max} = 0.135 \text{ e \AA}^{-3}$
 $\Delta\rho_{\min} = -0.123 \text{ e \AA}^{-3}$
 Extinction correction: none
 Atomic scattering factors from *International Tables for Crystallography* (1992, Vol. C, Tables 4.2.6.8 and 6.1.1.4)
 Absolute configuration: Flack (1983)
 Flack parameter = $-0.4(6)$

Table 1. Fractional atomic coordinates and equivalent isotropic displacement parameters (\AA^2)

$$U_{eq} = (1/3)\sum_i \sum_j U_{ij} a_i^* a_j^* \mathbf{a}_i \cdot \mathbf{a}_j$$

	<i>x</i>	<i>y</i>	<i>z</i>	U_{eq}
C1	0.3146 (2)	0.3157 (2)	-0.0978 (2)	0.0685 (10)
C2	0.3808 (3)	0.2744 (2)	-0.1356 (2)	0.0717 (10)
C3	0.4408 (3)	0.3192 (3)	-0.1763 (2)	0.0916 (14)
C4	0.4368 (4)	0.4012 (4)	-0.1792 (3)	0.104 (2)
C5	0.3735 (4)	0.4410 (3)	-0.1405 (3)	0.107 (2)
C6	0.3105 (3)	0.4000 (2)	-0.0996 (2)	0.0848 (12)
C7	0.2382 (4)	0.4451 (3)	-0.0611 (3)	0.110 (2)
C8	0.1540 (6)	0.4519 (6)	-0.1017 (5)	0.202 (5)
C9	0.3848 (3)	0.1860 (3)	-0.1338 (3)	0.0873 (12)

C10	0.4312 (6)	0.1462 (4)	-0.1920 (4)	0.157 (3)
N11	0.2438 (2)	0.2722 (2)	-0.06674 (14)	0.0661 (8)
C12	0.2369 (2)	0.2595 (2)	0.0000 (2)	0.0615 (9)
N13	0.2968 (2)	0.2861 (2)	0.0500 (2)	0.0717 (8)
C14	0.3059 (2)	0.2571 (3)	0.1210 (2)	0.0650 (9)
C15	0.3252 (2)	0.1761 (3)	0.1338 (2)	0.0778 (11)
C16	0.3339 (3)	0.1522 (4)	0.2038 (3)	0.1033 (15)
C17	0.3248 (4)	0.2061 (5)	0.2586 (2)	0.110 (2)
C18	0.3072 (3)	0.2835 (5)	0.2457 (2)	0.102 (2)
C19	0.2974 (3)	0.3114 (3)	0.1768 (2)	0.0811 (12)
C20	0.2746 (4)	0.3979 (4)	0.1661 (3)	0.119 (2)
C21	0.3524 (6)	0.4537 (4)	0.1680 (5)	0.155 (3)
C22	0.3391 (4)	0.1175 (4)	0.0737 (3)	0.112 (2)
C23	0.4111 (5)	0.0598 (4)	0.0835 (5)	0.159 (3)
N24	0.1649 (2)	0.2150 (2)	0.02549 (14)	0.0636 (7)
C25	0.1112 (2)	0.1770 (3)	-0.0295 (2)	0.0710 (10)
C26	0.0447 (3)	0.1201 (3)	0.0045 (2)	0.0849 (11)
O27	-0.0116 (2)	0.1614 (2)	0.0527 (2)	0.0979 (9)
C28	0.0404 (3)	0.1972 (4)	0.1067 (2)	0.0971 (14)
C29	0.1060 (3)	0.2563 (3)	0.0769 (2)	0.0839 (12)

Table 2. Selected geometric parameters (Å, °)

C1—N11	1.414 (5)	N13—C14	1.430 (5)
N11—C12	1.280 (4)	N24—C25	1.458 (4)
C12—N13	1.376 (5)	N24—C29	1.481 (5)
C12—N24	1.395 (5)		
C12—N11—C1	123.6 (3)	C12—N13—C14	126.4 (3)
N11—C12—N13	124.5 (3)	C12—N24—C25	114.4 (3)
N11—C12—N24	119.3 (3)	C12—N24—C29	115.9 (3)
N13—C12—N24	116.2 (3)	C25—N24—C29	109.9 (3)
C12—N11—C1—C2	106.4 (4)	N13—C12—N24—C25	-170.5 (3)
C12—N13—C14—C15	58.8 (5)	N13—C12—N24—C29	60.1 (4)
C12—N24—C25—C26	171.0 (3)	N24—C12—N11—C1	-179.3 (3)
C12—N24—C29—C28	-172.0 (3)	N24—C12—N13—C14	16.8 (5)
N11—C12—N13—C14	-162.4 (4)	C1—C2—C9—C10	158.0 (6)
N11—C12—N24—C25	8.8 (5)	C1—C6—C7—C8	-83.9 (7)
N11—C12—N24—C29	-120.7 (4)	C14—C15—C22—C23	139.5 (6)
N13—C12—N11—C1	-0.1 (6)	C14—C19—C20—C21	-99.4 (6)

H atoms bonded to C atoms were refined using a riding model, with the torsion angles of the methyl groups defined by the expected staggered conformation (SHELXL93; Sheldrick, 1993). H-atom displacement parameters were restricted to be 1.2U of the parent atom, except for the methyl groups, in which $U_H = 1.5U_C$. The H(N) atom was located from a difference Fourier calculation and was then treated using the riding model. The positioning of H(N) at N13 and not at N11 is supported by the C12—N bond lengths [C12—N13 1.376 (5) and C12—N11 1.280 (4) Å] and by the modes of intermolecular interactions; N13—H is involved in a hydrogen bond, with $N13 \cdots O27(\frac{1}{2} + x, \frac{1}{2} - y, z)$ 3.000 (4) Å, whereas N11 has no potential hydrogen-bond acceptor within a radius of 4 Å. This treatment of H atoms was used because displacement parameters of the structure are generally very high. Since the structure contains only light atoms, the orientation of the polar axis (z) cannot be unambiguously determined from the Flack parameter (Flack, 1983).

Data collection: CAD-4 Software (Enraf-Nonius, 1989). Cell refinement: CAD-4 Software. Data reduction: CAD-4 Software. Program(s) used to solve structure: SHELXS86 (Sheldrick, 1990). Molecular graphics: ORTEPII (Johnson, 1976). Software used to prepare material for publication: SHELXL93.

KS thanks the Deutscher Akademischer Austauschdienst for a grant to stay in Berlin. LS and NS wish to thank CSIR, New Delhi, India, for financial support. The authors thank Professor W. Saenger, Berlin, for providing the X-ray equipment.

Lists of structure factors, anisotropic displacement parameters, H-atom coordinates and complete geometry have been deposited with the IUCr (Reference: KA1214). Copies may be obtained through The Managing Editor, International Union of Crystallography, 5 Abbey Square, Chester CH1 2HU, England.

References

- Brown, C. J. & Sengier, L. (1984). *Acta Cryst.* C40, 1294–1295.
Enraf-Nonius (1989). *CAD-4 Software*. Enraf-Nonius, Delft, The Netherlands.
Flack, H. D. (1983). *Acta Cryst.* A39, 876–881.
Johnson, C. K. (1976). *ORTEPII*. Report ORNL-5138. Oak Ridge National Laboratory, Tennessee, USA.
Molina, M., Alajarin, M. & Saez, J. (1983). *Synth. Commun.* pp. 67–70.
Ramadas, K. & Srinivasan, N. (1995). *Tetrahedron Lett.* 36, 2841–2844.
Sheldrick, G. M. (1990). *Acta Cryst.* A46, 467–473.
Sheldrick, G. M. (1993). *SHELXL93. Program for the Refinement of Crystal Structures*. University of Göttingen, Germany.
Sudha, L., Subramanian, K., Senthil Selvan, J., Steiner, Th., Koellner, G., Ramdas, K. & Srinivasan, N. (1996). *Acta Cryst.* C52, 3238–3240.
Wong-Ng, W., Nyburg, S. C., Awwal, A., Jankie, R. & Kresge, A. J. (1982). *Acta Cryst.* B38, 559–664.

Acta Cryst. (1997). C53, 90–92

Hexakis(mercaptopmethyl)benzene: a Structure Possessing Well Ordered Homodromic [SH...S]₆ Interactions

PAUL R. MALLINSON, DAVID D. MACNICOL, KIRSTY L. MCCORMACK, DMITRII S. YUFIT, JAMES H. GALL AND R. KEITH HENDERSON

Chemistry Department, University of Glasgow, Glasgow G12 8QQ, Scotland. E-mail: paul@chem.gla.ac.uk

(Received 10 July 1996; accepted 3 October 1996)

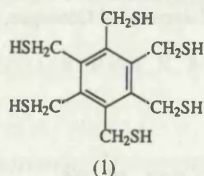
Abstract

In the molecular crystal of the title compound, 1,2,3,4,5,6-phenylhexakis(methanethiol), C₁₂H₁₈S₆, an intermolecular [SH]₆ grouping around a point of $\bar{3}$ symmetry is found between molecules which are stacked infinitely along the *c*-axial direction.

Comment

The title compound, (1), was selected as an attractive candidate for *ab initio* and experimental electron-density studies owing to the potentially high site symmetry in its molecular crystal. The resulting small 'covalently anchored' asymmetric unit was expected to exhibit atten-

ated thermal motion effects compared with a corresponding smaller molecule containing the functional group of interest, for example, CH₃SH (m.p. 150 K).



The molecular conformation, which is of the *ababab* type, generated by crystallographic $\bar{3}$ symmetry, is shown in Fig. 1. Adjacent molecules along the *c* axis are involved in interactions between the SH groups and S atoms of pairs such that the six S atoms adopt a chair-like arrangement. The $\bar{3}$ symmetry of the [SH]₆ grouping imposes a homodromic (Saenger, 1984) arrangement on the hydrogen-bonded network. The measured S—H distance of 1.24 (3) Å is somewhat shortened, a value of *ca.* 1.35 Å being expected. A similar effect has been reported for 4-*p*-mercaptophenyl-2,2,4-trimethylchroman in its CCl₄ clathrate (Hardy, McKendrick, MacNicol & Wilson, 1979). The H···Sⁱⁱⁱ and S···Sⁱⁱⁱ interatomic distances are 2.838 (2) and 4.053 (1) Å, respectively, and the S—H···Sⁱⁱⁱ angle is 165.7 (5)° (see Table 2 for symmetry code).

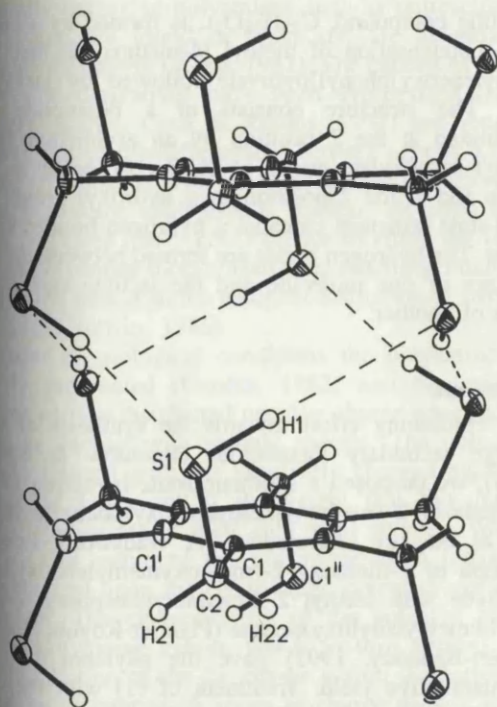


Fig. 1. A view normal to the *c* axis showing the juxtaosition of molecules of (1) along *c*. Displacement ellipsoids are drawn at the 50% probability level. The S—H···S hydrogen bonds are represented by dashed lines.

While the S···S distance is essentially a van der Waals contact, it is interesting to note that the S—H bond appears to lie in the expected direction of an acceptor S lone pair. This is reflected in the IR S—H stretching peak which is observed at 2510 cm⁻¹ compared with 2610 cm⁻¹ for an isolated S—H bond (Paul, 1974).

Close contacts exist between S atoms in adjacent molecules in the *xy* plane. These are shown as dashed lines in Fig. 2, in which the S···H interactions are also indicated. The intermolecular S···S($\frac{1}{3}-y, \frac{2}{3}+x-y, z-\frac{1}{3}$) distance of 3.623 (1) Å is considerably shorter than the S···S van der Waals distance of 3.70 Å (Pauling, 1960).

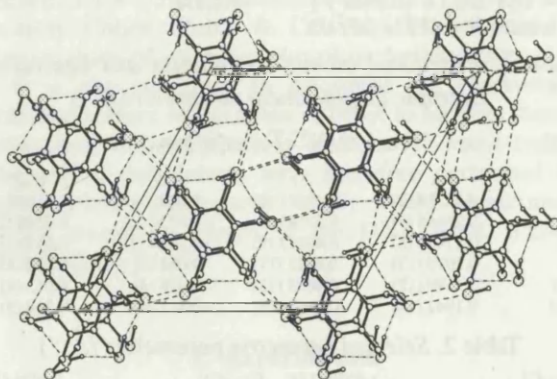


Fig. 2. A view along *c* showing the packing of (1) in its molecular crystal. S—H···S hydrogen bonds and S···S intermolecular interactions are indicated by dotted/dashed and dashed lines, respectively.

Experimental

The title hexathiol was prepared according to the literature method of Backer (1935) and purified by conversion to its hexathioacetate C₆(CH₂SCOCH₃)₆ (m.p. 507–508 K) by refluxing in acetic anhydride and pyridine. Conversion back to the hexathiol (m.p. 499–500 K) was then effected by refluxing in MeOH/conc. HCl.

Crystal data

C₁₂H₁₈S₆
M_r = 354.62
 Trigonal
*R*3̄
a = 16.088 (2) Å
c = 5.197 (1) Å
V = 1164.9 (3) Å³
Z = 3
D_x = 1.517 Mg m⁻³
D_m not measured

Mo *K*α radiation
λ = 0.71073 Å
 Cell parameters from 25 reflections
θ = 16.57–19.21°
μ = 0.860 mm⁻¹
T = 120 (1) K
 Needle
 0.4 × 0.1 × 0.1 mm
 Colourless

Data collection

Enraf–Nonius CAD-4 diffractometer

*R*_{int} = 0.0648
*θ*_{max} = 49.92°

ω -2 θ scans	$h = -34 \rightarrow 0$
Absorption correction:	$k = 0 \rightarrow 34$
none	$l = 0 \rightarrow 11$
2715 measured reflections	5 standard reflections
2705 independent reflections	frequency: 120 min
1261 observed reflections	intensity decay: 2%
$[I > 2\sigma(I)]$	

Refinement

Refinement on F^2	$(\Delta/\sigma)_{\max} < 0.001$
$R(F) = 0.0554$	$\Delta\rho_{\max} = 0.87 \text{ e } \text{Å}^{-3}$
$wR(F^2) = 0.1040$	$\Delta\rho_{\min} = -0.45 \text{ e } \text{Å}^{-3}$
$S = 1.076$	Extinction correction: none
2701 reflections	Atomic scattering factors
40 parameters	from <i>International Tables</i>
All H-atom parameters	for <i>Crystallography</i> (1992),
refined	Vol. C, Tables 4.2.6.8 and
$w = 1/[\sigma^2(F_o^2) + (0.045P)^2]$	6.1.1.4)
where $P = (F_o^2 + 2F_c^2)/3$	

Table 1. Fractional atomic coordinates and equivalent isotropic displacement parameters (Å^2)

$$U_{eq} = (1/3)\sum_i\sum_j U_{ij}a_i^*a_j^*a_i \cdot a_j$$

	x	y	z	U_{eq}
S1	0.12756 (2)	0.42611 (2)	-0.00817 (6)	0.01645 (8)
C1	0.25648 (7)	0.57146 (7)	-0.3339 (2)	0.0108 (2)
C2	0.17428 (8)	0.46913 (8)	-0.3324 (2)	0.0125 (2)
H1	0.2075 (17)	0.4515 (17)	0.088 (5)	0.039 (6)
H21	0.1199 (12)	0.4625 (13)	-0.428 (4)	0.013 (4)
H22	0.1942 (14)	0.4292 (14)	-0.405 (4)	0.019 (5)

Table 2. Selected geometric parameters (Å , $^\circ$)

S1—C2	1.8340 (13)	C1—C1 ⁱ	1.4074 (10)
S1—H1	1.24 (3)	C1—C2	1.5107 (15)
C2—S1—H1	94.7 (11)	C1—C2—S1	112.72 (8)
C1 ⁱ —C1—C1 ⁱⁱ	120	S1 ⁱⁱⁱ ...H1—S1	165.7 (5)
C1 ⁱ —C1—C2	119.77 (9)		

Symmetry codes: (i) $\frac{2}{3} + x - y, \frac{1}{3} + x, -\frac{2}{3} - z$; (ii) $y - \frac{1}{3}, \frac{1}{3} - x + y, -\frac{2}{3} - z$; (iii) $\frac{2}{3} + x - y, \frac{1}{3} + x, \frac{1}{3} - z$.

Data collection: *CAD-4 Express* (Enraf-Nonius, 1995). Cell refinement: *CAD-4 Express*. Data reduction: *GX* (Mallinson & Muir, 1985). Program(s) used to solve structure: *SHELXS86* (Sheldrick, 1990). Program(s) used to refine structure: *SHELXL93* (Sheldrick, 1993). Software used to prepare material for publication: *SHELXL93*.

Lists of structure factors, anisotropic displacement parameters, H-atom coordinates and complete geometry have been deposited with the IUCr (Reference: BM1105). Copies may be obtained through The Managing Editor, International Union of Crystallography, 5 Abbey Square, Chester CH1 2HU, England.

References

- Backer, H. J. (1935). *Recl. Trav. Chim. Pays-Bas*, **54**, 905.
 Enraf-Nonius (1995). *CAD-4 Express*. Enraf-Nonius, Delft, The Netherlands.
 Hardy, A. D. U., McKendrick, J. J., MacNicol, D. D. & Wilson, D. R. (1979). *J. Chem. Soc. Perkin Trans. 2*, pp. 729–734.
 Mallinson, P. R. & Muir, K. W. (1985). *J. Appl. Cryst.* **18**, 51–53.
 Paul, I. C. (1974). *The Chemistry of the Thiol Group*, edited by S. Patai, Part 1, ch. 2. London: Wiley.
 Pauling, L. (1960). *The Nature of the Chemical Bond*, p. 260. Ithaca: Cornell University Press.

© 1997 International Union of Crystallography
 Printed in Great Britain – all rights reserved

- Saenger, W. (1984). *Inclusion Compounds*, Vol. 2, edited by J. L. Atwood, J. E. D. Davies & D. D. MacNicol, ch. 8, p. 253. London: Academic Press.
 Sheldrick, G. M. (1990). *Acta Cryst.* **A46**, 467–473.
 Sheldrick, G. M. (1993). *SHELXL93. Program for the Refinement of Crystal Structures*. University of Göttingen, Germany.

Acta Cryst. (1997). **C53**, 92–95

Methyl 4-Hydroxy-3-[4-methoxy-2-(methoxymethyleneoxy)phenyl]-2-[[4-methoxy-2-(methoxymethyleneoxy)phenyl]methyl]-5-oxo-2,5-dihydrofuran-2-carboxylate

TODD R. BOEHLW, NIGAM P. RATH AND CHRISTOPHER D. SPILLING

Department of Chemistry, University of Missouri–St. Louis, 8001 Natural Bridge Road, St. Louis, MO 63121, USA.
 E-mail: nigam_rath@umsl.edu

(Received 23 April 1996; accepted 18 September 1996)

Abstract

The title compound, C₂₅H₂₈O₁₁, is formed by a hom aldol condensation of methyl [4-methoxy-2-(methoxymethyleneoxy)phenyl]pyruvate followed by lactonization. The structure consists of a butenolide ring substituted at the 2 position by an arylmethyl and a methyl carboxylate group, at the 3 position by an aryl group and at the 2 position by a hydroxyl group. The solid-state structure contains a hydrogen-bonded cyclic dimer. The hydrogen bonds are formed between the enol H atom of one molecule and the lactone carbonyl O atom of another.

Comment

In a continuing effort towards the synthesis of some sponge secondary metabolites (Boehlow & Spilling 1995), we proposed a synthetic route involving methyl [4-methoxy-2-(methoxymethyleneoxy)phenyl]pyruvate, (2), as the key intermediate. A Wadsworth–Emmons reaction of 4-methoxy-2-(methoxymethyleneoxy)benzaldehyde with methyl 2-dimethoxyphosphoryl-2-(tert-butyl)dimethylsilyloxyacetate (Plantier-Royon, Anker & Robert-Baudouy, 1991) gave the silylenol ether (1) in quantitative yield. Treatment of (1) with the complex triethylamine tris(hydrogen fluoride) in methanol yielded methyl [4-methoxy-2-(methoxymethyleneoxy)phenyl]pyruvate. Attempted isolation of pyruvate (2) by SiO₂ chromatography yielded a white crystalline solid.

Acta Crystallographica Section C
 ISSN 0108-2701 © 1997

Experimental and Theoretical Studies of the Charge Density Distribution in *E*-Tetraethyl-1,4-diammoniumbut-2-ene.2PF₆

KIRSTY L. MCCORMACK, PAUL R. MALLINSON,* BRIAN C. WEBSTER, DMITRII S. YUFIT, LINDSAY A. SLATER AND DAVID J. ROBINS

Chemistry Department, University of Glasgow, Glasgow G12 8QQ, Scotland. E-mail: paul@chem.gla.ac.uk

(Received 31 May 1996; accepted 10 September 1996)

Abstract

The [PF₆]⁻ salt of *E*-tetraethyl-1,4-diaminobut-2-ene has been synthesized and the crystal structure determined. The experimental electronic charge distribution has been obtained by fitting a multipole model to low-temperature, high-resolution, single-crystal X-ray diffraction data. A high-level *ab initio* molecular orbital calculation has also been performed for the cation, which is used as an antifungal agent. Both experimental and theoretical Laplacian distributions display maxima only at the bond critical points. This correlates with a calculated electrostatic potential which is positive at all points.

1. Introduction

Naturally occurring polyamines such as putrescine and spermidine are found in fungi and are essential for normal cell growth (Tabor, 1981). The cations of several putrescine derivatives have been synthesized (Havis, Walters, Martin, Cook & Robins, 1994) and found to exhibit considerable fungicidal activity against a range of plant pathogens. The exact reason for the activity of these putrescine analogues is unclear, although it has been suggested that it could be due to either the inhibition of polyamine biosynthesis or competitive binding to polyamine sites with the resultant disruption of structure (Porter & Suffrin, 1986).

Under physiological conditions the polyamines are largely protonated (Ganem, 1982) and the resulting cations carry a distributed positive charge which allows them to interact with anionic species. The polyamine cations interact with the negatively charged phosphate groups of DNA and it is thought that this interaction is the source of their antifungal activity (Walters, 1995). The nature of the polyamine/anion interaction is dependent upon the electrostatic potential surface of each ion. The characteristics of the potential surface of the polyamine cation, which in turn depend upon the distribution of the 2+ charge within the cation, are therefore of interest. A series of charge density studies of related polyamines of varying antifungal activity would therefore provide information from which structure/property relationships may be drawn. This study

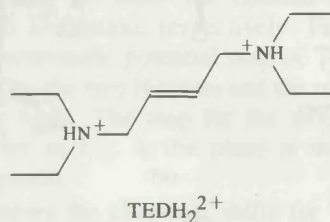
represents one of the first of such a series and its purpose is to investigate the electronic charge distribution of a polyamine cation with known fungicidal properties, [*E*-tetraethyl-1,4-diammoniumbut-2-ene]²⁺, TEDH₂²⁺. Very recently Cohen, Ruble & Craven (1996) reported a similar study of spermine phosphate hexahydrate.

It is also necessary to determine the electrostatic potential surface of the anion in order to confirm that an interaction with the anion is feasible. *Ab initio* molecular orbital calculations were therefore performed on the simplest model group which would approximate to the phosphate groups of the DNA helix, namely [PO₂(OCH₃)₂]⁻.

2. Experimental

2.1. Synthesis of *E*-tetraethyl-1,4-diammoniumbut-2-ene bis(hexafluorophosphate)

The synthesis of the free base was carried out by the general procedure of Biel & DiPierro (1958). *E*-Tetraethyl-1,4-diaminobut-2-ene, TED,



was dissolved in dry ether and a solution of HCl in ether was added. The resulting precipitate was filtered and washed with ether to give TEDH₂²⁺ dichloride as a white solid. Samples of the bis(hexafluorophosphate) were made by ligand exchange. TEDH₂²⁺ dichloride was dissolved in water and 1.2 equiv. of ammonium hexafluorophosphate in water was added. The resulting cream solid was filtered off and washed with water to give TEDH₂²⁺ bis(hexafluorophosphate); ν_{\max} (KBr disc), cm⁻¹: 3425.9 (N—H), 972.2 [(*E*) HC=CH], 838.0 (P—F); ¹³C NMR (CD₃OD): 8.6 (CH₃), 47.9 (CH₂—CH₃), 52.8 (CH₂—CH), 129.4 (CH); *m/z* 200

($M^+ - 2PF_6^-$, 2.3%), 126 (76.0%), 110 (13.2%), 86 (100%), 72 (74.8%), 56 (62.3%), 42 (47.7%). Crystals suitable for this study were grown from a solution of methanol/ether and obtained as colourless plates (m.p. 462–462.5 K).

2.2. X-ray data collection

Single-crystal, high-resolution, low-temperature data were collected using the same equipment as described in an earlier paper (Howard, Hursthouse, Lehmann, Mallinson & Frampton, 1992). Data reduction was performed with the *DREADD* program package (Blessing, 1989). The intensities of standard reflections were fitted to cubic polynomials, which were used for scaling the data. The crystal faces were indexed, the two largest faces having indices of 100 and $\bar{1}00$; the sides were bounded by the 011, $0\bar{1}\bar{1}$, $0\bar{1}1$ and $01\bar{1}$ faces. This information was used to perform a Gaussian analytical correction for absorption by the crystal using *ABSORB* (DeTitta, 1984). Thermal diffuse scattering was not corrected for.

2.3. Molecular orbital calculations

Ab initio molecular orbital calculations were performed for the cation at the crystalline geometry, and also for the model phosphate group, in order to gain

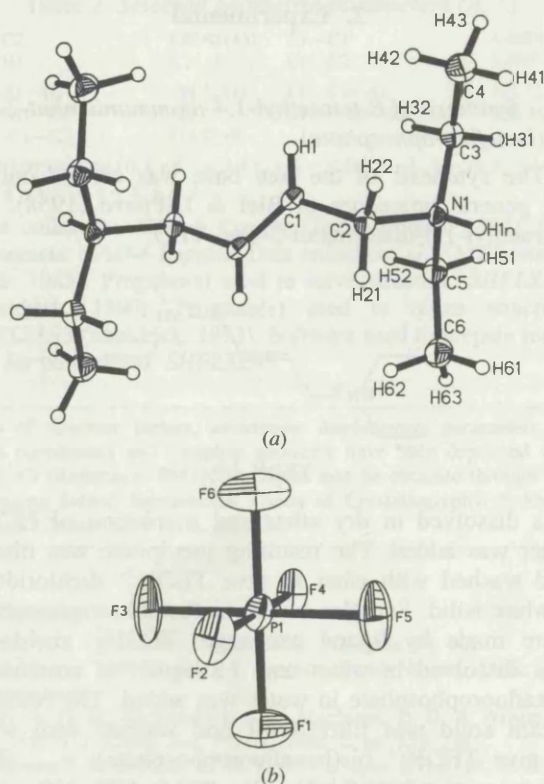


Fig. 1. (a) The crystallographically centrosymmetric structure of $TEDH_2^+$. (b) The PF_6^- anion. Thermal ellipsoids are drawn at 50% probability.

information about the electronic charge distribution of these species. The geometry of the model system, $[PO_2(OCH_3)_2]^-$, was optimized. All *ab initio* calculations were performed using the *GAMESS* program (Schmidt *et al.*, 1993) at the HF-SCF 6-311G** level. The critical point information and Laplacian map of the polyamine cation were obtained from the HF-SCF wavefunction using the *AIMPAC* suite of programs (Biegler-König, Bader & Tang, 1982). The electrostatic potential maps were plotted with the *MEPMAP* program of the graphics package of *GAMESS* (Schmidt *et al.*, 1993).

2.4. Multipole refinement

The crystal structure was solved using *SHELXS86* (Sheldrick, 1985) and refined with *SHELXL93* (Sheldrick, 1993). At room temperature the $[PF_6]^-$ group is disordered, four of the F atoms appearing as a 'spinning wheel' around the F2—P—F4 axis. This is dynamic disorder as no significant disorder is observed at low temperature. The space group requires the cation in the crystal to have point symmetry C_i , the centre of inversion being located at the midpoint of the C—C double bond, Fig. 1. The computational details of the multipole refinement are as reported in an earlier paper by McCormack, Mallinson, Webster & Yufit (1996). The refinement was performed using the program *XDLSM* of *XD* (Koritsansky *et al.*, 1995).

An overall electroneutrality constraint was applied to the monopole charges. In addition, the anions and cation were constrained to have net charges of -1 and $+2$, respectively.

In this refinement the expansion was truncated at the hexadecapole level ($l_{max} = 4$) for all non-H atoms. This level of expansion was considered to be reasonable as there was significant occupation of the hexadecapoles on all non-H atoms. For H atoms the expansion was truncated at the $l_{max} = 1$ level, using one bond-directed dipole per H atom. Significant occupation of the other two dipoles was not observed and so they were removed from the expansion in order to improve the observations-to-variables ratio.

Separate κ' and κ'' were employed for each non-H atom type. It was thought initially that partitioning the C atoms into chemically equivalent sets, which would each have separate κ' and κ'' parameters, might improve the description of the ethyl groups. It was found, however, that the carbon κ sets refined to values which were not significantly different from each other. The C atoms were therefore assigned to the same κ set in order to improve the observations-to-variables ratio. For H atoms κ' and κ'' were fixed at 1.2, an average value obtained from theoretical models (Howard, 1992). Values of κ'' were initially fixed at 1.0 for non-H atoms, but were allowed to vary after all other parameters had been refined. The κ'' values for the four sets of multipoles ($1 \leq l \leq 4$) in

Table 1. *Experimental details*

Crystal data	$C_{12}H_{28}F_{12}N_2P_2$
Chemical formula	490.3
Chemical formula weight	Monoclinic
Crystal setting	$P2_1/c$
Space group	6.282 (1)
a (Å)	13.252 (1)
b (Å)	13.112 (1)
c (Å)	98.08 (9)
β (°)	1079.5 (2)
V (Å ³)	2
D (Mg m ⁻³)	1.51
Refinement type	Mo $K\alpha$
Wavelength (Å)	0.71069
No. of reflections for cell	25
Parameters	13–15
Range (°)	0.300
$\Delta\rho$ (mm ⁻¹)	100
Temperature (K)	Plate
Crystal form	0.3 × 0.3 × 0.1
Crystal size (mm)	Colourless
Crystal colour	
Data collection	
Diffractometer	Enraf–Nonius CAD-4
Data collection method	ω -2 θ scans
Scan correction	Gaussian quadrature (DeTitta, 1984)
T_{min}	0.931
T_{max}	0.979
No. of measured reflections	19 338
No. of independent reflections	6884
No. of observed reflections	3611
Criterion for observed reflections	$I > 2\sigma(I)$
R_{int}	0.034
R_{σ} (°)	55
Range of h, k, l	-15 → h → 15 -24 → k → 24 -12 → l → 23
No. of standard reflections	6
Frequency of standard reflections	120
Δ (mm)	
Density decay (%)	None
Refinement	
Refinement on	F
R	0.021
R_w	0.022
S	1.003
No. of reflections used in refinement	3611
No. of parameters used	513
Atom treatment	See text
Weighting scheme	$w = 4F^2/[\sigma^2(F^2) + 0.0006F^4]$
Δ/σ_{max}	0.1
$\Delta\rho_{max}$ (e Å ⁻³)	0.3
$\Delta\rho_{min}$ (e Å ⁻³)	-0.2
Source of atomic scattering factors	<i>International Tables for X-ray Crystallography</i> (1974, Vol. IV, Tables 2.2B and 2.3.1)
Computer programs	
Data collection	CAD-4 Express (Enraf–Nonius, 1992)
Refinement	CAD-4 Express (Enraf–Nonius, 1992)
Structure reduction	DREADD (Blessing, 1989)
Structure solution	SHELXS86 (Sheldrick, 1985)
Structure refinement	SHELXL93 (Sheldrick, 1993) and XD (Koritsanzsky <i>et al.</i> , 1995)
Preparation of material for publication	XD (Koritsanzsky <i>et al.</i> 1995)

Each κ set were constrained to have the same value. The final κ values are: $\kappa'_C, \kappa''_C = 0.963$ (4), 0.835 (6); $\kappa'_N, \kappa''_N = 0.99$ (1), 0.84 (3); $\kappa'_P, \kappa''_P = 1.03$ (1), 0.71 (1); $\kappa'_F, \kappa''_F = 0.979$ (2), 1.03 (1).

Table 2. *Fractional atomic coordinates and equivalent isotropic displacement parameters (Å²)*

$$U_{eq} = (1/3)\sum_i\sum_j U^{ij} a_i^* a_j^* \mathbf{a}_i \cdot \mathbf{a}_j$$

	x	y	z	U_{eq}
P1	-0.54040 (2)	0.32589 (1)	0.81703 (1)	0.015
F1	-0.5598 (4)	0.4123 (3)	0.7306 (2)	0.037
F2	-0.28358 (19)	0.32999 (14)	0.82658 (14)	0.024
F3	-0.5454 (3)	0.2391 (2)	0.7293 (2)	0.034
F4	-0.80117 (19)	0.31994 (14)	0.80455 (13)	0.024
F5	-0.5399 (3)	0.4124 (2)	0.9030 (2)	0.035
F6	-0.5249 (4)	0.2415 (2)	0.9055 (3)	0.042
N1	0.03394 (14)	0.15113 (7)	0.66671 (7)	0.013
C1	0.02006 (13)	0.00150 (7)	0.55129 (6)	0.014
C2	0.16022 (12)	0.08027 (6)	0.60768 (7)	0.014
C3	-0.07967 (15)	0.09909 (7)	0.74585 (8)	0.018
C4	0.0703 (2)	0.0368 (1)	0.8213 (1)	0.026
C5	-0.12225 (14)	0.21602 (7)	0.59781 (7)	0.017
C6	-0.01186 (18)	0.28627 (8)	0.53094 (8)	0.023

Bond lengths to hydrogen were fixed at the average values obtained from neutron diffraction by Allen *et al.* (1987), 1.06 Å for the C—H bond and 1.033 Å for the N—H bond. The bond directions and H-atom isotropic temperature factors were fixed at values obtained from an independent atom model refinement, in which all atoms were treated as spherical.

The Laplacian map and the critical point information were obtained using the program *XDPROP* in the *XD* package.

3. Results

Details of the final R factors and goodness-of-fit for the 3611 reflections used in the multipole refinement are given in Table 1. The observations-to-variables ratio is 7. Atomic coordinates are given in Table 2 and anisotropic displacement parameters are shown in Table 3.*

Figs. 2(a) and (b) show the residual density maps for the cation and anion, respectively. Fig. 3 shows a theoretical electrostatic potential map of $TEDH_2^+$ in the plane defined by the two N atoms and the midpoint of the C—C double bond. The map for the model phosphate group is shown in Fig. 4; the plane is that defined by the PO_2 fragment.

Table 4 shows the chemical shifts for the ¹H NMR spectra of the free base, TED, and for $TEDH_2^+$. Valence monopole and Mulliken charges from the experimental and theoretical charge density studies, respectively, are shown in Table 5. The results of the critical point analyses are listed in Table 6. The experimental and theoretical Laplacian maps for the carbon–carbon double bond are shown in Figs. 5(a) and (b), respectively.

* Lists of structure factors, complete geometry, multipole population coefficients and local coordinate systems have been deposited with the IUCr (Reference: CF0001). Copies may be obtained through The Managing Editor, International Union of Crystallography, 5 Abbey Square, Chester CH1 2HU, England.

Table 3. Mean-square atomic displacements (Å²)The form of the anisotropic displacement factor is: $\exp[-2\pi^2 \sum_i \Sigma_j U^{ij} h_i a_j^* a_k^*]$

	U ¹¹	U ²²	U ³³	U ¹²	U ¹³	U ²³
P1	0.0106 (1)	0.0150 (1)	0.0185 (1)	-0.0016 (1)	0.0024 (1)	-0.0044 (1)
F1	0.0299 (8)	0.0390 (10)	0.0404 (10)	0.0002 (8)	0.0048 (8)	0.0155 (9)
F2	0.0104 (4)	0.0268 (6)	0.0341 (7)	-0.0034 (4)	0.0025 (4)	-0.0107 (6)
F3	0.0141 (5)	0.0388 (8)	0.0490 (9)	-0.0043 (6)	0.0075 (6)	-0.0308 (8)
F4	0.0107 (4)	0.0294 (6)	0.0311 (6)	-0.0021 (4)	0.0051 (4)	-0.0134 (6)
F5	0.0236 (7)	0.0420 (9)	0.0405 (9)	-0.0098 (7)	0.0125 (7)	-0.0260 (9)
F6	0.032 (1)	0.048 (1)	0.043 (1)	-0.012 (1)	-0.004 (1)	0.021 (1)
N1	0.0137 (3)	0.0120 (3)	0.0143 (4)	-0.0006 (2)	0.0022 (3)	-0.0030 (2)
C1	0.0152 (3)	0.0119 (3)	0.0138 (3)	-0.0015 (2)	0.0028 (3)	-0.0017 (3)
C2	0.0119 (3)	0.0145 (3)	0.0169 (3)	-0.0006 (2)	0.0027 (2)	-0.0038 (3)
C3	0.0207 (3)	0.0165 (3)	0.0180 (4)	-0.0007 (3)	0.0071 (3)	-0.0011 (3)
C4	0.0371 (5)	0.0198 (4)	0.0208 (4)	0.0040 (4)	0.0057 (4)	0.0032 (4)
C5	0.0167 (3)	0.0165 (3)	0.0184 (4)	0.0024 (3)	0.0031 (3)	-0.0008 (3)
C6	0.0287 (4)	0.0195 (4)	0.0195 (4)	-0.0006 (4)	0.0038 (3)	0.0024 (3)
H1N	0.022					
H1	0.030					
H21	0.034					
H22	0.021					
H31	0.025					
H32	0.015					
H41	0.031					
H42	0.039					
H43	0.042					
H51	0.021					
H52	0.025					
H61	0.053					
H62	0.034					
H63	0.051					

4. Discussion

The residual density maps, Figs. 2(a) and (b), show randomly distributed regions of low residual density, indicating that the electron distribution is satisfactorily described by the multipole model. Application of the rigid-bond test (Hirshfeld, 1976) shows that three of the bonds in the anion, P1—F1, P1—F5 and P1—F6, have differences in mean-square displacement amplitudes in the bond directions slightly greater than 0.001 Å², which may be related to larger than normal displacement amplitudes for these F atoms (Table 3), perhaps due to a small degree of residual disorder of the [PF₆]⁻ group. All bonds in the cation satisfy the test criterion.

The shortest interionic distances correspond to hydrogen-bond interactions between H1N of the cation and F3 and F4 of an anion related by the symmetry operation $x - 1, y, z$. These distances are 1.993 (1) and 2.050 (1) Å, respectively, and the N1—H1N—F3/F4 angles are 144.7 (1) and 146.9 (1)°. The bond critical point of such an interaction is typically characterized by a low value of the total density and a positive Laplacian, which is found to be the case here. The critical point information for these bonds is shown in Table 6.

The atomic charges within the cation (Table 5), relevant to the polyamine-phosphate interaction, show differences in magnitudes between the experimental valence monopole and theoretical Mulliken values. This is due to the different partitioning of the molecular charge in the two cases (Mulliken, 1955; Stewart, 1976).

Table 4. ¹H NMR data for TED and TEDH₂⁺, δ values in ppmAll spectra were carried out in CD₃OD with TMS as an internal standard.

Proton environment	TED	TEDH ₂ ⁺	Δ (ppm)
CH ₂ —CH ₂	1.04	1.32	+0.28
CH ₃ —CH ₂ —N	1.54	3.22	+0.68
N—CH ₂ —CH	3.12	3.88	+0.76
CH	5.70	6.15	+0.45

However, a qualitative comparison can be made and would be expected to show the same general trends in both sets of results. The experimental and theoretical charges both show the C and N atoms to carry partial negative charges, whilst all the H atoms are positively charged. This is confirmed by the ¹H NMR spectra of the non-protonated form of the molecule, TED, and of TEDH₂⁺, see Table 4. In TEDH₂⁺ each of the N atoms carries a formal positive charge and so they act as powerful electron-withdrawing groups. As a result the +2 charge is not located on the nitrogens, but is distributed over the H atoms and the proton environments in the cation are thus deshielded, leading to downfield shifts in δ, i.e. higher values of δ.

The shift is largest for those protons bonded to C atoms which are α to nitrogen as here the effect will be greatest; as expected, the shift of the methylene protons next to a nitrogen is of the order +0.7 p.p.m. The effect is still appreciable for protons on carbons β to the N

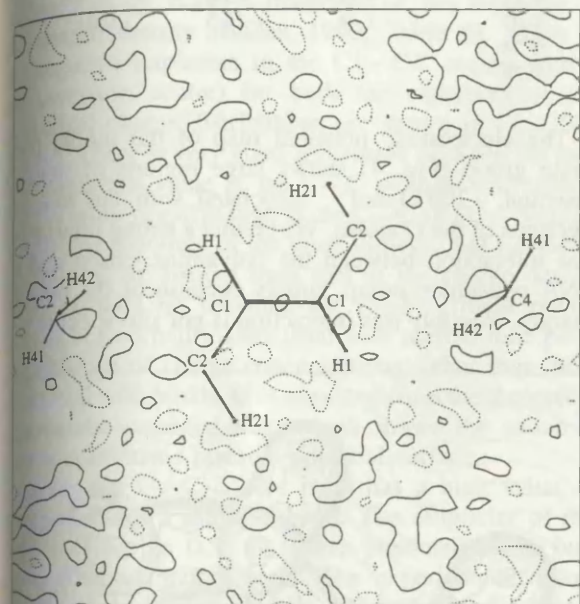
atom. The relative magnitudes of the charge depletion can be compared with those obtained from the valence monopole charges. The proton NMR shows the largest electron depletion to be on the H atoms bonded to C2, followed by those bonded to C3/C5, C1 and C4/C6 in order of decreasing electron depletion of the proton. The ¹H NMR averages the environments of the chemically

Table 5. Atomic charges for the atoms in $TEDH_2^{2+}$

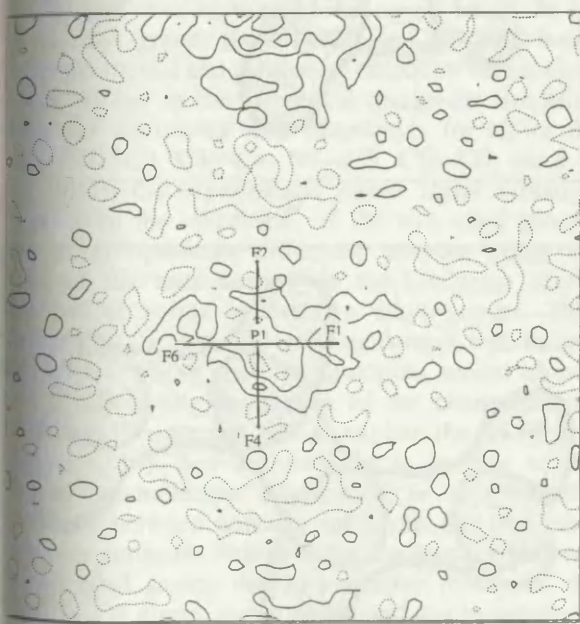
	Atomic charge (electrons)	
	Valence monopole	Mulliken
C1	-0.245	-0.067
C2	-0.344	-0.009
N1	-0.040	-0.394
C3	-0.329	-0.068
C4	-0.585	-0.146
C5	-0.439	-0.053
C6	-0.588	-0.145
H1	0.240	0.078
H1N	0.332	0.277
H21	0.219	0.146
H22	0.278	0.174
H31	0.241	0.151
H32	0.287	0.132
H41	0.332	0.110
H42	0.198	0.079
H43	0.237	0.140
H51	0.364	0.144
H52	0.255	0.135
H61	0.185	0.110
H62	0.258	0.076
H63	0.106	0.129

equivalent protons. Averaging the chemically equivalent monopole charges gives the sequence: H atoms bonded to C3/C5 followed by C2, C1 and C4/C6. The H atoms on carbons α to nitrogen are thus reordered.

Both experiment and theory show the proton with the largest positive charge to be that bonded to N1. That



(a)



(b)

Fig. 2. Residual density for: (a) the cation in the plane C2—C1—C1'—C2'; (b) the anion in the plane F1—P1—F2. Contour interval $0.1 \text{ e } \text{\AA}^{-3}$, solid lines are positive contours, dotted lines are negative. Here and elsewhere the prime denotes an atom related by crystallographic inversion (symmetry operator $x, -y, 1 - z$).

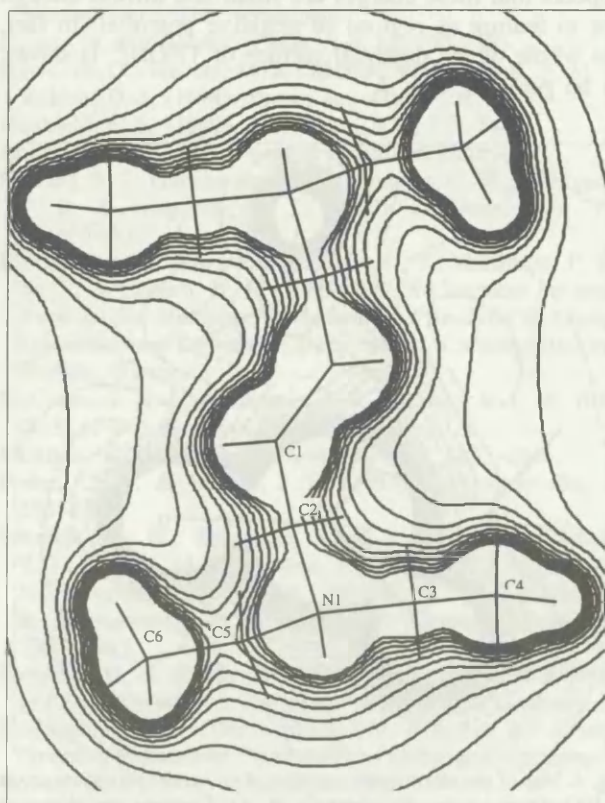


Fig. 3. Map of the theoretical electrostatic potential of the $TEDH_3^{2+}$ ion, in the plane of N1, C1 and C1'. Contour interval 100 kJ mol^{-1} .

Table 6. Critical point data for selected bonds

Atoms	Bond length (Å)	ρ ($e \text{ \AA}^{-3}$)	Experimental Laplacian ($e \text{ \AA}^{-5}$)	Ellipticity	ρ ($e \text{ \AA}^{-3}$)	Theoretical Laplacian ($e \text{ \AA}^{-5}$)	Ellipticity
C1—C1'	1.334 (2)	3.01 (9)	-44.3 (3)	0.47	2.41	-27.9	0.43
C1—C2	1.493 (2)	2.13 (6)	-26.9 (2)	0.14	1.86	-19.4	0.02
C2—N1	1.511 (2)	1.84 (7)	-22.3 (3)	0.11	1.56	-10.8	0.11
N1—C3	1.507 (2)	1.83 (9)	-22.6 (5)	0.42	1.52	-5.3	0.12
C3—C4	1.512 (2)	2.00 (6)	-26.4 (2)	0.40	1.76	-17.4	0.01
N1—C5	1.506 (2)	1.76 (9)	-25.4 (5)	0.15	1.52	-5.8	0.14
C5—C6	1.512 (2)	2.11 (6)	-25.0 (2)	0.07	1.76	-17.5	0.01
H1N—F3	1.994 (2)	0.09 (2)	2.1 (1)	0.38			
H1N—F4	2.050 (2)	0.08 (1)	1.7 (1)	0.58			

is with the exception of H51 in the experiment, which has a valence monopole charge not significantly different from that of H1N.

The N atoms should carry a greater negative charge than the C atoms, considering that a formally positive N atom is extremely electronegative. This is found to be the case in theory, but not from experiment.

It is difficult to predict the nature of intermolecular interactions from atomic charges alone, particularly in this case where the experimental and theoretical values disagree in the respect mentioned above. Theoretical electrostatic potential maps were therefore plotted for $TEDH_2^+$ and for the model phosphate group. The negative charges on the C and N atoms might disfavour an interaction with the negatively charged phosphate. It appears that these charges are small and diffuse enough not to feature as regions of negative potential. In fact, the whole of the potential surface of $TEDH_2^+$ is shown to be positive, Fig. 3.

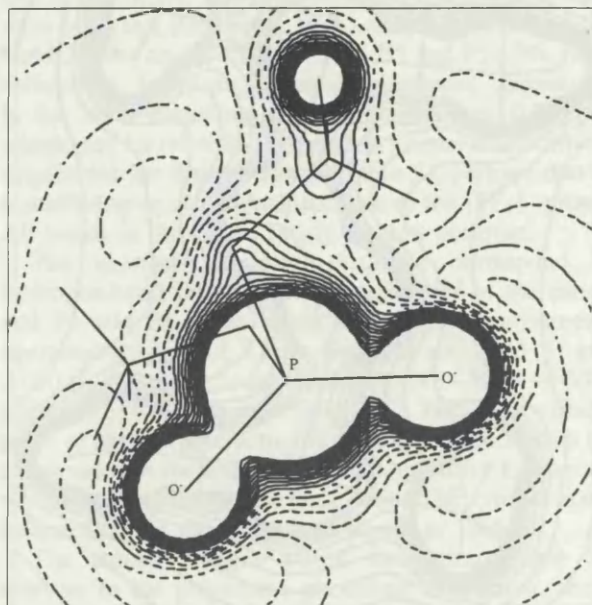
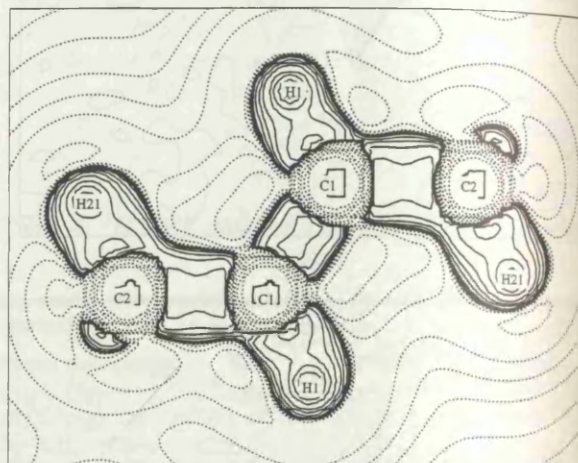
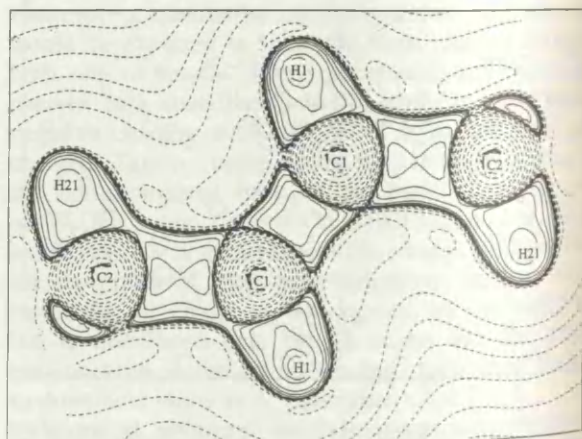


Fig. 4. Map of the electrostatic potential of the model phosphate group $[PO_2(OCH_3)_2]^-$, in the plane O—P—O. Contours are plotted at intervals of 100, from -700 to 1200 kJ mol^{-1} . Solid lines are positive contours, dashed lines are negative.

The electrostatic potential map of the model phosphate group (Fig. 4) shows large regions of negative potential, -700 kJ mol^{-1} , associated with the lone-pair electrons of the O atoms. We predict a strong intermolecular interaction between the polyamine cation and the DNA phosphate group, simply because of the opposite charges. Possibly this interaction is not site-specific with



(a)



(b)

Fig. 5. Laplacian distribution of $TEDH_2^+$ in the plane defined by the central C atoms: (a) experimental; (b) theoretical. Contours at logarithmic intervals in $-\nabla \rho^2 e \text{ \AA}^{-5}$.

respect to TEDH_2^{2+} as all points on the surface have large positive potentials. It is interesting to note that a similar conclusion was reached by Cohen, Ruble & Craven (1996) concerning the interaction of spermine with the phosphate groups of DNA.

We now come to the key point of this discussion. The charge density distributions resulting from both the multipole model and the *ab initio* calculation were analysed using Bader's treatment of the topology of the charge density (Bader, 1990; Table 6). Maps of the negative Laplacian in the C1—C1' region (across the inversion centre) for both the experimental and theoretical charge distributions are shown in Figs. 5(a) and (b). There is very good agreement between the two. The Laplacian value at the C—C double-bond critical point is more negative than in the C—C and C—N single bonds. The topology of the three-dimensional Laplacian distribution, as distinct from that of the charge density itself, exhibits no maxima, *i.e.* (3, -3) critical points, such as are normally associated with atomic lone pairs. The absence of charge concentrations, other than those associated with bonds, is as expected from the theoretical electrostatic potential map which shows the cation to have a continuous positive potential surface.

ρ_b for the C=C double bond has a high value, as expected for a multiple bond. The ellipticity of this bond is close to 0.5, the value predicted for a pure carbon-carbon double bond. The experimental values for the ellipticities of the N1—C3 and C3—C4 bonds, around 0.4, are anomalous, while the theoretical values are in accord with expectation for single bonds. In the second ethyl group, the N1—C5 and C5—C6 bonds have experimental and theoretical ellipticity values close to zero, so that in the theoretical results the two ethyl groups are equivalent with ellipticities for all of the bonds (N1—C3, C3—C4, N1—C5, C5—C6) close to zero. Whilst the experimental results show a marked difference in the ellipticities of the two ethyl groups, there is no significant difference between either the values of the total density or the Laplacian at the bond critical points in the two ethyl groups. This, together with the generally good agreement with theory, leads us to believe that the multipole model chosen gives a satisfactory description of the charge density distribution. We are not able to explain the anomalous ellipticities, but they are unlikely to be due to the effect of intermolecular interactions, as no substantial differences between contacts involving the two ethyl groups are apparent. Neither is the discrepancy between the two ethyl groups due to excessive motion of the N1—C3—C4 group, as the rigid-bond test is satisfied.

5. Conclusions

Multipole analysis of the charge density distribution of TEDH_2^{2+} supports the conclusion from the *ab*

initio molecular orbital calculation that the electrostatic potential is positive at all points on the surface of the cation. We hope that these investigations will prove fruitful in the modelling of interactions associated with the antifungal activity of the cation.

We thank the EPSRC for a research fellowship for DSY (GR/J 22702) and a postgraduate studentship for KLM (94310222) and we also thank The Wellcome Trust for a postgraduate studentship for LAS.

References

- Allen, F. H., Kennard, O., Watson, D. G., Brammer, L., Orpen, A. G. & Taylor, R. (1987). *J. Chem. Soc. Perkin Trans. 2*, pp. S1–S19.
- Bader, R. F. W. (1990). *Atoms in Molecules: A Quantum Theory*. Oxford University Press.
- Biegler-König, F. W., Bader, R. F. W. & Tang, T. (1982). *J. Comput. Chem.* **3**, 317–328.
- Biel, J. H. & DiPierro, F. (1958). *J. Am. Chem. Soc.* **80**, 4609–4614.
- Blessing, R. H. (1989). *J. Appl. Cryst.* **22**, 396–397.
- Cohen, A. E., Ruble, J. R. & Craven, B. M. (1996). *Acta Cryst.* **A52**, C-261.
- DeTitta, G. (1984). *ABSORB*. Medical Foundation of Buffalo, USA.
- Enraf-Nonius (1992). *CAD-4 Express*. Version 5.1. Enraf-Nonius, Delft, The Netherlands.
- Ganem, B. (1982). *Acc. Chem. Res.* **15**, 290–298.
- Havis, H. D., Walters, D. R., Martin, W. P., Cook, F. M. & Robins, D. J. (1994). *Pestic. Sci.* **41**, 71–76.
- Hirshfeld, F. L. (1976). *Acta Cryst.* **A32**, 239–244.
- Howard, S. T. (1992). Personal communication.
- Howard, S. T., Hursthouse, M. B., Lehmann, C. W., Mallinson, P. R. & Frampton, C. S. (1992). *J. Chem. Phys.* **97**, 5616–5630.
- Koritsansky, T., Howard, S. T., Richter, T., Mallinson, P. R., Su, Z. & Hansen, N. K. (1995). *XD. A Computer Program Package for Multipole Refinement and Analysis of Charge Densities from Diffraction Data*. Berlin, Cardiff, Glasgow, Buffalo, Nancy.
- McCormack, K. L., Mallinson, P. R., Webster, B. C. & Yufit, D. S. (1996). *Faraday Trans.* **92**, 1709–1716.
- Mulliken, R. S. (1955). *J. Chem. Phys.* **23**, 1833–1846.
- Porter, C. W. & Suffrin, J. R. (1986). *Anticancer Res.* **6**, 525–542.
- Schmidt, M. W., Baldridge, K. K., Boatz, J. A., Elbert, S. T., Gorgon, M. S., Jensen, J. J., Koseki, S., Matsunaga, N., Nyugen, K. A., Su, S., Windus, T. L., Dupuis, M. & Montgomery, J. A. (1993). *J. Comput. Chem.* **14**, 1347–1363.
- Sheldrick, G. M. (1985). *SHELXS86. Program for the Solution of Crystal Structures*. University of Göttingen, Germany.
- Sheldrick, G. M. (1993). *SHELXL93. Program for Crystal Structure Refinement*. University of Göttingen, Germany.
- Stewart, R. F. (1976). *Acta Cryst.* **A32**, 565–574.
- Tabor, C. W. (1981). *Med. Biol.* **59**, 272–278.
- Walters, D. R. (1995). *Mycol. Res.* **99**, 129–139.

SHORT COMMUNICATIONS

Acta Cryst. (1997). B53, 188

Neutron powder diffraction study of α -Ti(HPO₄)₂·H₂O and α -Hf(HPO₄)₂·H₂O; H-atom positions. Erratum

MIGUEL A. SALVADÓ,^a PILAR PERTIERRA,^a SANTIAGO GARCÍA-GRANDA,^a JOSÉ R. GARCÍA,^b JULIO RODRÍGUEZ^b AND M. T. FERNÁNDEZ-DÍAZ^c at ^aDepartamento de Química Física y Analítica and ^bArea de Química Inorgánica, Facultad de Química, Universidad de Oviedo, 33006 Oviedo, Spain, and ^cInstitut Laue-Langevin, BP 156, F-38042 Grenoble CEDEX 9, France.
E-mail: sgg@dwarf1.quimica.uniovi.es

(Received 30 November 1996)

Fractional atomic coordinates and isotropic displacement parameters (Å²) for H atoms

Abstract

The H-atom coordinates were omitted from Tables 2 and 3 on p. 897 [Salvadó, Pertierra, García-Granda, García, Rodríguez & Fernández-Díaz, *Acta Cryst.* (1996), B52, 896–898]. The values are now listed.

	x	y	z	U _{iso}
α-TiP				
H1	0.4133 (17)	0.245 (3)	0.7235 (9)	0.0415 (17)
H2	0.1440 (19)	0.943 (3)	0.7289 (9)	0.0415 (17)
H3	0.1948 (17)	0.390 (3)	0.7548 (11)	0.0415 (17)
H4	0.3083 (18)	0.233 (4)	0.8353 (8)	0.0415 (17)
α-HfP				
H1	−0.100 (2)	0.811 (4)	0.7167 (15)	0.052 (3)
H2	0.659 (3)	0.076 (4)	0.7282 (16)	0.052 (3)
H3	0.294 (3)	0.079 (4)	0.763 (2)	0.052 (3)
H4	0.212 (2)	0.221 (5)	0.6681 (10)	0.052 (3)

A Charge Density Analysis of Cationic and Anionic Hydrogen Bonds in a "Proton Sponge" Complex

Paul R. Mallinson^{a*}, Krzysztof Woźniak^b, Garry T. Smith^{a,c}, and Kirsty L. McCormack^a

^aChemistry Department, University of Glasgow, Glasgow G12 8QQ, UK

^bChemistry Department, University of Warsaw, 02-093 Warszawa, ul. Pasteura 1, Poland

^cPresent address: Chemistry Department, Queen's University, Kingston, Ontario K7L 3N6, Canada

*e-mail: paul@chem.gla.ac.uk; fax +44(141) 330 4888

Abstract

The charge density distribution in crystals of the 1,2-dichlorohydrogen maleate salt formed by 1,3-bis(dimethylamino)naphthalene (DMAN) has been obtained by high-resolution X-ray and neutron diffraction at 100K. The asymmetric $[\text{Me}_2\text{N}-\text{H}\cdots\text{NMe}_2]^+$ hydrogen bond in the monoprotonated cation is characterised by non-linear interaction lines, constrained by crystallographic symmetry to lie in the plane of the DMAN molecule: the critical point situated between the proton and the acceptor nitrogen atom lies in a region of positive Laplacian of the charge density. The lone pair of this nitrogen atom is polarised in the direction of the hydrogen bond. The N-C(aromatic) bond paths are slightly curved. Magnitudes of the charge density at critical points in covalent and hydrogen bonds within both ions are compared with values obtained from an *ab initio* M.O. single point calculation for a cation-anion pair. Properties of the charge density in a number of weak C-H...O inter-ionic interactions are found to be systematically related to the donor-acceptor separation. A series of *ab initio* calculations on a model formate ion-benzene complex shows that the density at C-H...O hydrogen bond critical points is systematically lower than the density of the super-posed moieties, but by an amount which is on the threshold of current experimental measurements analysed with multipole-based models.

Introduction

Proton sponges are organic diamines with unusually high basicity. The very first proton sponge, 1,3-bis(dimethylamino)naphthalene (DMAN) was reported in 1968 [1]. This compound has a basicity *ca.* 10 million times higher ($pK_a=12.1$) than other similar organic amines as for example aniline ($pK_a=5.1$). With mineral or organic acids proton sponges form very stable ionic complexes containing very strong, charge supported, intramolecular $[R_2N-H...NR_2]^+$ hydrogen bonding. Properties of such hydrogen bonds are used in discussion of the role of hydrogen bonding in low energetic enzymatic catalysis [2, 3]. The charge in these strong, charged hydrogen bonds has been studied theoretically at the Hartree-Fock level [4, 5, 6] but not at all experimentally.

1,8-diaminonaphthalenes show a wide range of basic strengths, depending on the substituents in the amine groups, observed pK_a values ranging up to 16.3 [7]. Some data for typical "proton sponge" compounds are given in Table 1. The ammonium ion, for comparison, has $pK_a = 9.25$. Proton sponges and their complexes have attracted considerable interest giving rise to over 70 structural and 100 spectroscopic papers. Among others the DMAN structure itself has been intensively studied by means of theoretical methods [4], X-ray [8, 9] and neutron diffraction [10], solid-state NMR [11, 12] and NQR spectroscopies [9, 13, 14]. The older results regarding proton sponges are nicely summarised in three important review papers by Alder [15], Staab and Saupe [7] and Llamas-Saiz and co-workers [16].

Platts and Howard [4] located the nitrogen lone pair in *ab initio* M.O. calculations on a series of amines. Lone pairs appear as (3,-3) critical points in the negative Laplacian distribution $-\nabla^2\rho$ of the charge density. Comparison of the values of ρ , and $\nabla^2\rho$ at the lone pair position, and the distance of the lone pair from the nucleus, shows no obvious trend in these properties. It seems that the unusual basic strength of DMAN is not attributable to unusual characteristics of the N lone pair. It has been explained in terms of a "proximity effect" of the two amino groups [7, 15, 16].

Here we report the first example of an experimental charge density analysis of a proton sponge complex - the crystalline acid salt formed by DMAN with 1,2-dichloromaleic acid (ClMH₂). The DMAN molecule in the crystalline complex is protonated, and the naphthalene nucleus lies in a crystallographic mirror plane. The 1,2-dichlorohydrogen maleate anion lies in the same mirror plane, giving rise to a number of relatively weak C-H...O interactions. The salt contains two strong, asymmetric hydrogen bonds $[Me_2N-H...NMe_2]^+$ and $[O-H...O]^-$ [17].

The presence of both cationic and anionic hydrogen bonding, and weak C-H...O hydrogen bonds make this DMAN-maleic acid complex an ideal candidate for an experimental study. The X-ray and neutron diffraction structures of the complex have already been published [18, 19]. In this paper we concentrate on the charge density analysis of strong ionic [N-H...N]⁺ and [O-H...O]⁻ hydrogen bonds in the DMANH⁺ cation and the ClMH⁻ anion (both of which appear to be asymmetric [19]) and, on the other hand, on a series of the weakest C-H...X interactions where X stands for O or Cl atoms.

Experimental

Crystals of the acid salt formed by DMAN with 1,2-dichloromaleic acid are colourless prisms. Single-crystal, high resolution X-ray diffraction data were collected on a CAD4 diffractometer using graphite-monochromated Mo K α radiation. The crystal was cooled by a stream of cold nitrogen gas from an Oxford Cryosystems Cryostream cooler. Data reduction was carried out with the DREAM suite of programs [20], including an analytical absorption correction computed with ABSORB [21]. The intensities of standard reflections were fitted to cubic polynomials, which were used for scaling the data. Corrections were made for absorption by the crystal, but not for thermal diffuse scattering. The range of corrections, agreement factor for the averaging of equivalent reflections, crystal data and other experimental details are summarized in Table 2.

Multipole refinement

The space group requires both cation and anion in the crystal to have point symmetry C_s [18]. The refinement minimized the function $\sum w(|F_o| - K|F_c|)^2$, where $w = 1/\sigma^2(F) = 4F^2/\sigma^2(F^2)$; $\sigma^2(F^2) = \sigma_{\text{counting}}^2(F^2) + P^2 F^4$. The instrumental instability factor P was estimated from errors in the time-dependent scaling polynomials and the fluctuations of the standards. Anisotropic temperature factors were used to describe the thermal motion of all atoms. For hydrogen atoms, positional and thermal parameters obtained from refinement with neutron diffraction data were used. Scattering factors for C, H, N, O, and Cl were derived from wavefunctions tabulated in reference [22]. The program XDLSM of the package XD [23] was used for the multipole refinement. The rigid pseudoatom model [24] has become the established tool in the extraction of the charge density from experimental data: a detailed account of the technique is given in reference [25]. The electron density $\rho(\mathbf{r})$ in the crystal is

described by a sum of aspherical 'pseudoatoms' with nuclear positions $\{\mathbf{R}_j\}$

$$\rho(\mathbf{r}) = \sum_j \rho_j(\mathbf{r} - \mathbf{R}_j) \quad (1)$$

In XDLSM the pseudoatom density has the form

$$\rho_j(\mathbf{r}_j) = P_c \rho_c(r_j) + \kappa'^3 P_v \rho_v(\kappa' r_j) + \sum_{l=0}^{l_{\max}} \sum_{m=-l_{\max}}^{+l_{\max}} \kappa''^3 P_{lm} R_l(\kappa'' r_j) d_{lm p}(\theta_j, \phi_j) \quad (2)$$

where $\mathbf{r}_j = \mathbf{r} - \mathbf{R}_j$. Each pseudo-atom is described by three components. The first, $P_c \rho_c$ describes the core density. The core population P_c is fixed (at 2 for first-row atoms) and ρ_c is the spherically-averaged Hartree-Fock core density for the atom. The second term describes the spherical part of the valence density. This is usually also obtained from the Hartree-Fock wavefunction: κ' is an expansion-contraction coefficient which allows the radial density to become more or less diffuse, being varied in the least-squares refinement along with the valence population P_v . The final, double summation term describes the deviation of the pseudo-atom density from sphericity. This is represented by deformation functions taking the shape of density-normalised spherical harmonics $d_{lm p}$ of order l oriented with index m and sign p [26]. The radial term for the deformation functions can take the form of a normalised Slater function $R_l(r) = r^{n_l} e^{-\zeta r}$, with an expansion-contraction parameter κ'' again in place to alter the radial dependence of the functions. The n_l and ζ are taken from reference [26]. Alternatively, Hartree-Fock radial functions may be used in the deformation term. The deformation functions with $l \geq 1$ are defined with respect to cartesian axes which are local to each pseudoatom. This makes possible the description of any chemical or crystallographic symmetry in the molecule.

XDLSM provides an overall neutrality constraint, which may be expressed as a constraint on the monopole charges q_j :

$$\sum_j (Z_j - P_c - P_v) = \sum_j q_j = 0 \quad (3)$$

Further, specified groups of atoms may be constrained so that each has a particular net charge. The population parameters are on an absolute scale, and an overall scale factor is usually refined to scale the calculated to the observed structure factors.

In the multipole refinement, the expansion was truncated at the octapole level ($l_{\max} = 3$) for carbon and nitrogen atoms, and at the dipole level ($l_{\max} = 1$) for all hydrogen atoms except strongly H-bonded H1nn and H1oo, for which quadrupole functions ($l_{\max} = 2$) were included. For all other hydrogen atoms a single, bond-directed dipole was used, and in each methyl group the three hydrogen atoms were constrained to have the same multipole coefficients. Hexadecapole functions ($l_{\max} = 4$) were included for the oxygen and chlorine

atoms. The space group symmetry restricts the allowed multipoles d_{lm} for atoms on the mirror plane (all except those of the methyl groups) such that only combinations with (even l , even m) and (odd l , odd m) are non-zero. Separate κ' , κ'' were employed for aromatic C, methyl C, anionic C, amino-bonded C, N, O, Cl, and H. Their values were allowed to vary, except those relating to H which were fixed at 1.2, an average value found from theoretical models [27]. Highly contracted κ'' values (1.6) for Cl were obtained in the multipole refinement. Variation of the model by forcing equality of their multipole populations did not change this result, for which we find no obvious explanation.

Coordinates and temperature factors for the hydrogen atoms were fixed at the values obtained from a separate neutron diffraction experiment [19]. A charge constraint was applied such that the cation and anion charges are +1 and -1 e. Refinement without this charge constraint led to ionic charges +0.9 and -0.9 e. These are not significantly different from the formal charges and the constraint was applied in the final refinement.

Results

Details of the final R factors and goodness of fit for the 4826 reflections used in the multipole refinement are given in Table 2. Atom labelling is shown in Figure 1. Residual densities in the planes of the cation and anion are shown in Figure 2.

Figures 3(a) and (c) show the Laplacian distributions in these planes found experimentally, computed using the program XDPROP of the XD package [23]. This was used also to obtain a critical point (CP) analysis for the bonds within the cation and anion, and for intermolecular hydrogen bonds. The bond paths (lines along which charge is concentrated, and on which the CPs are situated) are depicted in Figure 4, together with the charge densities ρ_b calculated at the bond critical points. In addition to the strong $[\text{Me}_2\text{N-H}\dots\text{NMe}_2]^+$ and $[\text{O-H}\dots\text{O}]^-$ bonds within the cation and anion there are a number of relatively weak inter-ionic $[\text{C-H}\dots\text{O}]$ bonds. These are listed in Table 3, with their geometrical parameters calculated from the nuclear positions refined with neutron diffraction data.

Hirshfeld's rigid bond test [30] was applied to the thermal parameters obtained from the refinement. It is supposed that the relative vibrational motion of a pair of covalently bonded atoms has an effectively vanishing component in the direction of the bond. If $\langle u_{A,B}^2 \rangle$ denotes the mean square displacement amplitude of atom A in

the direction of atom B, then for every covalently bonded pair of atoms A and B

$$\Delta_{A,B} = z_{A,B}^2 - z_{B,A}^2 = 0$$

Two bonds have $\Delta_{A,B}$ values slightly greater than Hirshfeld's upper limit of 0.001 \AA^2 for atoms at least as heavy as carbon, viz. C3 - C9 0.0011 , O2a - Cl1a 0.0016 \AA^2 .

For comparison with the experimental charge density distribution an *ab initio* wavefunction has been used to compute a reference theoretical distribution. The Laplacian maps derived from this using AIMPAC [28] are shown in Figures 3(b) and (d). Values of ρ_b are shown on Figure 4 for both cation and anion, along with the experimental values. The *ab initio* M.O. calculation used a 6-311G** basis set at the Hartree-Fock level of theory and included a complete, therefore neutral, cation-anion pair situated in a plane of symmetry. The single point calculation of the wavefunction was carried out using GAUSSIAN94 [29], with nuclear positions obtained from the neutron diffraction experiment [19].

Discussion

Figure 4a shows values of the charge density at bond CPs, ρ_b , for the bonds in the cation. The lines are the experimentally-determined bond paths between nuclear positions. The last figure (DMANH₂⁺) is the value of ρ_b found in the crystal: the first two figures (DMAN and DMANH⁺) are obtained from *ab initio* M.O. calculations for a molecule of unprotonated DMAN by Platts *et al.* [4], and for a molecule of protonated DMANH⁺ as described above.

In the crystal, the proton H1nn is covalently bonded to N2. The Laplacian ($\nabla^2 \rho_b$) value at the N2-H1nn CP is negative, but the N1-H1nn CP is in a region of positive $\nabla^2 \rho$, $4.3(1) \text{ e\AA}^{-5}$ at the CP. This is typical of an ionic interaction between donor hydrogen and acceptor atom. In very strong cationic [N-H...N]⁺ bonds, the lone pair of the hydrogen-bonded nitrogen becomes strongly polarized (stretched) in the direction of the hydrogen bond: this effect is clearly seen in Figure 3a and to a lesser extent in the theoretical Laplacian distribution shown in Figure 3b. The same effect was noted in a theoretical Laplacian distribution for the proton sponge 1,6-diaza[4.4.4]bicyclictetradecane by Howard *et al.* [5].

The [N-H...N]⁺ bond paths are not linear (Figure 4a). This calls into question the precise meaning of one of the conventional geometrical parameters used in characterising hydrogen bonds, namely the bond angle at the

H atom. Repulsion between N1 and N2 is evident through their outward displacements relative to C1 and C3. The attractive effect of the proton apparently does not completely counteract this. There is good agreement between the ρ_b values for DMAN and $DMANH^+$, except, as might be expected, in the neighbourhood of the hydrogen bond. These theoretical values suggest that protonation decreases the density in the C-N bonds. The $DMANH^+_{exp}$ values, however, are systematically higher than the theoretical values for $DMANH^+$, except in the C-H bonds, where they are lower.

In the anion, according to the experiment, the critical points in the strong $[O-H...O]^-$ hydrogen bond lie in regions of negative $\nabla^2\rho$ within the valence shell charge concentration (VSCC) of the H atom, reflecting some degree of apparent polarisation in a direction inclined to the O...O internuclear vector, observable on the Laplacian map (Figure 3c). The hydrogen bond paths are linear, unlike those in the cation. Furthermore, the bond angle at H is close to 180° . The H atom VSCC is separated from those of the O atoms, and there appears to be an ionic interaction between H and both donor and acceptor oxygens. The theoretical Laplacian distribution in Figure 3d, on the other hand, shows the hydrogen atom covalently bonded to O1a. Lone pairs on the chlorine atoms clearly seen in Figure 3d are not evident in the experimental map. Presumably this is a consequence of the highly contracted κ'' values for Cl noted above.

Within experimental error, the anion is symmetrical with respect to ρ_b across a line passing mid-way between C2a, C3a and O1a O4a (Figure 4b), except in the bond paths to the hydrogen atom, which carries a valence monopole charge of $+0.44(2)$ e. The formal C=O and C-O bonds have quite similar values of ρ_b , although the formally double bonds C1a-O2a and C4a-O3a are markedly shorter [$1.221(2)$ Å] than the formally single bonds C1a-O1a and C4a-O4a [$1.283(2)$, $1.287(2)$ Å]. The experimental ellipticity values for these bonds are anomalous in that more nearly equal values (0.14, 0.17) occur for C1a-O1a, C1a-O2a than for the other $-CO_2$ group. The proton is a little closer to O1a than to O4a and one might expect the left hand $-CO_2$ group to be more likely to show one single and one double bond than the right-hand one, in which the ellipticities are 0.02, 0.12.

The ellipticities computed from the wavefunction are systematically smaller but do not show this anomaly. C1a-O2a has an ellipticity of 0.09, compared with 0.00 for the formally single bond C1a-O1a. The difference between C4a-O3a (0.03) and C4a-O4a (0.00) is smaller than for the $-COOH$ group.

Protonation of DMAN to $DMANH^+$ causes de-shielding of the outer carbons as a result of migration of charge towards the positive charge of the proton. Hence the ^{13}C solid state NMR chemical shifts for the outer

carbons increase and the difference $\delta(\text{DMAN})-\delta(\text{DMANH}^+)$ is negative. The monopole charges for the carbon atoms correlate with these chemical shift differences. The outer, protonated carbons are negatively charged while the inner, quaternary carbons are positively charged. This is illustrated in Figure 5; the NMR data are taken from reference [12].

Relations exist between properties at critical points in the weak hydrogen bonds (Table 3) and their geometrical parameters. For the last few years such interactions have been a subject of intensive studies [31] - [44], and a recent review [45]. As a result of calculations of properties at CPs we have obtained the values of ρ_b and $\nabla^2\rho_b$ for non-bonded contacts defining stronger and weaker hydrogen bonds. A question can be asked whether these parameters describing properties of electron density at CPs are somehow related to the commonly accepted structural parameters for interactions such as the donor-hydrogen distances (D-H), the donor-acceptor separations (D...A), hydrogen-acceptor distances (H...A) or donor-hydrogen-acceptor angles (D-H...A), and in fact properties of the electron density at CPs have already been used to characterise different types of weak interactions [46], and, in particular, C-H...O hydrogen bonding [47].

It appears that for all C-H...A contacts listed in Table 3 (with the exception of three) the values of ρ_b are at least 10 times larger than their esds. In three cases from Table 3 (numbers 8, 9, and 11) we could not find any CPs for the H...A contacts. The value of ρ_b correlates very well with the neutron H...A internuclear distances, with correlation coefficient equal to -0.97 for the seven C-H...O contacts. The shorter the H...O distance the more electron density is accumulated at the CPs for these contacts. This relationship is illustrated in Figure 6. In general such relationships between ρ_b and structural parameters characterising a weak interaction are probably not linear ones. This seems to be the case, for example, when all types of hydrogen bonds (the strongest $[\text{N-H}\dots\text{N}]^+$ and $[\text{O-H}\dots\text{O}]^-$ through the weakest C-H...O type) in the complex $\text{DMANH}^+\text{ClMH}^-$ are considered on the same scale.

Additionally, there is a very good correlation between ρ_b and the values of $\nabla^2\rho_b$ at CPs for weak C-H...O contacts, with the correlation coefficient equal to 0.99 for seven data points (Figure 7). This means that ρ_b and $\nabla^2\rho_b$ can carry the same information for weak C-H...O contacts. The values of $\nabla^2\rho_b$ for C-H...O contacts also correlate with the H...O internuclear distances (Figure 8; correlation coefficient = -0.97).

We have carried out an *ab initio* M.O. calculation for a model system consisting of a benzene molecule and a formate ion, arranged to mimic the C-H...O bridged hydrogen bonding system found in the crystal. The

6-31G** [48] basis set supplemented with a set of anion diffuse functions [49] for the two oxygen atoms was used at the Hartree-Fock level, employing GAMESS [50]. A stable (hypothetical) complex is formed, and the values of ρ_b at the CPs located between a hydrogen atom of a benzene molecule and each oxygen atom of the ion agree well with those found in the weak C-H...O interactions in the DMAN salt (Figure 9). The ρ_b values are systematically different for the complex compared to the summed fragments obtained by superposition of the benzene and formate ion densities, but the difference in ρ_b values at the equilibrium distance for the two cases is only about twice the experimental e.s.d. on ρ_b . The difference gets larger at shorter distances than the equilibrium distance. The ρ_b value is consistently smaller for the interacting case, consistent with an ionic interaction making the atomic density distributions contract towards the nuclei.

Conclusions

This is the first experimental charge density study to explore the nature of the charged hydrogen bonds found in proton sponge complexes. The technique gives a description of properties of molecules in terms of the electron density which is more detailed than could be obtained from geometrical parameters alone. The $[\text{Me}_2\text{N}-\text{H}\dots\text{NMe}_2]^+$ hydrogen bond in the cation is bent ($\text{N}-\text{H}\dots\text{N} = 153.5^\circ$), also the bond paths are bent. On the basis of the shape of the bond paths it appears that this bond has multi-centre character with a minor contribution from an oxygen atom (O2a) in a neighbouring anion. As a result of interplay between H-bonding attractive interactions and steric repulsion between bulky NMe_2 groups, N-C(aromatic) bond paths are slightly curved, and the N atoms are pushed outwards. The lone pair of this acceptor nitrogen atom is polarised in the direction of the hydrogen bond.

Ab initio theoretical ρ_b values for DMAN and DMANH^+ moieties differ in the neighbourhood of the H-bonding site. For the DMANH^+ cation the experimental ρ_b values for C-C, C-N, and N-H bonds are systematically higher than the theoretical values. The H-bond in the ClMH^- anion is asymmetrical and almost linear in bond paths and in bond angle.

Properties at critical points appear to be useful in the description of the weakest (C-H...O) hydrogen bonds. Such weak hydrogen bonds are difficult to characterise by the use of geometrical parameters (such as donor-H...acceptor distances and angles), or by the use of thermal parameters associated with these atoms. However it is possible to obtain significant relationships between critical point properties and geometrical parameters

for these bonds. The charge density distribution provides information about weak interactions which would be missed if only geometrical parameters were analysed. The model study of the benzene...formate anion shows that the density at C-H...O hydrogen bond critical points is systematically lower than the density of the superposed moieties, but by an amount which is on the threshold of current experimental measurements analysed with multipole-based models. It suggests that improved models (or measurements) will be required before diffraction-based charge density studies can give reliable information on such weak hydrogen bonds.

Acknowledgements

We are very grateful to Dr. S.T. Howard (University of Wales, Cardiff) for a calculation of the wavefunction for the DMAN salt using the EPSRC 'Columbus' computational chemistry facility; also for useful discussions regarding the analysis of hydrogen bonding, and for a critical reading of the manuscript. We thank the Department of Chemistry, University of Warsaw, for a grant 12-501-07-BW-1343/41/96, and the UK EPSRC for a graduate studentship (for K.L.McC).

References

- [1] Alder, R.W.; Steele, W.R.S.; Winterman, D.R. *J. Chem. Soc., Chem. Commun.* 1968, 723.
- [2] Cleland, W.W.; Kreevey, M.M. *Science* 1995, 269, 104.
- [3] Frey, P.A. *Science* 1995, 269, 104.
- [4] Platts, J.A.; Howard, S.T.; Woźniak, K. *J. Org. Chem.* 1994, 59, 4647.
- [5] Howard, S.T.; Platts, J.A.; Alder R. W. *J. Org. Chem.* 1995, 60, 6085.
- [6] Platts, J.A.; Howard, S.T. *J. Org. Chem.* 1996, 61, 4480.
- [7] Staab, H.A.; Saupe, T. *Angew. Chem., Int. Ed. Engl.* 1988, 27, 865.
- [8] Einspahr, H.; Robert, J.-B.; Marsh, R.E.; Roberts, J.D. *Acta Cryst.* 1973, B29, 1611.
- [9] Woźniak, K.; He, H.; Klinowski, J.; Nogaj, B.; Lemanski, D.; Hibbs, D.; Hursthouse M.; Howard, S.T. *J. Chem. Soc., Faraday Trans.* 1995 91, 3925.
- [10] Woźniak, K.; Wilson, C.C. in preparation.

- [11] Woźniak, K. *J. Mol. Struct.* 1996, 374, 227; Grech, E.; Stefaniak, L.; Ando, I.; Yoshimizu H.; Webb, G.A. *Bull. Chem. Soc. Jpn.* 1991, 64, 3761; Woźniak, K.; He, H.; Klinowski, J.; Jones, W.; Barr, T.L.; Hardcastle, S. *J. Phys. Chem.* 1996, 100, 11408.
- [12] Woźniak, K.; He, H.; Klinowski, J.; Barr, T.L.; Milart, P. *J. Phys. Chem.* 1996, 100, 11420.
- [13] Nogaj, B.; Woźniak, K.; Lemanski, D.; Ostafin, M.; Grech, E. *Solid State NMR* 1995 4, 187.
- [14] Stephenson, D.; Smith, J.A.S. *Proc. Roy. Soc. Lond.* 1988, A416, 149.
- [15] Alder, R.W. *Chem. Rev.* 1989, 89, 1215.
- [16] Llamas-Saiz, A.L.; Foces-Foces, C.; Elguero, J. *J. Mol. Struct.* 1994, 328, 297.
- [17] Woźniak, K.; He, H.; Klinowski, J.; Grech, E. *J. Phys. Chem.* 1995, 99, 1403.
- [18] Woźniak, K.; He, H.; Klinowski, J.; Jones, W.; Barr, T.L. *J. Phys. Chem.* 1995, 99, 14667.
- [19] Woźniak, K.; Wilson, C.C.; Knight, K.S.; Jones, W.; Grech, E. *Acta Cryst.* 1996, B52, 691.
- [20] Blessing, R.H. *J. Appl. Cryst.* 1989, 22, 396, and references cited therein.
- [21] DeTitta, G. *Computer program ABSORB*. Medical Foundation of Buffalo, U.S.A., 1984.
- [22] Clementi, E.; Roetti, C. *Atomic Data and Nuclear Data Tables* 1974, 14, 177.
- [23] Koritsanszky, T.; Howard, S.T.; Richter, T.; Mallinson, P.R.; Su, Z.; Hansen, N.K. *XD, a computer program package for multipole refinement and analysis of charge densities from X-ray diffraction data*. 1995.
- [24] Stewart, R.F. *Acta Cryst.* 1976, A32, 565.
- [25] Coppens, P. *X-Ray Charge Densities and Chemical Bonding*; Oxford University Press: IUCr Texts on Crystallography No.4, 1997.
- [26] Hansen N.K.; Coppens, P. *Acta Cryst.* 1978, A34, 909.
- [27] Howard, S.T. personal communication.
- [28] Biegler-König, F.W.; Bader, R.F.W.; Tang, T.H. *J. Comput. Chem.* 1982, 3, 317.
- [29] Frisch, M.J.; Trucks, G.W.; Head-Gordon, M.; Gill, P.M.W.; Wong, M.W.; Foresman, J.B.; Johnson, B.G.; Schlegel, H.B.; Robb, M.A.; Replogle, E.S.; Gomperts, R.; Andres, J.L.; Raghavachari, K.; Binkley, J.S.;

Gonzales, C.; Martin, R.L.; Fox, D.J.; Defrees, D.J.; Baker, J.; Stewart, J.J.P.; Pople, J.A. *Gaussian 94*, Gaussian Inc., Pittsburgh PA, 1994.

- [30] Hirshfeld, F.L. *Acta Cryst.* 1976, *A32*, 239.
- [31] Steiner, T.; Saenger, W. *Acta Cryst.* 1994, *B50*, 348.
- [32] Braga, D.; Grepioni, F.; Sabatino, P.; Desiraju, G.R. *Organometallics* 1994, *13*, 3532.
- [33] Steiner, T. *J. Chem. Soc. Chem. Commun.* 1994, 2341.
- [34] Sharma, C.V.K.; Desiraju, G.R. *J. Chem. Soc. Perkin 2* 1994, 2345.
- [35] Steiner, T.; Saenger, W. *Carbohydrate Research* 1995, *266*, 1.
- [36] Steiner, T. *Acta Cryst.* 1995, *D51*, 93.
- [37] Braga, D.; Grepioni, F.; Biradha, K.; Pedireddi, V.R.; Desiraju, G.R. *J. Amer. Chem. Soc.* 1995, *117*, 3156.
- [38] Steiner, T. *J. Chem. Soc. Perkin 2* 1995, 1315.
- [39] Steiner, T.; Saenger, W. *J. Chem. Soc. Chem. Commun.* 1995, 2087.
- [40] Steiner, T.; Starikov, E.B.; Tamm, M. *J. Chem. Soc. Perkin 2* 1996, 67.
- [41] Steiner, T.; Kanters J.A.; Kroon J. *Chem. Comm.* 1996, 1277.
- [42] Desiraju, G.R. *Accounts of Chemical Research* 1996, *29*, 441.
- [43] Subramanian, K.; Lakshmi, S.; Rajagopalan, K.; Koellner, G.; Steiner, T. *J. Mol. Struct.* 1996, *384*, 121.
- [44] Steiner, T.; Lutz, B.; van der Maas, J.; Veidman, N.; Schreurs, A.M.M.; Kroon, J.; Kanters, J.A. *Chem. Comm.* 1997, 191.
- [45] Steiner, T. *Chem. Comm.* 1997, 727.
- [46] Tsirelson, V.G.; Zou, P.F.; Tang, T.-H.; Bader, R.F.W. *Acta Cryst.* 1995 *A51*, 143.
- [47] Koch, U.; Popelier, P.L.A. *J. Phys. Chem.* 1995, *99*, 9747.
- [48] Hehre, W.J.; Ditchfield, R.; Pople, J.A. *J. Chem. Phys.* 1972, *56*, 2257. Ditchfield, R.; Hehre, W.J.; Pople, J.A. *J. Chem. Phys.* 1971, *54*, 724. Harihavan, P.C.; Pople, J.A. *Theoret. Chim. Acta* 1973, *28*, 213.

[49] Frisch, M.J.; Pople, J.A.; Binkley, J.S. *J. Chem. Phys.* 1984, 80, 3265.

[50] Schmidt, M.W.; Baldrige, K.K.; Boatz, J.H.; Elbert, S.T.; Gordon, M.S.; Jensen, J.J.; Koseki, S.; Matsunaga, N.; Nguyen, K.A.; Su, S.; Windus, T.L.; Dupuis, M.; Montgomery, J.A. *J. Comp. Chem.* 1993, 14, 1347.

Supporting information available:

Fractional atomic coordinates and anisotropic displacement parameters. Monopole charges, κ' and κ'' values obtained from the refinement. Critical point data. Multipole population coefficients. Definitions of local axes. Observed and calculated structure factors. Bond lengths and angles from this work and ref. [19] (pp). Ordering information is given on any current masthead page.

Table 1

Basicities of some substituted 1,8-diaminonaphthalenes

R ¹	R ²	R ³	pK _a
NH ₂	NH ₂	H	4.61
NHMe	NHMe	H	5.61
NMe ₂	NHMe	H	6.43
NMe ₂	NMe ₂	H	12.1
NEt ₂	NEt ₂	H	12.7
NMe ₂	NMe ₂	OMe	16.1
NEt ₂	NEt ₂	OMe	16.3

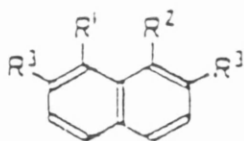


Table 2

Experimental data for the complex of 1,8-bis(dimethylamino)naphthalene
with 1,2-dichloromaleic acid

Formula	$[\text{C}_{14}\text{H}_{19}\text{N}_2]^+ [\text{C}_4\text{HCl}_2\text{O}_4]^-$
Molecular weight	399.3
Space group (orthorhombic)	<i>Pmna</i>
Temperature/K	100(5)
Unit cell dimensions/Å	
<i>a</i>	18.078(2)
<i>b</i>	6.977(1)
<i>c</i>	14.356(3)
<i>V</i> /Å ³	1810.7(6)
<i>Z</i>	4
<i>D_c</i> /g cm ⁻³	1.46
Crystal dimensions/mm	0.4 x 0.2 x 0.2
Absorption coefficient/cm ⁻¹	3.8
Range of corrections for absorption by crystal	0.906 - 0.939
Radiation	Mo K _α ; λ = 0.7107 Å
Scan type	θ - 2θ
$\frac{\sin \theta}{\lambda} \text{ max}/\text{Å}^{-1}$	1.102
(hkl) lower limit-upper limit	-39 39: -14 14: -30 30
Time period/h	574
No. of standard reflections	6 (2 2 $\bar{1}$, 1 1 1, 0 0 2 0 6 0, 2 $\bar{2}$ $\bar{1}$, 4 1 $\bar{2}$)
No. of reflections measured	17224
No. of symmetry-independent reflections	4931
No. of <i>I</i> > 2σ(<i>I</i>) reflections	3922
No. of symmetry-related and repeated reflections	4826
Agreement factor $R = \Sigma I - \bar{I} /\Sigma I$	0.029
Refined on	<i>F</i>
<i>R</i>	0.0241
<i>R_w</i>	0.0244
<i>S</i>	0.925
$\frac{N_{obs}}{N_{var}}$	8.3
Weighting scheme	$w = \frac{1}{\sigma^2(F)} = \frac{4F^2}{\sigma^2(F^2)}$
Positional and thermal parameters for H atoms taken from refinement with neutron data	$\sigma^2(F^2) = \sigma_{counting}^2(F^2) + P^2 F^4$

Table 3

Geometry of the hydrogen bonds in DMANH⁺ CIMH⁻ calculated from neutron data

(D signifies donor, A acceptor)

	D-H/A	H...A/A. Symmetry	D...A/A	DHA(°)
1	N2-H1nn 1.106(5)	H1nn...N1 1.608(6)	N2...N1 2.644(2)	N2-H1nn...N1 153.3(5)
2	O1a-H1oo 1.149(7)	H1oo...O4a 1.235(7)	O1a...O4a 2.383(4)	O1a-H1oo...O4a 178.5(6)
3	C11-H111 1.084(4)	H111...O2a. 0.5+X, Y, 2.5-Z 2.410(6)	C11...O2a 3.118(3)	C11-H111...O2a 121.6(4)
4	C14-H141 1.095(4)	H141...O2a. 0.5+X, Y, 2.5-Z 2.535(6)	C14...O2a 3.235(3)	C14-H141...O2a 120.8(3)
5	N2-H1nn 1.106(5)	H1nn...O2a. 0.5+X, Y, 2.5-Z 2.437(6)	N2...O2a 3.055(3)	N2-H1nn...O2a 113.7(4)
6	C7-H7 1.087(6)	H7...O3a 2.107(7)	C7...O3a 3.193(4)	C7-H7...O3a 176.1(6)
7	C14-H142 1.096(5)	H142...O4a. -X, -Y, 2-Z 2.353(5)	C14...O4a 3.408(3)	C14-H141...O4a 160.9(4)
8	C14-H141 1.095(4)	H141...O1a. 0.5+X, Y, 2.5-Z 2.815(5)	C14...O1a 3.844(3)	C14-H141...O1a 156.6(4)
9	C14-H142 1.096(5)	H142...O3a. -X, -Y, 2-Z 2.778(7)	C14...O3a 3.514(4)	C14-H142...O3a 124.2(4)
10	C14-H143 1.091(5)	H143...O3a 2.570(6)	C14...O3a 3.575(4)	C14-H143...O3a 152.8(4)
11	C11-H111 1.084(4)	H111...C11a. 0.5+X, Y, 2.5-Z 3.029(5)	C11...C11a 4.028(3)	C11-H111...C11a 153.5(5)
12	C11-H112 1.084(5)	H112...C12a. 0.5-X, -Y, Z-0.5 2.941(5)	C11...C12a 3.654(2)	C11-H112...C12a 123.0(4)
13	C11-H113 1.090(6)	H113...O4a. -X, -Y, 2-Z 2.718(6)	C11...O4a 3.749(3)	C11-H113...O4a 157.7(4)
14	C11-H113 1.090(6)	H113...O1a. -X, -Y, 2-Z 2.797(6)	C11...O1a 3.586(3)	C11-H113...O1a 129.1(5)
15	C4-H4 1.099(6)	H4...C11a. X, Y, Z-1 2.760(6)	C4...C11a 3.338(3)	C4-H4...C11a 166.4(5)
16	C5-H5 1.100(6)	H5...C11a. X, Y, Z-1 3.137(7)	C5...C11a 4.123(3)	C5-H5...C11a 149.6(5)

Figure captions

Figure 1. Anisotropic displacement ellipsoids for (a) the cation and (b) the anion, drawn at 50% probability, showing the labelling of the atoms.

Figure 2. Residual density in the plane of (a) the cation and (b) the anion. Contour interval = $0.1 \text{ e}\text{\AA}^{-3}$. Zero and negative contours are broken and dotted, respectively.

Figure 3. Laplacian maps (a) in the plane of the cation computed from the experimental multipole populations; (b) from the *ab initio* wavefunction; (c) for the anion, from the experiment; (d) from the wavefunction. Contours at logarithmic intervals in $-\nabla^2 \rho \text{ e}\text{\AA}^{-5}$.

Figure 4. Bond paths (lying in the crystallographic mirror plane of the ions), showing locations of critical points and values of ρ_b , in (a) the cation (DMANH_{22p}^+) and (b) the anion. The values labelled DMAN and DMANH^+ are obtained from *ab initio* theoretical calculations for the free base (ref. [4]) and protonated base, respectively.

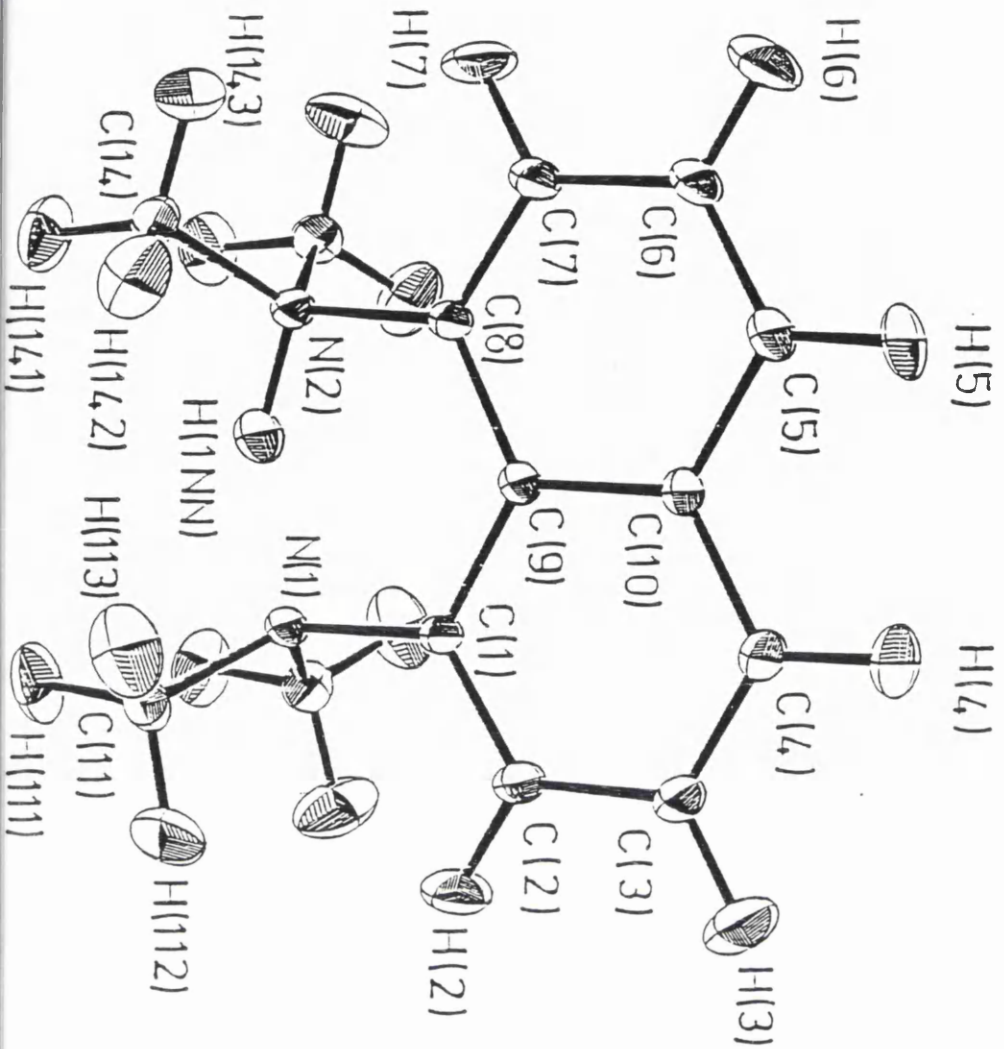
Figure 5. Chemical shift differences, $\delta(\text{DMAN})-\delta(\text{DMANH}^+)$ (/ppm, italic, from ref. [12]), and monopole charges (/e).

Figure 6. Plot of ρ_b vs H...A internuclear distance (A signifies acceptor); $\rho_b = -0.13(2)\text{H}\dots\text{A} + 0.37(4)$; $R = -0.97$ for $n = 7$ data points.

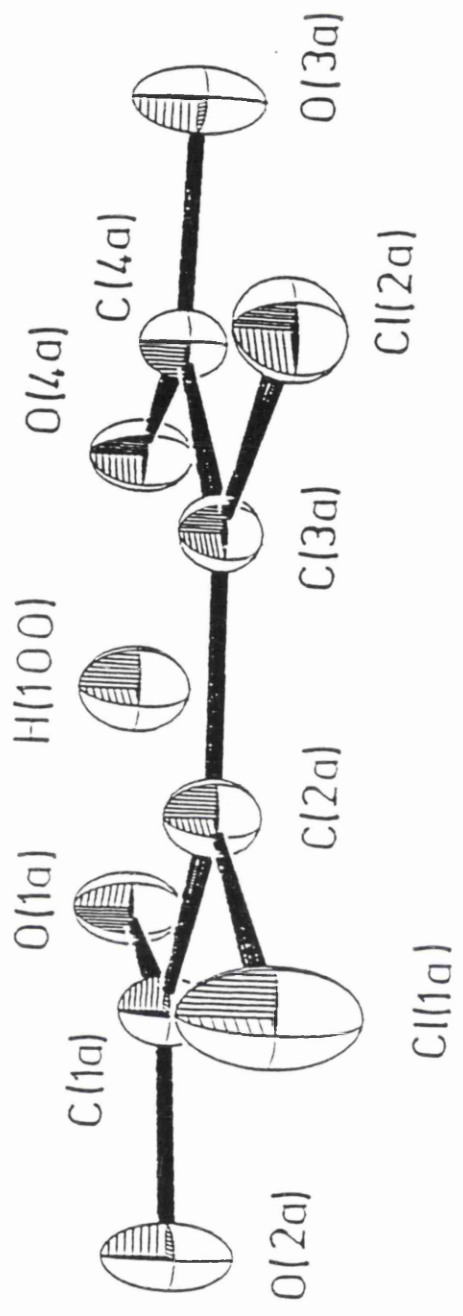
Figure 7. Plot of ρ_b vs $\nabla^2 \rho_b$; $\rho_b = 0.056(4)\nabla^2 \rho_b + 0.003(4)$; $R = 0.99$ for $n = 7$ data points.

Figure 8. Plot of $\nabla^2 \rho_b$ vs H...A internuclear distance: $\nabla^2 \rho_b = -2.2(2)\text{H}\dots\text{A} + 6.5(6)$; $R = -0.97$ for $n = 7$ data points.

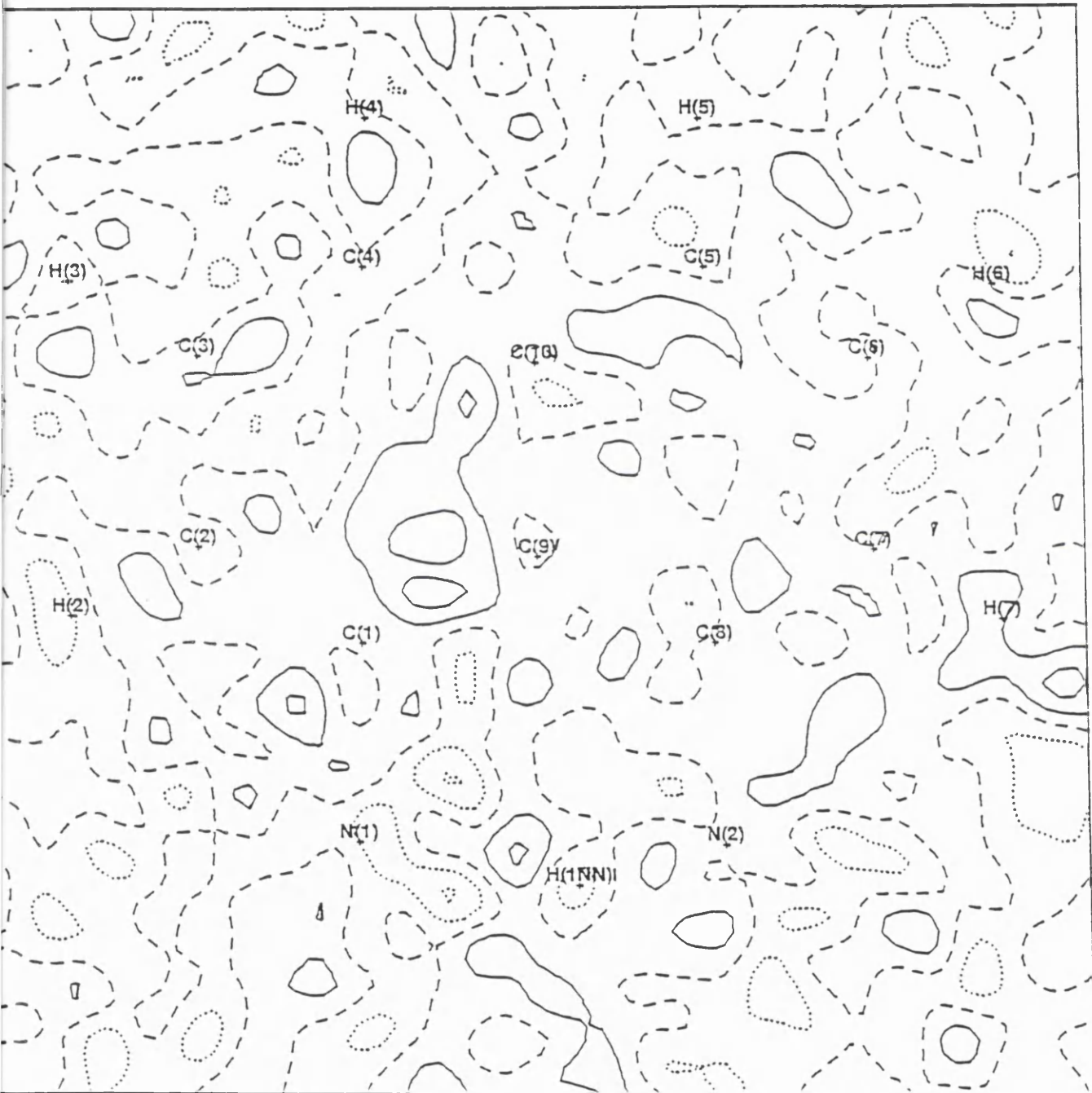
Figure 9. Plot of ρ_b vs H...O internuclear distance for the formate ion and benzene molecule model system. Data points marked by circles show ρ_b values for the complex: $\rho_b = 10.625 \exp(-2.073\text{H}\dots\text{O})$; squares for the summed fragments: $\rho_b = 13.457 \exp(-2.102\text{H}\dots\text{O})$.



2

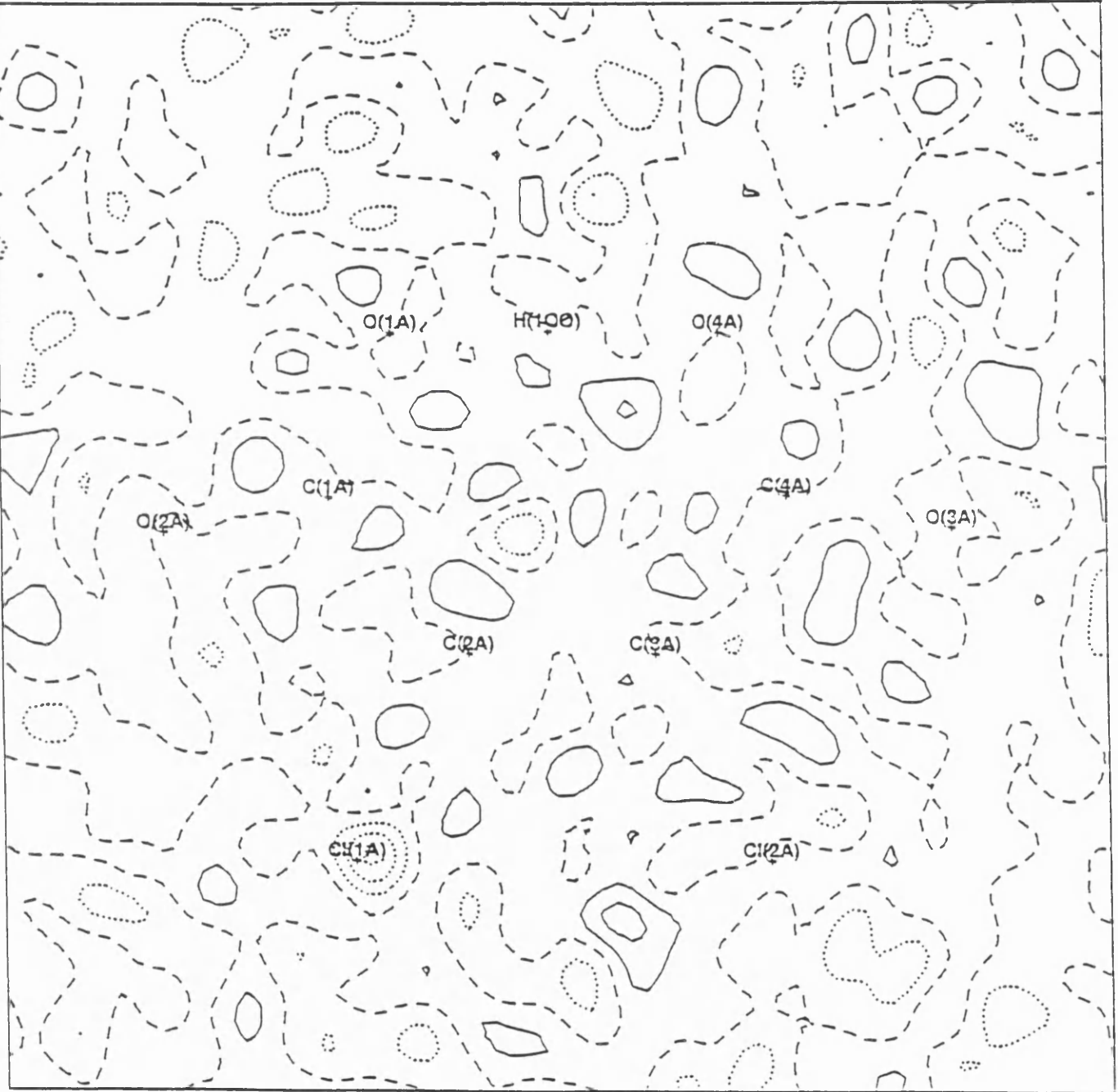


16

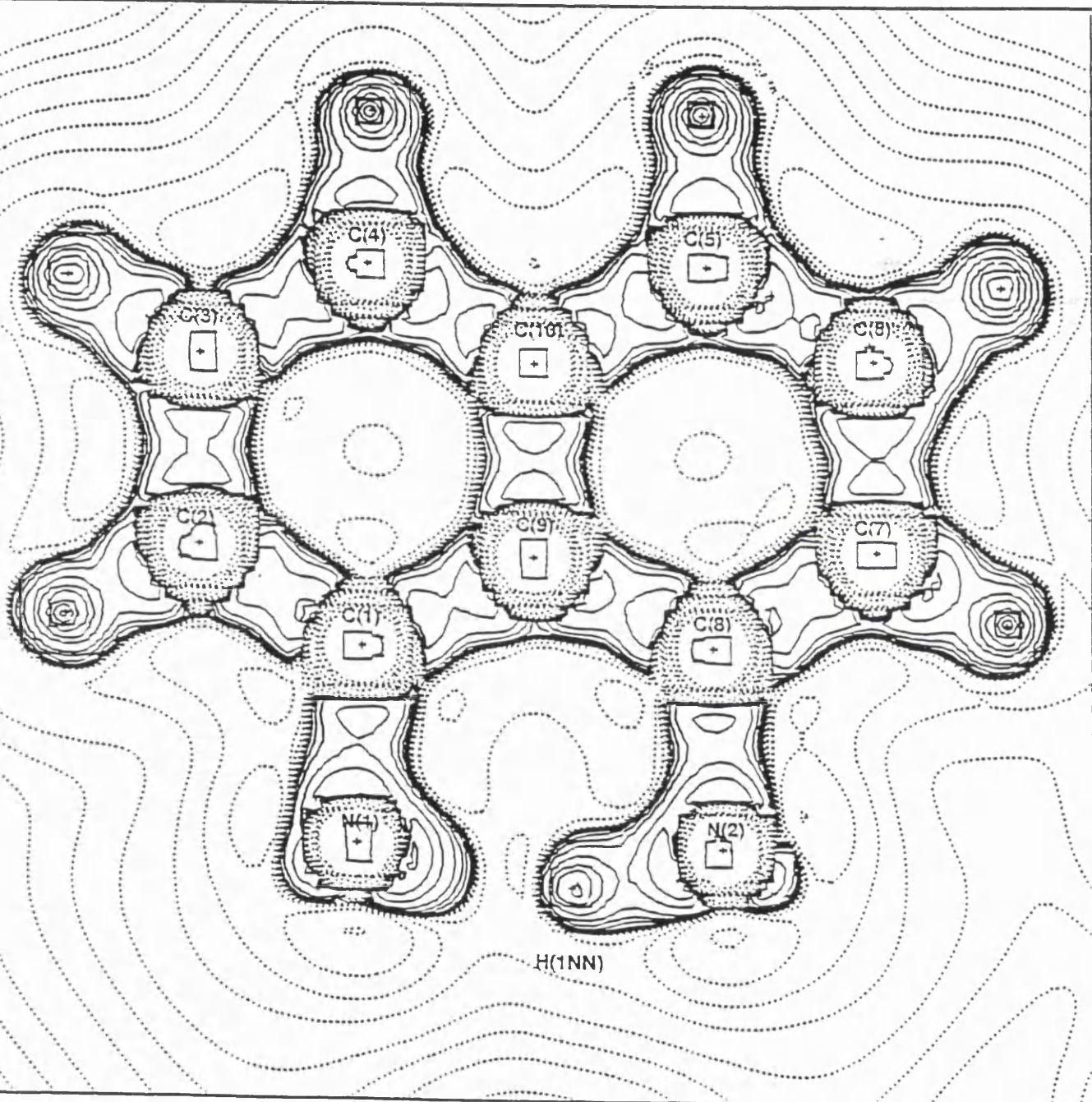


FOU

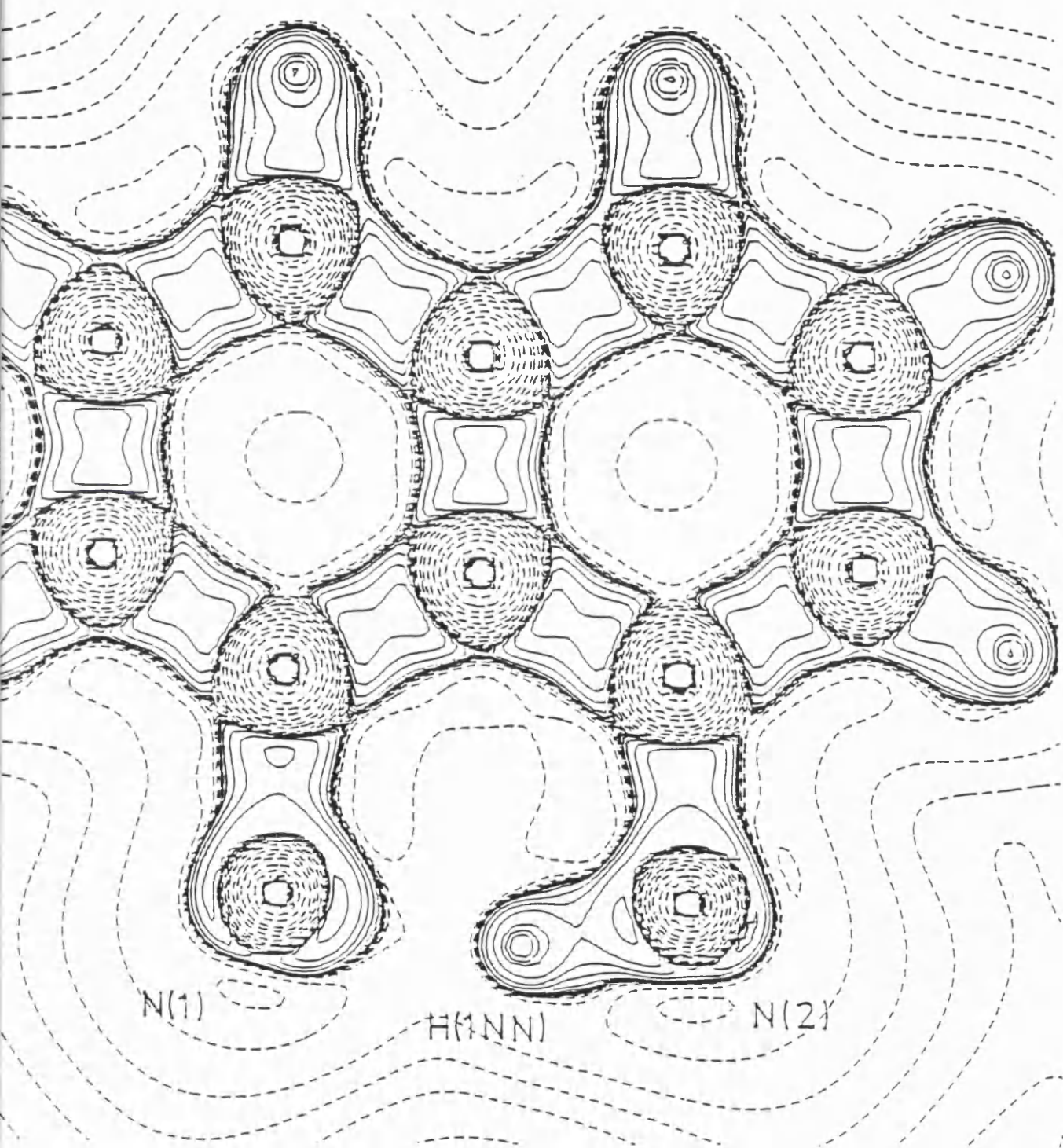
2a

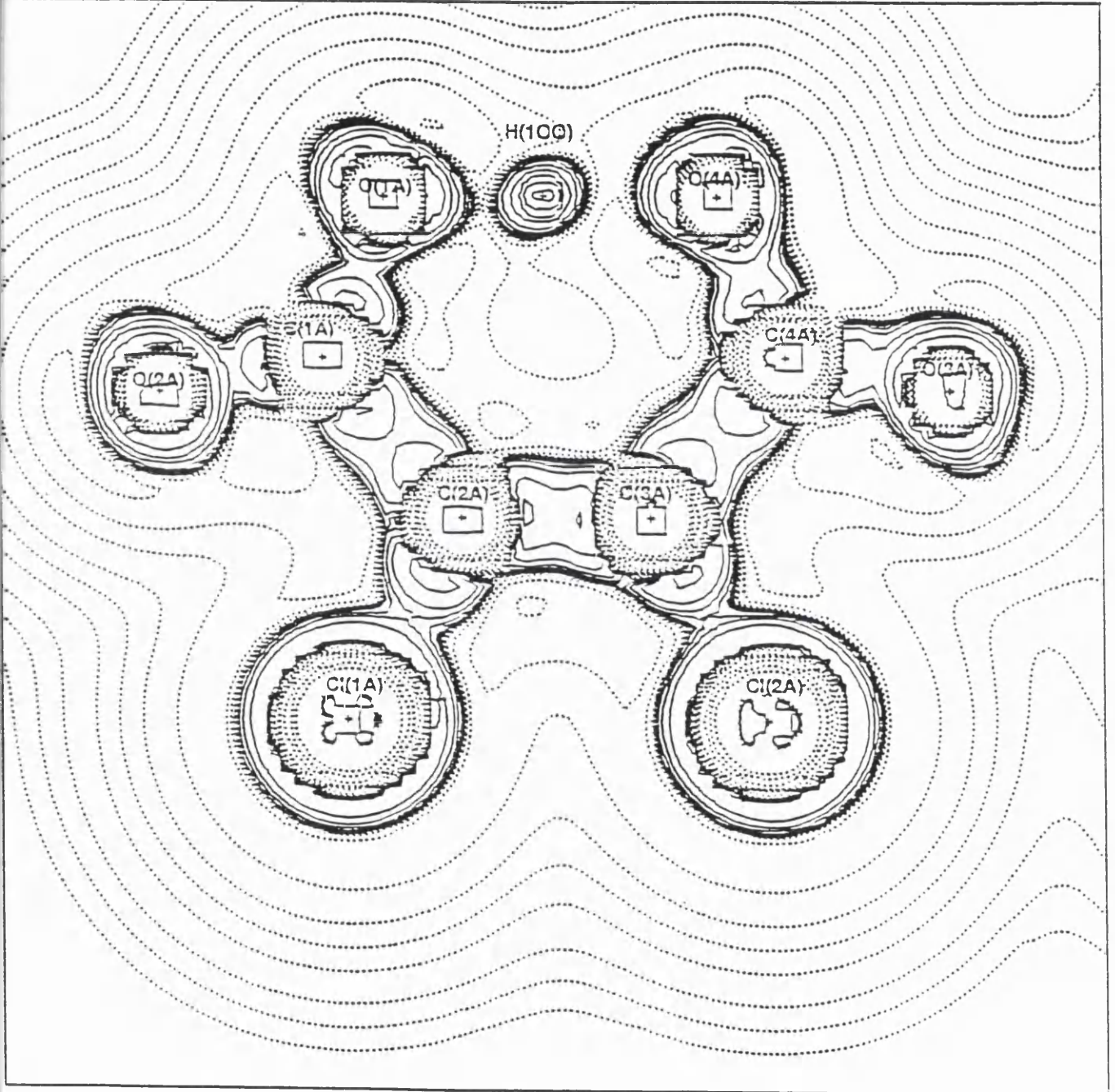


FOU

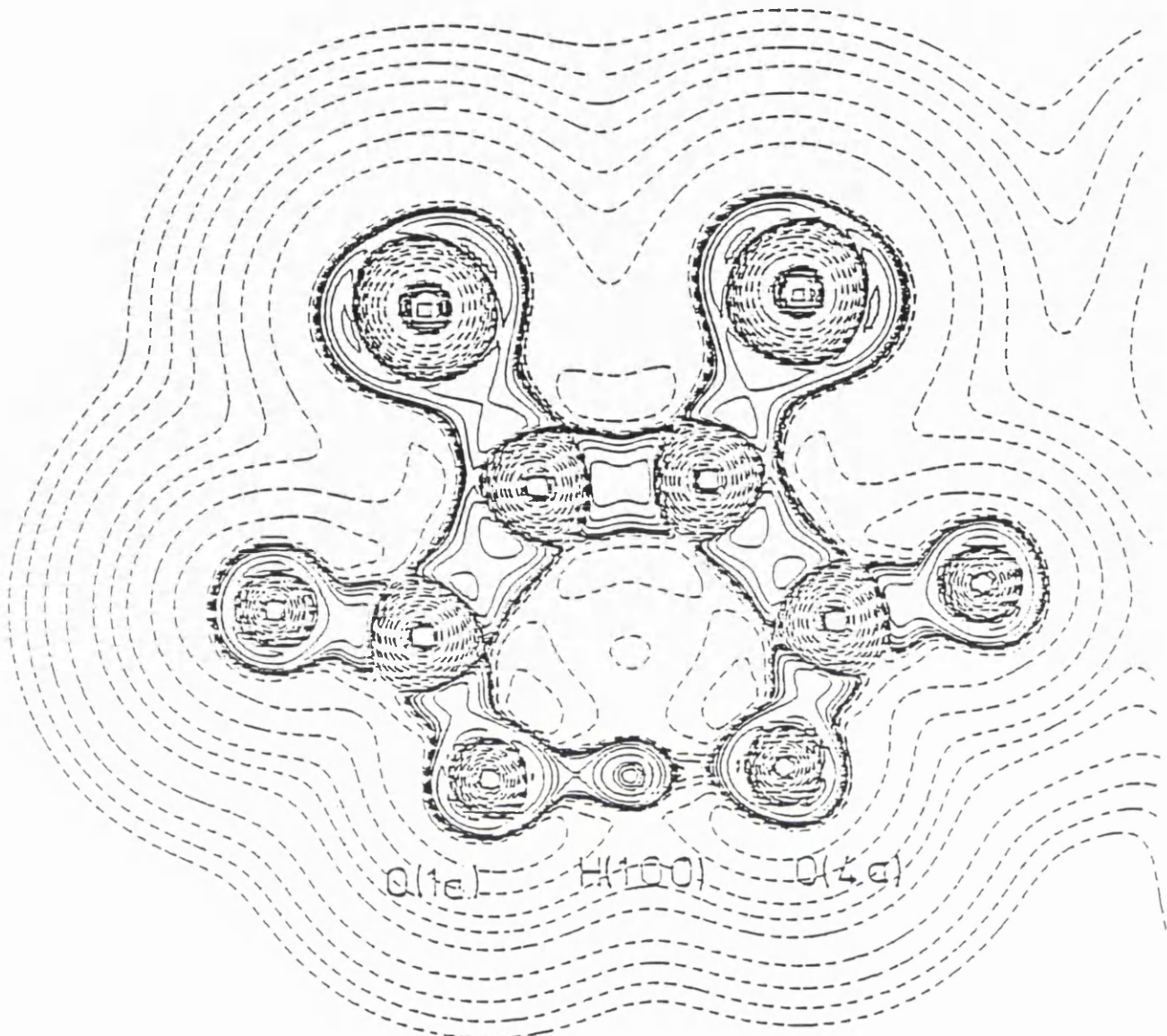


3a

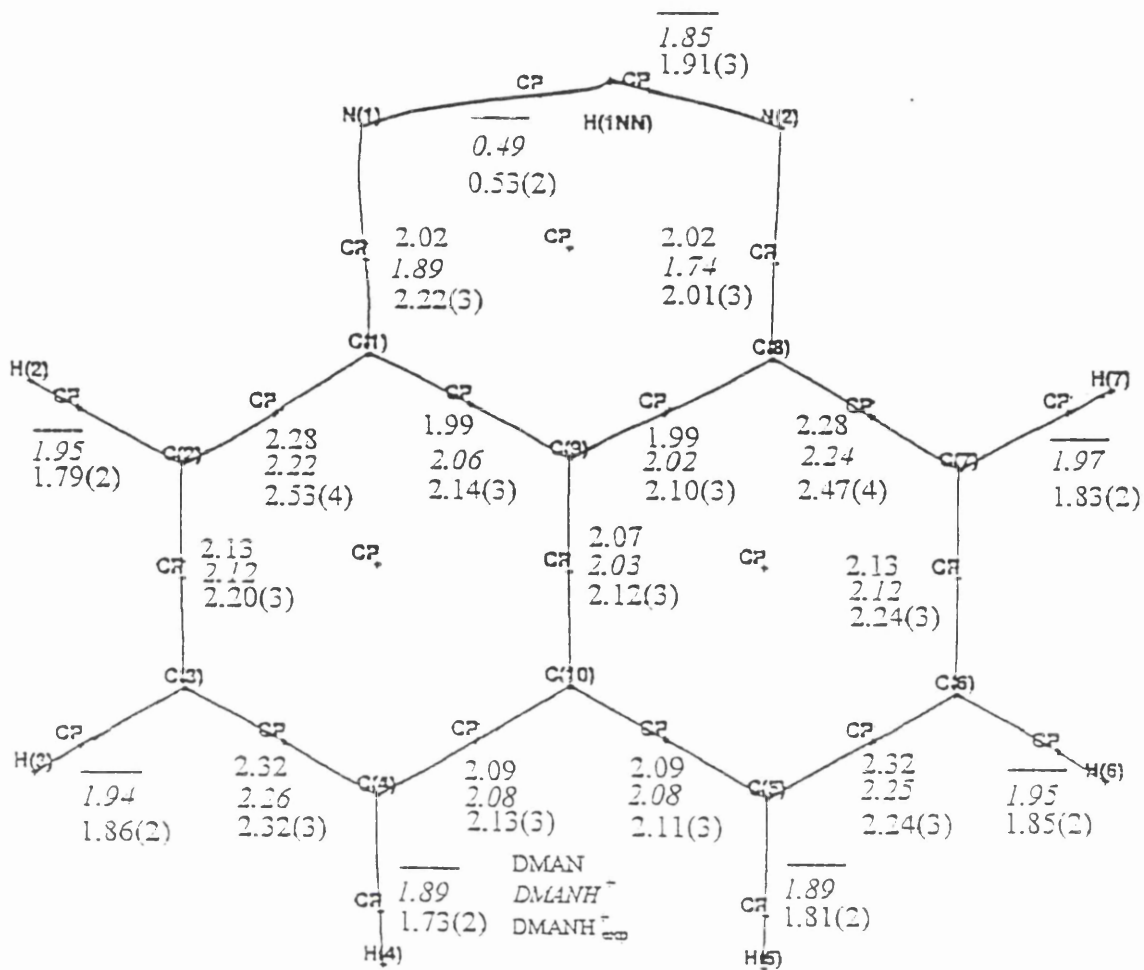


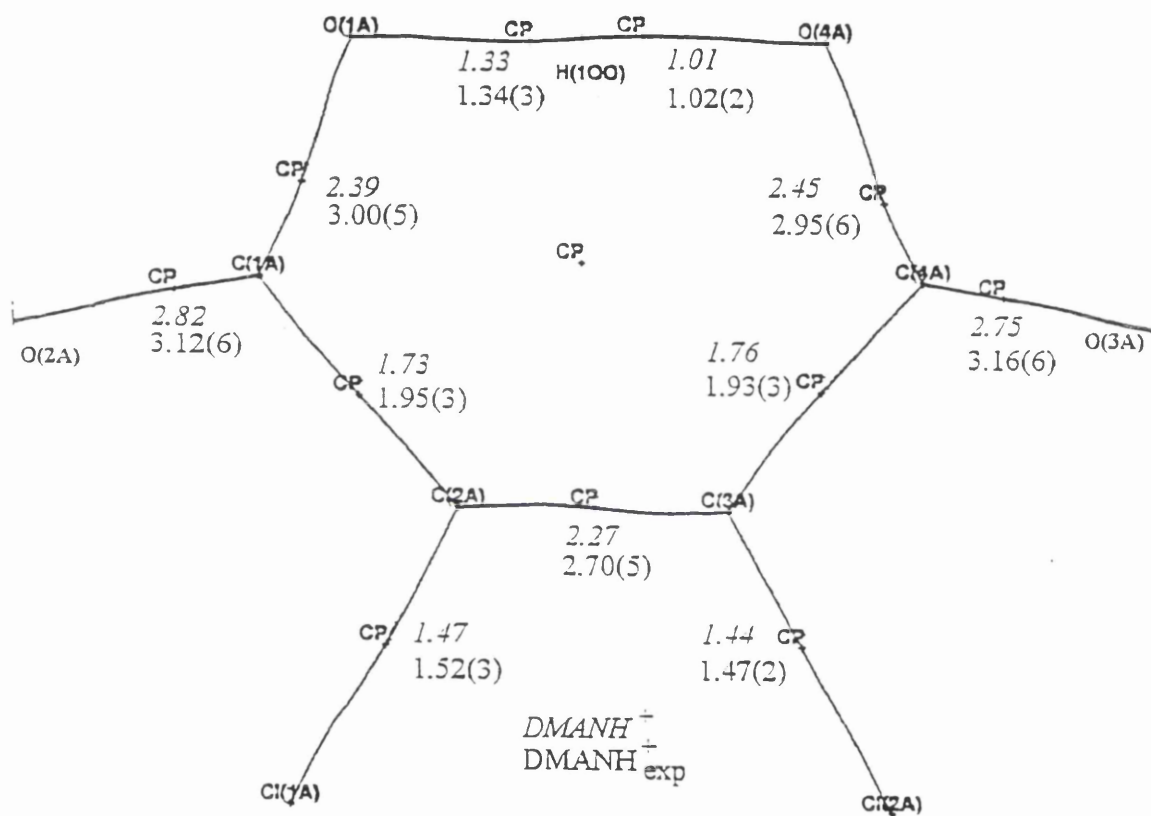


3c

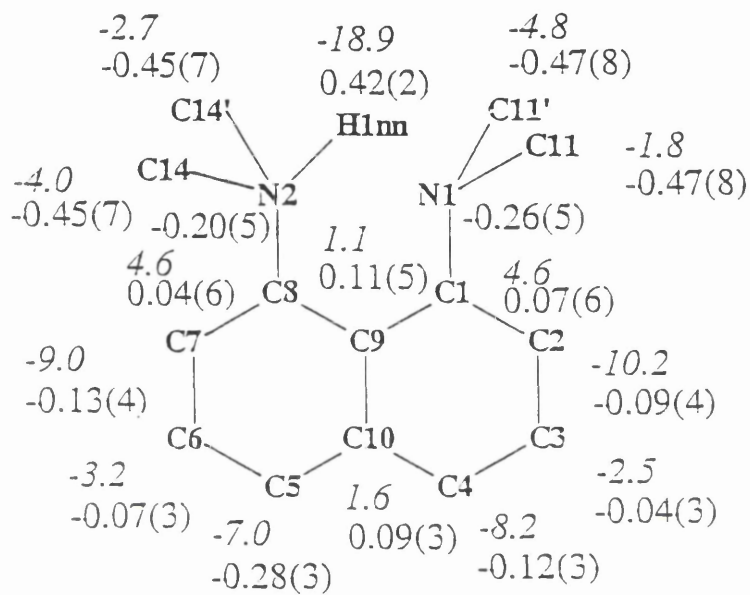


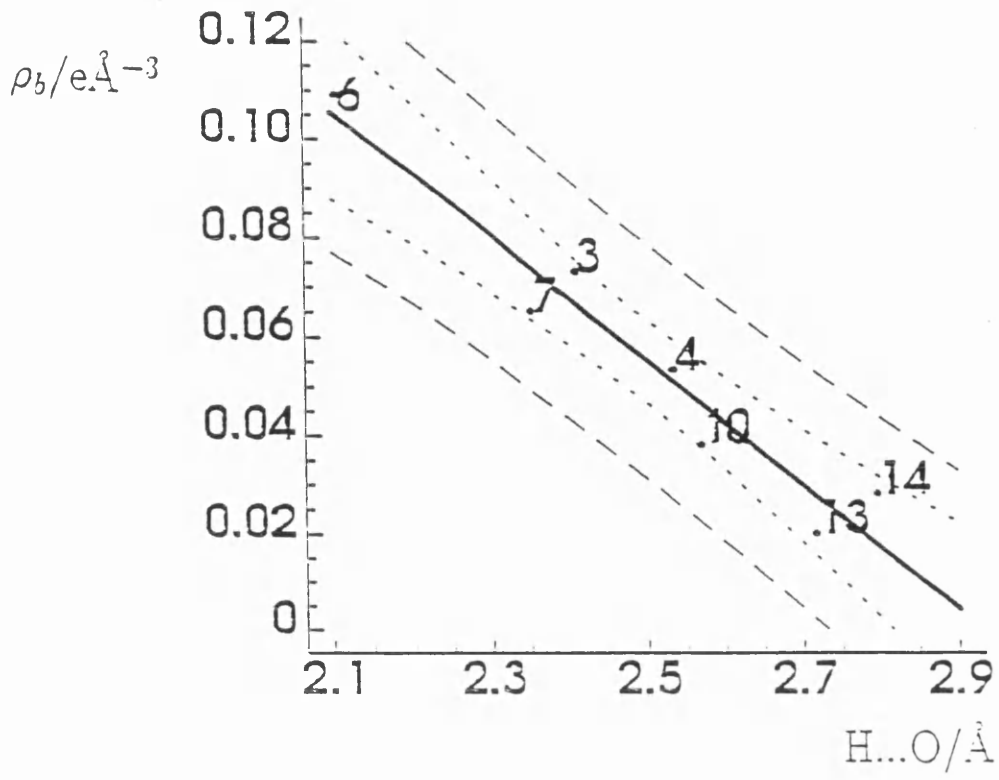
3d



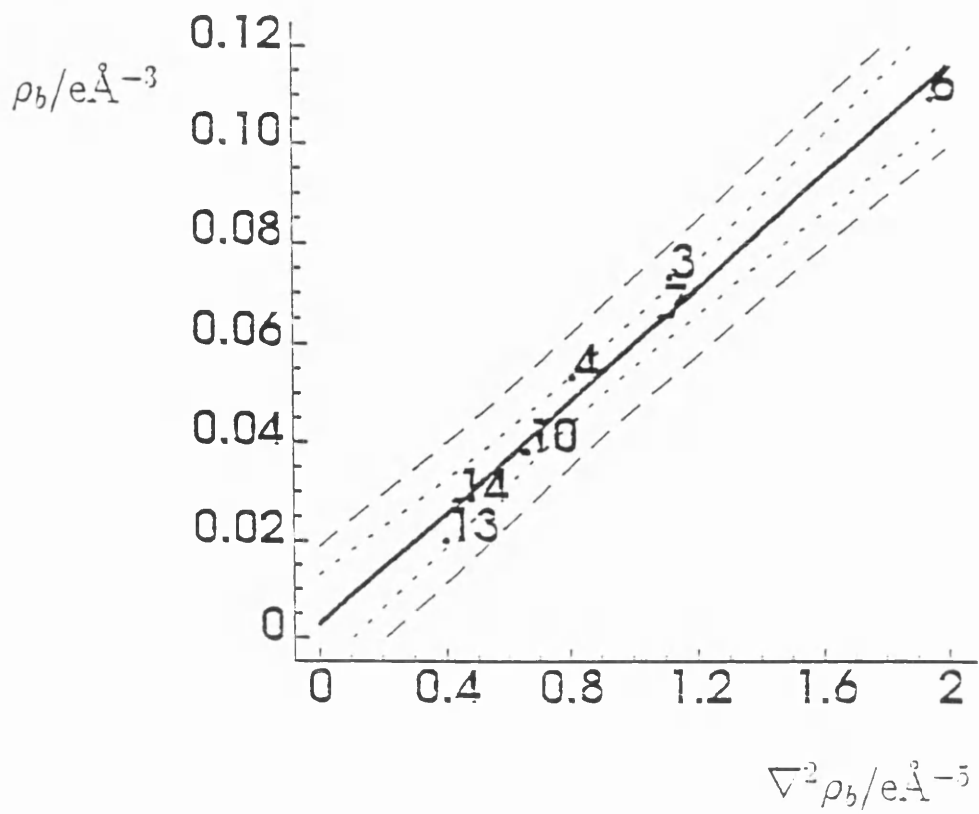


46

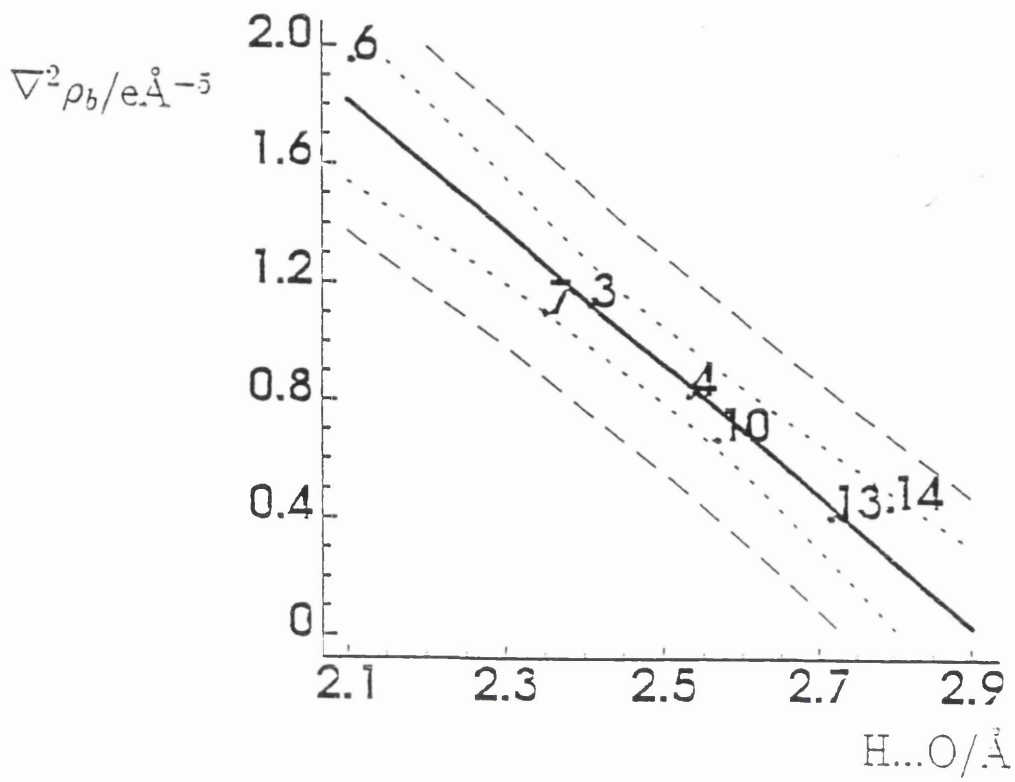




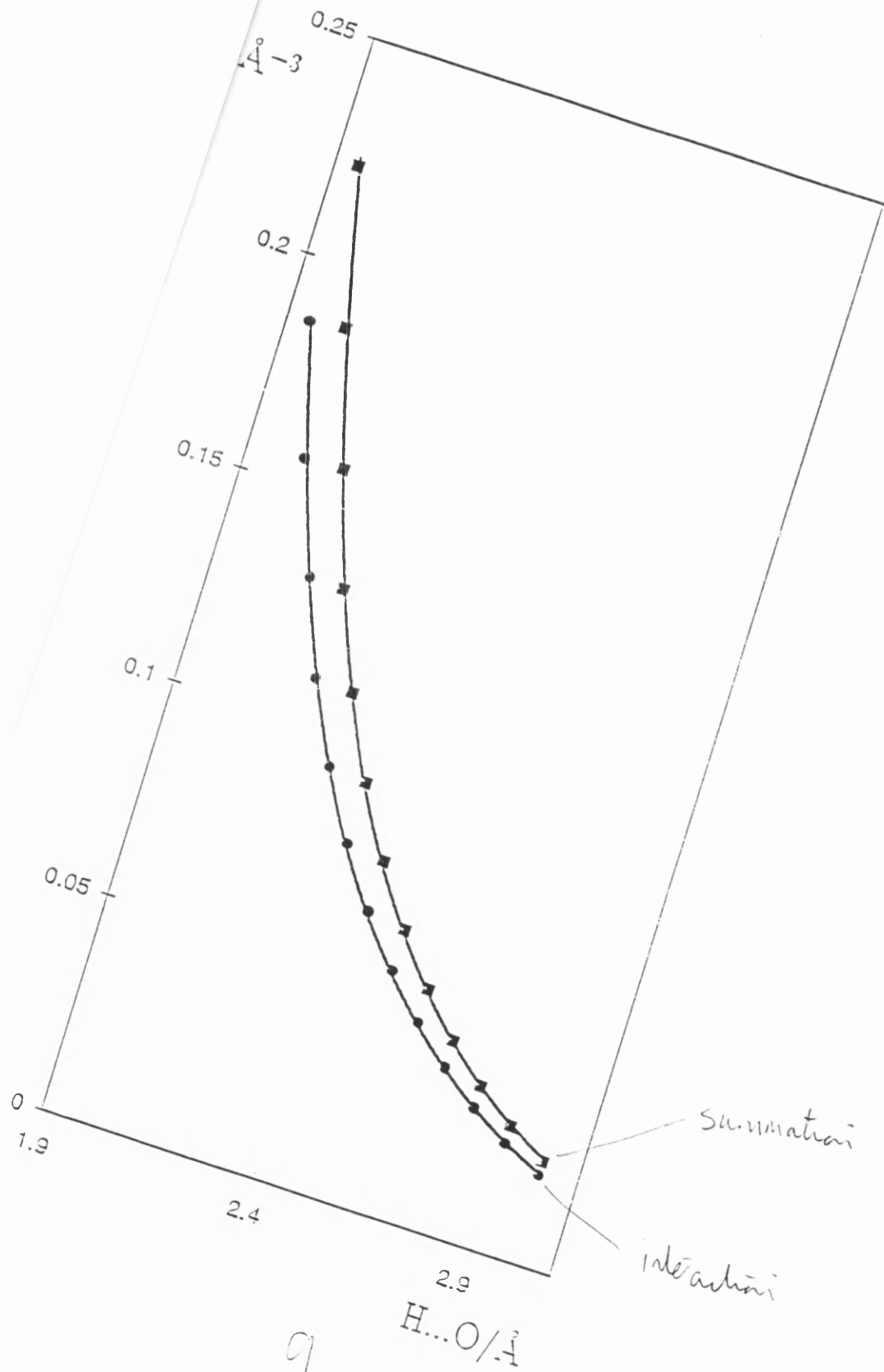
6



7



8



9.

Reprinted from

CHEMICAL PHYSICS LETTERS

Chemical Physics Letters 273 (1997) 179–182

Muonium radical formation in elemental sulphur

S.F.J. Cox ^{a,b}, I.D. Reid ^c, K.L. McCormack ^d, B.C. Webster ^d

^a *ISIS Facility, Rutherford Appleton Laboratory, Chilton, Oxfordshire OX11 0QX, UK*

^b *Department of Physics, University College London, WC1E 6BT London, UK*

^c *Muon Spectroscopy Group, Paul Scherrer Institute, CH 5232 Villigen PSI, Switzerland*

^d *Department of Chemistry, University of Glasgow, Glasgow G12 8QQ, UK*

Received 24 March 1997; revised 16 May 1997



ELSEVIER

ADVISORY EDITORIAL BOARD

Australia
B.J. ORR, Sydney

Canada
P.A. HACKETT, Ottawa
J.W. HEPBURN, Waterloo
C.A. McDOWELL, Vancouver

Czech Republic
Z. HERMAN, Prague

Denmark
F. BISENBACHER, Aarhus
G.D. BILLING, Copenhagen

France
E. CLEMENTI, Strasbourg
J. DURUP, Toulouse
J.-M. LEHN, Strasbourg
J.-L. MARTIN, Palaiseau
B. SOEP, Orsay

Germany
R. AHLRICHS, Karlsruhe
V.E. BONDYBEY, Garching
W. DOMCKE, Dusseldorf
G. ERTL, Berlin
G. GERBER, Würzburg
G.L. HOFACKER, Garching
D.M. KOLB, Ulm
J. MANZ, Berlin
M. PARRINELLO, Stuttgart
S.D. PEYERIMHOFF, Bonn
R. SCHINKE, Göttingen
E.W. SCHLAG, Garching
J. TROE, Göttingen
H.C. WOLF, Stuttgart
W. ZINTH, Munich

India
C.N.R. RAO, Bangalore

Israel
J. JORTNER, Tel Aviv
R.D. LEVINE, Jerusalem

Italy
V. AQUILANTI, Perugia

Japan
H. HAMAGUCHI, Tokyo
M. ITO, Okazaki
T. KOBAYASHI, Tokyo
K. KUCHITSU, Sakado
H. NAKATSUJI, Kyoto
K. TANAKA, Tokyo
K. YOSHIHARA, Okazaki

People's Republic of China
C.-H. ZHANG, Beijing

Poland
Z.R. GRABOWSKI, Warsaw

Russian Federation
A.L. BUCHACHENKO, Moscow
V.S. LETOKHOV, Troitzk
Yu.N. MOLIN, Novosibirsk

Spain
A. GONZÁLEZ UREÑA, Madrid

Sweden
P.E.M. SIEGBAHN, Stockholm
V. SUNDSTRÖM, Lund

Switzerland
M. CHERGUI, Lausanne-Dorigny
R.R. ERNST, Zurich
M. QUACK, Zurich

Taiwan, ROC
Y.T. LEE, Taipei

The Netherlands
A.J. HOFF, Leiden
A.W. KLEYN, Amsterdam
D.A. WIERSMA, Groningen

United Kingdom
M.N.R. ASHFOLD, Bristol
G.S. BEDDARD, Leeds
M.S. CHILD, Oxford

D.C. CLARY, London
R. FREEMAN, Cambridge
R.H. FRIEND, Cambridge
N.C. HANDY, Cambridge
A.C. LEGON, Exeter
R.M. LYNDEN-BELL, Belfast
J.P. SIMONS, Oxford
I.W.M. SMITH, Birmingham

USA
P. AVOURIS, Yorktown Heights, NY
A.J. BARD, Austin, TX
A.W. CASTLEMAN Jr., University Park, PA
S.T. CEYER, Cambridge, MA
D. CHANDLER, Berkeley, CA
F.F. CRIM, Madison, WI
A. DALGARNO, Cambridge, MA
C.E. DYKSTRA, Indianapolis, IN
K.B. EISENTHAL, New York, NY
M.A. EL-SAYED, Atlanta, GA
M.D. FAYER, Stanford, CA
G.R. FLEMING, Chicago, IL
R.M. HOCHSTRASSER, Philadelphia, PA
J.L. KINSEY, Houston, TX
S.R. LEONE, Boulder, CO
M.I. LESTER, Philadelphia, PA
W.C. LINEBERGER, Boulder, CO
B.V. McKOY, Pasadena, CA
W.H. MILLER, Berkeley, CA
K. MOROKUMA, Atlanta, GA
S. MUKAMEL, Rochester, NY
A. PINES, Berkeley, CA
A.R. RAVISHANKARA, Boulder, CO
S.A. RICE, Chicago, IL
P.J. ROSSKY, Austin, TX
R.J. SAYKALLY, Berkeley, CA
H.F. SCHAEFER III, Athens, GA
G.C. SCHATZ, Evanston, IL
R.E. SMALLEY, Houston, TX
W.C. STWALLEY, Storrs, CT
D.G. TRUHLAR, Minneapolis, MN
J.J. VALENTINI, New York, NY
G.M. WHITESIDES, Cambridge, MA
C. WITTIG, Los Angeles, CA
P.G. WOLYNES, Urbana, IL
J.T. YATES Jr., Pittsburgh, PA
R.N. ZARE, Stanford, CA

Contributions should, preferably, be sent to a member of the Advisory Editorial Board (addresses are given in the first issue of each volume) who is familiar with the research reported, or to one of the Editors:

A.D. BUCKINGHAM
D.A. KING
Editor of Chemical Physics Letters
University Chemical Laboratory
Lensfield Road
Cambridge CB2 1EW, UK
FAX 44-1223-336362

A.H. ZEWAİL
Editor of Chemical Physics Letters
A.A. Noyes Laboratory of Chemical Physics
California Institute of Technology
Mail Code 127-72
Pasadena, CA 91125, USA
FAX 1-818-4050454

After acceptance of the paper for publication, all further correspondence should be sent to the publishers (Ms. S.A. Hallink, Issue Management (Chemistry), Elsevier Science B.V., P.O. Box 2759, 1000 CT Amsterdam, The Netherlands; telephone 31-20-4852664, FAX 31-20-4852775, telex 10704 espom nl; electronic mail X400: C=NL; A=400NET; P=SURF; O=ELSEVIER; S=HALLINK, I=S or RFC822: S.HALLINK@ELSEVIER.NL).

Publication information: Chemical Physics Letters (ISSN 0009-2614). For 1997, volumes 264–280 are scheduled for publication. Subscription prices are available upon request from the publisher. Subscriptions are accepted on a prepaid basis only and are entered on a calendar year basis. Issues are sent by surface mail except to the following countries where Air delivery via SAL is ensured: Argentina, Australia, Brazil, Canada, Hong Kong, India, Israel, Japan, Malaysia, Mexico, New Zealand, Pakistan, PR China, Singapore, South Africa, South Korea, Taiwan, Thailand, USA. For all other countries airmail rates are available upon request. Claims for missing issues must be made within six months of our publication (mailing) date.

Copyright © 1997, Elsevier Science B.V. All rights reserved

0009-2614/1997/\$17.00

US mailing notice – Chemical Physics Letters (ISSN 0009-2614) is published weekly by Elsevier Science B.V., Molenwerf 1, P.O. Box 211, 1000 AE Amsterdam. Annual subscription price in the USA US\$ 7818.00, including air speed delivery, valid in North, Central and South America only. Periodicals postage paid at Jamaica, NY 11431. USA POSTMASTERS: Send address changes to Chemical Physics Letters, Publications Expediting, Inc., 200 Meacham Avenue, Elmont, NY 11003. Airfreight and mailing in the USA by Publication Expediting.

Printed in The Netherlands

Published weekly

Library of Congress Catalog Card Number 68-26532



Muonium radical formation in elemental sulphur

S.F.J. Cox ^{a,b}, I.D. Reid ^c, K.L. McCormack ^d, B.C. Webster ^d

^a ISIS Facility, Rutherford Appleton Laboratory, Chilton, Oxfordshire OX11 0QX, UK

^b Department of Physics, University College London, WC1E 6BT London, UK

^c Muon Spectroscopy Group, Paul Scherrer Institute, CH 5232 Villigen PSI, Switzerland

^d Department of Chemistry, University of Glasgow, Glasgow G12 8QQ, UK

Received 24 March 1997; revised 16 May 1997

Abstract

The formation of a molecular radical following muon implantation in sulphur S₈ is established experimentally by level crossing resonance. The position of the resonance determines the hyperfine constant as 233 ± 5 MHz. Of various possible assignments evaluated by ab initio molecular orbital calculations, the most promising appears to be the muonic sulfanyl radical, $\dot{S}\text{Mu}$. © 1997 Published by Elsevier Science B.V.

1. Introduction

Positive muons mimic the chemical behaviour of protons. In particular, these short-lived elementary particles can form a one-electron atom known as muonium, $\text{Mu} = \mu^+e^-$, which behaves as a light isotope of hydrogen [1,2]. With due regard for the large isotopic mass ratio ($m_{\text{Mu}}/m_{\text{H}} \approx 1/9$), the local structure and spectroscopic characteristics of muonium and hydrogen centres in solids are similar; this is well established for a variety of dielectric and semiconducting materials [1–4]. Muonium may therefore be used as a model for atomic hydrogen in materials where the behaviour of hydrogen itself is not known and in this Letter we present preliminary results for the solid state of sulphur.

The muonium states can be detected and characterised by μSR spectroscopy; this employs an unconventional detection technique which exploits the unique properties of muon production and decay but otherwise gives information similar to that from conventional magnetic resonance [1–3]. It is equally

sensitive to closed shell and open shell species. Early μSR studies found evidence for a muon–electron hyperfine coupling characteristic of a radical-like state in sulphur, by means of measurements of the magnetic field required to decouple the muon and electron spins [1]. Similar measurements made recently at ISIS (a) estimate the radical contact term as $A = 220 \pm 60$ MHz (together with a small anisotropic or dipolar term) and (b) find a second step in the decoupling suggestive of simultaneous detection of the muonium precursor, itself with a contact hyperfine constant lying between 50% and 100% of the vacuum-state value, i.e. between 2250 and 4500 MHz [5].

2. Level crossing resonance

Confirmation of this interpretation requires a spectroscopic signature of the radical state. In experiments at the PSI muon source we have therefore looked for the *level crossing resonance* [6] which

should occur in a magnetic field of $\pi A \left\{ \frac{1}{\gamma_{\mu}} - \frac{1}{\gamma_e} \right\} = 0.81 \pm 0.2$ mT. Roughly stated, this is the condition where the applied field tunes out the longitudinal component of the hyperfine field, leaving the muon to depolarize by precession about transverse components. (This is a property of the muon–electron hyperfine tensor; the scarce ^{33}S nuclei are not involved.) A weak but reproducible resonance is indeed detected [7]: the spectrum is given in Fig. 1.

The field for resonance, 857.5 ± 17 mT, corresponds to a hyperfine constant of

$$A = (\pm) 233 \pm 5 \text{ MHz.}$$

For a powder sample, this is the perpendicular component of the hyperfine tensor, although the narrow linewidth suggests a degree of motional averaging, so that the residual anisotropy is probably small. This is a more precise value than could be determined from the earlier decoupling measurements but the symmetric lineshape means that the sign remains indeterminate. The small amplitude of the resonance, together with indications that it narrows with increasing temperature, suggest motion about some privileged axis of rotation such that the level crossing is only weakly avoided: similar characteristics are known for C_{70}Mu – analogue of the monohydride of C_{70} – when the resonance for this radical is at the limits of detection [8].

3. Calculations and discussion

To assign this resonance, various possible chemical species must be considered. Firstly, there is a simple attachment of muonium to an S_8 ring by a three-centre bond, i.e. a muonium bridge [9]. Secondly, the ring can open to yield a chainlike species $\dot{\text{S}}-\text{S}_7-\text{Mu}$ with the radical electron at one terminal site and the muonium atom at the other. Thirdly, abstraction of S from the ring could yield a the diatomic species $\dot{\text{S}}\text{Mu}$; in support of this postulate, it is worth noting that the surface reaction of $\dot{\text{H}}$ atoms produced in a microwave discharge above elemental sulphur (itself at ambient temperature) is an excellent source of gas-phase sulfanyl radicals, $\dot{\text{S}}\text{H}$ [10].

In an attempt to distinguish between these possibilities, ab initio molecular orbital calculations using the program GAMESS95 were performed at the unrestricted Hartree–Fock (UHF) level using a 6-31G** basis set [11]. Table 1 lists the energies and muon–electron contact hyperfine coupling constants for various bridging configurations, namely for the muonium atom situated in the mean plane of the ring, both inside and outside, and directly above the centre of an S–S bond. (These sites are denoted ‘in’, ‘out’ and ‘up’, respectively.) The S–Mu distance is in each case set to the typical SH value of 120 pm and the S_8 ring is constrained to have the geometry

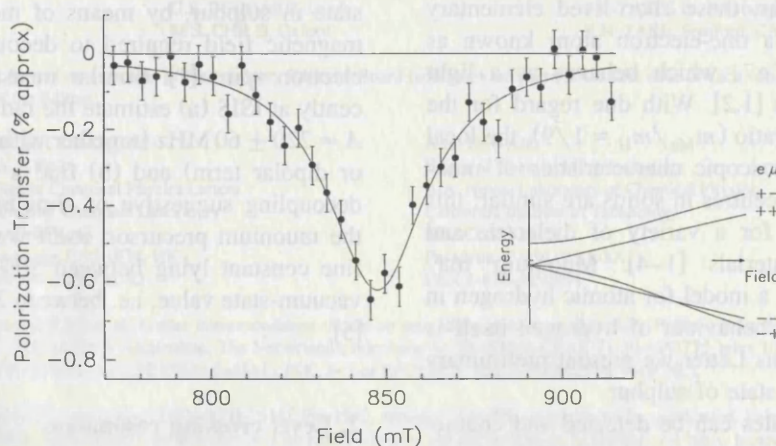
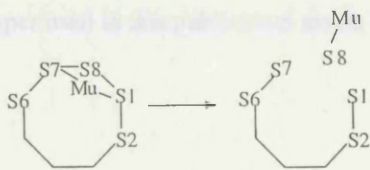


Fig. 1. Muon level crossing resonance in polycrystalline sulphur S_8 , recorded at about 50 K. The insert shows the relevant energy level diagram for the electron and muon spin states coupled by a predominantly isotropic hyperfine interaction of the form $A\mathbf{S} \cdot \mathbf{I}$ (drawn for A negative) but with a degree of anisotropy which is responsible for the avoidance of the crossing and consequent muon depolarization via mixing of the states $|--\rangle$ and $|+-\rangle$.

observed in crystalline γ -sulphur [12]. The energy differences between the reactants $S_8 + \text{Mu}$ and radicals $S_8\text{Mu}$ are positive in all cases and these sites prove unstable against geometry optimization. While noting that the value for A , the muon–electron hyperfine constant, of -163 MHz for the out position is the closest of the three to our experimental value we conclude that none of these bridging sites is a good candidate for the observed resonance.

For most starting sites for Mu about the S_8 ring, geometry optimization leads to an $\dot{S}-S_7-\text{Mu}$ radical having negligible muon–electron contact interaction. This species is a possible candidate for the fraction of implanted muons which appear from our muon spin rotation signal to reach electronically diamagnetic states (i.e. are responsible for a precession signal in transverse fields at or near the muon Larmor frequency). Again, it is not a candidate for the longitudinal field resonance.

We therefore focus our attention on the diatomic species $\dot{S}\text{Mu}$, i.e. the muonic analogue of the sulfanyl radical $\dot{S}\text{H}$. Sketched below is a schematic pathway to its formation in elemental sulphur. With muonium starting at an intra-annular bridging site (between atoms S1 and S7), optimization results in a dramatic elongation of both the S1–S8 and S7–S8 separations, i.e. a fragmentation yielding the radical $\dot{S}\text{Mu}$ together with the diradical S_7 . At the UHF level using the 6-31G** basis, the calculated energy difference $\Delta E = E(S_8\text{Mu}) - E(S_8) - E(\text{Mu})$ for the bridged species is 372 kJ mol^{-1} , while the difference $\Delta E = E(\text{SMu}) + E(S_7) - E(S_8) - E(\text{Mu})$ for the product state is -98 kJ mol^{-1} .



For this configuration, the calculated value for the muon–electron isotropic hyperfine interaction is -209 MHz , although this result is likely to be basis-set dependent. It is probably necessary to allow for the diffuse nature of the $S(3d)$ orbitals by inclusion of several polarization functions in the calculation. For this purpose we consider simply the isolated

Table 1

Calculated energies E_h , energy differences $\Delta E = E(S_8\text{Mu}) - E(S_8) - E(\text{Mu})$, and muon–electron hyperfine coupling constants A for different bridging sites of the $S_8\text{Mu}$ radical

Position of Mu	Energy E_h	$\Delta E/\text{kJ mol}^{-1}$	A/MHz
in	-3180.36161	558	-509
out	-3180.38714	491	-163
up	-3180.32313	659	81

$$E(S_8) = -3180.07606 E_h; E(\text{Mu}) = -0.49823 E_h.$$

diatomic species, changing the basis set to the McLean Chandler (MC) basis [11] and adding three sets of 3d functions on S with three sets of p functions on Mu or H. The computed energy of SMu or $\text{SH}^2\Pi$ at the UHF level is then $-398.004088 E_h$. The calculated equilibrium internuclear distance is 132.3 pm , to be compared with the experimental value of 134.07 pm for $\text{SH}^2\Pi$ [10]. The calculated spin density on the proton corresponds to a Fermi contact interaction of -57.8 MHz . This isotropic component of the proton–electron hyperfine coupling is in good accord with the experimental value for $\text{SH}^2\Pi_{3/2}$ despite a minor ambiguity (Ashworth and Brown give the Fermi contact term as -63.4 MHz in Table V of their paper [10] but the parameters of their Table III imply a value of -52.6 MHz). Being at the UHF level there is evidence of slight spin contamination, with $\langle S^2 \rangle$ equalling 0.77 rather than 0.75.

Scaled for the ratio of the muon to the proton magnetic moment (3.1883), our calculation predicts an isotropic muon–electron hyperfine term of -184 MHz for the isolated $\dot{S}\text{Mu}$ radical at equilibrium geometry. Allowance must in due course be made for the fact that the muon executes higher amplitude zero-point vibrations than the proton. A detailed theoretical investigation is underway to evaluate this isotope effect as well as solid-state influences on the structure. Pending the outcome of this we conclude that the species $\dot{S}\text{Mu}$, while by no means established, is the most promising candidate for the resonance of Fig. 1 to emerge from the present calculations. Further experimental studies are required before it can be distinguished positively from muonium bridging an S–S bond; such bridging sites do not appear in our optimizations of the $\text{Mu} + S_8$ system, from any starting configuration, but they

Orders, claims, and product enquiries: please contact the Customer Support Department at the Regional Sales Office nearest to you:

New York
Elsevier Science
P.O. Box 945
New York, NY 10159-0945
USA
Tel. (+1)212-633-3730
[Toll free number for North
American customers:
1-888-4ES-INFO (437-4636)]
Fax (+1)212-633-3680
e-mail: usinfo-f@elsevier.com

Amsterdam
Elsevier Science
P.O. Box 211
1000 AE Amsterdam
The Netherlands
Tel. (+31)20-4853757
Fax (+31)20-4853432
e-mail: ninfo-f@elsevier.nl

Tokyo
Elsevier Science
9-15 Higashi-Azabu 1-chome
Minato-ku, Tokyo 106
Japan
Tel. (+81)3-5561-5033
Fax (+81)3-5561-5047
e-mail: kyf04035@niftyserve.or.jp

Singapore
Elsevier Science
No. 1 Temasek Avenue
#17-01 Millenia Tower
Singapore 039192
Tel. (+65)434-3727
Fax (+65)337-2230
e-mail: asiainfo@elsevier.com.sg

Advertising information: Advertising orders and enquiries may be sent to: **International:** Elsevier Science, Advertising Department, The Boulevard, Langford Lane, Kidlington, Oxford OX5 1GB, UK, Tel. (+44)(0)1865 843565, Fax (+44)(0)1865 843976. **USA and Canada:** Weston Media Associates, Daniel Lipner, P.O. Box 1110, Greens Farms, CT 06436-1110, USA, Tel. (+1)(203)261-2500, Fax (+1)(203)261-0101. **Japan:** Elsevier Science Japan, Marketing Services, 1-9-15 Higashi-Azabu, Minato-ku, Tokyo 106, Japan, Tel. (+81)3-5561-5033, Fax (+81)3-5561-5047.

Electronic manuscripts: Electronic manuscripts have the advantage that there is no need for the rekeying of text, thereby avoiding the possibility of introducing errors and resulting in reliable and fast publication.

Your disk plus three, final and exactly matching printed versions should be submitted together. Double density (DD) or high density (HD) diskettes (3¹/₂ or 5¹/₄ inch) are acceptable. It is important that the file saved is in the native format of the wordprocessor program used. Label the disk with the name of the computer and wordprocessing package used, your name, and the name of the file on the disk. Further information may be obtained from the Publisher.

Authors in Japan please note: Upon request, Elsevier Science Japan will provide authors with a list of people who can check and improve the English of their paper (*before submission*). Please contact our Tokyo office: Elsevier Science Japan, 1-9-15 Higashi-Azabu, Minato-ku, Tokyo 106; Tel. (03)-5561-5032; Fax (03)-5561-5045.

Chemical Physics Letters has no page charges.

For a full and complete Instructions to Authors, please refer to *Chemical Physics Letters*, Vol. 272, No. 5,6, pp. 527-528. The instructions can also be found on the World Wide Web: access under <http://www.elsevier.nl> or <http://www.elsevier.com>.

© The paper used in this publication meets the requirements of ANSI/NISO Z39.48-1992 (Permanence of Paper)

Paramagnetic Muonium States in Elemental Sulfur

Brian Webster and Kirsty L. McCormack

Chemistry Department, University of Glasgow, Glasgow, G12 8QQ.

Roderick M. Macrae

Muon Science Laboratory, Institute of Physical and Chemical Research, (RIKEN), 2-1 Hirosawa, Wako-shi, Saitama 351-01, Japan.

Zero-point vibrational corrections are calculated by *ab initio* molecular orbital methods for the energy, and the reduced hyperfine tensor for the muonated sulfanyl radical $\text{SMu}^{\cdot 2}\text{II}$. Only a small α -isotope effect is found for the reduced isotropic muon-electron hyperfine coupling constant of SMu relative to SH . Interstitial muonium in S_8 is also investigated. The results are discussed in the light of recent observations on muonium in elemental sulphur.

Muonium, symbol Mu , is a bound state of an electron with a positive muon. With a half-life of a few microseconds the muon nucleus decays yielding positrons. Muons have a mass of about a ninth of the proton mass. Consequently muonium acts like a radioactive, light isotope of hydrogen and as such is used to simulate the behavior of hydrogen in semiconductors and other materials. After the stopping of muons in a sample, muonium forms by electron capture. Reaction with the substrate yields muonium-substituted radicals and diamagnetic species. The latter are characterized by only a single Larmor precession frequency and little is known about the diamagnetic species formed in most substances. In contrast, there is a wealth of data on muonium-substituted radicals obtained by the technique known as μSR , an acronym for muon spin rotation, relaxation, or resonance. Some recent, elegant reviews describe some experimental aspects of μSR while Claxton gives an interesting account of contemporary theoretical studies of muonium species [1,2,3].

Following the deposition of positive muons in elemental sulfur recent experiments suggest that at least three different species are created: a diamagnetic species, a molecular radical, and interstitial muonium. From repolarization measurements, determining the magnetic field needed to decouple the electron and muon spins, an estimate of 220 ± 60 MHz was obtained for the hyperfine interaction in this radical [4]. Most recently using

the technique of avoided level crossing resonance, ALC, the muon-electron hyperfine coupling constant for the radical was measured to equal 233 ± 5 MHz [5]. The sign for the hyperfine coupling constant was not determined.

It was proposed that this radical signal derives either from muonium, bridging an S-S bond in a simple three-centre arrangement, or from the extraction of a sulfur atom from S_8 to form a muonated sulfanyl radical SMu. Some preliminary calculations were presented on SMu and now we pursue these in more depth. First, we consider whether the zero-point vibrational excursions of large amplitude often encountered with Mu can significantly enhance the muon-electron hyperfine interaction in this α -radical, SMu, compared with a sulfanyl radical SH. For comparison with protium species, it is useful to cite muon-electron hyperfine coupling constants, A_μ , in a reduced form $A'_\mu = A_\mu (\mu_p/\mu_\mu) = 0.3141 A_\mu$, where μ_p is the magnetic moment of a proton and μ_μ is the muon magnetic moment. Accordingly the measured value of A'_μ is 73.2 ± 1.6 MHz for the reduced muon-electron hyperfine coupling constant of the radical detected in elemental sulfur.

Computational details and results

Aligning a sulfanyl radical $SH^2\Pi$ along the z-axis we have the choice of assigning the radical electron to a $2\pi_x$ or $2\pi_y$ orbital since SH is a degenerate open shell species. A ground state configuration for $SH^2\Pi$ is $1\sigma^2 2\sigma^2 3\sigma^2 1\pi^4 4\sigma^2 5\sigma^2 2\pi_x^2 2\pi_y^1$. Procedures for dealing with such cases are well-known, with Jackels and Davidson giving a clear account of equivalence-restricted open shell SCF theory [6]. In practice one performs an SCF calculation with fractional occupancy of the 2π orbitals as $2\pi_x^{1.5} 2\pi_y^{1.5}$. The effect is to maintain the degeneracy of the π levels and the total energy is slightly raised from that for the configuration noted above $2\pi_x^2 2\pi_y^1$. For example, taking the triple-zeta split valence McLean Chandler basis set, MC** [7], extended with three sets of 2p orbitals centred at H and one 3d set centred on S for $SH^2\Pi$, the computed energy of the configuration $2\pi_x^2 2\pi_y^1$ is $-398.092038 E_h$, and the orbital energies are $-0.39 E_h$ for $2\pi_x$ and $-0.22 E_h$ for $2\pi_y$. In the same basis the energy of SH with a configuration $2\pi_x^{1.5} 2\pi_y^{1.5}$ is $-398.050687 E_h$ and the degeneracy of $2\pi_x$ and $2\pi_y$ is maintained with the orbital energies equal at $-0.31 E_h$. The internuclear distance is 133 pm in both cases. This subtle change in calculation is required if one is interested in dissociation energies.

Here we are primarily concerned with the hyperfine interaction in $X\text{S } ^2\Pi$, $X = \text{T, D, H, and Mu}$ and anticipate that the calculation of this property requires the mixing of excited configurations of SH with the ground state configuration. We have allowed for all single excitations, CIS, and then all single and double excitations, CISD, using the configuration $2\pi_x^2 2\pi_y^1$ as a single reference configuration and the MC** basis for SH. A CISD calculation in this basis involves 22686 configurations. Using the program MELD the calculated equilibrium distance R_e is 133.8 pm for $\text{SH } ^2\Pi$ at the CISD level and the energy E_h is -398.272271 [8]. This calculated value for R_e is in good accord with the highly accurate experimental value of 134.06630 pm determined for $\text{SH } ^2\Pi$ by laser magnetic resonance measurements[9].

(a) Zero-point vibrational energies for isotopomers of SH.

A one-dimensional grid in the internuclear distance coordinate was constructed and the total energy, isotropic hyperfine coupling constant and the anisotropic hyperfine parameters in the principal magnetic axis system were calculated at each point. The energies were fitted to a Morse potential, the vibrational energies located, and the Morse zero-point wavefunction used to calculate vibrationally-modified values of each parameter. Table 1 lists values of the CISD Morse parameters R_e , D_e , ω_e and $\omega_e x_e$ for the isotopomers of SH. Figure 1 shows the potential energy curve with some of the energy levels for SMu. There are 8 vibrational levels below the dissociation limit compared with 23 levels calculated for $\text{SH } ^2\Pi$.

Calculations were performed with other basis sets and also at the UHF level. Table 2 lists the results. First, we will focus on the CISD MC** findings. Naturally the inclusion of zero-point vibrational effects distinguishes the isotopomers of SH. Recalling that the zero-point vibrational energy,

ZPE , is $\frac{1}{2}\omega_e - \frac{1}{4}\omega_e x_e$ the calculated value is 1402 cm^{-1} for SH. This

compares favorably with an experimental value of 1336 cm^{-1} for the zero-point vibrational energy of $\text{SH } ^2\Pi$ [10]. The zero-point vibrational level of SMu lies substantially higher in the potential curve at 4183 cm^{-1} . Figure 2 shows the probability distribution function $D(R)$ for the coordinate R . This function indicates the probability of observing the SX internuclear distance in the range dR at the point R . Clearly SMu has much wider excursions from the equilibrium value for R than SH and it is this behavior that usually leads to significant isotope effects for Mu in comparison with H and D. Accordingly

one finds that the expectation value $\langle R - R_e \rangle$ is 1.64 pm for SMu compared with 0.55 pm for SH and 0.39 for SD. Examination of Table 2 indicates that $\langle R - R_e \rangle$ does not show any significant basis set dependence.

Now we turn to the key question as to whether muonium, with a mass so different from hydrogen, produces a significant isotope effect on the hyperfine interaction in SMu.

(b) Hyperfine coupling in the isotopomers of SH $^2\Pi$

In an early study of the electron resonance spectrum of the sulfanyl radical SH, $^2\Pi_{3/2}$, Radford and Linzer sought a signature which could serve to identify interstellar SH [11]. Further investigations by Meerts and Dymanus using molecular beam electric resonance provided values of the magnetic parameters, a , b , and c for SH and its deuterium isotopomer SD [12]. For SH, Meerts and Dymanus report values, $a = 32.58(5.03)$ MHz, $b = -63.44(-9.65)$ MHz and $c = 32.44(4.95)$ MHz. The values noted in parentheses are their values for SD. From an EPR study of the proton hyperfine interactions in the gas phase for SH, Tanimoto and Uehara extracted a value for the magnetic parameter $d = 29 \pm 17$ MHz. These workers were unable to deduce all of the parameters independently but cite a value of -65 ± 3 MHz for the Fermi contact term in SH [13]. Using the technique of laser magnetic resonance Ashworth and Brown have determined values for the hyperfine parameters of SH described as significantly improved over previous work [9]. Taking $b + c/3$ to specify the value for A_{iso} one obtains -52.60 MHz for the isotropic proton electron hyperfine coupling constant of SH in its ground vibrational level. Using the parameters of Meerts and Dymanus A_{iso} is -52.63 MHz for SH and -8.0 MHz for SD. On scaling the deuterium result by 6.514 to allow for the different magnetic moment and spin of the deuteron compared with a proton, the equivalent proton coupling is -52.11 MHz. This shows that for the deuterium isotopomer the α -isotope effect amounts to about 0.52 MHz.

Now looking at Table 2 we see that for SH the CISD MC** calculations yield a value of -47.2 MHz for A_{iso} , as compared with values for the reduced coupling constant of -48.3 MHz for SMu and -47.0 MHz for SD. The sign of the muon-electron hyperfine coupling constant is not surprising when one recalls the simple spin polarization picture of this interaction [3]. The deuterium isotope effect of 0.2 MHz is less than predicted and the calculated muonium isotope effect is -1.1 MHz.

In the calculation of the isotropic hyperfine coupling constant for the isotopomers of SH there is some basis set dependence at the CISD level. A

smaller basis 6-31G **, having one H(2p) and one S(3d) set reduces the CI to just 5785 spin adapted configurations. For SH itself Table 2 shows that A_{iso} alters to -54.5 MHz again in fair agreement with experiment. A CIS calculation using the MC** basis involves just 201 spin adapted configurations and yields a value of -49.7 MHz of A_{iso} for SH. All of these results include the zero-point vibrational level correction to A_{iso} . The values at the equilibrium distance of SH specific to each calculation A_{iso}^e are noted beneath Table 2. However the isotope effects on A_{iso} are almost independent of the basis and the number of configurations involved in the calculation. The calculated deuterium shift is again 0.2 MHz and the largest muonium shift is -1.3 MHz. Both the CISD and CIS calculations clearly underestimate the isotope shift for D and probably for muonium.

Elsewhere, we have cited the value - 57.78 MHz for A_{iso}^e of SH as obtained from a conventional UHF calculation [5]. We include in Table 2 the corresponding zero-point vibrational corrections at this level where the basis is MC ** with three H(2p) and three H(3d) sets of polarisation functions. We see that the zero-point vibrational corrections to A_{iso} are now significantly larger than for the CI calculations. Figure 3 illustrates the difference between the types of calculation. Although with stretching of the S-H bond one expects the value of A_{iso} to become increasingly negative, a UHF calculation yields a negative spin density at the proton which rapidly increases as R increases from the equilibrium value. In the CI calculations this change is far less marked as we can see in the Figure. The UHF calculations produce a deuterium isotope effect of 0.8 MHz and the muonium isotope effect for the reduced coupling constant is -6.9 MHz for SMu. It is interesting to compare these UHF results with some values for the zero-point vibrationally corrected values of A_{iso} for OD, OH, and OMu [3,14] obtained by the UHF method with a standard 6-31G basis. For OH, the calculated value of A_{iso} is -38.6 MHz, which does not match the observed value of -74 MHz, but the calculated deuterium isotope effect is 0.8 MHz and the muonium isotope effect is -8.9 MHz for the reduced coupling constant of OMu.

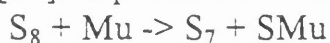
(c) The hyperfine tensor

Figure 4 illustrates the variation with internuclear distance of the anisotropic components T_{xx}' , T_{yy}' and T_{zz}' of the hyperfine interaction for SH $^2\Pi$. These results refer to the CISD calculation using the MC** basis. After averaging for the zero-point vibrational motion one obtains the vibrationally averaged components for the reduced hyperfine tensor. Values for A_{xx}' , A_{yy}' ,

and A_{zz}' , are listed in Table 2. The computed value for the anisotropic components are nearly independent of the level of calculation. It is the different computed values for A_{iso}' which lead to the changes in A_{xx}' , A_{yy}' , and A_{zz}' , at each level of calculation. It is important to note that these results pertain to a non-rotating molecule. In the vapour phase one expects the measured anisotropic terms to be significantly smaller due to rotational averaging. Even so there remains a significant anisotropy in the hyperfine interaction of $SH^2\Pi_{3/2}$. The magnetic b parameter, which provides the value for the perpendicular component of the hyperfine interaction is - 63.409 MHz [9].

(d) The Muonium Radical in S_8 .

Elsewhere we describe the calculations which led us to conjecture that Mu could abstract S from S_8 following the deposition of positive muons in a sulfur sample[5]. Briefly, by bridging of next-nearest neighbour sulfur atoms in γ -sulfur, taking the geometry from the observed crystal structure, geometry optimisation led to ring opening to yield SMu and a diradical S_7 . The bridged structure is 367 kJ mol⁻¹ higher in energy than the reactants, and the products are -104 kJ mol⁻¹ lower in energy than the reactants. These calculations were performed using the GAMESS program at the UHF level with a 6-31G** basis [15]. A possible reaction is



though whether it is epithermal muonium which engages in such a reaction is a matter of speculation. However it is desirable that following the extraction of S, ring closure occurs to S_7 so that no other paramagnetic species remain in evidence. It is worth noting that the surface reaction of H with S_8 is a ready source of SH radicals for vapour phase studies [9].

The computed equilibrium value for A'_{μ} in the SMu... S_7 aggregate is - 65.6 MHz. After allowance now for a zero-point correction of -8 MHz, which is appropriate for an isolated SMu radical in this basis at the UHF level we find A'_{μ} is -73.6 MHz. We recall that the measured value of A'_{μ} is 73.2 ± 1.6 MHz. The similarity between the calculated and observed values is indeed striking and it is this fact which led us to tentatively assign the muonium radical observed in S_8 as SMu.

From the present investigation we now know that the UHF method as applied to SMu is strongly basis set dependent and probably overestimates zero-point vibrational corrections to A'_{μ} . It is essential to note that, in contrast with SH in the gas phase, the radical detected in S_8 is likely to be

orientated particularly at low temperatures. The measured hyperfine interaction by ALC for the sulfur sample is described as representing the perpendicular component of the hyperfine tensor. From the CISD calculations using the MC** basis on SMu we find a value of -71.7 MHz for the A_{xx} component of the reduced hyperfine tensor of SMu. This calculation, we know, slightly underestimates the hyperfine interaction. Again this result matches well the observed coupling constant.

(e) Interstitial Muonium in S_8 .

Calculations at the UHF level using a 6-31G basis with a single p and d set of polarisation functions are likely to be more accurate for investigating the hyperfine interaction involving interstitial muonium with a single electron localized on Mu. Figure 5 shows the interstitial site investigated here with Mu positioned along the interatomic vector between atoms S and S(A) in a crystal of γ -sulfur[16]. Table 3 lists the variation in the energy and muonium coupling constant A_μ with motion of the Mu along this vector. We see that the energetically favored site is at the midpoint of the vector 199 pm from either S. This position also corresponds with the highest calculated value for the hyperfine coupling constant, equal to 4013 MHz. This is slightly lower than the value of A_μ for muonium *in vacuo* of 4463.3 MHz or 4509 ± 3 MHz for muonium in quartz.

Figure 6, which is a spline-fit to the calculated points, shows that the hyperfine interaction decreases rapidly with motion of Mu away from the midpoint of the vector towards S. Displacement by 50 pm towards S, roughly halves the contact interaction to 2339 MHz. Similarly a displacement by 50 pm towards S(A) reduces the contact hyperfine interaction even more to 1654 MHz.

Experimentally, a muonium precursor of the radical observed in S_8 is also detected [4]. This muonium species has a contact hyperfine interaction estimated to lie between 50% and 100% of the *in vacuo* value. It seems highly likely that this species is interstitial muonium oscillating about the midposition between a pair of atoms as S and S(A). It is interesting that muonium and muonium radicals appear to coexist. If this is the case it leads one to surmise, by analogy of muonium behavior in fullerenes, that perhaps there are topologically distinct subspaces in S_8 , separated by a barrier, possessing qualitatively different reactivity to muonium.

Conclusions

From the CISD and CIS calculations we find that the zero-point vibrational correction to the reduced muon-electron isotropic hyperfine coupling constant in a muonated sulfanyl radical $\text{SMu } ^2\Pi$ is small and probably about -3MHz. Of itself this is insufficient to enhance the experimental, gas phase, coupling constant of $\text{SH } ^2\Pi$ to approach the value observed for the muonium radical in S_8 . However the zero-point vibrationally averaged component A_{xx} of the reduced hyperfine tensor does match well with the observed hyperfine interaction and we should anticipate that the radical is orientated in the powder sample.

A definitive assignment of this radical requires further theoretical and experimental studies. In particular, ALC measurements are needed of the temperature and orientational dependence of the radical signal using a crystalline γ -sulfur sample. ALC observations using a sample enriched with ^{33}S will prove enlightening. Calculations, using some CI, on the behavior of Mu in S_8 and $^{77}\text{Se}_8$ are in progress.

Acknowledgments

We thank Professor S. F. J. Cox for many stimulating discussions on this topic and one of us (K. M.) expresses her gratitude to the EPSRC for the award of a grant.

References

1. E. Roduner, *Chem. Soc. Revs.*, 1993, **22**, 337.
2. S. F. J. Cox, *J. Phys. C: Solid State Physics*, 1987, **20**, 3187.
3. T. A. Claxton, *Chem. Soc. Revs.*, 1995, **24**, 437.
4. S. F. J. Cox, S. P. Cottrell, G. A. Hopkins, M. Kay and F. L. Pratt, *Hyp. Int.*, 1996, in press
5. S. F. J. Cox, I. D. Reid, K. L. McCormack and B. C. Webster, *Chem. Phys. Letts.*, to be published.
6. C. F. Jackels and E. R. Davidson, *Int. J. Quantum Chem.*, 1974, **VIII**, 707.
7. A. D. McLean and G. S. Chandler, *J. Chem. Phys.*, 1980, **72**, 5639.

8. E. R. Davidson et alia, *Quantum Chem. Program Exchange*, Program 580.
9. S. H. Ashworth and J. M. Brown, *J. Mol. Spectrosc.*, 1992, **153**, 41.
10. R. S. Ram, P. F. Bernath, R. Engleman, Jr. and J. W. Brault, *J. Mol. Spectrosc.*, 1995, **172**, 34.
11. H. E. Radford and M. Linzer, *Phys. Rev. Letts.*, 1963, **10**, 443.
12. W. L. Meerts and A. Dymanus, *Can. J. Phys.*, 1975, **53**, 2123.
13. M. Tanimoto and H. Uehara, *Mol. Phys.*, 1973, **25**, 1193.
14. T. A. Claxton, A. M. Graham, S. F. J. Cox, D. M. Maric, P. F. Meier, and S. Vogel, *Hyp. Int.*, 1990, **65**, 913.
15. M. W. Schmidt, K. K. Baldrige, J. A. Boatz, S. T. Elbert, M. S. Gordon, J. J. Jensen, S. Koseki, N. Matsunaga, K. A. Nguyen, S. Su, T. L. Windus, M. Dupuis and J. A. Montgomery, *J. Comput. Chem.*, 1993, **14**, 1347.
16. A. C. Gallacher and A. A. Pinkerton, *Acta Cryst.*, 1993, **C49**, 125.

Table 1. Calculated Morse parameters at the CISD level, equilibrium internuclear distance R_e /pm, dissociation energy wavenumber D_e /cm⁻¹, fundamental vibrational wavenumber ω_e /cm⁻¹ for the isotopomers of SH ²Π.

XS	R_e	D_e	ω_e	$\omega_e x_e$
Mu	133	35842	8234	483
H			2832	56
D			2033	29
T			1686	20

Table 2. Zero-point vibrational wavenumbers ZPE/cm^{-1} , expectation values $\langle R - R_e \rangle$ for the internuclear distance R/pm , vibrationally averaged reduced isotropic hyperfine coupling constants, A_{iso}' / MHz , and vibrationally averaged components of the hyperfine tensor A_{xx}' / MHz , A_{yy}' / MHz , A_{zz}' / MHz , calculated at CIS, CISD, and UHF levels for isotopomers of SH $^2\Pi$.

BASIS, LEVEL	XS X	ZPE	$\langle R - R_e \rangle$	A_{iso}'	A_{xx}'	A_{yy}'	A_{zz}'
MC**	Mu	4183	1.52	-51.0	-74.6	-49.0	-29.4
CIS ^a	H	1448	0.51	-49.7	-73.3	-48.1	-27.7
	D	1043	0.37	-49.5	-73.1	-48.0	-27.5
	T	865	0.30	-49.5	-73.0	-47.0	-27.4
MC**	Mu	4041	1.64	-48.3	-71.7	-45.6	-27.5
CISD ^b	H	1402	0.55	-47.2	-70.6	-44.8	-26.0
	D	1009	0.39	-47.0	-70.5	-44.9	-25.7
	T	838	0.33	-46.0	-70.4	-44.8	-25.6
6-31G**	Mu	4005	1.51	-55.8	-79.1	-54.2	-34.1
CISD ^c	H	1392	0.57	-54.5	-77.8	-53.4	-34.3
	D	1002	0.41	-54.3	-77.6	-53.2	-32.2
	T	832	0.34	-54.2	-77.5	-53.2	-32.2
MC**	Mu	4139	1.46	-67.4			
UHF ^d	H	1436	0.54	-60.5			
	D	1034	0.39	-59.7			
	T	858	0.32	-59.3			

a: $A_{iso}^e = -49.1 \text{ MHz}$, b: $A_{iso}^e = -46.6 \text{ MHz}$, c: $A_{iso}^e = -53.9 \text{ MHz}$, d: $A_{iso}^e = -57.8 \text{ MHz}$.

Table 3. Calculated Energies E_n at the UHF level, 6-31G** basis, for an interstitial muonium atom in sulfur, $R(\text{Mu}\dots\text{S})/\text{pm}$ distant from one S_8 molecule and $R(\text{Mu}\dots\text{S}(\text{A}))/\text{pm}$ from a second molecule, and values for the isotropic hyperfine coupling constant A_μ/MHz .

$R(\text{Mu}\dots\text{S})/\text{pm}$	$R(\text{Mu}\dots\text{S}(\text{A}))/\text{pm}$	E_n	A_μ/MHz
49	349	-6358.1815	1240
99	299	-6360.4470	440
149	249	-6360.5658	2339
199	199	-6360.5794	4013
249	149	-6360.5693	1654

Figure Legends.

Fig.1 A Morse Potential energy curve for $\text{SMu } ^2\Pi$ calculated at the CISD level.

Fig.2 Probability distributions for the zero-point level of SH, upper curve, and SMu, lower curve.

Fig.3 A comparison of the reduced muon-electron isotropic hyperfine coupling constant A_{iso}' /MHz with internuclear distance R/pm calculated at the CISD level, upper dotted curve, with a UHF calculation, lower curve, using an MC** basis in each case.

Fig.4 The variation with internuclear distance R/pm of the calculated components of the reduced anisotropic interaction for SMu, T_{xx}' /MHz, diamond curve, T_{yy}' /MHz, star curve, and T_{zz}' /MHz, squares curve.

Fig.5 An interstitial site for muonium in the unit cell of γ -sulfur.

Fig.6 The calculated variation with S-S(A) distance, R/pm , of the isotropic hyperfine coupling constant A_{iso} for interstitial Mu in S_8 .

FIGURE 1

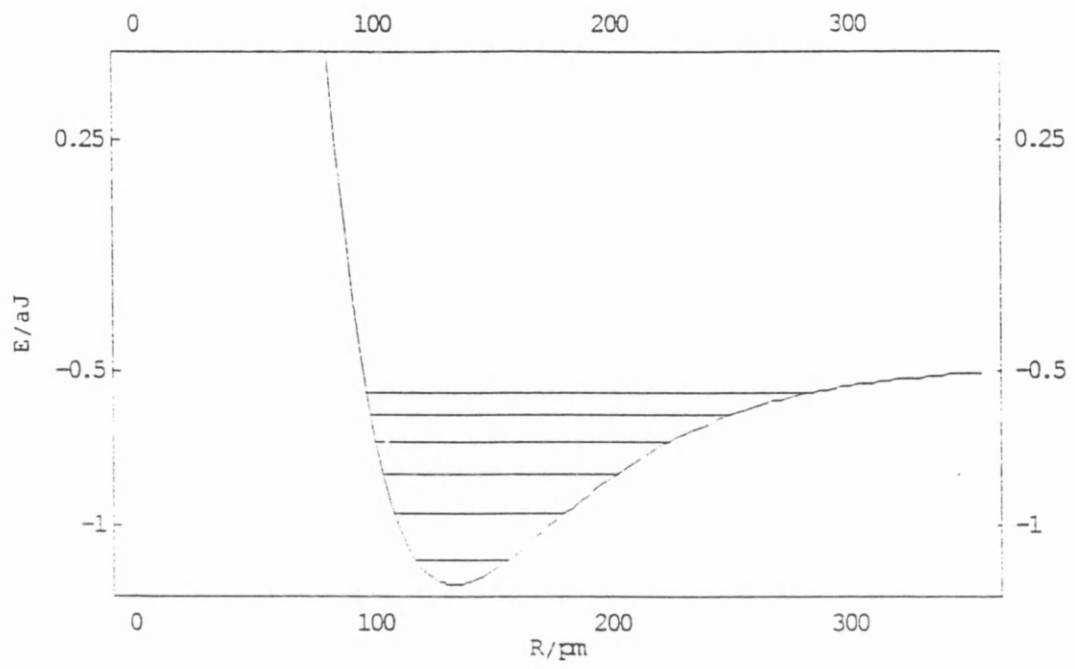


FIGURE 2

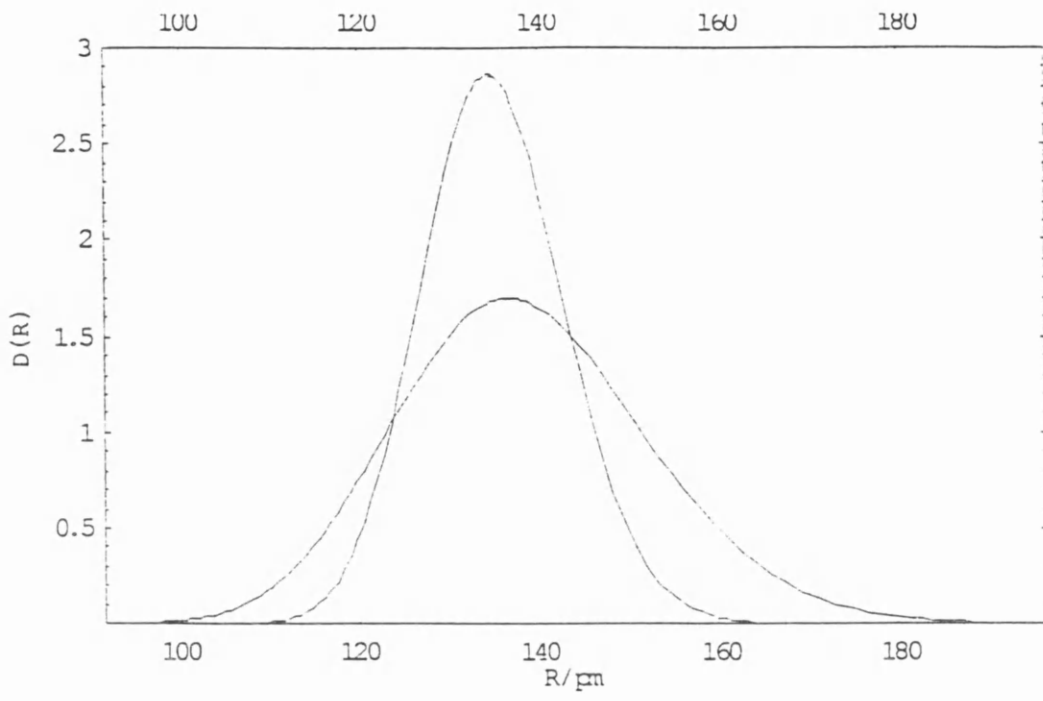


FIGURE 3

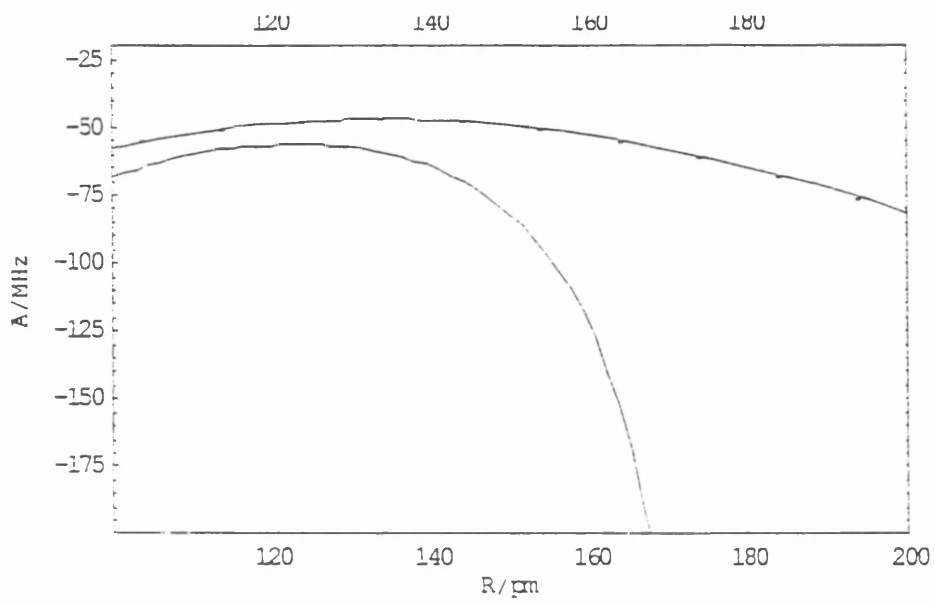


FIGURE 4

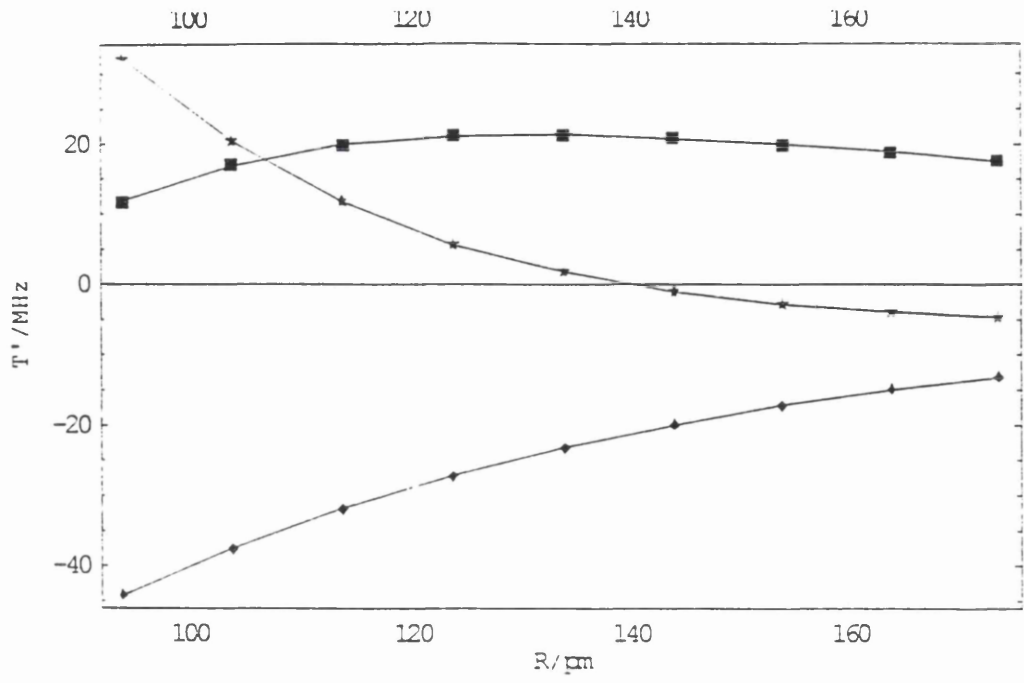


FIGURE 5

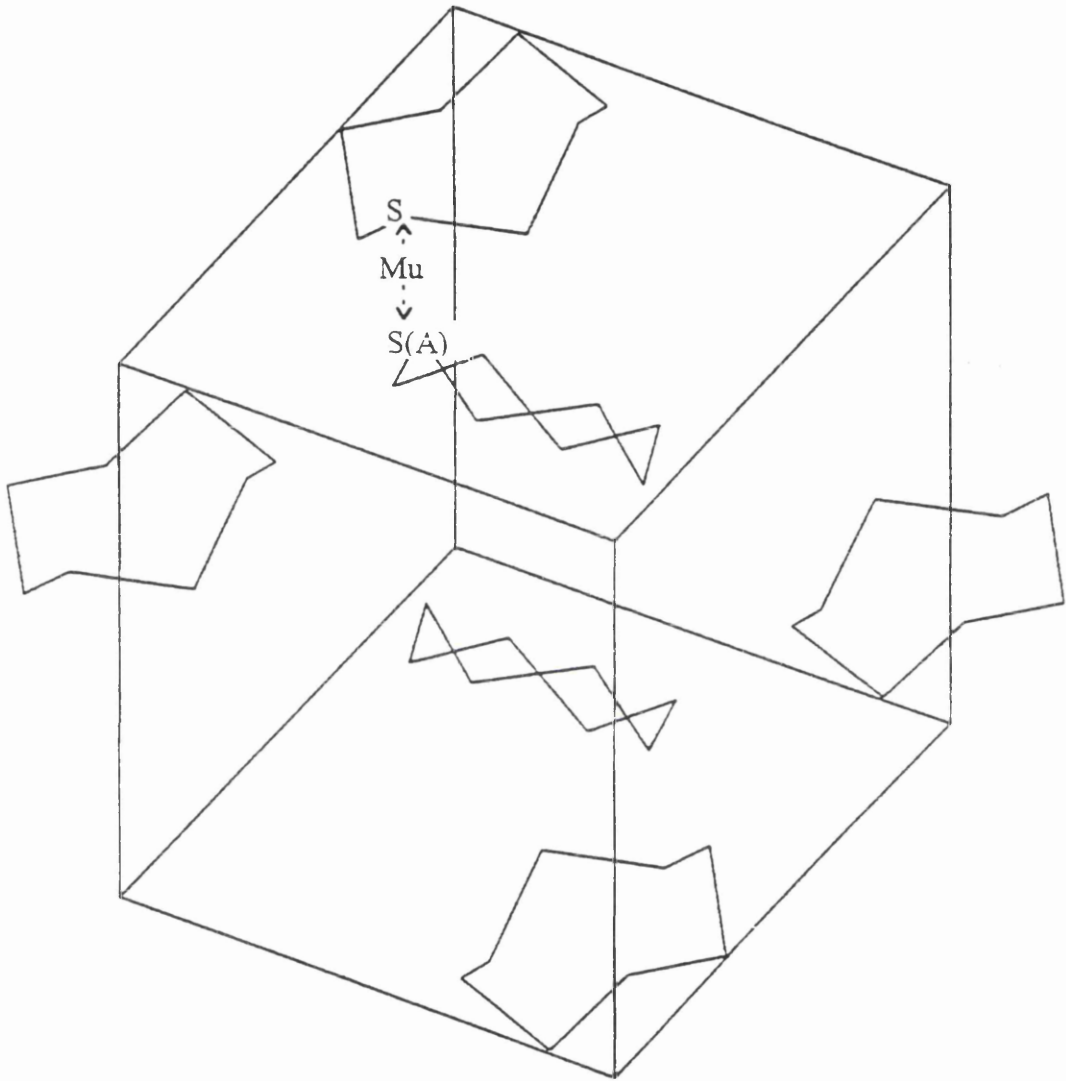


FIGURE 6

